

GROWTH AND SURFACE CHARACTERISTICS OF OXIDE  
THIN FILMS FOR CHEMICAL SENSOR APPLICATIONS

By

DARREN R. BURGESS

A DISSERTATION PRESENTED TO THE GRADUATE SCHOOL  
OF THE UNIVERSITY OF FLORIDA IN PARTIAL FULFILLMENT  
OF THE REQUIREMENTS FOR THE DEGREE OF  
DOCTOR OF PHILOSOPHY

UNIVERSITY OF FLORIDA

1999

STONHURST  
PARCHMENT DEED  
100% COTTON PAPER

Copyright 1999  
by  
Darren R. Burgess

SOUTHWORTH  
FARMHMENT DEED  
100% COTTON FIBER

To My Wife,

Dana

## ACKNOWLEDGMENTS

I would like to express my gratitude to Professor Tim Anderson, my thesis advisor, whose forward thinking in the area of graduate education made this highly valuable industrial Ph.D. thesis research program possible. His numerous trips to Wilmington, DE, during the progress of this research are greatly appreciated.

I am extremely grateful to Dr. Pat Morris Hotsenpiller for serving as my mentor and thesis co-advisor. Her patience and guidance during my time at the Experimental Station are greatly appreciated. Her steadfast teaching of the value of pursuing scientific excellence by example in her own research for The DuPont Company has been invaluable in my training. Also, her end goal of having me pursue whatever career I believed would be fulfilling is an invaluable trait which I greatly admire.

The DuPont Company especially Drs. Jan Lerou, Kathy Saturday and Jim Trainham are thanked for providing me with the research funding and opportunity to gain industrial experience during my graduate education.

Mr. George Wilson will always have my appreciation for his constant willingness to teach me about the construction, operation and maintenance of all types of laboratory equipment. Without his broad knowledge in these areas, many experiments would have been far more difficult to perform.

Drs. Jim Hohman, Stephens Thé and Sandy Witman, along with other former members of the reaction engineering research group, are thanked for their efforts in helping to start my research at DuPont and always being available to help in any way thereafter.

Drs. Kirstine Myers and Jim McCambridge are thanked for their efforts in teaching me to use the x-ray diffraction equipment which is under the supervision of the DuPont superconductivity group.

Mr. Scott McLean is thanked for his unselfish willingness to perform a large amount of analysis by atomic force microscopy which proved to be very valuable in the explanation of various results.

Dr. Victor Lusvardi is thanked for sharing his expertise in UHV material analyses and his willingness to do x-ray photoelectron spectroscopy analysis. His camaraderie and encouragement in the last year of my research are also appreciated.

The staff and my colleagues at the University of Florida Department of Chemical Engineering especially Shirley Kelly, Nancy Krell, Bill Epling, Todd Dann and Michelle Griglione are thanked for helping with the many tasks I could not perform while I was away from campus.

My family and friends are thanked for their endless support and encouragement during my graduate education. Dr. Howard Gerlach is especially appreciated for being a mentor in recent years.

Very special thanks and gratitude are reserved for my wife, Dana, who has shown unlimited patience and understanding throughout my graduate education. Ultimately, I am thankful to the Lord for His grace and mercy.

## TABLE OF CONTENTS

	<u>Page</u>
ACKNOWLEDGMENTS.....	iv
LIST OF TABLES.....	xi
LIST OF FIGURES.....	xii
ABSTRACT.....	xvii
CHAPTERS	
1. INTRODUCTION.....	1
1.1 Motivation.....	1
1.2 Objective.....	2
1.3 Approach.....	2
2. LITERATURE REVIEW.....	4
2.1 Rutile Thin Film Deposition.....	4
2.1.1 Physical Vapor Deposition.....	5
2.1.2 Chemical Vapor Deposition.....	5
2.1.2.1 Metalorganic chemical vapor deposition.....	7
2.1.2.2 CVD related techniques.....	7
2.1.3 Heteroepitaxy.....	8
2.2 Rutile Gas Sensors.....	11
2.2.1 Oxygen Sensors.....	11
2.2.2 Humidity Sensors.....	12
2.3 Rutile Properties.....	13
2.3.1 Crystal and Band Structure.....	13
2.3.2 Conductivity.....	16
2.3.2.1 Defects and mechanism.....	16
2.3.2.2 Activation energy and mobility.....	19
2.3.2.3 Intrinsic band-gap states.....	21
2.3.3 Doped rutile.....	21

2.3.3.1 Donor and acceptor defect chemistries.....	21
2.3.3.2 Structure and conductivity effects.....	22
2.3.4 UHV Surface Characterization.....	24
2.3.4.1 (110)-oriented rutile.....	25
2.3.4.2 (100)-oriented rutile.....	25
2.3.4.3 (001)-oriented rutile.....	25
2.4 Other Metal Oxides.....	26
2.4.1 Gallium Oxide.....	26
2.4.1.1 Deposition.....	26
2.4.1.2 Gas sensitivity.....	27
2.4.2 Aluminum oxide.....	27
<b>3. EXPERIMENTAL METHODS.....</b>	<b>29</b>
3.1 Thin Film Deposition.....	29
3.1.1 Reactors.....	29
3.1.2 Precursors.....	33
3.1.3 Substrates.....	34
3.1.4 Ion-Beam Sputter Deposition.....	35
3.2 Physical Characterization.....	36
3.2.1 X-ray Diffraction.....	36
3.2.2 Rutherford Backscattering Spectrometry.....	38
3.2.3 Atomic Force Microscopy.....	41
3.2.4 X-ray Photoelectron Spectroscopy.....	45
3.2.5 Secondary Ion Mass Spectrometry and Auger Electron Spectroscopy.....	46
3.3 Electrical Characterization.....	48
3.3.1 Sample Preparation.....	48
3.3.2 Environmental Chamber.....	50
3.3.2.1 Chamber design.....	50
3.3.2.2 Testing procedure.....	52
3.3.2.3 Sample heaters.....	53
3.3.3 Impedance Measurements.....	53
3.3.3.1 Theory of measurement.....	54
3.3.3.2 Calculations from impedance measurements.....	55
3.3.3.3 Data approximations.....	57
3.4 Equipment Safety.....	59

4. RUTILE FILM DEPOSITION.....	60
4.1 Undoped Rutile Films.....	60
4.1.1 Deposition.....	60
4.1.1.1 Precursor deposition efficiency.....	60
4.1.1.2 Precursor.....	61
4.1.1.3 Activation energy.....	63
4.1.2 Crystalline Quality.....	65
4.1.2.1 Bulk crystalline quality.....	65
4.1.2.2 Heteroepitaxy.....	68
4.1.3 Morphology.....	70
4.1.3.1 Orientational effects.....	70
4.1.3.2 Substrate effects.....	79
4.2 Doped Rutile Films.....	81
4.2.1 Deposition.....	82
4.2.1.1 Bulk dopant concentration.....	82
4.2.1.2 Surface dopant concentration.....	83
4.2.2 Nb-doping Structural Effects.....	87
4.2.2.1 Bulk crystal structure.....	87
4.2.2.2 Surface morphology.....	91
4.2.3 Ga-doping Structural Effects.....	94
4.2.3.1 Bulk crystal structure.....	94
4.2.3.2 Surface morphology.....	98
4.3 Summary.....	101
4.3.1 Undoped Rutile Film Deposition.....	101
4.3.2 Doped Rutile Film Deposition.....	102
5. RUTILE GAS SENSORS.....	104
5.1 Film Orientation Results Summary.....	104
5.2 Film Orientation Discussion.....	106
5.2.1 Measurements.....	106
5.2.2 Mechanisms.....	108
5.2.2.1 Film conductivity.....	108
5.2.2.2 Activation energy.....	109
5.2.2.3 Oxygen sensitivity.....	111

5.2.2.4 Humidity sensitivity.....	112
5.2.3 (101) and (001) Orientations Comparison.....	113
5.2.3.1 Surface Morphology.....	113
5.2.3.2 Surface Chemistry.....	121
5.2.3.3 Electron Mobility.....	123
5.2.4 (100) Orientation Discussion.....	125
5.3 Film Composition Results Summary.....	128
5.4 Nb-doped films.....	130
5.4.1 Nb-doped Film Results.....	130
5.4.2 Nb-doped Films Discussion.....	132
5.4.2.1 Oxygen sensitivity.....	132
5.4.2.2 Humidity sensitivity.....	133
5.5 Other Compositions.....	134
5.5.1 Undoped and Ga-doped Films Results.....	134
5.5.2 Undoped Films Discussion.....	135
5.5.3 Ga-doped Films Discussion.....	139
5.5.3.1 Carbon monoxide sensitivity.....	140
5.5.3.2 Sensitivity with other dopants.....	141
5.5.3.3 P-type conducting films.....	142
5.5.3.4 Adsorption enhancement by a thin surface layer.....	145
5.5.3.5 Adsorption enhancement by film reduction.....	148
5.5.4 Mobility and Composition.....	155
5.6 Engineering Sensitivity Assessment.....	156
5.7 Summary.....	159
 6. METAL OXIDE FILM DEPOSITION.....	 161
6.1 Gallium Oxide.....	161
6.2 Aluminum Oxide.....	171
6.3 Summary.....	174
 7. CONCLUSIONS AND RECOMMENDATIONS FOR FUTURE WORK.....	 176
7.1 Conclusions.....	176
7.1.1 Undoped Rutile Film Deposition.....	176
7.1.2 Doped Rutile Film Deposition.....	177
7.1.3 Rutile Gas Sensors.....	178

7.1.4	Deposition of Other Metal Oxides.....	180
7.2	Recommendations for Future Work.....	180
7.2.1	Undercoordinated Surface Cation Reactivity.....	180
7.2.1.1	Zinc Oxide.....	180
7.2.1.2	Sensitivity to other donor- or acceptor-type molecules.....	181
7.2.1.3	UHV analyses.....	181
7.2.2	Tailored Materials.....	182
7.2.3	P-type Conducting Sensors.....	182
7.2.4	Gallium Oxide Films.....	183
	REFERENCES.....	184
APPENDIX		
SAFETY DOCUMENTATION FOR GAS SENSITIVITY		
	EXPERIMENTS.....	196
	BIOGRAPHICAL SKETCH.....	222

## LIST OF TABLES

<u>Table</u>	<u>Page</u>
2.1 Cationic and anionic lattice mismatch for heteroepitaxial rutile deposited on sapphire substrates.....	10
2.2 Oxygen sensor examples.....	12
2.3 Humidity sensor examples.....	13
2.4 Dominant impurity trends in TiO <sub>2</sub> .....	19
2.5 Representative activation energy and mobility data for TiO <sub>2</sub> .....	20
3.1 Growth variable ranges for quartz reactor growth study.....	30
3.2 Sublimation temperatures of metal precursors determined by TGA...	34
4.1 Reported rutile growth rate dependence on Ti precursor.....	62
4.2 Reported MOCVD of TiO <sub>2</sub> growth rate activation energies.....	65
5.1 A measure of photoreactivity as a function of thin film orientation....	123
6.1 Summary of Ga <sub>2</sub> O <sub>3</sub> growth from Ga(TMHD) <sub>3</sub> precursor.....	164
6.2 Dangling bond densities of surface oxygen atoms.....	166
6.3 Summary of Al <sub>2</sub> O <sub>3</sub> growth from Al(TMHD) <sub>3</sub> precursor.....	173

## LIST OF FIGURES

<u>Figure</u>	<u>Page</u>
2.1 Rutile unit cell. From A. von Hippel et al. <sup>77</sup> , Fig. 2.....	14
3.1 Solid source MOCVD reactor schematic.....	30
3.2 Precursor schematic.....	33
3.3 Thin film x-ray diffraction geometry.....	38
3.4 Schematic of essential Rutherford backscattering equipment.....	39
3.5 RBS spectra of TiO <sub>2</sub> on sapphire with RUMP model.....	41
3.6 AFM equipment schematic (Courtesy of R. S. McLean).....	43
3.7 TM AFM images of a Ga <sub>2</sub> O <sub>3</sub> thin film (a) normal and (b) phase shift.....	44
3.8 Schematic of alumina sample holder with attached film.....	49
3.9 Environmental chamber feedthrough schematic.....	51
3.10 Environmental chamber gas flow architecture schematic.....	51
3.11 Impedance bridge simplified measurement circuit schematic.....	55
3.12 Complex impedance data as a function of sample temperature for an undoped (101)-oriented rutile thin film in N <sub>2</sub> .....	57
3.13 Complex Z plot for 1e9 Ω resistor in parallel with 1 pF capacitor.....	58
3.14 Complex Z plot for 5e9 Ω resistor in parallel with 1 pF capacitor.....	58
4.1 Rutile film growth rate as a function of Ti or O <sub>2</sub> partial pressure.....	61
4.2 Logarithm of growth rate as a function of reciprocal temperature.....	64
4.3 Rc fwhm of undoped rutile XRD peaks as a function of substrate temperature and deposition reactor.....	66
4.4 (100) rutile XRD peak rc fwhm as function of PO <sub>2</sub> .....	68
4.5 (001)-oriented 70 Å rutile film AFM image.....	71

4.6	(001)-oriented 400 Å rutile film AFM image.....	71
4.7	(001)-oriented 3350 Å rutile film AFM image.....	72
4.8	(101)-oriented 70 Å rutile film AFM image.....	72
4.9	(101)-oriented 400 Å rutile film AFM image.....	73
4.10	(101)-oriented 3350 Å rutile film AFM image.....	73
4.11	(100)-oriented 70 Å rutile film AFM image.....	74
4.12	(100)-oriented 400 Å rutile film AFM image.....	74
4.13	(100)-oriented 3350 Å rutile film AFM image.....	75
4.14	RMS roughness as a function of thickness taken from AFM images of undoped oriented rutile films and their respective sapphire substrates.....	75
4.15	Characteristic planar dimension of surface features as a function of film thickness for undoped, oriented rutile films.....	77
4.16	Ratio of characteristic height to planar dimension of surface features as a function of film thickness for undoped, oriented rutile films.....	79
4.17	(0001)-oriented sapphire.....	80
4.18	(11 $\bar{2}$ 0)-oriented sapphire with unremovable surface features.....	80
4.19	(101)-oriented 70 Å rutile film on "featured" (11 $\bar{2}$ 0) sapphire substrate.....	81
4.20	(101)-oriented 3350 Å rutile film on "featured" (11 $\bar{2}$ 0) sapphire substrate.....	81
4.21	XPS spectra of Ga 2p <sub>3/2</sub> core electron binding energy for Ga atom in (001)-oriented rutile thin film.....	84
4.22	Ga 2p <sub>3/2</sub> core electron binding energy as a function of Ga oxidation state.....	85
4.23	Nb 3d <sub>5/2</sub> core electron binding energy as a function of Nb oxidation state.....	86
4.24	XPS spectra of Nb 3d <sub>5/2</sub> and 3d <sub>3/2</sub> core electron binding energies for Nb atom in (001)-oriented rutile thin film.....	87
4.25	(002) rutile plane d-spacing as a function of Nb doping.....	89
4.26	(101) rutile plane d-spacing as a function of Nb doping.....	89

4.27	(001) and (101) rutile peak $\theta$ rc fwhm as a function of Nb doping.....	90
4.28	(001) and (101) rutile $\phi$ scan peak fwhm as a function of Nb doping.....	91
4.29	Nb-doped (001)-oriented thin film AFM images (a) 70 Å (b) 3350 Å.....	92
4.30	Nb-doped (101)-oriented thin film AFM images (a) 70 Å (b) 3350 Å.....	92
4.31	Nb-doped (100)-oriented thin film AFM images (a) 70 Å (b) 3350 Å.....	93
4.32	(002) rutile plane d-spacing as a function of Ga doping.....	94
4.33	(101) rutile plane d-spacing as a function of Ga doping.....	95
4.34	(001) and (101) rutile peak $\theta$ rc fwhm as a function of Ga doping.....	97
4.35	(001) and (101) rutile $\phi$ scan peak fwhm as a function of Ga doping.....	98
4.36	Ga-doped (001)-oriented thin film AFM images (a) 70 Å (b) 3350 Å.....	99
4.37	Ga-doped (101)-oriented thin film AFM images (a) 70 Å (b) 3350 Å.....	99
4.38	Ga-doped (100)-oriented thin film AFM images (a) 70 Å (b) 3350 Å.....	100
5.1	Conducting electrons removed as a function of film orientation calculated from resistance values measured in N <sub>2</sub> and O <sub>2</sub> atmospheres at 240 °C.....	105
5.2	Conducting electrons added as a function of film orientation calculated from resistance values measured in N <sub>2</sub> and humidified N <sub>2</sub> atmospheres at 240 °C.....	106
5.3	Activation energy of conductance as a function of film orientation in different atmospheres.....	110
5.4	Surface proton conduction on undoped thin film near room temperature and electronic conductivity at higher temperatures measured over several temperature cycles.....	113
5.5	Orientation stability diagram for rutile at 1273K.....	115

5.6	AFM images of (001)-oriented rutile thin films (a) deposited by MOCVD (b) deposited by IBSD.....	116
5.7	Schematic of facets on (001)-oriented rutile surface.....	117
5.8	AFM images of (101)-oriented rutile films (a) deposited by MOCVD on "smooth" substrate (b) deposited by MOCVD on "featured" substrate (c) deposited by IBSD.....	117
5.9	Schematic of facets on (101)-oriented rutile IBSD and MOCVD deposited surfaces.....	119
5.10	Electrons donated to an undoped (101)-oriented film as a function of mobility.....	125
5.11	AFM images of (100)-oriented rutile films (a) deposited by MOCVD (b) deposited by IBSD.....	126
5.12	Conducting electrons removed as a function of film composition calculated from resistance values measured in N <sub>2</sub> and O <sub>2</sub> atmospheres at 240 °C.....	129
5.13	Conducting electrons added as a function of film composition calculated from resistance values measured in N <sub>2</sub> and humidified N <sub>2</sub> atmospheres at 240 °C.....	130
5.14	[V <sub>O</sub> <sup>2•</sup> ] calculation as a function of PO <sub>2</sub> at 240 °C by Marucco model.....	137
5.15	Calculated electrons resulting from [V <sub>O</sub> <sup>2•</sup> ] as a function of [V <sub>O</sub> <sup>2•</sup> ] enthalpy of formation.....	138
5.16	Comparison of conducting electrons added by humidity to an Fe-doped film compared to other compositions.....	142
5.17	Estimated time required for O <sub>2</sub> diffusion through a 3300 Å thick rutile film as a function of temperature.....	144
5.18	Comparison of conducting electrons added by humidity to a film with a Ga-doped surface layer (Ga*) to other compositions.....	147
5.19	Comparison of conducting electrons removed by oxygen from a film with a Ga-doped surface layer (Ga*) to other compositions.....	148
5.20	N <sub>2</sub> atmosphere resistance values measured at 240°C and calculated activation energies for (001)-oriented, reduced and unreduced samples.....	150
5.21	Impedance spectra as a function of atmosphere at 240 °C for (001)-oriented rutile film reduced 12 hrs in H <sub>2</sub> at 500 °C.....	151

5.22	Impedance spectra as a function of atmosphere at 240 °C for (001)-oriented rutile film reduced 6 hrs in H <sub>2</sub> at 500 °C.....	152
5.23	Comparison of conducting electrons removed by oxygen from reduced films to other compositions.....	153
5.24	Comparison of conducting electrons added by humidity to reduced films to other compositions.....	154
5.25	Sensitivity of various films to the introduction of 1.332e-3 atm O <sub>2</sub> (R) to an atmosphere of less than 1e-10 atm O <sub>2</sub> (R <sub>0</sub> ).....	157
5.26	Sensitivity of various films to the introduction of humid N <sub>2</sub> (R) to an atmosphere of dry N <sub>2</sub> (R <sub>0</sub> ).....	158
6.1	Schematic of β-Ga <sub>2</sub> O <sub>3</sub> unit cell (a) Oblique (b) Normal to b-axis.....	162
6.2	AFM images of β-Ga <sub>2</sub> O <sub>3</sub> deposited on (0001) sapphire (a) 600 °C deposition, normal image (b) 600 °C deposition, phase contrast image (c) 700 °C deposition, normal image (d) 700 °C deposition, phase contrast image.....	168
6.3	AFM images of β-Ga <sub>2</sub> O <sub>3</sub> deposited on (111) Si (a) 600 °C deposition, normal image (b) 600 °C deposition, phase contrast image (c) 700 °C deposition, normal image (d) 700 °C deposition, phase contrast image.....	170
6.4	AFM images of β-Ga <sub>2</sub> O <sub>3</sub> deposited on (111) at 700°C and annealed at 800°C in air for one hour (a) normal image (b) phase contrast image.....	171

Abstract of Dissertation Presented to the Graduate School  
of the University of Florida in Partial Fulfillment of the  
Requirements for the Degree of Doctor of Philosophy

GROWTH AND SURFACE CHARACTERISTICS OF OXIDE  
THIN FILMS FOR CHEMICAL SENSOR APPLICATIONS

By

Darren R. Burgess

August 1999

Chairman: Timothy J. Anderson  
Major Department: Chemical Engineering

The effects of surface chemistry, orientation and morphology on the gas sensing properties of rutile thin films were investigated. The motivation for this work was to improve the limited understanding of gas sensing mechanisms in semiconducting materials. The metalorganic chemical vapor deposition of rutile phase  $\text{TiO}_2$  thin films on sapphire substrates was studied and thoroughly developed to prepare materials with well-defined physical characteristics for the gas sensor investigation.

Heteroepitaxial (001)-, (101)- and (100)-oriented rutile films were deposited on (10 $\bar{1}$ 0)-, (11 $\bar{2}$ 0)- and (0001)-oriented sapphire substrates, respectively, using solid source metalorganic precursors. X-ray diffraction (XRD) analysis determined the films' crystalline characteristics. Atomic force microscopy identified the facet planes on (001)- and (101)-oriented film surfaces.

The films were doped with Ga, an acceptor-type dopant, or Nb, a donor-type dopant. XRD proved that heteroepitaxy was maintained to 6.5 at%. The lattices of (001)- and (101)-oriented films were observed to expand linearly with increasing dopant

concentration. Changes in surface morphologies due to doping were related to increased film stress and defects caused by lattice expansion.

The gas sensor properties of each undoped film orientation and (001)-oriented films with various compositions were investigated. Impedance spectroscopy measurements were used to arrive at overall changes in the number of conducting electrons as a function of changing environment. The number of conducting electrons added by dissociatively adsorbed water or removed by oxygen was substantially greater for a (101)-oriented film than an (001)-oriented film. This behavior was related to the density of Ti atoms with low oxygen coordination present on facet planes and their intersections. A previously unknown relationship was discovered between surface cation oxygen coordination, photochemical reactivity and enhanced adsorption of acceptor- or donor-type molecules. Undercoordinated surface cations were also created by Ga-doping and hydrogen reduction resulting in enhanced adsorption. The electronic compensation of Nb dopant atoms also resulted in enhanced oxygen adsorption.

Oriented thin films of  $\text{Ga}_2\text{O}_3$  and  $\text{Al}_2\text{O}_3$  were also deposited from solid metalorganic precursors. The amount and relative orientation of crystalline material was found to increase with increasing deposition temperature.

# CHAPTER 1 INTRODUCTION

## 1.1 Motivation

Increasing needs for pollution monitoring and control have given rise to the need for gas sensors which demonstrate higher selectivity and sensitivity.<sup>1,2</sup> Among the more familiar examples is the oxygen sensor contained in an automobile's exhaust system. The function of this sensor is to control the air-to-fuel ratio to minimize the concentration of uncombusted hydrocarbons or nitrous oxides released into the atmosphere.<sup>3,4</sup> This sensor, which is commonly made from zirconium oxide, suffers from inadequate operation at low temperatures. This characteristic renders it unable to control the engine combustion process until a built-in heater brings the material to an adequate temperature. Therefore, a large amount of pollution is released just after a car is started due to a lack of sensitivity over the desired temperature range of operation.

Many efforts have been made to improve sensitivity and selectivity of gas sensors. Approaches have included modifying a material's bulk or surface characteristics through doping or annealing. Also, the observed electrical response has been changed through the use of different contact materials and configurations. These efforts have met with varying degrees of success. A lack of understanding of gas sensing mechanisms has limited the innovation in gas sensor technology.

To engineer an improved gas sensor, a better understanding of the fundamental processes occurring during sensing is necessary. The mechanism of gas sensing can be separated into the adsorption of a gaseous species and its observable effect on the electrical conductivity. Each must be understood individually as a function of the material and the

environment. This knowledge can then be correlated to create a complete picture of the sensing mechanism and variables of interest. The primary motivation for this work is to improve the understanding of gas sensing mechanisms by investigating the relationship between a material's bulk and surface properties and its sensitivity.

### 1.2 Objective

The first objective of this work is to further the understanding of complex metal oxide thin film deposition by metalorganic chemical vapor deposition (MOCVD). This thin film deposition method is characterized by high throughput which makes it attractive for mass production. The primary goal for using MOCVD in production is to not sacrifice crystalline film quality at the faster growth rates. The investigation of films' physical characteristics as a function of growth conditions and doping furthers the understanding of MOCVD as applied to more complex material systems.

The second objective of this work is to create changes in a gas sensitive material by doping and relate those changes to the observed gas sensing behavior. To accomplish this objective, a gas sensitive material must be obtained in a configuration where both the bulk and surface properties can be characterized. The ability must also exist to identify the changes caused by the addition of dopant atoms using these same characterization methods. The actual effect of various dopants on the gas sensitivity of a material can then be more accurately assessed as an aid to future gas sensor design.

### 1.3 Approach

To fulfill the objective of creating a material whose bulk and surface properties can be identified with available methods, rutile phase titanium dioxide ( $\text{TiO}_2$ ) was chosen.  $\text{TiO}_2$  has been widely studied as a model for the behavior of transition-metal oxides

because of its stability over a wide range of temperatures and environments. In addition,  $\text{TiO}_2$  exhibits semiconductive behavior at high temperatures as a function of oxygen partial pressure. A wealth of literature exists on the expected physical, electrical and adsorptive characteristics of  $\text{TiO}_2$ .

Among the available forms of  $\text{TiO}_2$  (e.g., powder, single crystal), non-porous, crystalline thin films lend themselves to the simultaneous study of bulk and surface properties. The first objective of this work is met by depositing rutile  $\text{TiO}_2$  thin films by MOCVD. The (001), (101) and (100) crystal orientations are grown heteroepitaxially on the (10 $\bar{1}$ 0), (11 $\bar{2}$ 0) and (0001) orientations of sapphire, respectively. The films are doped with donor- and acceptor-type atoms to assess their effects on deposition and later, sensitivity. The films are primarily characterized by x-ray diffraction for their crystalline quality and atomic force microscopy for their surface morphologies.

Having created undoped and doped rutile thin films with well-defined bulk and surface properties, the second objective is met by investigating these films as gas sensors. An environmentally-controlled chamber is used to subject the films to reducing and oxidizing atmospheres and humidity. The observed changes in the electrical behavior are analyzed with respect to the rutile electrical properties literature and the ultra-high vacuum surface characterization literature to create a mechanistic model of oxygen and humidity sensing.

## CHAPTER 2 LITERATURE REVIEW

### 2.1 Rutile Thin Film Deposition

The basic processes involved in thin film deposition are adsorption, nucleation and growth.<sup>5-7</sup> First, a sufficient number of atoms from the vapor phase must adsorb onto the growth surface to form a permanent nucleus of material. Depending on the binding energy of the depositing material, relative to itself and the growth surface, and the energy supplied through heat by the growth surface, material will deposit by one of three mechanisms. One mechanism is two-dimensional or layer-by-layer growth. In two-dimensional growth, material addition to a stable nuclei is predominantly in the plane as opposed to building upward. The growth takes place in a sheet-like manner and is more typical of slow deposition rates and low strain in the growing material. The opposite of two-dimensional growth is island or Volmer-Weber growth which is characterized by growth in three dimensions. Island growth can occur for a couple of reasons. One is when the adsorbing atoms are more strongly bound to themselves than the growth surface. This condition makes adsorption on top of previously deposited material more favorable. Another cause is deposition occurring at a higher rate than the atoms can transport across the growth surface to extend a stable nucleus in two dimensions, so the atoms simply pile up. The Stranski-Krastonov growth mode is a mixture of the layer and island mechanisms. Atoms initially deposit in layers but due to a strain induced defect or other instability, island formation begins to occur.

TiO<sub>2</sub> thin film deposition first received interest for optical applications such as anti-reflection coatings and for electrical applications because of the material's high dielectric

constant.<sup>8</sup> In the ensuing period, the deposition of TiO<sub>2</sub> has been attempted by a variety of physical and chemical vapor deposition (CVD) methods. Rutile is the high-temperature phase of TiO<sub>2</sub> which is desirable for most applications. The deposition rate and temperature dependence for obtaining this phase has been documented for different deposition techniques.<sup>9-14</sup> Rutile phase films have been deposited by CVD at a substrate temperature of 450 °C and higher. Physical vapor deposition (PVD) methods have used a substrate temperature as low as 550 °C. The fraction of rutile material has been observed to decrease using either deposition method at high deposition rates in combination with low deposition temperatures resulting in a portion of the material being amorphous or anatase phase.

### 2.1.1 Physical Vapor Deposition

The objective of PVD is to transfer atoms from a source to a growth surface where the film is deposited atomistically. Traditional PVD processes are characterized by high vacuum and the absence of chemical reactions.<sup>5</sup> Among the PVD methods with higher energy requirements, rutile TiO<sub>2</sub> has been deposited by rf and dc plasma sputtering,<sup>15-20</sup> ion-assisted evaporation<sup>21-24</sup> and ion beam sputter deposition.<sup>14</sup> Increased film density, reduced film stress, and increased control of doping at very low levels are some of the advantages of these methods.

### 2.1.2 Chemical Vapor Deposition

CVD is the process of reacting a volatile compound, often with other gases, to produce a solid which deposits on a surface. The volatile compounds and gases are known as precursors, and the deposition surface is known as a substrate. The substrate is normally heated to facilitate a reaction which forms a solid film. The desired product may

form in the gas phase and deposit molecularly, or one or more of the precursors may adsorb on the substrate and react to create the film. Which of these processes occurs depends on the energy required to separate the desired atom(s) from the remainder of the precursor molecules and to motivate a reaction. The advantages of CVD are its ability to controllably create films with widely varying stoichiometry, and its adaptability to semi-continuous or batch processing.<sup>5</sup>

The foremost way in which the CVD process has been enhanced is the use of a plasma.<sup>25-29</sup> A plasma aids in decomposing the precursor molecules so that their reaction is not solely dependent upon energy provided by a heated substrate. Plasma-enhanced CVD is especially helpful when the energy to create a reactive form of a precursor is beyond the capabilities of a resistively heated substrate. A good example is the deposition of nitride compounds such as WN or TiN. The plasma forms nitrogen radicals which are reactive with metal atoms from normally inert N<sub>2</sub> gas.<sup>30-34</sup>

When one of the reactants is a compound containing a metal atom bound in an otherwise organic molecule, the compound is labeled a metalorganic and the deposition process is known as MOCVD. Metalorganic precursors first received prominent attention for the deposition of room temperature semiconductors. Compounds such as trimethylgallium and triethylarsine have been used along with many others.<sup>35</sup>

The CVD of TiO<sub>2</sub> has been widely studied. TiCl<sub>4</sub> is the non-metalorganic precursor which has received the most attention.<sup>9-11,26,36</sup> Deposition with this precursor has been motivated by two factors. First, TiCl<sub>4</sub> is low cost in comparison to other Ti precursors.<sup>9,36</sup> Second, TiCl<sub>4</sub> is used in the manufacture of TiO<sub>2</sub> powder for white pigment applications.<sup>37</sup> The biggest disadvantage associated with this precursor is the chlorinated byproducts resulting from the TiO<sub>2</sub> formation reaction. Depending on the precursor used with TiCl<sub>4</sub>, HCl or Cl<sub>2</sub> can be formed. These compounds can degrade the reactor and are considered harmful pollutants in the environment. The low cost advantage of this precursor is therefore reduced by the cost of properly disposing of its byproducts.

2.1.2.1 Metalorganic chemical vapor deposition. Outside of the use of  $\text{TiCl}_4$  as a precursor, a large portion of CVD of  $\text{TiO}_2$  has been carried out with metalorganic precursors. One of the advantages of metalorganic precursors is that film contamination is minimized because the reaction byproducts are hydrocarbons in low concentrations. Another advantage is that films can be deposited with relatively low-energy input to separate the relatively weakly bound metal atom from the organic ligands. Several metalorganic compounds have been used in research, with titanium isopropoxide ( $\text{Ti}(\text{OC}_3\text{H}_7)_4$ ) chief among them.<sup>27,28,38-52</sup> This liquid precursor is normally transported by an inert carrier gas or  $\text{O}_2$  while being maintained at a temperature of  $\sim 100^\circ\text{C}$ . Other approaches to delivery have been to heat the liquid to  $270^\circ\text{C}$  and allow the reactor's pressure gradient to force transport toward the substrate<sup>53</sup> and to enhance the liquid's dispersion in the reactor by pulsed injection using an ultrasonic nozzle.<sup>54</sup> Titanium ethoxide ( $\text{Ti}(\text{OC}_2\text{H}_5)_4$ ) is another liquid metalorganic precursor which has been employed for the deposition of  $\text{TiO}_2$ .<sup>55,56</sup> A summary of these CVD studies is that the film density and crystalline phase of is most affected by substrate temperature and partial pressures of the precursors.

2.1.2.2 CVD related techniques. Value exists in noting several non-traditional CVD techniques which have been applied to  $\text{TiO}_2$  deposition. Atomic layer deposition (ALD) consists of alternating the introduction of precursors such that nominally one monolayer of  $\text{TiO}_2$  is deposited for each cycle. This technique has been performed with both  $\text{Ti}(\text{OC}_3\text{H}_7)_4$  and  $\text{TiCl}_4$  precursors.<sup>10,13,55,57</sup> The advantages of ALD are obviously a high degree of control and the uniformity of film thickness. As a result, this technique can be applied to substrates with very large surface areas. Some researchers substitute the term epitaxy for deposition in ALD, although this can only accurately be applied when the film is epitaxial as discussed later.

Sol-gel processing requires dramatically lower energy input. The deposition consists of dipping a substrate into a titanium precursor and stabilizer mixture. The liquid film is allowed to dry and is then heat treated at temperatures in the 100 °C to 300 °C range.<sup>58</sup> The advantages of sol-gel processing are the ability to use heat sensitive substrates and low cost. The films are, however, amorphous and porous. The deposition of TiO<sub>2</sub> thin films on organic self-assembled monolayers is another technique which requires low energy input.<sup>59,60</sup> Sulfonate surface functional groups on Si wafers act as nucleation sites for TiO<sub>2</sub> from Ti precursors in solution. Uniform, polycrystalline anatase films were grown from a TiCl<sub>4</sub> in aqueous HCl solution and Ti(OC<sub>3</sub>H<sub>7</sub>)<sub>4</sub> in non-aqueous ethanol solution over a 80 to 100 °C temperature range.

### 2.1.3 Heteroepitaxy

The word epitaxy is derived from the Greek words 'epi' which means 'resting upon' and 'taxis' which means 'arrangement'.<sup>5</sup> In the field of thin film deposition, the term refers to the growth of a 'single' crystal film on a crystalline substrate. Homoepitaxy is the growth of a film on a substrate of the same material. An example is the growth of Si on Si. The advantages are that a film can be deposited with fewer defects and a higher purity than the substrate. Also, there is a higher control of doping.<sup>6</sup>

Heteroepitaxy is the growth of a crystalline film on a crystalline substrate of a different material.<sup>5,6</sup> A well known application of heteroepitaxy is the manufacture of compound semiconductor devices. In these devices, it is desirable to have multiple layers of high quality crystalline materials which exhibit different electrical properties. The pertinent issues are the minimization of interlayer diffusion and defect densities which degrade the electronic properties. Interdiffusion is activated by temperature. Therefore, the deposition of all layers must take place below a critical temperature to avoid interdiffusion.

Defects fall into five principle categories.<sup>7,35</sup> An example is the propagation of a substrate defect such as a screw dislocation into a depositing film. The atoms preferentially deposit at the lower energy ledge sites of the dislocation continuing its pattern. The continuation of a screw dislocation would be heavily dependent on the growth taking place by a layer or two-dimensional mechanism. Of the five defect categories, there are two main types of dislocations pertinent to the three-dimensional or island-type growth to be presented in this thesis. They are the formation of low-angle grain boundaries and twins and misfit dislocations. Low-angle grain boundaries and twins occur when islands of different orientation with respect to the plane of the film coalesce. In the case of twins, the islands coalesce such that their orientation is the mirror image of one another across the boundary perpendicular to the plane. Misfit dislocations occur when the elastic strain energy in a film caused by it being in compression or tension to fit the lattice of the substrate becomes greater than the energy of the film with the inclusion of a defect. For example, a film whose lattice in a direction is smaller than the lattice of the substrate will be in tension in that direction. With layer upon layer of the film being in tension there is an energy release at a critical thickness which relaxes the tension. As a simple illustration, a relaxed layer could grow such that five unit lengths of the lattice match to four unit lengths of the lattice in tension. This allows the film to grow with less strain on top of this misfit layer. Further explanations, examples, and discussion of thin film defects, especially with respect to the deposition of room temperature semiconductors, are available.<sup>7,35</sup>

Heteroepitaxial  $\text{TiO}_2$  thin films are desirable for their improved optical and electrical properties. The use of an electrically insulating substrate allows one to probe and exploit only the characteristics of the  $\text{TiO}_2$  without interference. The heteroepitaxial deposition of  $\text{TiO}_2$  has been accomplished by several deposition methods. Representative of the literature are growth by reactive ion cluster beam (RICB) deposition,<sup>22</sup> ion-beam sputter deposition (IBSD),<sup>14</sup> CVD using a  $\text{TiCl}_4$  precursor<sup>9,26,36</sup> and MOCVD using a  $\text{Ti}(\text{OC}_3\text{H}_7)_4$  precursor.<sup>38-42,44</sup> Of these studies, the crystalline quality of the films grown

by IBSD<sup>14</sup> are representative or superior as judged by the x-ray diffraction (XRD) theta rocking-curve full-width-at-half-maximum (rc fwhm). The  $\theta$  rc fwhm is a measure of the crystalline alignment perpendicular to the plane of the film. Table 2.1 is a summary of the three rutile orientations important to this work along with the parallel directions in the plane and the calculated cationic mismatch.

Given the large mismatch values in Table 2.1, it is the opinion of many researchers in the field that matching between the oxide sublattices as opposed to the cation lattices is the driving force for the observed  $\text{TiO}_2$  growth orientation. Excellent schematic illustrations can be found for (101) and (100) oriented rutile films on the respective sapphire substrates,<sup>42</sup> and values have been calculated for the (001) orientation.<sup>14</sup> The mismatch is dramatically reduced by this analysis as shown in Table 2.1.

Table 2.1 Cationic and anionic lattice mismatch for heteroepitaxial rutile deposited on sapphire substrates

Rutile	Sapphire	In-plane crystal lattice relationship	Cationic Mismatch	Anionic Mismatch
(001)	(10 $\bar{1}$ 0)	[100] // [11 $\bar{2}$ 0] [010] // [0001]	11.5% 6.0%	3.6% 5.7%
(101)	(11 $\bar{2}$ 0)	[ $\bar{1}$ 01] // [ $\bar{1}$ 100] [010] // [0001]	14.8% 6.0%	0.9% 5.8%
(100)	(0001)	[0 $\bar{1}$ 0] // [ $\bar{1}$ 2 $\bar{1}$ 0] [001] // [10 $\bar{1}$ 0]	3.6% 3.0%*	3.8% 7.3%

\* Mismatch of 3 lattice units

## 2.2 Rutile Gas Sensors

### 2.2.1 Oxygen Sensors

TiO<sub>2</sub> has received considerable attention as an oxygen sensor because of the automotive industries search for a suitable oxygen sensor to be placed in an automobile's exhaust system.<sup>4,61,62</sup> The semiconducting characteristics of TiO<sub>2</sub> at higher temperature have been utilized for this purpose. Semiconduction occurs when Ti<sup>4+</sup> and Ti<sup>3+</sup> ions coexist or synonymously when oxygen vacancies are present. In this regime the resistance (R) varies with the O<sub>2</sub> partial pressure PO<sub>2</sub> and the absolute temperature (T) according to the following equation

$$R = R_0 PO_2^n e^{E/kT} \quad (2.1)$$

where E is the activation energy for electronic conduction and the remaining variables are constants.<sup>3,4,62</sup> Therefore, any change in the oxygen partial pressure may be measured because it directly affects TiO<sub>2</sub>'s resistance.

Table 2.2 shows some representative oxygen sensors from the literature.<sup>61-64</sup> The second column of the table shows the form of the rutile sensor. Thick films are normally more porous than thin films and are deposited as a printed paste and annealed to increase uniformity.<sup>65</sup> The term ceramic as used here is representative of materials that are pressed from powders and sintered. The second column is the logarithm of the resistance change in response to the change in O<sub>2</sub> partial pressure shown in the third column. Note that resistance increases with increasing PO<sub>2</sub> as explained above. The polycrystalline ceramic and thick film materials tend to be more sensitive due to higher available surface area. This increased sensitivity suggests that a surface phenomena is important in the sensing mechanism. The majority of oxygen sensor studies ignore specific surface characterization

of the materials as a means of understanding more about the interaction of the surface with oxygen.

Table 2.2 Oxygen sensor examples

Material	Form	Response* Log 10 <sup>X</sup> (ohms)	-Log PO <sub>2</sub> (atm) response* range	T(°C)	Reference
TiO <sub>2</sub>	Thick Film	3 - 7	35 - 5	350	61
		0.2 - 3.5	16 - 0	800	61
TiO <sub>2</sub> /9at% Nb	Thin Film	2 - 4	3 - 0	1000	63
TiO <sub>2</sub>	Thin Film	2.2 - 2.4	4.3 - 1.7	1000	64
TiO <sub>2</sub>	Ceramic	3.5 - 8	30 - 10	400	62

### 2.2.2 Humidity Sensors

Deposited thin films and ceramic forms of TiO<sub>2</sub> are commonly used as humidity sensors for industrial processes and human comfort.<sup>66,67</sup> The majority of TiO<sub>2</sub> humidity research has studied the ceramic form at or near room temperature. Several sources explain the mechanism by which the humidity sensing proceeds at room temperature.<sup>66-68</sup> The first layer of water chemisorbs on a ceramic surface. Subsequent layers are physisorbed and dissociate into hydronium and hydroxyl ions due to the high electrostatic fields in the chemisorbed layer when an electric field is applied. Ionic conduction occurs when a hydronium ion releases a proton to another physisorbed water molecule and this becomes a chain reaction. The behavior of these sensors is governed by the number of chemisorption sites and the porosity of the ceramic (i.e., surface area). Researchers have doped with ions such as Li<sup>+</sup>, K<sup>+</sup>, and Cr<sup>3+</sup> with some success in increasing the number of chemisorption

sites.<sup>67,69</sup> Mixed results have been obtained when others have tried to improve sensor response through engineering the porosity by mixing  $\text{TiO}_2$  with other oxides such as  $\text{V}_2\text{O}_5$  and  $\text{Nb}_2\text{O}_5$ .<sup>68,70,71</sup> The characterization of a humidity sensor at high temperatures where the behavior and effects of chemisorbed water can be studied cannot be found in the literature.

Table 2.3 displays data from representative research on humidity sensors.<sup>65,72-74</sup> Column three shows the logarithm of the decrease in resistance of each sensor with the corresponding increase in percent relative humidity (RH). Some researchers have chosen to measure the DC resistance while others measure the AC resistance at a single frequency. Using either of these approaches it is impossible to determine whether or not a change in the material-contact barrier resistance or the actual material is being probed.

Table 2.3. Humidity sensor examples

Material	Form	Response* Log $10^X$ (ohms)	%RH range of response*	T(°C)	Response/ Freq (Hz)	Reference
$\text{TiO}_2/$ $0.5\%\text{Nb}_2\text{O}_5$	Ceramic	8 - 4	10 - 90	RT	AC/400	65
$\text{TiO}_2$	Ceramic	7 - 3	15 - 95	25	AC/200	72
$\text{Ba}_{.5}\text{Sr}_{.5}\text{TiO}_3$	Thick Film	8 - 5	10 - 90	RT	AC/400	65
$\text{TiO}_2$ reactively sputtered	Thin Film	11 - 5	0 - 90	RT	DC	73
$85\%\text{TiO}_2$ $15\%\text{V}$	Thin Film	7 - 5	0 - 100	25	AC/50	74

## 2.3 Rutile Properties

### 2.3.1 Crystal and Band Structure

TiO<sub>2</sub> can exist in three crystalline structures: rutile, anatase, and brookite. The phase transition from anatase to rutile occurs around 700 °C, and the reverse transition is kinetically limited. The unit cell of rutile is tetragonal with  $a=4.595 \text{ \AA}$  and  $c=2.959 \text{ \AA}$ . A picture of the unit cell is shown in Figure 2.1 with bond angles and lengths shown. Filled circles represent Ti atoms in the figure. For rutile, the space group is  $D_{4h}^{14}$  and symmetry is  $P4_2/mnm$ .<sup>75</sup>

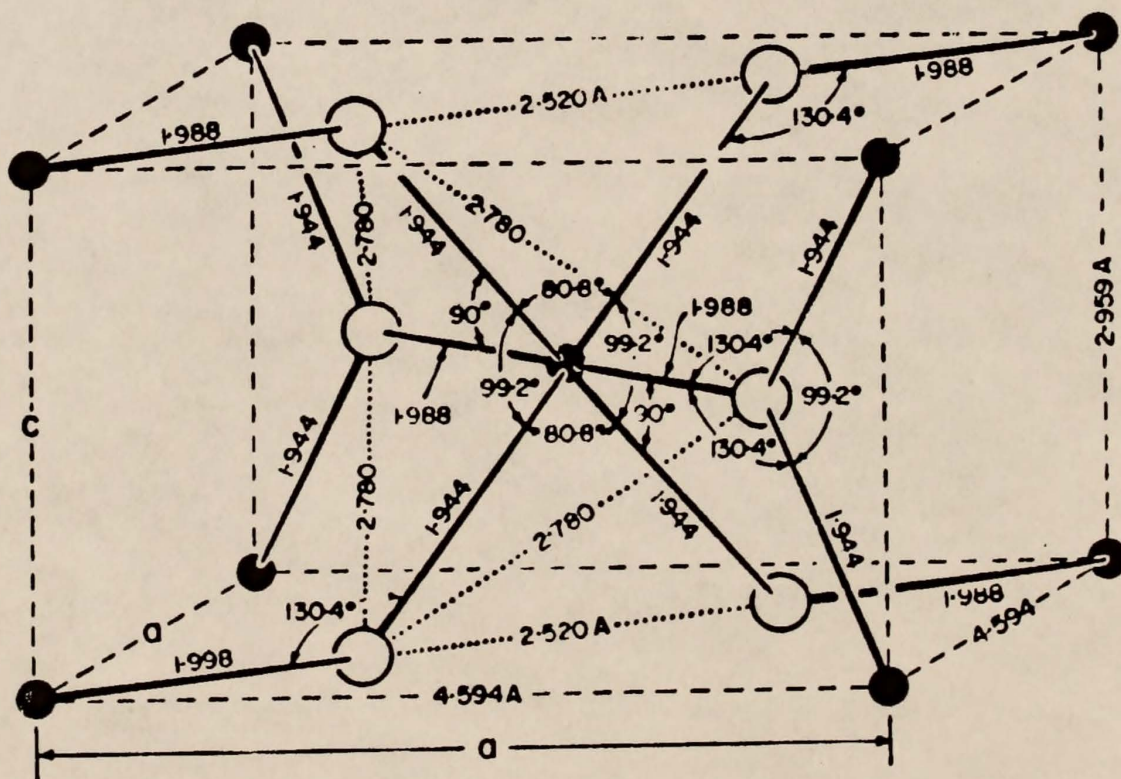


Figure 2.1 Rutile unit cell. From A. von Hippel et al.<sup>77</sup>, Fig. 2

A number of rutile's properties are of interest for gas sensor applications. First, rutile has a very high refractive index and dielectric constant. The following equations give the refractive indices as a function of wavelength,  $\lambda$  (Å):

$$n^2 = 7.197 + 3.322 \times 10^7 / (\lambda^2 - 0.843 \times 10^7) \quad \text{extraordinary} \quad (2.2)$$

$$n^2 = 5.913 + 2.441 \times 10^7 / (\lambda^2 - 0.803 \times 10^7) \quad \text{ordinary.}^{76} \quad (2.3)$$

At room temperature, the low frequency dielectric constants are 170 and 86, and the high frequency dielectric constants are 8.427 and 6.843, parallel to the c- and a-axes respectively.<sup>75</sup> Also, TiO<sub>2</sub> is a wide band gap semiconductor. Controversy exists among different studies as to the fundamental optical absorption edge in rutile. Values ranging from 3.033 to 3.062 eV have been reported for the direct band gap perpendicular to the c-axis. The transition is indirect parallel to c-axis, and values from 3.049 to 3.101 have been reported. Both sets of values are at 1.6 K and 280 K, respectively.<sup>75</sup>

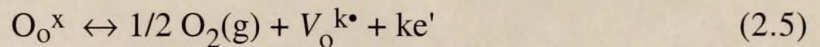
Finally, the intrinsic electrical conductivity is an important piece of information which can be described by the equation

$$\ln \sigma = A - B/T \quad (2.4)$$

where  $\sigma$  is the conductivity in (ohm-cm)<sup>-1</sup> and T is the absolute temperature<sup>75</sup>. Perpendicular to the c-axis, A equals 7.92 and 11.10, and B equals 17,600 and 21,200, below and above 1123 K respectively. Parallel to the c-axis, A equals 8.43 and 11.30, and B equals 17,600 and 21,200, below and above 1223 K respectively.

### 2.3.2 Conductivity

2.3.2.1 Defects and mechanism. As described above, conductivity in pure  $\text{TiO}_2$  is a function of temperature and oxygen partial pressure. The combination of these two variables creates oxygen vacancies or titanium interstitials. These defects are believed to be the source of conduction electrons. The electron density dependence on the oxygen partial pressure can be determined from an analysis of defect equilibrium which is well-known in the literature. For example, using Kroger-Vink notation oxygen vacancies are formed according to the defect equilibrium equation<sup>78-83</sup>



where  $k$  is the charge of the oxygen vacancy relative to the lattice and  $\text{e}'$  is a quasi-free electron. At high temperatures  $k$  may have the value 1 or 2 representing a partially or completely ionized oxygen vacancy, respectively. There is also the equation



where  $\text{h}^\bullet$  represents a hole. Holes are, however, considered to be a minor defect in  $\text{TiO}_2$ , except at extremely high temperatures and oxygen partial pressures or high concentrations of acceptor impurities.<sup>78,80</sup> Outside of that realm, the corresponding equilibrium constants for reaction 2.5 are

$$K_1 = [\text{V}_\text{o}^{\bullet}] n \text{PO}_2^{1/2} \quad (2.7)$$

$$K_2 = [\text{V}_\text{o}^{\bullet\bullet}] n^2 \text{PO}_2^{1/2} \quad (2.8)$$

where  $k = 1$  or  $2$ , respectively. Brackets denote the concentration of the species. The electroneutrality condition is then

$$n = [V_o^\bullet] + 2[V_o^{\bullet\bullet}] \quad (2.9)$$

Solving for the electron concentration using equations 2.7, 2.8 and 2.9 gives

$$n^3 = K_1 n PO_2^{-1/2} + 2K_2 PO_2^{-1/2}. \quad (2.10)$$

There are two limiting cases to equation 2.10:  $[V_o^\bullet] \gg [V_o^{\bullet\bullet}]$  and  $[V_o^{\bullet\bullet}] \gg [V_o^\bullet]$  which represent singly ionized oxygen vacancies or doubly ionized oxygen vacancies being predominant, respectively. If singly ionized oxygen vacancies are predominant then  $K_1 \gg K_2$ , and the electroneutrality equation simplifies to

$$n = K_1^{1/2} PO_2^{-1/4}. \quad (2.11)$$

If doubly ionized oxygen vacancies are predominant then  $K_2 \gg K_1$ , and the electroneutrality equation simplifies to

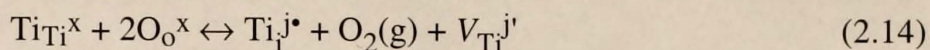
$$n = (2K_2)^{1/3} PO_2^{-1/6}. \quad (2.12)$$

Given that the conductivity,  $\sigma$ , is a function of  $n$  according to the equation

$$\sigma = n e \mu \quad (2.13)$$

one can see that the conductivity should exhibit a  $-1/4$  or  $-1/6$  dependence on  $PO_2$  depending on which defect is predominant.

By the same analysis of the titanium interstitial defect formation equation<sup>78-83</sup>



at equilibrium, the dependence of conductivity on  $\text{PO}_2$  when partially ionized titanium interstitials,  $\text{Ti}_{\text{i}}^{3\bullet}$ , or fully ionized titanium interstitials,  $\text{Ti}_{\text{i}}^{4\bullet}$ , are the predominant defects can be found. When  $[\text{Ti}_{\text{i}}^{3\bullet}] \gg [\text{Ti}_{\text{i}}^{4\bullet}]$ ,  $\sigma \propto \text{PO}_2^{-1/4}$ , and  $\sigma \propto \text{PO}_2^{-1/5}$  in the reverse limit. Obviously, the  $\text{PO}_2$  dependence of conductivity is the same in the limit of  $[\text{Ti}_{\text{i}}^{3\bullet}]$  or  $[\text{V}_{\text{O}}^{\bullet}]$  being the predominant defect. These defects are expected only to be observed in very nearly stoichiometric  $\text{TiO}_2$ . Their observance is open to a great deal of speculation since conductivity dominated by the presence of acceptor impurities exhibits the same  $\text{PO}_2$  dependence.<sup>82,84</sup>

A review of representative literature reveals several important trends concerning the dependence of  $\text{TiO}_2$  conductivity on temperature and partial pressure. Over an oxygen partial pressure range from  $10^0$  to  $10^{-20}$  atmospheres where the transition between the terms "low  $\text{PO}_2$ " and "high  $\text{PO}_2$ " is around  $10^{-7}$  atm, these trends are displayed for single crystal and ceramic samples in Table 2.4. The temperature ranges are guidelines given that there must be some transition region between each case. Obviously, other potential defects such as oxygen interstitials and titanium vacancies can be associated with  $\text{TiO}_2$ . This table is shown as a summary of the available literature and is not intended to imply that all possible experiments will conform to these trends.

Table 2.4. Dominant impurity trends in TiO<sub>2</sub>

Sample Treatment	Temperature Range (°C)	Dominant Defect	
		low PO <sub>2</sub>	high PO <sub>2</sub>
Unreduced <sup>80,84,85</sup>	1000 - 1200	Impurity, Ti <sub>i</sub> <sup>4•</sup>	V <sub>o</sub> <sup>••</sup>
	1200 - 1500	decreasing impurity, Ti <sub>i</sub> <sup>4•</sup>	Ti <sub>i</sub> <sup>4•</sup>
Reduced <sup>79,83</sup>	800 - 1000	V <sub>o</sub> <sup>••</sup>	V <sub>o</sub> <sup>••</sup>
	1000 - 1200	Ti <sub>i</sub> <sup>4•</sup>	V <sub>o</sub> <sup>••</sup>
	1200 - 1500	Ti <sub>i</sub> <sup>4•</sup>	Ti <sub>i</sub> <sup>4•</sup>
Highly reduced <sup>82</sup>	60 - 225	V <sub>o</sub> <sup>••</sup>	V <sub>o</sub> <sup>••</sup>
	250 - 550	Ti <sub>i</sub> <sup>4•</sup>	Ti <sub>i</sub> <sup>4•</sup>

A summary of these trends found in the literature is that with increasing degree of reduction, which is a function of higher temperatures and lower oxygen partial pressures, titanium interstitials appear to become the predominant defect over oxygen vacancies.

2.3.2.2 Activation energy and mobility. In addition to studying the relationship between the conductivity and defect chemistry of TiO<sub>2</sub>, there have been assessments of the activation energy and electronic mobility of conduction. Table 2.5 is a summary of typical research and the results.

Table 2.5. Representative activation energy and mobility data for TiO<sub>2</sub>

Sample Treatment	Temperature Range (°C)	Activation Energy (eV)	Electronic Mobility (cm <sup>2</sup> /Vsec)	Comments
Unreduced <sup>86</sup>	350 - 850 850 - 1400	1.53 1.83	0.1 - 10	None on temp. dep. of $\mu$
Unreduced <sup>84</sup>	1000 - 1500	1.9 (air) 1.5 (1 atm O <sub>2</sub> )		None on $\mu$
Reduced <sup>87</sup>	25	0.04 - 0.08	0.2 ( $\perp$ c) 1.0 ( $\parallel$ c)	>150K E <sub>a</sub> ( $\mu$ ) = 0.10 eV Measurements in vacuum
Reduced <sup>82</sup>	25- 350 350 - 600	0.19 0.50		E <sub>a</sub> at all PO <sub>2</sub> None on $\mu$
Reduced <sup>83</sup>				$\mu$ ind. of defect type or concentration at const T >> $\mu$ is not a hopping process
Reduced <sup>88</sup>	<400 high T		$\propto T^{-3/2}$ ~ constant	$\mu$ fxn of acoustic phonon scat. $\mu$ weak fxn of T by optical phonon scattering
Reduced <sup>89</sup>	25 60 - 300	0.028	1.0	Measurements in vacuum
Reduced <sup>90</sup>	25		0.1 - 1.0	$\mu$ fxn of optical phonon scat.
Reduced <sup>91</sup>	25 - 325		1e6(T/K) <sup>-2.5</sup>	$\mu$ fxn of phonon scattering

The data show that there is a great deal of sample to sample variation even when tested under the same conditions. The trends that can be observed are the differences between unreduced and reduced samples. There is a dramatic change in the activation energy from greater than 1.5 eV for unreduced samples to 0.5 eV and much less depending on the degree of reduction. The activation energy of a highly reduced sample is attributed to the conduction of free electrons affected by phonon scattering. This is the consensus of all studies on reduced samples in the analysis of activation energy or mobility data.<sup>82,83,87-90</sup>

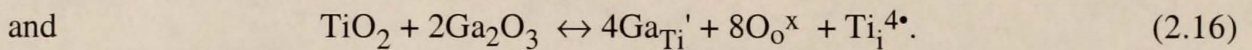
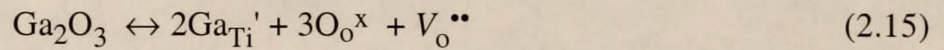
Conduction was not found to be a strongly activated or "hopping" process which would be indicative of a polaronic influence. In the case of the unreduced samples, the high activation energies are indicative of conduction by electrons which are trapped at defects such as oxygen vacancies.<sup>84,86</sup> After being activated into the conduction band, they may conduct long distances without being retrapped.

2.3.2.3 Intrinsic band-gap states. To separate the activation energy of conduction from the mobility term, others have performed investigations into the electronic nature of defects as to their place in the band structure. Several modeling efforts have identified electronic states in the band gap of  $\text{TiO}_2$  resulting from oxygen vacancies. Without respect to crystal orientation, levels were calculated to be 0.7 eV below the conduction band edge.<sup>92-94</sup> Oxygen vacancy band gap states were calculated at 0.95 eV below the conduction band for the (001) surface and 1.78 eV for the (110) surface.<sup>95</sup> Investigations on single crystals by ultraviolet photoelectron spectroscopy found oxygen vacancy band gap states around 1 eV below the conduction band edge for (001)- and (100)-oriented single crystals.<sup>96,97</sup> Angle resolved photoemission spectroscopy also identified an oxygen vacancy state at approximately 1 eV for an (001)-oriented single crystal.<sup>98,99</sup> Finally, an analysis of thermally and photonically induced conductivity data revealed an electronic state 0.62 eV below the conduction band edge due to an oxygen vacancy.<sup>90</sup>

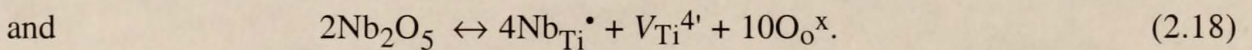
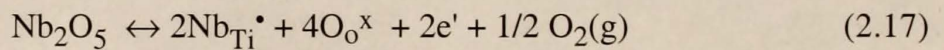
### 2.3.3 Doped rutile

2.3.3.1 Donor and acceptor defect chemistries. In addition to the oxygen vacancy and titanium interstitial defects created in pure  $\text{TiO}_2$  as a function of temperature and oxygen partial pressure, defects may be created by dopants. Dopants that are of interest for their effects on  $\text{TiO}_2$ 's electrical properties include both donors and acceptors. Along with the defect equations 2.5, 2.6, and 2.14 for the creation of oxygen vacancies and titanium

interstitials in pure  $\text{TiO}_2$ , the addition of dopants can create these same defects and others. Ga in its most stable oxidation state, 3+, is a representative acceptor atom with respect to the  $\text{TiO}_2$  crystal because the Ti cation is in a 4+ oxidation state. The inclusion of Ga in the crystal substitutionally on a Ti site may be compensated by oxygen vacancies or titanium interstitials according to the following defect formation equations:<sup>231,232</sup>



Nb in its most stable oxidation state, 5+, is a representative donor atom with respect to the  $\text{TiO}_2$  crystal. The inclusion of Nb in the crystal substitutionally on a Ti site may be compensated electronically or by titanium vacancies according to the following defect formation equations:<sup>116,232-234</sup>



2.3.3.2 Structure and conductivity effects. The doping of  $\text{TiO}_2$  with Ga has rarely been investigated, however, doping with a variety other trivalent atoms has been. A notable study investigated which valence state of a number of atoms would be most stable in the band gap using a two body shell model.<sup>100</sup> The 3+ valence state of V, Fe, Cr and Ga were found to reside in the band gap. It is significant that in the case of Ga and Fe, 3+ is also a stable, naturally occurring valence state. It was also calculated that the most energetically favorable lattice site for a Ga atom is in substitution for a titanium atom as opposed to being interstitial. Another modeling study calculated that the 2+ valence state of

Cr and Mn and the 3+ valence state of V and Mn to be in the band gap approximately 1 eV below the conduction band edge.  $\text{Fe}^{2+}$  was calculated to be in the conduction band.<sup>101</sup> Of these four atoms, only  $\text{Mn}^{3+}$  residing approximately 1.8 eV below the conduction band and  $\text{Fe}^{2+}$  in the conduction band could be verified by experiment.

Aluminum is a common impurity in  $\text{TiO}_2$  single crystals, so it has received the most attention in analyses of electrical conductivity data for trivalent atoms. Representative studies have been performed at temperatures above 1000 °C where titanium interstitials are known to be the dominant defect as was shown in Table 2.5.<sup>64,80,102</sup> The data revealed that Al doping decreased the n-type conductivity of  $\text{TiO}_2$  at low  $\text{PO}_2$  and resulted in a transition to p-type conductivity at high  $\text{PO}_2$ . The decrease in conductivity resulted from Al acting as an electron acceptor deep in the band gap with no discussion of the titanium interstitial effect. By explaining the data in terms of titanium interstitials, these studies have assumed Al to be substitutionally incorporated via equation 2.16. There is some disagreement, however, from x-ray diffraction and thermogravimetric studies which concluded that Al is incorporated interstitially.<sup>103,104</sup> Other trivalent dopants like  $\text{Cr}^{3+}$ ,  $\text{Fe}^{3+}$ , and  $\text{Mn}^{3+}$  in  $\text{TiO}_2$  also exhibit a decrease in conductivity and transition to p-type behavior at high temperatures and oxygen partial pressures.<sup>105-109</sup>

A great deal of work has been done on the electrical and structural effects of doping  $\text{TiO}_2$  with Nb. The modeling work mentioned earlier further calculated that the  $\text{Nb}^{5+}$  valence state is stable in the band gap, and it is energetically favorable for  $\text{Nb}^{5+}$  to incorporate substitutionally on a Ti site in the lattice.<sup>100</sup> Other studies confirmed the substitutional replacement of Ti with Nb by density measurements as a function of  $\text{PO}_2$ <sup>110</sup> and thermogravimetric experiments.<sup>111</sup> The rutile structure was observed to accommodate seven to eight atomic percent Nb before creating a secondary phase.<sup>111-116</sup> Since  $\text{Nb}^{5+}$  is a larger ion than  $\text{Ti}^{4+}$ , the lattice volume of substitutionally doped crystals would be expected to expand. This was the finding when investigated.<sup>110,111,114</sup>

The defect equations 2.17 and 2.18 show that Nb can be compensated electronically or by titanium vacancies. A dramatic increase in conductivity was attributed to electronic compensation.<sup>116-118</sup> In one case, an activation energy of 0.08 eV was measured around room temperature. Mobility values of approximately 0.8 and 0.5 cm<sup>2</sup>/V•sec were measured at 25 and 225 °C, respectively. Mobility was only found to be activated below 60 K.<sup>87</sup> The donor ionization energy measured at and below room temperature for another sample was 0.03 to 0.12 eV. In this instance the energy was thought to be characteristic of electron ionization from a Nb donor level. Mobility was shown to be inversely related to temperature due to scattering mechanisms.<sup>118</sup>

#### 2.3.4 UHV Surface Characterization

Research in the field of heterogeneous catalysis has motivated the surface characterization of metal oxides. The goal is to understand the relationship between specific surface characteristics and the bonding and reactivity of adsorbed species.<sup>119-123</sup> Among other applications, this type of research has permitted substantial advances in the photo-oxidation of carbon monoxide and methyl chloride for the reduction of environmental pollutants.<sup>124-127</sup>

Two key adsorbents of interest are oxygen and water. The common practice in this field is to characterize single crystal TiO<sub>2</sub> surfaces reduced by heating, heating with exposure to H<sub>2</sub>, or noble gas ion bombardment in comparison to unreduced surfaces. The type of defects present and their adsorption characteristics are investigated by a very large number of techniques.<sup>123</sup> The literature indicates that Ar ion sputtering is the most reliable means of adequately reducing the surface which results in a high enough defect density to be detected.<sup>119</sup>

2.3.4.1 (110)-oriented rutile. The (110) surface of  $\text{TiO}_2$  is the most stable because Ti atoms in the surface plane are five coordinated.<sup>95,128</sup> Therefore, this orientation has received a greater amount of investigation than others. Representative work on (110) surfaces shows that oxygen was chemisorbed at oxygen vacancies on a reduced surface.<sup>91,96,129,130</sup> Both molecular,  $\text{O}_2^-$ , and dissociated,  $\text{O}^{2-}$ , oxygen species were observed on the surface.<sup>91,96</sup> Water was also observed to adsorb dissociatively on (110) with both a large and small amount of defects, suggesting that no combination of neighboring defect sites was required to induce the dissociation.<sup>130-134</sup> Using a more highly sensitive technique, synchrotron radiation photoemission, an apparent charge transfer from the adsorbed species to the material was observed.<sup>131</sup>

2.3.4.2 (100)-oriented rutile. The (100) orientation of  $\text{TiO}_2$  has also been the subject of a few studies. Both oxygen and water were found to physically adsorb in a disordered manner on the stoichiometric surface. On the reduced surface, however, oxygen was observed chemisorbed as  $\text{O}_2^-$ , behaving as an electron acceptor.<sup>135</sup> Water was also observed to dissociatively chemisorb on the reduced surface.<sup>135,136</sup> Nondestructive SIMS detected a number of different ways in which the water was bound to the surface including  $\text{OH}^-$ ,  $\text{O}_2\text{H}^-$ ,  $\text{TiOH}^+$ , and  $\text{TiOOH}^+$ . A thermal programmed desorption investigation of this surface found evidence for both chemisorbed and physisorbed water on a partially reduced (100) surface.<sup>137</sup>

2.3.4.3 (001)-oriented rutile. The (001) surface of  $\text{TiO}_2$  is not a naturally occurring face because of its relative instability compared to the (110), (101), and (100) faces. On an unfaceted (001) surface the Ti atoms are only four-coordinated as compared to five or six coordination for (110) surface Ti's for example.<sup>128</sup> Due to this relative instability, the (001) surface has been observed to reconstruct to form {101} facet planes when annealed below 1200K and {114} facet planes when annealed at higher temperatures.<sup>97,128,138</sup>

These planes consist of five coordinated Ti's which is the driving force for their formation. The defects on this interesting surface structure have been thoroughly investigated as a function of different reducing and annealing techniques.<sup>119,123</sup> Investigation of oxygen adsorption on this surface as to the molecular or atomic structure of the adsorbate has, however, been generally ignored. Water, on the other hand, has been observed to adsorb dissociatively on the reduced and {101} facet plane reconstructed surface. Both spectroscopic and thermally induced desorption techniques were used to reach this conclusion. The adsorbed species was detected as OH<sup>-</sup>. There was further evidence that the excess H atom bonded to a surface O for a net formation of two hydroxyl radicals per adsorbed water molecule.<sup>139-141</sup>

## 2.4 Other Metal Oxides

### 2.4.1 Gallium Oxide

2.4.1.1 Deposition. Several low-temperature, metastable phases of gallium oxide have been reported. The hexagonal  $\alpha$ -phase is the only one to have been consistently reported.<sup>142,143</sup> The only stable form of Ga<sub>2</sub>O<sub>3</sub> is the  $\beta$ -phase which has a monoclinic unit cell.<sup>142-145</sup> The dimensions are  $a = 12.23 \pm 0.02$ ,  $b = 3.04 \pm 0.01$ , and  $c = 5.80 \pm 0.1$  Å with an angle of  $103.7 \pm 0.3^\circ$  between the a and c axes. Care must be taken in reviewing this literature due to some authors reversing the designation of the a and c axes. The unit cell consists of four Ga<sub>2</sub>O<sub>3</sub> molecules. There are two crystallographically non-equivalent Ga atoms in the unit cell. One is surrounded by a distorted tetrahedron of O atoms, and the other is surrounded by a severely distorted octahedron of O atoms. The coordination of the Ga atoms results in three non-equivalent O atoms in the unit cell.

Ga<sub>2</sub>O<sub>3</sub> has been deposited by many techniques including MBE,<sup>146</sup> thermal<sup>147</sup> and e<sup>-</sup>-beam<sup>148</sup> evaporation, spray pyrolysis,<sup>149</sup> ALD,<sup>150</sup> IBSD,<sup>151</sup> and rf magnetron

sputtering.<sup>152</sup> No deposition of Ga<sub>2</sub>O<sub>3</sub> by CVD has been reported. Only ALD and IBSD resulted in the deposition of any crystalline material. The films were found to be mixtures of both amorphous and polycrystalline material when deposited at 430 to 520 °C and 500 °C substrate temperatures, respectively. A portion of the polycrystalline material in the IBSD film was identified as β-phase. Annealing in air at 800 °C and above converts all material to the β-phase.<sup>149,151</sup>

2.4.1.2 Gas sensitivity. The most common application of Ga<sub>2</sub>O<sub>3</sub> is gas sensing. Ga<sub>2</sub>O<sub>3</sub> in thin and thick film and ceramic forms has been investigated as a sensor of oxidizing gases,<sup>152-154</sup> reducing gases<sup>155</sup> and various hydrocarbons.<sup>156-159</sup> Because the proposed environment is a combustion gas products stream, the sensor should be stable with respect to high temperatures. Therefore, research for this application has focused on obtaining β-phase material on substrates which do not interdiffuse with the Ga<sub>2</sub>O<sub>3</sub>. Among the substrates tested, BeO was found to be superior by exhibiting no detectable interdiffusion with the Ga<sub>2</sub>O<sub>3</sub> below 1200 °C.<sup>151</sup> The deposition of thin layers of Ga<sub>2</sub>O<sub>3</sub> are also of interest as an As free layer on the surface of GaAs.<sup>150,160</sup> The presence of As in the oxide surface layer has been shown to degrade the electrical properties in metal-oxide-semiconductor field-effect transistors.

## 2.4.2 Aluminum oxide

Aluminum oxide is well-known as an electrically insulating material. This property is utilized in thin layers of Al<sub>2</sub>O<sub>3</sub> in a multi-layered electronic device.<sup>161-163</sup> Al<sub>2</sub>O<sub>3</sub> has been deposited by a number of techniques including MBE,<sup>164</sup> CVD,<sup>165</sup> MOCVD,<sup>162,163,166-169</sup> e<sup>-</sup>-beam evaporation<sup>170</sup> and ALD.<sup>171</sup> The majority of these efforts have resulted in amorphous films, and the electrical properties of amorphous films are satisfactory for most applications. In one investigation, however, a heteroepitaxial film

of  $\gamma$ -phase  $\text{Al}_2\text{O}_3$  was grown on (111) Si at 750 to 900 °C substrate temperature by MBE to serve as the substrate for a semiconducting layer.<sup>164</sup> In another, a polycrystalline  $\text{Al}_2\text{O}_3$  film was deposited on (100) Si over a 700 to 900 °C temperature range by CVD using  $\text{AlCl}_3$ ,  $\text{CO}_2$  and  $\text{H}_2$ .<sup>165</sup>

## CHAPTER 3 EXPERIMENTAL METHODS

### 3.1 Thin Film Deposition

#### 3.1.1 Reactors

Two reactors were employed to grow the thin films. A schematic diagram representing the essential components of both is shown in Figure 3.1. The majority of the undoped work investigating growth rate as a function of temperature and precursor partial pressures was done in a prototype reactor. This reactor was constructed from quartz glass to test the applicability of an inverted pedestal, hot-walled reactor to solid-source MOCVD for the growth of metal oxides. The idea for using solid precursors in metal oxide film deposition originated at Hewlett-Packard.<sup>172</sup> The simple design of the quartz reactor necessitated that it be opened to the atmosphere to introduce or remove precursors and substrates between runs. A mechanical pump was used to reach a base pressure of less than 10 mTorr prior to beginning the deposition process. The standard growth conditions in this reactor were 730 °C substrate temperature, 2.5 Torr O<sub>2</sub> partial pressure, 3.9 mTorr Ti precursor partial pressure, 5.5 Torr total pressure, and a total flow rate of 300 sccm. Table 3.1 shows the value range each variable was varied over in that study. When O<sub>2</sub> partial pressure was decreased in this study, He flow rate was increased to maintain a total pressure of 5.5 Torr. This reactor was also used to deposit gallium oxide and aluminum oxide thin films. Growth variables within the ranges shown in Table 3.1 were used in the deposition of both these types of films on a variety of substrates.

Table 3.1 Growth variable ranges for quartz reactor growth study

Substrate temperature	400 - 775 °C
O <sub>2</sub> partial pressure	0.0 - 2.5 Torr
Ti precursor partial pressure	0.39 - 20 mTorr
Total pressure	5.5 Torr

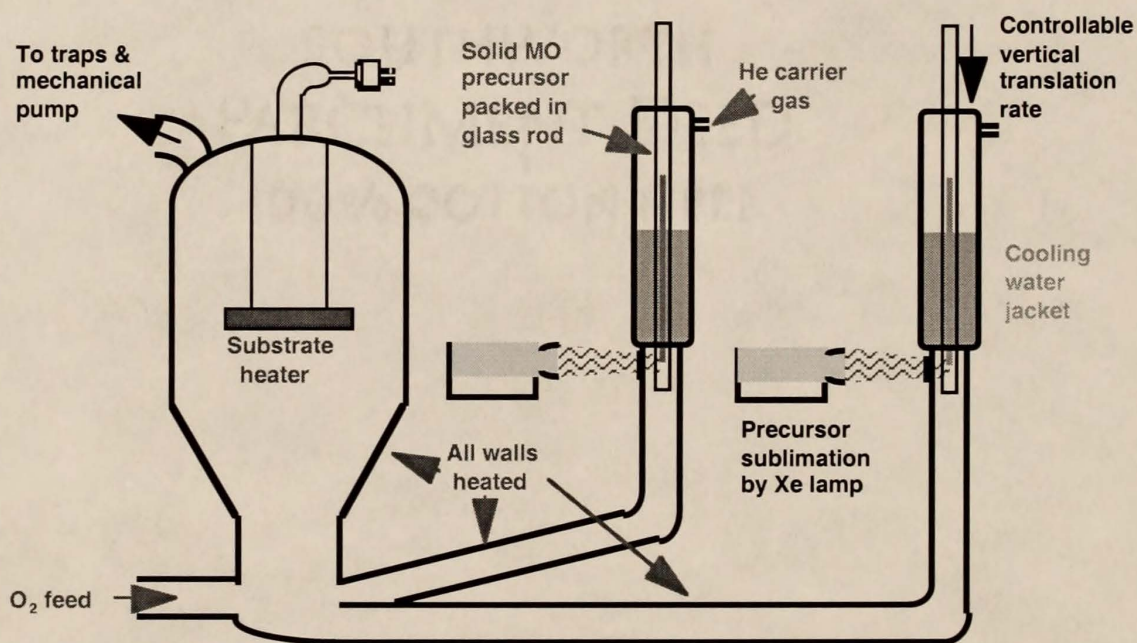


Figure 3.1 Solid source MOCVD reactor schematic

After successful exhibition of metal oxide thin film deposition in this type of reactor, a second reactor was constructed of stainless steel. This reactor used both a mechanical and a turbomolecular pump to maintain a base pressure of 10  $\mu$ Torr and will heretofore be referred to as the HV reactor. Substrates were introduced through a load-lock system. A precursor was placed in an apparatus that could be removed from the reactor and reattached using a secondary mechanical pump without breaking system vacuum. The

reactor was equipped with three separate precursor introduction arms, each with this removable piece, which allowed for deposition with multiple metals or other non-gas phase precursors. The load-lock and precursor introduction modifications allowed the reactor body to remain isolated from the atmosphere except in the case of maintenance and cleaning. This minimizes the introduction of excess humidity and other gaseous and solid contaminants.

In reference to Figure 3.1, both reactors can be described in three basic sections: precursor introduction, growth chamber and exhaust system. Solid precursors, which will be described in detail later, were used as sources of the metal atoms. Precursors were delivered to the reactor by passing the solid material through an optically heated zone, at which point the material was flash sublimed in a He carrier gas. A weighed amount of the precursor was first tightly packed into a hollow glass rod with an internal diameter of approximately 2 mm. This step was performed in a dry box with an Ar atmosphere to avoid any potential reactions between a precursor an air or moisture prior to placing the precursor in the reactor. The packed precursor's height in the rod varied  $\pm 3\%$  suggesting that uniform packing density was a reasonable assumption. Using this height, a precursor's molecular weight, the mass of material in the rod, and the desired molar addition rate, a simple calculation determined the necessary translation rate of a packed glass rod.

Precursor introduction for deposition began by lowering a rod at a set rate from the water cooled portion of a precursor introduction arm (Figure 3.1) into the focused light of a Xe filament bulb. Sublimed material then escaped through a lengthwise slit in the glass rod. Carried by He gas, the now gas-phase material flowed through the remainder of a fully heated arm to the growth chamber. The sublimation process was allowed at least 15 minutes to reach steady-state while  $O_2$  was fed to the top of the reactor's growth chamber. Both were exhausted at the bottom of the chamber. Steady-state sublimation could also be confirmed by viewing a distinct point in a lowering rod below which all precursor material

was gone. This visual confirmation was done through welder's glass to avoid eye damage from a lamp's bright light.

Upon reaching a steady state precursor delivery, the O<sub>2</sub> introduction and exhaust were switched to the bottom and top of the growth chamber, respectively. The O<sub>2</sub> and precursor could then meet at the bottom of the reactor and proceed toward the substrate via the pressure gradient established across the growth chamber. All portions of the reactor prior to the cold trap on the exhaust line were nominally heated to 275°C to avoid precursor condensation prior to the growth surface. This temperature was assumed to be low enough to avoid an appreciable amount of wall deposition as evidenced by a lack of change in the general appearance of the chamber walls viewed during maintenance and cleaning. All walls in both reactors were heated by wrapping with resistively heated strips of insulating material ("heat tape"). The temperatures were controlled by Northrup programmable controllers for the HV reactor and directly by setting the current flow to the heat tape on the quartz reactor. Temperatures were monitored by placing J-type thermocouples at a number of spots on a reactor's body.

Substrates were attached to a permanent nickel base using Ag paste (Ted Pella), so that the entire substrate heating element was removed for each run in the quartz reactor. For the HV reactor, substrates were attached to a nickel plate which was introduced via a load-lock system as mentioned previously. This plate was brought into physical contact with a permanent nickel plate which the heater was behind. After a great deal of trial-and-error heater design, a Ta wire coil vacuum sealed in quartz glass was found to have a long lifetime. This type of heater was constructed at the DuPont Experimental Station glass shop. The heaters were controlled by Fuji fuzzy-logic type controllers. The temperature was monitored by an S type thermocouple, and the actual substrate temperature was calibrated using an optical pyrometer. A nominal loss of 150 °C was found between the temperature measured by the thermocouple which was buried in the permanent Ni plate and the real substrate temperature.

### 3.1.2 Precursors

The precursors used are of a family of compounds known by their common ligand 2,2,6,6-tetramethyl-3,5-heptane dionato. A schematic of the Ti precursor of this family is shown in Figure 3.2. Note that the metal atom is attached to oxygen atoms. These precursors were purchased from STREM chemicals in powder form. They have a minimal room temperature vapor pressure.  $\text{TiO}_2$  films were grown using the Ti precursor and doped with Ga or Nb by directly mixing the precursor powders at the desired dopant level.  $\text{Ga}_2\text{O}_3$  and  $\text{Al}_2\text{O}_3$  films were also grown from their respective metal precursors.

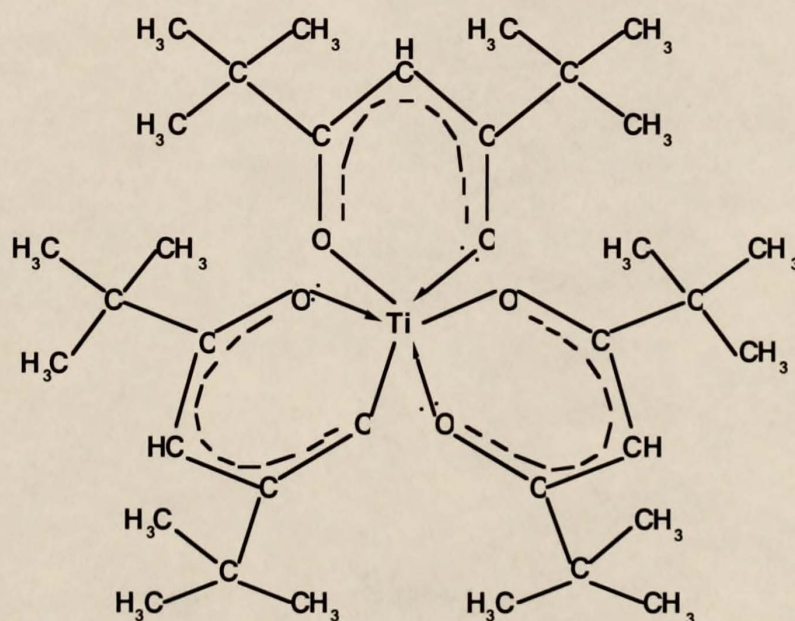


Figure 3.2 Precursor schematic

The notable characteristic of these precursors is their well-defined sublimation temperature. A thermal gravimetric analysis (TGA) was performed on several of the precursors. A TGA is a simple experiment which consists of monitoring the mass of a precursor on a combined scale / hot plate as the temperature is ramped upward. For each

precursor tested, approximately 90 % of a 7 to 10 mg mass was sublimed within a 10 °C window. Table 3.2 shows the chemical formula, molecular weight and sublimation temperature for the precursors used in the growth studies of this thesis. TGA's of the Fe and Cr precursors were not performed. When Fe(TMHD)<sub>3</sub> or Cr(TMHD)<sub>3</sub> was mixed with Ti(TMHD)<sub>3</sub> at one atomic percent, clean sublimation behavior from the precursor rod was observed in the same way as for the Ga and Nb precursors. This suggests that their sublimation temperatures fall in the range of 250 to 350 °C in agreement with the precursors for Ga and Al which are also stable in the 3+ oxidation state.

Table 3.2 Sublimation temperatures of metal precursors determined by TGA

Chemical Formula	Molecular Weight (g/mol)	Sublimation Temperature (°C)
Ti(TMHD) <sub>3</sub>	597.7	350
Ga(TMHD) <sub>3</sub>	619.5	300
Nb(TMHD) <sub>4</sub>	826.0	375
Al(TMHD) <sub>3</sub>	576.8	260
Fe(TMHD) <sub>3</sub>	605.7	-----
Cr(TMHD) <sub>3</sub>	601.8	-----

### 3.1.3 Substrates

A variety of substrates were used in the growth studies. TiO<sub>2</sub>, Ga<sub>2</sub>O<sub>3</sub> and Al<sub>2</sub>O<sub>3</sub> films were deposited on one or more of the following: Si, quartz and sapphire substrates. For the majority of the growth data presented in this thesis, the substrate preparation was limited to a degreasing which consisted of consecutively wiping a substrate surface with

cotton swabs soaked in acetone, methanol and ethanol. Later in this work, however, atomic force microscopy (AFM) became routinely available. AFM images showed that although the historical degreasing procedure was capable of removing most surface contaminants, some could remain. In addition, salts were found to potentially precipitate on a surface as a function of the cleaning procedure and reagent purity. The adequacy of a number of substrate preparation techniques were characterized by AFM. The following recipe was found to be capable of removing all organic surface contaminants and deterring the precipitation of salts. First, a substrate was doused with high purity methanol. Second, a piece of low-lint lens paper was used to scrub the surface but not dry it before redousing with methanol. Next, the substrate was doused with deionized water and immediately blown off with pressurized air which had been filtered for particles greater than 0.2 microns. A good sign that a surface was clean was beading of the deionized water. This procedure was used to clean the substrates for all the film morphology investigations presented in this thesis.

#### 3.1.4 Ion-Beam Sputter Deposition

To better analyze some of the data presented in this thesis, comparisons are made to  $\text{TiO}_2$  films deposited by ion-beam sputter deposition (IBSD) by Morris-Hotsenpiller in the same laboratories. The IBSD reactor had a base pressure of  $0.1 \mu\text{Torr}$ . Like the HV MOCVD reactor, substrates were introduced via a load-lock system to maintain system vacuum. Substrates were Ag pasted on a thin Ta plate which was heated from behind by halogen lamps. The temperature was monitored by a thermocouple after being calibrated with an optical pyrometer. Deposition occurred when a high-purity Ti target was sputtered with a Xe ion beam from a 3 cm Kaufmann-type source in the presence of  $\text{O}_2$ . The ion beam energy was 1 keV, and the current was 20 mA. The total pressure during deposition

was 0.2 mTorr due to equal partial pressures of Xe and O<sub>2</sub>. The data presented in this thesis are from films grown at 725 °C and approximately 3 Å/min for 12 hours.

### 3.2 Physical Characterization

#### 3.2.1 X-ray Diffraction

When atoms are arranged periodically on a lattice as they are in a crystalline solid, the x-rays scattered by them have a defined phase relation. Most incident beams are scattered in random directions and destructively interfere with one another. A diffracted beam is formed when constructive interference occurs in a scattering direction. Given that the incident and diffracted beams and the normal to the plane of reflection are coplanar, a diffracted beam is formed for all scattered beams which satisfy Bragg's law

$$\lambda = 2 d \sin\theta \quad (3.1)$$

where

$\lambda$  = x-ray wavelength

$d$  = spacing of atomic planes

$\theta$  = angle between incident or diffracted

beam and the atomic plane.

The larger the number of scattered beams which satisfy this equation, the higher the intensity of the diffracted beam. The relationship between the planar spacing  $d$  and the unit cell dimensions of a crystal is dependent on the unit cell geometry. Rutile has a tetragonal unit cell and the plane-spacing equation is

$$1/d^2 = (h^2 + k^2)/a^2 + l^2/c^2 \quad (3.2)$$

where

$h, k \text{ \& } l =$  crystal plane indices

$a = 4.595 \text{ \AA}$ , dimension of rutile unit cell

$c = 2.959 \text{ \AA}$ , dimension of rutile unit cell.

Combining equations 3.1 and 3.2 gives

$$\sin^2\theta = \lambda^2/4 [(h^2 + k^2)/a^2 + l^2/c^2] \quad (3.3)$$

which relates  $\theta$  to the indices of the plane(s) from which the beam is diffracting. If the values of  $h, k$  and  $l$  result in  $\sin^2\theta = 1$  then diffraction from the plane with those indices is impossible. XRD tables are typically given in  $(hkl)$ ,  $2\theta$  and  $d$ .

The typical diffractometer is capable of one geometry where the plane of incident and diffracted x-rays is perpendicular to the surface plane of the film and the x-ray source moves with respect to the film. This set-up was used in a Rigaku diffractometer for this thesis to check the bulk orientation and phase of all deposited films. The consistency of plane-to-plane spacing can also be assessed with this set-up by holding  $2\theta$  constant and varying  $\theta$ . This is known as the  $\theta$  rocking curve (rc). The full-width-at-half-maximum (fwhm) of the  $\theta$  rc peak gives a relative measure of the consistency of plane spacing. Other diffractometers are capable of moving the film with respect to the x-ray source. An important capability of this type of machine is the assessment of heteroepitaxial film growth and the in-plane crystal direction relationships between a heteroepitaxial film and its substrate. As shown in Figure 3.3, when a film is moved so that the surface normal is no longer in the plane of the x-ray beam, the angle through which the film is tilted is known as  $\chi$ . In a simple cubic lattice for example, the (101) plane would have a  $\chi$  value of  $45^\circ$  with respect to the (001) plane. If in this position, a film is then rotated about the normal to the (101) plane, the angle of rotation is known as  $\phi$ . If all planes of a film have the same in-plane orientation, the film is said to be heteroepitaxial. In the simple case of a cubic lattice, the diffraction pattern of a bulk-oriented film moved to  $\chi = 45^\circ$  and rotated through the  $360^\circ$

range of  $\phi$  would have four distinct peaks separated by  $90^\circ$  if the film is heteroepitaxial. This scheme was used to investigate the heteroepitaxial characteristics of rutile films on sapphire substrates and the matching in-plane directions between the two crystals. The fwhm of  $\phi$  peaks were also measured as a relative indication of the in-plane orientational consistency for some films. This work was performed on a Philips diffractometer. Thorough treatments of these topics and other XRD methods and applications are available in the literature.<sup>173,174</sup>

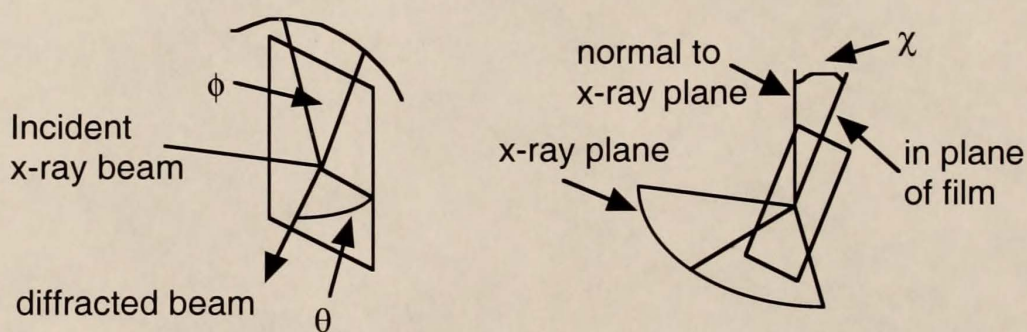


Figure 3.3 Thin film x-ray diffraction geometry

### 3.2.2 Rutherford Backscattering Spectrometry

Rutherford backscattering spectrometry (RBS) is a simple experiment in theory which requires some very large and high voltage equipment. A beam of monoenergetic and collimated alpha particles is impinged perpendicularly on a target. The particles which are scattered backward by angles of more than  $90^\circ$  from the incident direction can be detected. Figure 3.4 shows the basic components of an RBS experimental system.

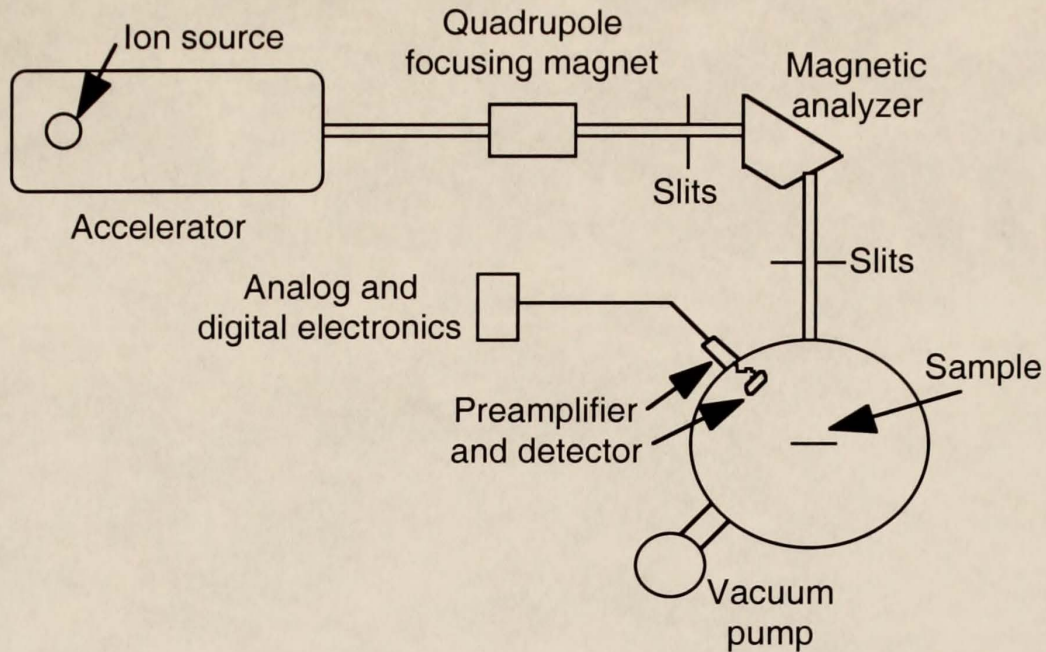


Figure 3.4 Schematic of essential Rutherford backscattering equipment

Charged particles are generated in the ion source. Their energy is raised to several MeV by an accelerator. The beam then travels through the quadrupole focusing magnet, magnetic analyzer and slits which together serve to collimate or focus the beam and filter it for the desired type of particle and energy. Next, the beam enters the scattering chamber and impinges on the sample. Some of the backscattered particles hit the detector. An electrical signal is generated by these particles which is amplified and processed by the analog and digital electronics. The resulting data is in the form of a spectrum which is why the technique is known as spectrometry. To gain information from the spectrum, it must be modeled.

RBS for this thesis was performed at the Laboratory for Research on the Structure of Matter (LRSM) which is cooperatively managed by several science and engineering departments at the University of Pennsylvania. The equipment is maintained by LRSM and for a fee users do the most basic processes of taking data and leave with a spectra file for each sample. The ions in the LRSM equipment are  $^4\text{He}^+$  and typically have an energy of 2

MeV. This information along with the defining angles of the source-sample-detector geometry and the spectra are contained in each data file. Figure 3.5 shows a typical spectrum for a  $\text{TiO}_2$  film deposited on sapphire ( $\text{Al}_2\text{O}_3$ ) with an applied model (smooth line). The spectra is in the form of peak intensity as a function of energy. The greater the mass of an element, the higher on the energy axis it appears. From left to right, the first knee is the oxygen peak, the second is the viewable end of the aluminum peak and finally the titanium peak can be viewed entirely.

A modeling program known as RUMP was developed at Cornell University for analyzing RBS spectra. The high energy or front edge of a peak for any atom has a well-defined energy as a function of the beam energy and equipment geometry. The spectra must be calibrated to fit the model and therefore the Ti and  $\text{O}_2$  peaks were used for calibration of  $\text{TiO}_2$  films deposited on sapphire. The substrate is modeled as 50,000 Å or infinitely thick with respect to the film. By inputting the atomic density of the crystalline film, the thickness of the film corresponds to the width of the Ti peak. The model is believed to be accurate to within 50 Å. As the film becomes thicker, the peaks increase in width toward lower energy. At approximately 5000 Å the Ti peak will intersect the Al peak and modeling becomes more difficult and less accurate. The relative amounts of atoms correspond to their peak height. For example, the model of a heavily oxidized  $\text{TiO}_2$  film would show the model peak as being higher than the actual Ti peak because Ti and O are not at a 1:2 ratio as input to the model. Using this same analysis any dopant which is distributed throughout the film will have a peak of the same width as the Ti peak. The height of the dopant peak defines its concentration relative to Ti. Dopant concentrations can be accurately modeled within 0.1% down to approximately 0.1% where the peak becomes indistinguishable from the signal noise. The model in Figure 3.5 shows that the film is not significantly oxidized or reduced and is 2400 Å thick. A complete treatment of RBS and its other abilities and applications is available in the literature.<sup>175</sup>

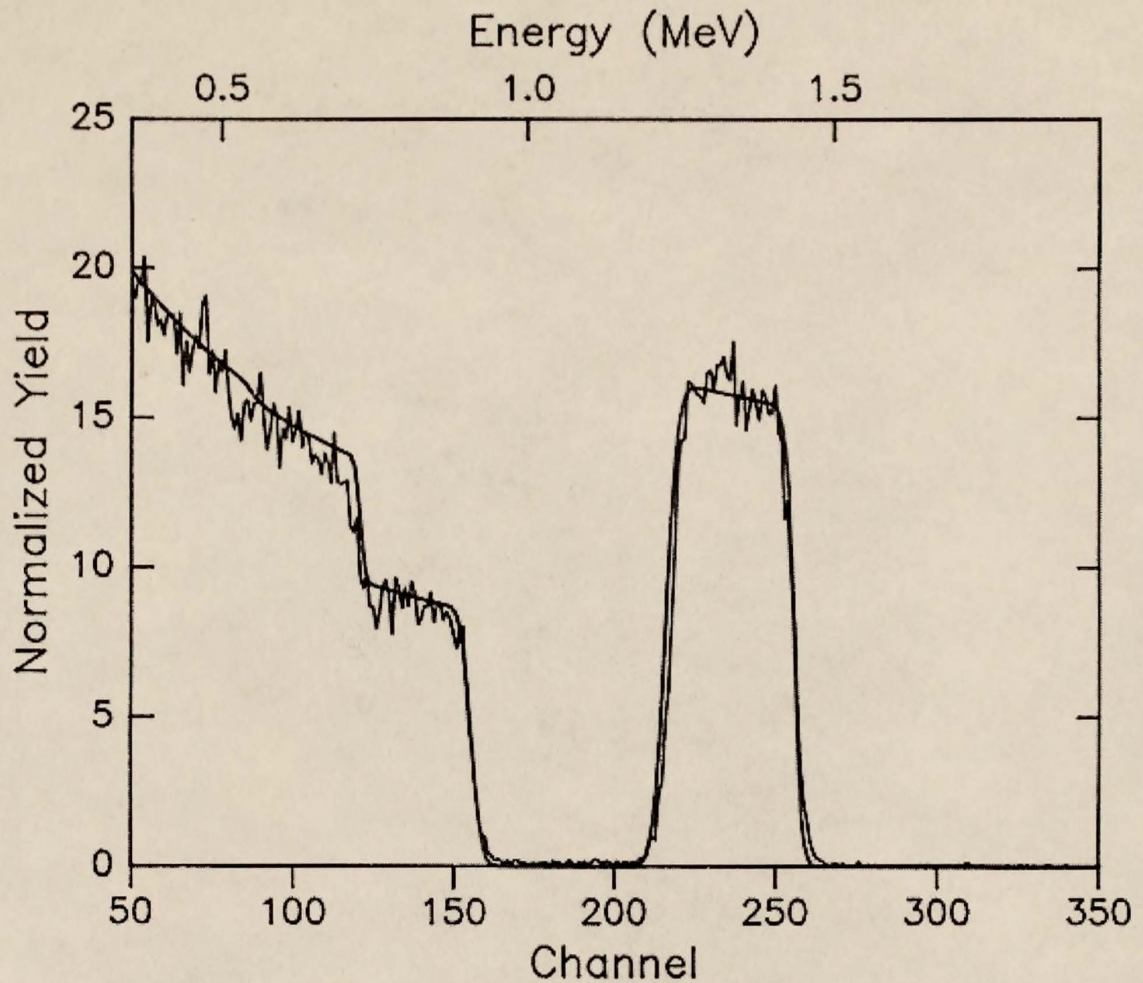


Figure 3.5 RBS spectra of  $\text{TiO}_2$  on sapphire with RUMP model

### 3.2.3 Atomic Force Microscopy

Atomic force microscopy (AFM) was used to measure the size and shape of surface features of the thin films. AFM can be used in a number of different modes to investigate surface morphology with the same equipment. A schematic of the equipment set-up used to take images for this thesis is shown in Figure 3.6. The essential parts of the equipment are the physical measurement apparatus consisting of the laser and tip, the conversion of the signal caused by changes in the reflected laser beam to information about the tip movement, and the feedback control loop which seeks to keep some measure of a physical

interaction between the tip and the surface constant. The mode of investigation defines which physical interaction is held constant.

With respect to the equipment shown in Figure 3.6 contact AFM (the tip is theoretically in constant contact with the surface) can be used in constant force or constant height mode. In constant force mode the vertical position of the tip would be continually adjusted to avoid deflection of the tip by the surface. The height adjustment information would be used to create the surface image. In constant height mode, the vertical position of the tip is not changed as it is moved across the surface. Deflections caused by the tip coming into contact with surface features are the information recorded and a control loop is not actually used. This technique is only useful for extremely flat surfaces because large features can cause very large deflections in the tip causing it to lose contact with the surface. Also, the tip has a limited vertical range when not being purposefully moved, so the tip could be damaged by large features in this measurement mode. The tip deflection information would be used to create the surface image. In a non-contact mode, the attractive van der Waals force which is present when the tip is close to the surface is used. The cantilever which is connected to the tip is vibrated at a slightly higher than its resonance frequency. As the tip approaches a surface feature out of the plane of the surface, for example, a change in the intensity of the attractive force changes the amplitude of the vibrational frequency. The height of the tip would be adjusted to maintain constant frequency, and as in constant force mode contact AFM, the height change information would be used to create a surface image.

Tapping-mode (TM) AFM is a hybrid between the modes discussed thus far. Tapping-mode consists of an oscillation of the tip normal to the plane of the surface. This intermittent contact technique has been discussed in detail in the literature.<sup>176-179</sup> TM AFM allows one to circumvent the adhesion and capillary forces which lead to uncontrollable high tip-sample contact forces in conventional contact-mode scanning AFM.<sup>176</sup> These forces can lead to surface damage in some materials. In tapping-mode, height data are

complemented with simultaneously measured phase-shift data. Topography is measured as the tip height is adjusted to retain a constant amplitude of the oscillating tip. "Phase" is measured as the phase shift between the drive signal from the feedback control loop and the actual tip response signal. Phase shift images are particularly useful for imaging the hard and soft segments of copolymers and the faceted surfaces of crystalline thin films. Figure 3.7 shows a normal image (a) and a phase shift image (b) of a  $\text{Ga}_2\text{O}_3$  film. The different crystal faces of the film's faceted structure are more clearly exhibited in the phase shift image.

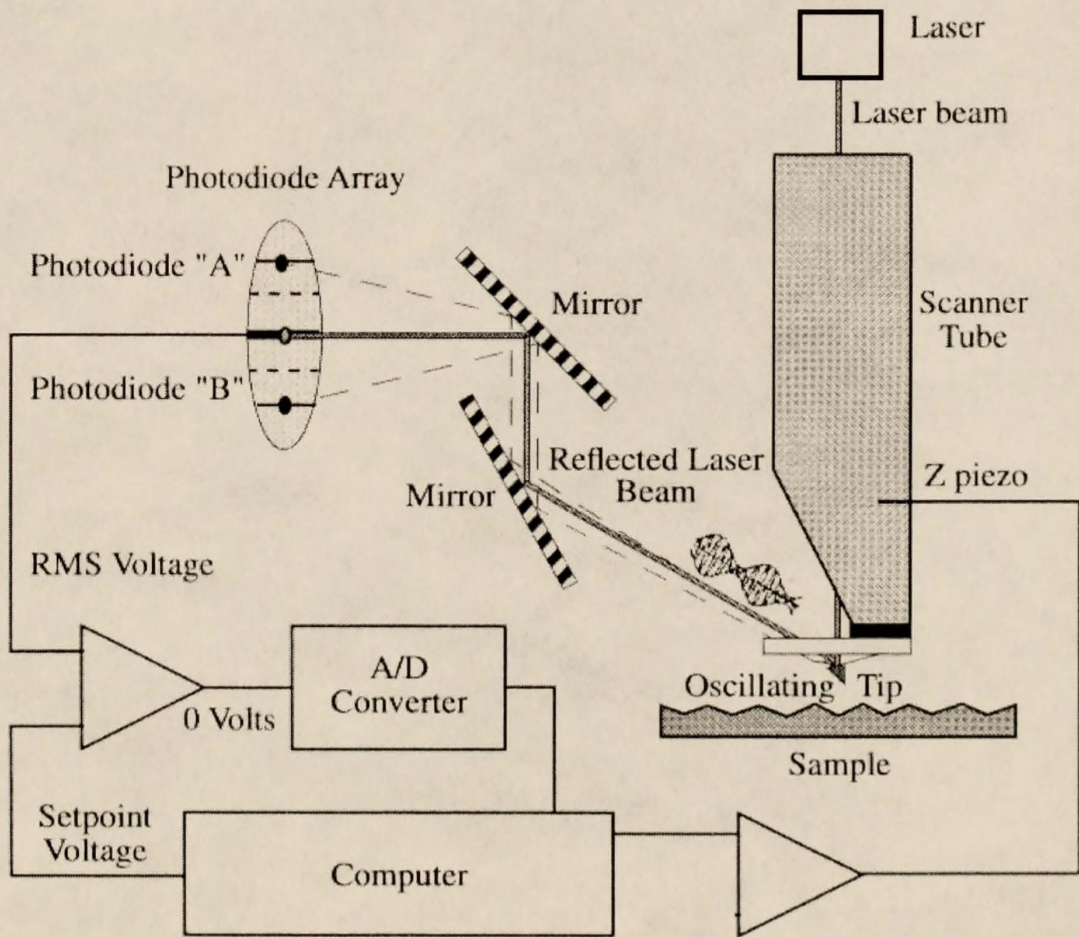


Figure 3.6 AFM equipment schematic (Courtesy of R. S. McLean)

To obtain the images shown in this thesis, TM AFM was performed by S. McLean at the DuPont Experimental Station to obtain height and phase imaging data simultaneously. The piece of equipment used was a Nanoscope IIIa AFM from Digital Instruments. Microfabricated cantilevers or silicon probes (Nanoprobes®, Digital Instruments) with 125  $\mu\text{m}$  long were used at their fundamental resonance frequencies. These frequencies varied from 270 to 350 kHz depending on the cantilever. Cantilevers had a very small tip radius of 50 to 100  $\text{\AA}$ . The AFM was operated in ambient conditions with a double vibration isolation system. Extender electronics were used to obtain the height and phase information simultaneously. The lateral scan frequency was about 1.2 Hz. The images presented in this thesis are not filtered.



Figure 3.7 TM AFM images of a  $\text{Ga}_2\text{O}_3$  thin film  
(a) normal and (b) phase shift

The primary source of error associated with AFM imaging of hard, crystalline surfaces is the size and shape of the tip. Surface features which are indented with respect to the surface plane and are smaller than the tip size cannot be fully probed. Also, small features which are out of the surface plane and are smaller than the tip will appear to have the same shape as the tip. These errors can lead to the groups of small features appearing

as one larger feature. In addition to size limitations, the sharpness of the tip can cause features such as facets which intersect at well defined to be rounded if the angle of intersection is greater than the angle of the tip.

### 3.2.4 X-ray Photoelectron Spectroscopy

X-ray photoelectron spectroscopy (XPS), also known as electron spectroscopy for chemical analysis (ESCA) is a widely used method for assessing the chemical composition of surfaces. Surface analysis by XPS involves irradiations of a solid sample with monoenergetic x-rays and energy analyzing the emitted electrons. Since the mean free path of electrons with 100 to 1000 eV energies is small, only the electrons which are emitted from the top few layers are detected.<sup>180</sup> XPS is an excellent tool for determining the composition of a multicomponent system because every element has a unique spectrum. The exact position of spectral peaks can be used to determine the chemical state of the element within the solid, which makes XPS able to discern the chemical state of elements in a multicomponent solid.<sup>181-183</sup>

Monoenergetic x-rays (Al Ka, 1486.6 eV) interact with the surface atoms by the photoelectric effect, causing the emission of electrons. Applying the conservation of energy, one can relate the kinetic energy (KE) of the emitted electron to the binding energy (BE) of the electron in the atomic orbital where it originated by the following equation

$$KE = h\nu - BE - \phi_s \quad (3.4)$$

where

$h\nu$  = photon energy

$\phi_s$  = work function.<sup>183</sup>

The electron energy analyzer collects a spectrum which represents electron intensity as a function of the electron kinetic energy. The electron energy analyzer acts as a filter, only

allowing electrons with a given kinetic energy to pass through to the detector (electron multiplier). The analyzer allows electrons within a range of energies (pass energy) about a given kinetic energy to pass, therefore the pass energy is very important for determining the breadth of spectral features. Increasing the pass energy results in an increase in electron detection and peak width, therefore pass energy must be optimized to produce a spectrum which still contains adequate intensity without sacrificing spectral resolution. To maintain adequate resolution of a surface component with a small concentration, multiple scans of a given region are often performed and the spectra are averaged.

XPS was performed on a few samples for this thesis by V. Lusvardi at the DuPont Experimental Station. The samples were doped and undoped rutile thin films. The tests served a few purposes. First, near surface concentration of dopants was measured to investigate their diffusion during the deposition process. Second, the oxidation state of the dopant atoms was investigated in light of discrepancies in the literature on this matter, especially for Nb. Third, the oxidation state of atoms at the surface was investigated to determine if reduced cations could be identified in as-grown thin films within the resolution of this technique. Finally, the work served Lusvardi by helping to define the behavior of a new piece of UHV equipment with a well-characterized material.

### 3.2.5 Secondary Ion Mass Spectrometry and Auger Electron Spectroscopy

Secondary Ion Mass Spectrometry (SIMS) and Auger Electron Spectroscopy (AES) were used to investigate a few samples by depth profile. SIMS depth profiling was performed by Charles Evans East, an analytical company. SIMS uses an energetic beam of primary ions to collide with the surface and dislodge them as secondary ions. Upon collision with the surface, the primary ion is implanted in the solid and its kinetic energy is transferred to atoms already in the solid. The transferred energy causes desorption of a solid species at the surface producing a gas phase ion. This process is equivalently known

as sputtering. The mass spectra of these secondary ions are then detected. Both positive and negative ions can be detected.

The escape depth of the secondary ions ranges from the immediate surface to more than 20 Å. The escape depth is a function of the material and the energy of the primary ion. The predominant secondary ion species observed in SIMS are singly charged atomic and molecular ions. Isotopic composition aids in identification of fragments which can be used as more information about the chemical composition of atomic layers at or near the surface. By using higher primary ion current densities, material is etched away and a profile of the film composition as a function of depth can be investigated. The primary source of error in this procedure is that the chemical composition of the material in the deeper layers can be changed during the bombardment of the surface. In addition to chemical reactions, more volatile components can be "boiled" off. Finally, surface material can be decomposed by the higher energy ion source making it appear that there are species present on the surface which were not initially present. SIMS depth profiles were performed on several Ga-doped rutile thin films for this thesis to investigate diffusion of the dopant atoms to the surface during growth as compared to annealing. In-depth discussions of materials analysis by SIMS and the associated sources of error are available in the literature.<sup>184,185</sup>

In AES, the incident electron beam ionizes an atomic core level electron. The energy released when a higher energy electron falls back to fill the core level is transferred to a valence electron, which is ejected into the gas phase. This gas phase electron is detected as an Auger electron with an electron spectrometer. The kinetic energy of the Auger electron is dependent on the difference between the Auger electron's energy level in the atom and the energy released when the originally excited electron returns to the core level. Since this relationship is atom specific, the energy of the Auger electron can be used to identify the atom it was released from. The Auger electron escape depth is only 4 to 25 Å depending on the material being analyzed, so it is a very surface sensitive technique. AES can be used in cooperation with sputtering to investigate the composition of a film as a

function of depth. This technique was performed at the University of Pennsylvania LRSM on a series of undoped rutile films grown at varying oxygen partial pressure to investigate carbon contamination in the films. In depth discussions of materials analysis by AES and the associated sources of error are available in the literature.<sup>186,187</sup>

### 3.3 Electrical Characterization

#### 3.3.1 Sample Preparation

After a film was deposited, it was removed from the nickel plate described in §3.1.1 using a razor blade edge and hand pressure. Overzealous scribing of a substrate back to denote in-plane crystal direction often resulted in fracturing during removal from the nickel plate in early experiments. This error resulted in changing to a very light single mark scribing of substrate backs and more careful notation of how substrates were oriented on the nickel plate with respect to in-plane crystal orientation. Upon detaching a film from the nickel plate, dried Ag paste residue remained on the substrate back. For very high resistance films the residue could potentially offer a path of lower resistance across the back of the substrate. For this reason the residue was scraped away with a previously unused razor blade to a level below eye detection.

To probe the electrical properties of a thin film on an insulating substrate such as sapphire, surface electrical contacts were used. Depositing a contact on a substrate surface prior to deposition and then a second contact on the film surface was considered. This contact arrangement, however, introduces two potential problems. First, as will be demonstrated in Chapter 4, surface impurities can have dramatic effects on film growth and surface morphology. The contact layer on the substrate would most likely be a deterrent to heteroepitaxial film formation and would definitely effect the surface morphology in an uncontrollable manner. Since a primary goal of this thesis is to investigate well-defined thin film materials, either of these effects would be unacceptable. Second, because the

melting point of potential contact materials like Ag and Au is approximately 1000 °C or less, diffusion of the contact material through the film during deposition would most likely occur. Because of its adaptability to evaporation and availability in paste form, Au was chosen as the contact material.

A mask was created from Kapton® tape which is known for its ability to withstand higher temperature than more common tapes. For the portion of the mask that was in contact with a film, pieces of desired shape were made by putting the adhesive side of two pieces of tape toward each other and joining these pieces with tape on the top side of the mask. The final mask consisted of two open spaces 0.5 mm wide and 8.0 mm long separated by 2.2 mm. The mask was capable of fully covering a film.

A film was placed on a glass slide and the mask secured over it. This object was placed in a Au evaporation chamber (Balzers Union). A turbo pump evacuated the chamber to at least 20  $\mu$ Torr. Nominally 0.25 g of high purity (99.999%) Au wire (Alfa Aesar) was attached to a W filament. High current flowing through the filament created enough heat to evaporate the Au which condensed on a film and mask surface. After removing the mask, 0.05 mm diameter Au wire was attached to the contact pads using Au paste (Ted Pella). These wires were put into physical contact with mechanically stiff Au wires ( $\phi=0.76$  mm) which were a permanent part of the sample holder. A schematic of the holder with attached film is shown in Figure 3.8.

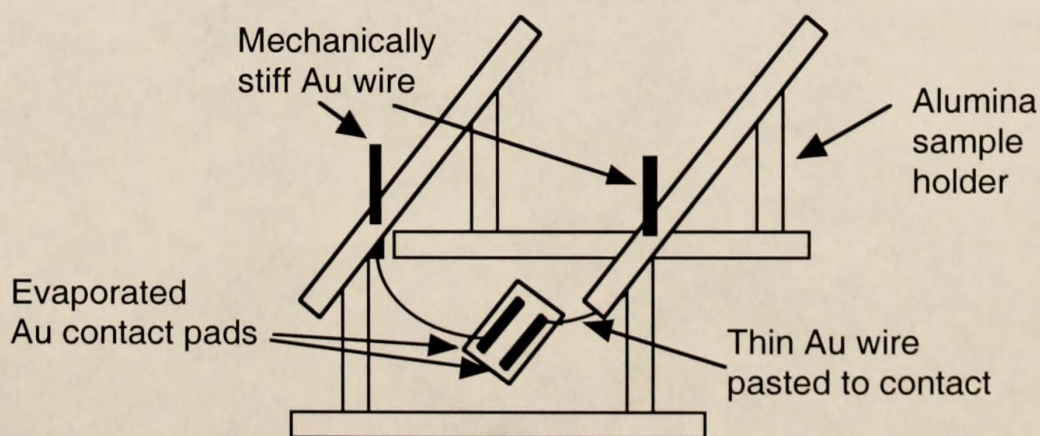


Figure 3.8 Schematic of alumina sample holder with attached film

### 3.3.2 Environmental Chamber

Small, coaxial cable ( $\phi=0.99\text{mm}$ ) was used to bring current from an 8-pin electrical feedthrough to the permanent wires of the sample holder. The cable was grounded to an excess thermocouple feedthrough whose atmosphere end was grounded to the building framework. Normal coaxial cable ( $\phi=5.0\text{mm}$ ) connected the high current and voltage ports of the impedance bridge to a pin of the electrical feedthrough and likewise for the low current and voltage ports. These cables were also grounded to the building framework.

3.3.2.1 Chamber design. These feedthroughs existed on the face of an environmental chamber designed and constructed for the electrical characterization work of this thesis by the investigator. Figures 3.9 and 3.10 are schematics of a detail of the feedthrough arrangement and gas flow architecture, respectively. The dimensions of the cubic chamber were 10 in. on the outer edge with a 6 in. ID opening on each face. The feedthroughs detailed on Figure 3.9 are 1.5 or 2.5 in. ID. All flanges were Conflat® type for UHV applications.

As shown in Figure 3.9, the chamber was equipped for impedance measurements, pressure and temperature measurements, current throughput for an internal heater, gas flow and evacuation. Figure 3.10 shows the gas flow architecture was capable of introducing dry and humidified  $\text{N}_2$ , moderate levels of  $\text{O}_2$  (1 to 760 Torr) and CO. Scientific grade gases were used (MG Industries, 99.9995%).

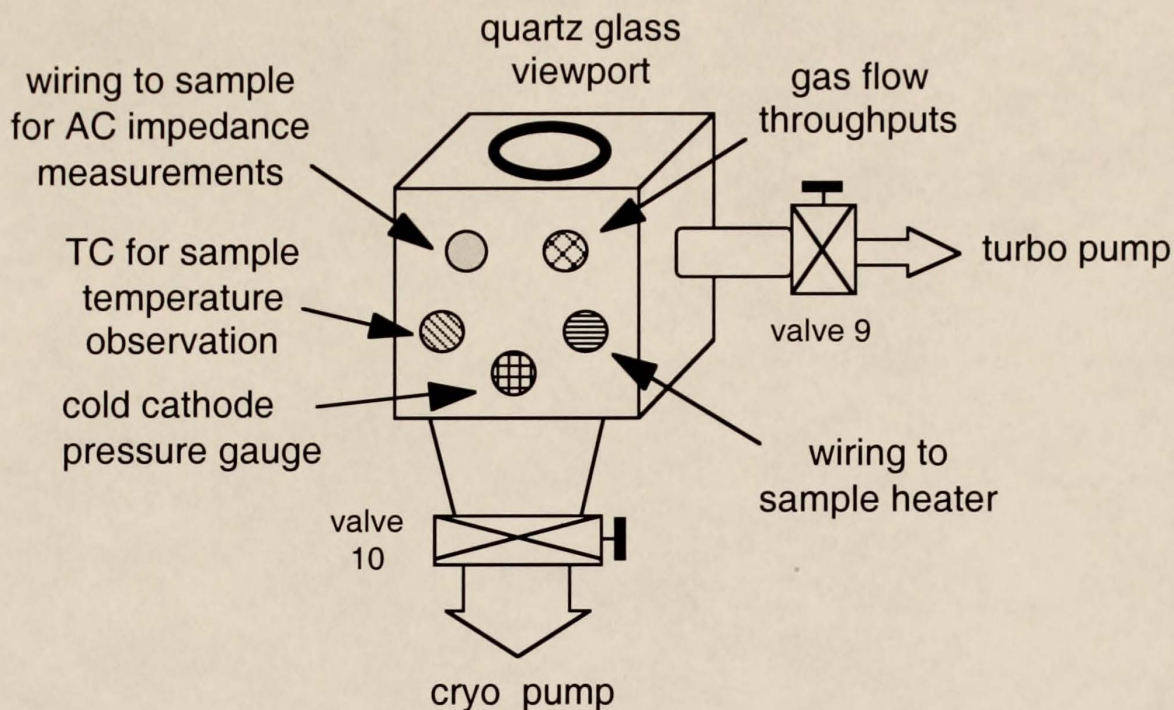


Figure 3.9 Environmental chamber feedthrough schematic

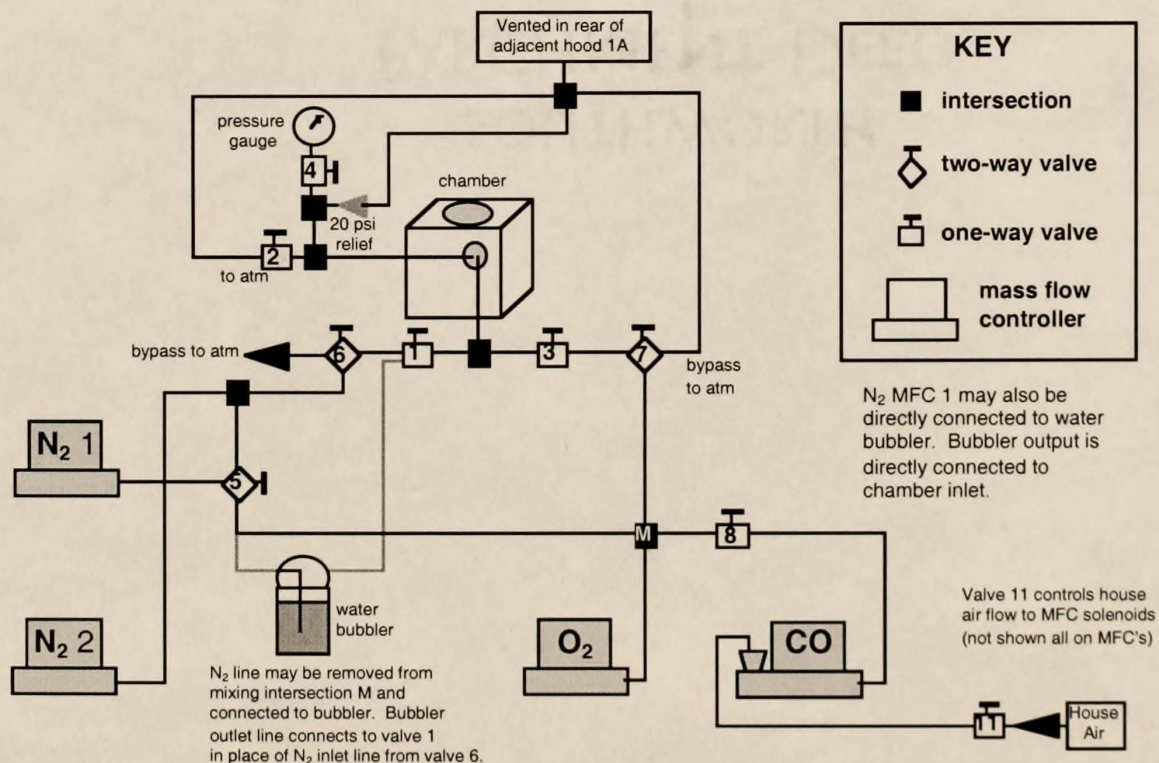


Figure 3.10 Environmental chamber gas flow architecture schematic

3.3.2.2 Testing procedure. The general procedure used in testing a film was as follows. After placing a sample in the chamber and resealing the removed flange, N<sub>2</sub> was flowed while the sample was heated at approximately 2 °C per minute to around 180 °C. Gas flow was then shut off, and the chamber was evacuated for approximately 14 hours. During the evacuation the chamber was wrapped in heat tape followed by Al foil and heated to 90 °C. This procedure served to remove the original moisture content from the chamber. After removing the foil and heat tapes, the chamber was filled with N<sub>2</sub> to atmospheric pressure, and the sample was heated at 2 °C/min to approximately 225 °C. The conditions were held constant for 24 hours while all chemically adsorbed water was driven off a sample. The bake-out procedure was carried out a second time to remove all humidity from the chamber. During this second bake-out, nominally 10 minutes were required for the chamber pressure to reach 2 mTorr. At this point the sample was cooled to 180 °C. After the bake-out, the chamber was filled with N<sub>2</sub> to atmospheric pressure and 150 sccm flow was established. The sample was reheated to 225 °C. From this point impedance data were taken as a function of sample temperature. O<sub>2</sub> was then introduced and impedance data were taken for changing temperature at one or more partial pressures. The chamber was then evacuated for approximately 20 hours and pure N<sub>2</sub> flow was reestablished. Flow was then switched to humidified N<sub>2</sub> for the collection of impedance data. The cited evacuation times resulted in a pressure not greater than 5 μTorr. The long equilibration times and bake-out procedure resulted in a minimum time of one week to collect reliable data in the three atmospheres described.

Through a great deal of trial and error, minimal partial pressures of humidity were discovered to be the source of inconsistent impedance data after reestablishing a pure N<sub>2</sub> atmosphere. Chemically adsorbed water is known to desorb from a rutile TiO<sub>2</sub> surface above 200 °C. Only through the two bake-out procedure could all humidity be removed from the chamber and a film surface so that a consistent impedance value was measured in a pure N<sub>2</sub> atmosphere independent of previous atmospheres in the chamber. Because of

the large mass and internal volume of the chamber, approximately 1.5 hours were required to establish equilibrium conditions after a change in sample temperature.

3.3.2.3 Sample heaters. Finally, sample heating was a source of some difficulty in this thesis. As was shown in Figure 3.8, the final sample holder design iteration allowed a sample to sit directly on a heater for heated surface. The original heater set-up consisted of a flat coil-type heater inside a glass finger which protruded into the chamber. The sample sat on a flat portion of the glass finger. The coiled heater was capable of producing a temperature near 600 °C, but over 200 °C was lost across the air gap and the glass to an actual temperature measured at a film surface. The ability to take a film to higher temperatures was desired, so wiring and the glass protrusion were redesigned to accommodate a ceramic, disk-type heater. This heater worked very well in non-oxidizing atmospheres. Its most significant design flaw was the use of carbon contacts. Pt was sputtered over the C in an effort to separate the contacts from the atmosphere and extend the life of the heater. Unfortunately, over time the contacts degraded and the time between breakages became so short combined with the repair time that little progress was being made in film testing. Therefore, the original heater set-up was reinstalled. The majority of the data presented in this thesis was taken at temperatures below the maximum sample temperature of this coil-type heater, 310 °C.

### 3.3.3 Impedance Measurements

Two bridges were employed to characterize a film's impedance behavior in the various atmospheres as a function of temperature. One was the 1689M RLC Digibridge® manufactured by GenRad. This device was computer controlled and averaged the capacitance and loss tangent values from three measurements at each frequency taken at the slowest available measurement speed (~1 sec). The frequency range was from 13 Hz to

100 kHz. The Hewlett-Packard 4275A Multi-Frequency LCR Meter was also employed to extend the measurement frequency range to 10 MHz. The two devices' frequency ranges overlapped from 10 to 100 kHz giving confirmation to a portion of the data.

3.3.3.1 Theory of measurement. The Digibridge RLC tester uses a patented measurement technique which is described in detail in the equipment manual. The advantage of the particular measurement technique and circuitry is that the only calibration adjustment in the Digibridge is the factory setting of the test-voltage-level reference. The only precision components in the instrument are four standard resistors and a quartz crystal stabilized oscillator. The capacitance and loss tangent values are calculated by the microprocessor from a set of eight voltage measurements, the frequency, and the calibrated resistance and charge of the applicable standard resistor. Figure 3.11 shows a simplified diagram of the measurement circuit in the bridge. A sine wave generator drives a current  $I_x$  through a film (or any device being tested) represented by  $Z_x$  and a standard resistor  $R_s$  which are in series. Two differential amplifiers with the same gain  $K$  produce voltages  $e_1$  and  $e_2$  where

$$e_1 = K Z_x I_x \quad (3.4)$$

and

$$e_2 = K R_s I_x. \quad (3.5)$$

Combining these equations, one gets an equation for a film's impedance

$$Z_x = R_s e_1 / e_2 \quad (3.6)$$

which is a complex ratio. The capacitance and loss tangent are automatically calculated by the Digibridge's microprocessor from the impedance, frequency and other information.

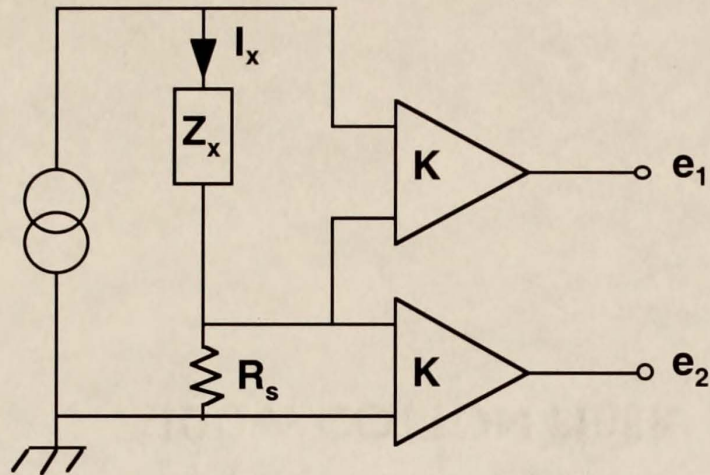


Figure 3.11 Impedance bridge simplified measurement circuit schematic

3.3.3.2 Calculations from impedance measurements. Having obtained the capacitance and loss tangent as a function of frequency at a selected atmosphere and temperature, the following equations were used to calculate the real ( $Z'$ ) and complex ( $Z''$ ) portions of the total impedance ( $Z$ ) to create a complex impedance plot where

$$Z = Z' + jZ'' \quad (3.7)$$

The computer program returned a table of values which had frequency ( $f$ ) in kHz and the capacitance ( $C$ ) in pF and loss tangent ( $D$ ) at each  $f$ . From these parameters,  $Z'$  and  $Z''$  can be calculated in two ways. One is via the time constant,  $\tau$ .

$$Z' = R / (1 + \omega^2 \tau^2) \quad (3.8)$$

and 
$$Z'' = -\omega \tau R / (1 + \omega^2 \tau^2) \quad (3.9)$$

where 
$$\tau = R C \quad (3.10)$$

and the resistance R is calculated by

$$R = 1 / (\omega C D) \quad (3.11)$$

where

$$\omega = 2 \pi f. \quad (3.12)$$

An equivalent calculation uses the loss tangent directly:

$$Z' = D^2 R / (1 + D^2) \quad (3.13)$$

$$Z'' = -1 / [\omega C (1 + D^2)]. \quad (3.14)$$

C and D values were put into a spreadsheet containing both sets of equations to calculate  $Z'$  and  $Z''$  at each  $f$ . These values were then transferred to a graphics package to create a complex impedance plot. A C value around 1 pF is typical of all data presented in this thesis with the observed changes in the impedance values resulting primarily from changes in D. Figure 3.12 shows the resulting complex impedance plots for an undoped, (101)-oriented rutile thin film at a series of sample temperatures in  $N_2$ . Note the symmetric shape of the plots. This behavior is also representative of all data presented in this thesis. The intercept of the complex Z plot with the  $Z'$  axis is the DC resistance of a film. This DC resistance is the value used in this thesis to calculate all data and comparisons based on resistance values.

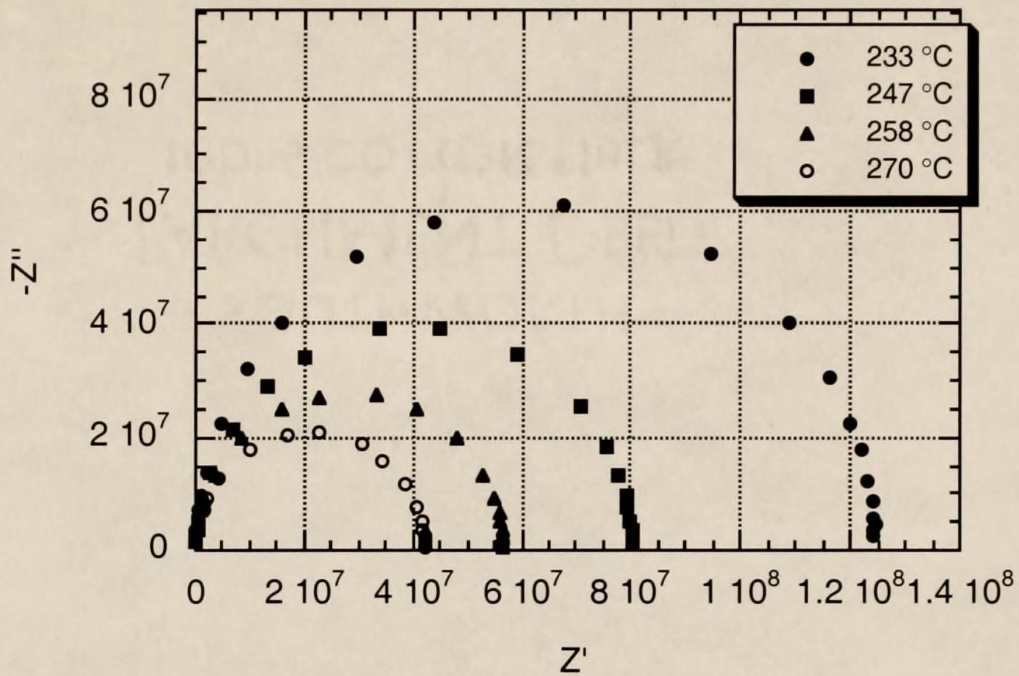


Figure 3.12 Complex impedance data as a function of sample temperature for an undoped (101)-oriented rutile thin film in  $N_2$

3.3.3.3 Data approximations. Some of the data presented in this thesis are derived from resistances with values greater than  $1e9 \Omega$ . At resistances of this magnitude, a complex impedance plot is no longer a complete semicircle. The portion that remains can be very difficult and error prone to fitting statistics to determine the  $Z'$  intercept. When the low frequency data no longer intercepted the real impedance ( $Z'$ ) axis, the  $Z'$  value at 40 Hz was used as an approximation to the  $Z'$  intercept value and therefore the DC resistance. As a test of this approximation and the high resistance measurement capabilities of the bridge, resistors with nominal values of  $1e9 \Omega$  and  $5e9 \Omega$  were obtained. Each was soldered in parallel with a 1 pF capacitor, connected to the sample holder and placed inside the chamber in the same way as a film being tested. Figures 3.13 and 3.14 show the complex  $Z$  plot obtained for both circuits with the  $R$  value at 40 Hz inset. The figures show that this approximation is valid.

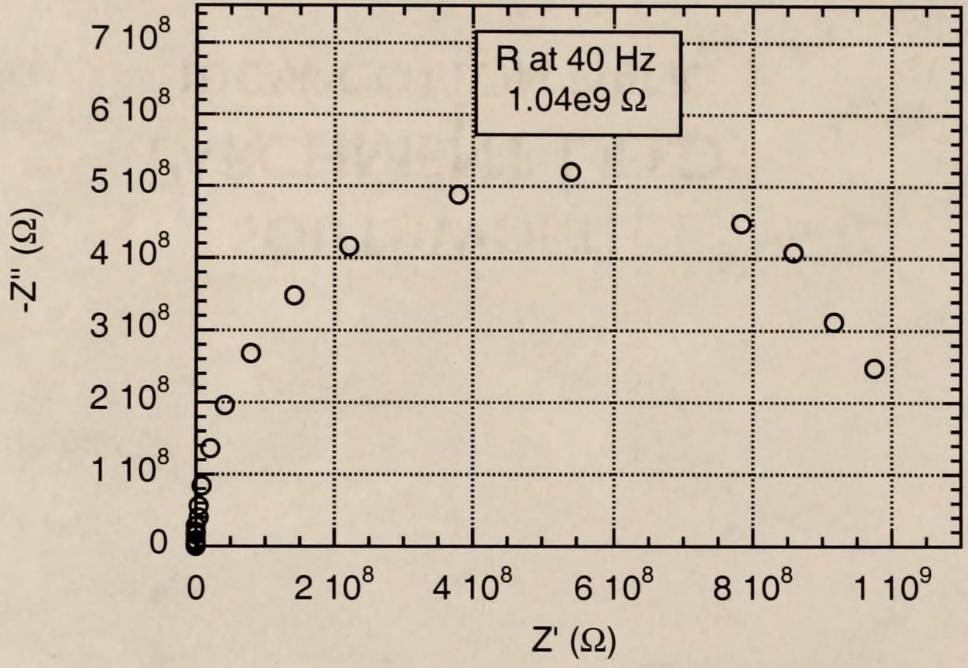


Figure 3.13 Complex Z plot for 1e9 Ω resistor in parallel with 1 pF capacitor

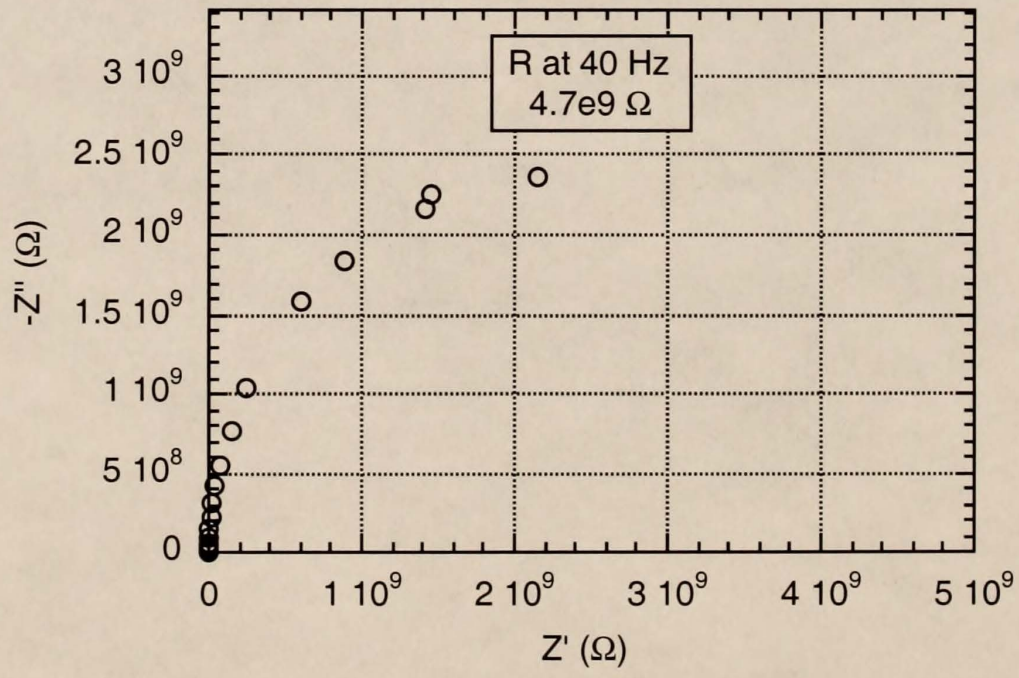


Figure 3.14 Complex Z plot for 5e9 Ω resistor in parallel with 1 pF capacitor

A value of  $4.7e9 \Omega$  obtained for the  $5e9 \Omega$  resistor is within error range for a resistor of this value according to the electrical professional by whom it was provided. This approximation method was used for values obtained at 40 Hz up to  $2e10 \Omega$ . Beyond this resistance, the C and D values at even the lowest frequencies became spurious as judged by the inconsistency of the three values averaged at each f. Any value in this thesis noted as an extrapolation was obtained with a linear extrapolation of at least three R values below  $2e10 \Omega$ . Extrapolation was only necessary for undoped and Ga-doped (001)-oriented rutile thin films in oxidizing atmospheres.

### 3.4 Equipment Safety

Safety is paramount to any research conducted at a DuPont Company site. To operate both the MOCVD reactor and the environmental chamber, a complete safety audit of the equipment and proposed experiments had to be performed. This audit consisted of an assessment, description and solution for the avoidance of all potential hazards associated with pressure, temperature, electrical shock and others. In addition, a complete operating procedure for all experiments must be written in detail noting the use of any necessary personal protective equipment and hazards associated with each step of the procedure. The safety audit completed for the environmental chamber is include in Appendix A.

## CHAPTER 4 RUTILE FILM DEPOSITION

### 4.1 Undoped Rutile Films

A series of experiments investigated the effects on growth rate (R) of changing various deposition parameters. As described in detail in §3.1.1, a prototype reactor constructed from quartz and a high-vacuum (HV) reactor constructed from stainless steel were used to deposit all films. The majority of the growth rate studies were carried out in the quartz reactor while the morphology and gas sensitivity studies characterized films grown in the HV reactor.

#### 4.1.1 Deposition

4.1.1.1 Precursor deposition efficiency. A calculation was performed to assess the deposition efficiency of the precursor. The unit cell volume of rutile  $\text{TiO}_2$  is  $6.38\text{e-}23 \text{ cm}^3$ . For a representative film thickness of  $3300 \text{ \AA}$  and dimensions of  $1 \times 0.5 \text{ cm}$ , the volume is  $1.65\text{e-}3 \text{ cm}^3$  of rutile. Knowing that there are two  $\text{TiO}_2$  molecules per rutile unit cell, a simple calculation revealed  $8.6\text{e-}7 \text{ mol TiO}_2$  in a  $3300 \text{ \AA}$  film. Eight such films could be grown simultaneously under conditions of adding  $1\text{e-}5 \text{ mol}$  per minute of Ti precursor for 90 minutes for a total of  $9\text{e-}4 \text{ mol}$  precursor. Calculating a growth efficiency by the following equation

$$E_G = \frac{\text{mol Ti in films}}{\text{mol Ti precursor added to reactor}} \quad (4.1)$$

yields 0.76% of the Ti added to the reactor became a part of the films. Even at this small efficiency, growth rate was found to be a function of Ti precursor partial pressure as will be shown later.

4.1.1.2 Precursor. As detailed in §3.1.2, a solid Ti precursor of the 2,2,6,6-tetramethyl-3,5-heptanedionato (TMHD) family was used as a precursor along with O<sub>2</sub> gas for the TiO<sub>2</sub> depositions described here. A plot of the growth rate as a function of Ti(TMHD)<sub>3</sub> or O<sub>2</sub> is shown in Figure 4.1. The Ti(TMHD)<sub>3</sub> partial pressure was varied from 0.39 to 20 mTorr in the presence of excess O<sub>2</sub> (PO<sub>2</sub>=2.5 Torr, quartz reactor) at a total pressure of 5.5 Torr and 731 °C substrate temperature. The observed slope of the Ti(TMHD)<sub>3</sub> data yielded the following growth rate expression

$$-R = k p_{\text{Ti}}^{0.8} \quad (4.2)$$

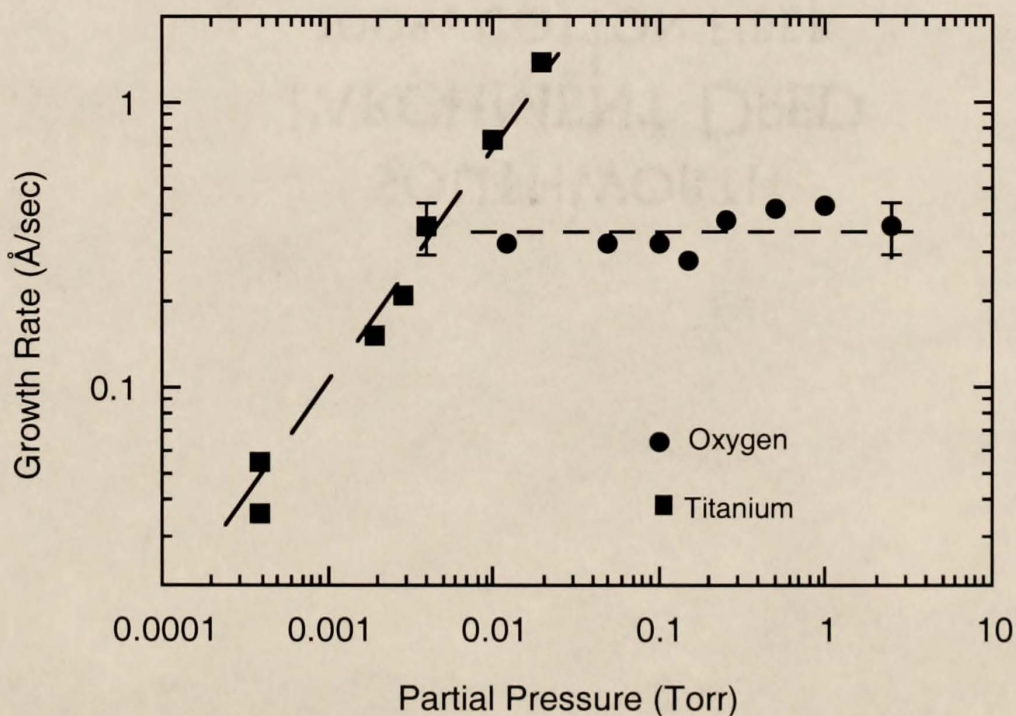


Figure 4.1 Rutile film growth rate as a function of Ti or O<sub>2</sub> partial pressure

The non-integer dependence suggests a complex growth mechanism possibly involving more than one molecule during the stages of transformation to  $\text{TiO}_2$ .

Table 4.1 shows growth rate dependencies on  $\text{Ti}(\text{OC}_3\text{H}_7)_4$  and  $\text{TiCl}_4$  precursors for a variety of substrates and growth conditions. Only  $\text{TiCl}_4$  at substrate temperatures below  $827^\circ\text{C}$  displayed a simple dependence of 1.0. Like  $\text{Ti}(\text{TMHD})_3$ ,  $\text{Ti}(\text{OC}_3\text{H}_7)_4$  must undergo a more complex series of reactions to deposit  $\text{TiO}_2$  as evidenced by the non-unity precursor dependencies. One explanation for the increased order of reaction with a  $\text{TiCl}_4$  precursor above  $827^\circ\text{C}$  is decomposition of the molecules becomes partially driven by heat independent of the  $\text{O}_2$ .

Table 4.1 Reported rutile growth rate dependence on Ti precursor

Precursor	Substrate	Temp ( $^\circ\text{C}$ )	$P_{\text{Ti}}$ (Torr)	$P_{\text{tot}}$ (Torr)	Order	Ref.
$\text{Ti}(\text{OC}_3\text{H}_7)_4$	Si(111)	360	$< 6.8\text{E}-4$ $> 6.8\text{E}-4$	11	1.35 0.14	43
$\text{TiCl}_4$	Si(111), (100),(110)	612-827 >827	0.03-0.9	760	1.0 >1.0	9
$\text{Ti}(\text{OC}_3\text{H}_7)_4$	Cu	220 250 280 300 220-300	0.04-0.3* 0.04-0.4* 0.04-0.8* 0.04-1.0* > $P^*$ , resp.	Equal to the $\text{Ti}(\text{OC}_3\text{H}_7)_4$ partial pressure	2.0    0	50

Experiments showed that  $\text{TiO}_2$  was deposited from the  $\text{Ti}(\text{TMHD})_3$  precursor without the addition of  $\text{O}_2$ , which suggests that two of the O atoms in the precursor molecule remained bonded to Ti when depositing  $\text{TiO}_2$ . The motivation for conducting the series of experiments at higher  $P_{\text{O}_2}$  was to determine if there was a change in the reaction mechanism in the presence of  $\text{O}_2$ . Given the large amount of H and C contained in the  $\text{Ti}(\text{TMHD})_3$  molecule,  $\text{O}_2$  might be expected to have influenced the decomposition

mechanism. The data suggest that excess  $O_2$  did not significantly increase the deposition rate at this temperature and therefore the growth was limited by decomposition of the Ti precursor or a fragment of the precursor.

4.1.1.3 Activation energy. Figure 4.2 is a plot of the logarithm of growth rate versus reciprocal temperature for (100) rutile deposited on (0001) sapphire. Growth rate was found to be substrate independent at all growth conditions studied, thus the same behavior was displayed for (001)- and (101)-oriented films. The data exhibit regions of increasing, decreasing, and flat growth rate dependence on the substrate temperature. First, the high temperature portion of the data measured using the quartz reactor show a positive slope. The decreasing growth rate is believed to have resulted from homogeneous decomposition of the precursor to yield non-depositing species. The decomposition was promoted by radiation or conduction from the hot nickel plate. The growth rate of films in the stainless steel reactor, however, continued to increase in the same temperature range. This disagreement resulted from differences in the materials of construction and operating pressures of the two reactors. Compared with the wall in the stainless steel system which was maintained at 275 °C for all experiments, the quartz reactor wall acted as an insulator, and the wall temperature was observed to increase above 275 °C when the substrate temperature exceeded 650 °C. For example, the quartz wall temperature was 380 °C for a 731 °C substrate temperature. The combination of the hotter reactor wall and higher operating pressure in the quartz reactor produced higher gas phase temperatures and longer reactant residence times, thus increasing the extent of homogeneous decomposition. The nearly horizontal segment of the low temperature quartz reactor data shown in Figure 4.2 suggests mass transfer limited growth under these conditions.

The data from the stainless steel reactor follow an Arrhenius relation consistent with heterogeneous reaction limited growth. The growth activation energy calculated from the temperature dependence is  $37 \pm 4$  kJ/mol and is independent of the sapphire orientation

used as a substrate. The primary barrier to growth is believed to have been the transformation of the precursor or an intermediate species to  $\text{TiO}_2$  after adsorption. Because Ti(III) is an unstable valence state, a first possible step in deposition would be to decompose one of the TMHD ligands completely, which would result in the more stable Ti(II) state. In addition, the weakest points in the six member ring are the C-O bonds. Upon breaking the ring open, many possibilities exist for further decomposition into stable species while leaving the Ti bound to an O from the ligand.

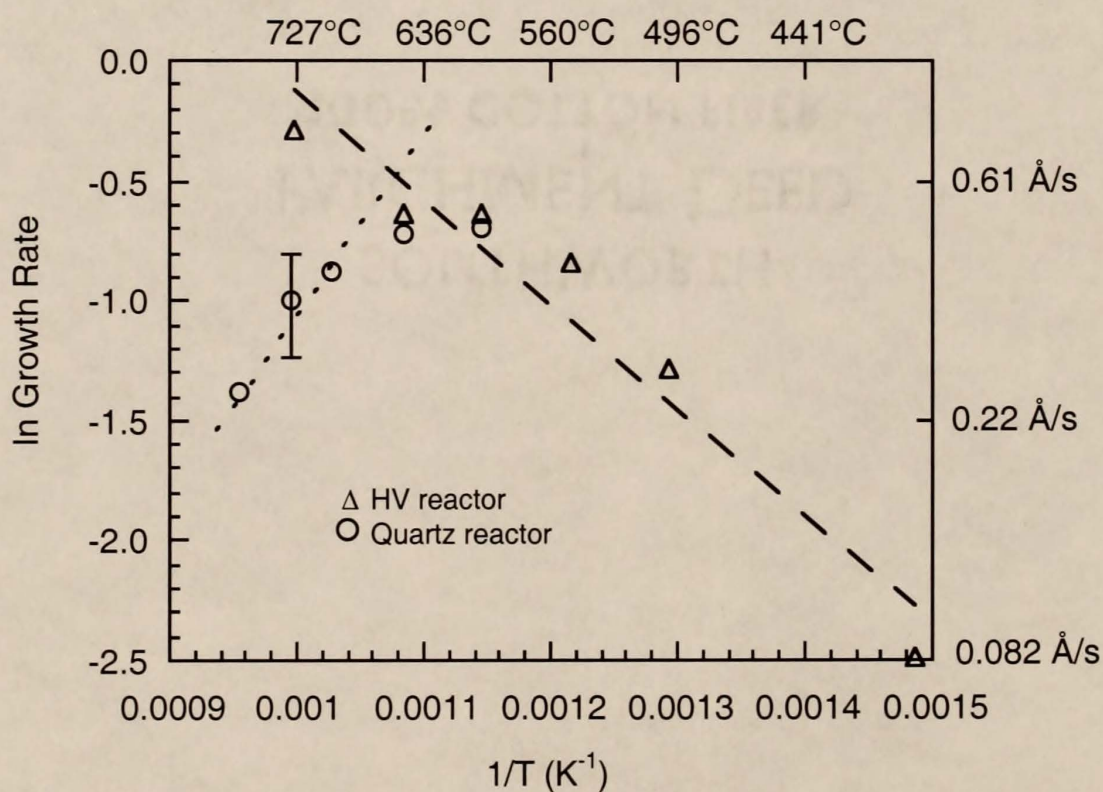


Figure 4.2 Logarithm of growth rate as a function of reciprocal temperature

Table 4.2 shows a number of  $\text{TiO}_2$  growth studies and their respective measured activation energies. The discrepancy in the data of the first and second entries in the table clearly show that activation energy was a function of more than the precursor. Each study measured the growth rate over similar temperature ranges and the resulting activation energies are considerably different. The  $\text{Ti}(\text{TMHD})_3$  growth rate dependence data and that

of Table 4.1 suggest that some amount of homogeneous decomposition occurred for these larger precursor molecules. In this case, reactor pressure and geometry, among other factors, is suggested to affect the extent of homogeneous decomposition.

Table 4.2 Reported MOCVD of TiO<sub>2</sub> growth rate activation energies

Precursor	Substrate	Temp Range(°C)	P <sub>tot</sub> (Torr)	Act. Energy (kJ/mol)	Ref.
Ti(OC <sub>3</sub> H <sub>7</sub> ) <sub>4</sub>	Si(111)	325 - 400	11	101±14	43
Ti(OC <sub>3</sub> H <sub>7</sub> ) <sub>4</sub>	(100) TiO <sub>2</sub>	227 - 377	na	57±8	52
Ti(OC <sub>3</sub> H <sub>7</sub> ) <sub>4</sub>	Crown glass	400 - 500	na	20 (anatase)	45
Ti(OC <sub>3</sub> H <sub>7</sub> ) <sub>4</sub>	Si(100)	300 - 350	0.75	87	49
Ti(OC <sub>3</sub> H <sub>7</sub> ) <sub>4</sub>	Cu	230 - 300	0.04-0.15 2.0	35 150	50
TiCl <sub>4</sub>	Si(111), (100),(110)	<850	760	74.8±4.2	9
TiCl <sub>4</sub>	Fused SiO <sub>2</sub> Si(111) Polyxtalin Si	400 - 900	760	17	57

#### 4.1.2 Crystalline Quality

4.1.2.1 Bulk crystalline quality. As explained in §3.2.1 x-ray diffraction (XRD) is a tool which can be used in a variety of ways to assess the crystalline qualities of thin films. The  $\theta$  rocking curve (rc) is obtained when the  $2\theta$  angle is held constant while varying  $\theta$ . The full-width-at-half-maximum (fwhm) of a rc peak is an indication of the consistency of plane-to-plane spacing of the planes parallel to a film's surface. Figure 4.3 shows the range of fwhm values for (001)-, (101)- and (100)-oriented rutile films grown by MOCVD

and IBSD. The numbers to the right of the range endpoints indicate the substrate temperature range over which the respective films were deposited.

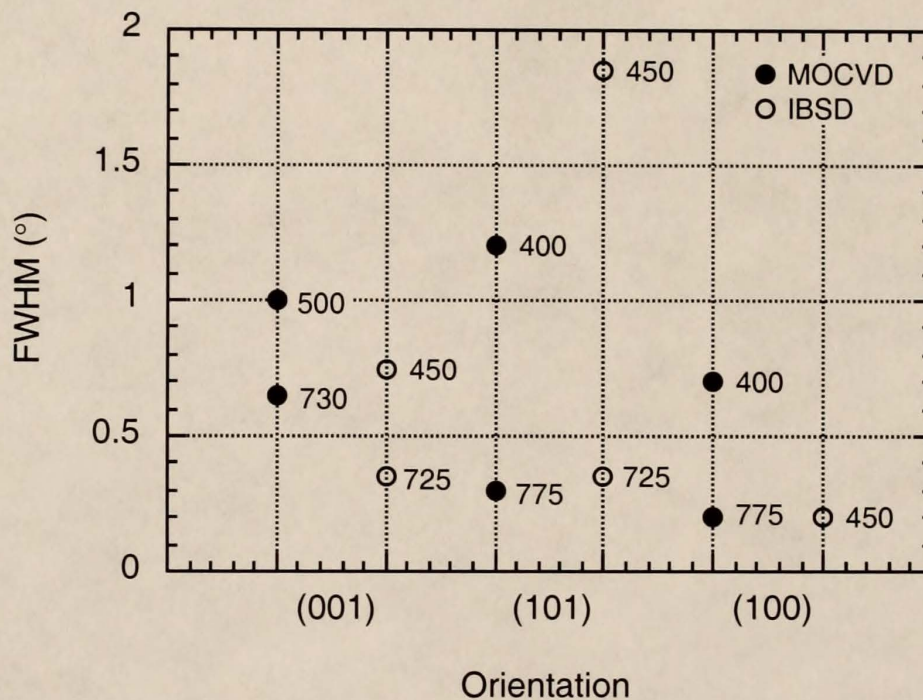


Figure 4.3 Rc fwhm of undoped rutile XRD peaks as a function of substrate temperature and deposition reactor

The data demonstrate that crystalline quality improved as a function of increasing growth temperature as expected. A fwhm value of  $0.20^\circ$  is indicated for all temperatures for (100) IBSD films. This value is known to be the resolution of the diffractometer used. The crystalline quality of these IBSD films is most likely to have improved with increasing temperature as well, but even the largest fwhm of this orientation was below the machine's resolution. The lower fwhm values for IBSD as compared to MOCVD films is directly related to growth rate differences. At the maximum deposition temperatures of the indicated ranges, the MOCVD growth rate was near  $40 \text{ \AA}/\text{min}$  whereas the IBSD growth rate was approximately an order of magnitude slower. In addition, because the Ti source in IBSD was atoms sputtered from a pure target, no reaction or combustion of a precursor molecule had to occur on or near the substrate surface prior to the Ti oxidation reaction.

The simple precursor and slow growth rate combined to provide longer time periods for the diffusion of adsorbed species on the growth surface to build structures with increased long-range order. The fwhm values shown in Figure 4.3 are comparable to those presented in the literature for (101)- and (100)-oriented growth.<sup>22,39,42,188</sup>

The  $\theta$ - $2\theta$  scans investigating film orientation normal to the plane of the film found some secondary characteristics that should be noted. First, small amounts, on the order of 1 to 5% of the (100) rutile peak, of (112) anatase were found in (100)-oriented films. No anatase was observed in (100) films grown by IBSD which suggests that its presence was a response to film stresses introduced by the much higher growth rate of MOCVD. Second, for film thicknesses above approximately 2500 Å, a small amount of (100)-oriented material was detected in (101)-oriented films. This was found to occur in films deposited by MOCVD and IBSD and was also observed in the literature.<sup>40</sup> The appearance of this second orientation in both MOCVD and IBSD films suggests that it resulted from stresses present at large film thicknesses. Cracks in IBSD films were actually observed at thicknesses greater than 4000 Å due to such stresses.

Another set of experiments investigated the effect of O<sub>2</sub> partial pressure on the rc fwhm. The corresponding growth rate data were shown in Figure 4.1. Although no significant growth rate effect was observed, Figure 4.4 demonstrates that the crystalline quality did decrease as indicated by an increasing rc fwhm. The ability to measure a rc fwhm indicates that these films continued to be crystalline and oriented. The observed changes must then have been the result of increased stress in the lattice. Depth profiles were performed on this set of films using Auger electron spectroscopy. The depth profiles revealed that less than 2 at% C (technique resolution) was present in a film grown with a large excess of O<sub>2</sub>. As the partial pressure of O<sub>2</sub> was decreased, however, the C content increased to approximately 15 at%. This finding suggests that without excess O<sub>2</sub> present to aid in carrying away the TMHD organic decomposition products, a portion was trapped in

the lattice as the film grew. These interstitial organic species expanded the lattice causing greater stress and larger number of defects as indicated by the fwhm values.

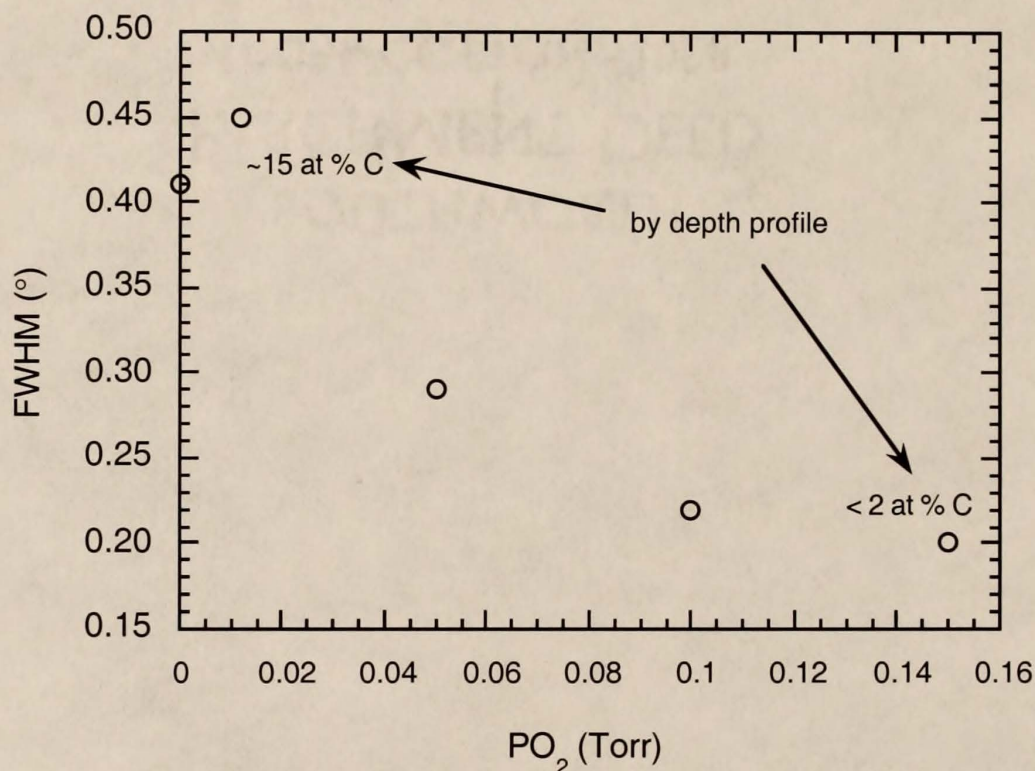


Figure 4.4 (100) rutile XRD peak rc fwhm as function of PO<sub>2</sub>

**4.1.2.2 Heteroepitaxy.** A diffractometer with three-dimensional sample movement capabilities was used to investigate heteroepitaxial deposition of the three rutile orientations on their respective sapphire substrates. (001)-oriented rutile was identified on (10 $\bar{1}0$ ) sapphire by a  $\theta$ -2 $\theta$  scan. To investigate the in-plane crystal directions of the substrate, a  $\phi$  scan was performed on the (11 $\bar{2}6$ ) plane ( $2\theta=57.5^\circ$ ,  $\chi=54.35^\circ$ ) (§3.2.1). Four peaks were observed separated by  $49^\circ$  or  $131^\circ$ . A projection of the [11 $\bar{2}6$ ] direction onto the (10 $\bar{1}0$ ) plane shows that [11 $\bar{2}6$ ] is separated from [0001] by  $24.5^\circ$  ( $49^\circ/2$ ) or  $65.5^\circ$  ( $131^\circ/2$ ). Next a  $\phi$  scan of the (101) TiO<sub>2</sub> plane ( $2\theta=36.08^\circ$ ,  $\chi=32.79^\circ$ ) was taken. Four peaks were observed separated by  $90^\circ$ . A projection of [101] onto (001) lies along [010]. The (101) peaks were found to have the same separation from (11 $\bar{2}6$ ) peaks as (11 $\bar{2}6$ ) peaks were calculated to have from (0001). Therefore, [010]//[0001] and along the perpendicular

direction  $[100]//[\bar{1}1\bar{2}0]$ . The heteroepitaxial growth of (001)  $\text{TiO}_2$  on  $(10\bar{1}0)$  sapphire has not been reported outside of this thesis and the corresponding IBSD research.<sup>14</sup>

The same type of procedure was carried out for a (100)  $\text{TiO}_2$  film on (0001)  $\text{Al}_2\text{O}_3$  substrate. A  $\phi$  scan of  $(11\bar{2}6)$   $\text{Al}_2\text{O}_3$  ( $2\theta=57.5^\circ$ ,  $\chi=42.3^\circ$ ) revealed six peaks separated by  $60^\circ$  corresponding to the 3-fold symmetry of this  $\text{Al}_2\text{O}_3$  orientation. A  $\phi$  scan of (110)  $\text{TiO}_2$  ( $2\theta=27.45^\circ$ ,  $\chi=45^\circ$ ) also showed six peaks at the same angles as the  $(11\bar{2}6)$   $\phi$  scan peaks. Only two peaks were expected given the symmetry of (100)  $\text{TiO}_2$ , so there must have been three equivalent in-plane orientations of  $\text{TiO}_2$  deposited in this case. The  $[11\bar{2}6]$  direction lies parallel to  $[11\bar{2}0]$  when projected into the (0001) plane, therefore one way of stating the in-plane crystal direction relationships is  $[010]//[\bar{1}1\bar{2}0]$  and  $[001]//[\bar{1}\bar{1}00]$ . This relationship has been characterized and reported by others in the field.<sup>41,42</sup>

Finally, this  $\phi$  scan procedure was performed on a (101) rutile film identified on  $(11\bar{2}0)$   $\text{Al}_2\text{O}_3$  by  $\theta$ - $2\theta$  scan. Again, the oblique plane investigated for the substrate was  $(11\bar{2}6)$  ( $\chi=47.7^\circ$ ), and the scan found two peaks separated by  $180^\circ$ . A  $\phi$  scan of the (110)  $\text{TiO}_2$  plane ( $\chi=67.5^\circ$ ) revealed four peaks separated by  $100^\circ$  or  $80^\circ$  where only two peaks were expected from symmetry. The two extra peaks result from a twin plane parallel to the surface of the film. The twin plane created two "layers" of material which were rotated  $180^\circ$  in the plane of the film with respect to each other. This plane has been observed by cross-sectional TEM.<sup>44</sup> The  $[110]$  projection onto the (101) plane is separated from  $[010]$  by  $40^\circ$ , and the (101) peaks were found to have the same relationship to the  $(11\bar{2}6)$  peaks. The in-plane crystal direction relationships are therefore  $[010]//[\bar{1}1\bar{2}0]$  and  $[\bar{1}01]//[\bar{1}\bar{1}00]$ . This relationship has also been characterized and reported by others in the field.<sup>39,44</sup>

The fwhm of the  $\phi$  scan peak is a value by which relative comparisons of the degree of in-plane alignment in heteroepitaxial films can be made. The values measured for (001)-, (101)- and (100)-oriented films were approximately  $1.1^\circ$ ,  $1.5^\circ$  and  $10^\circ$  respectively. The data suggest the (001)- and (101)-oriented films were of comparable in-plane alignment but the (100)-orientation was far worse. Recalling the data presented earlier for

(100)-oriented films having three equivalent in-plane orientations with respect an (0001) sapphire substrate, this finding came as no surprise.

### 4.1.3 Morphology

4.1.3.1 Orientational effects. The morphologies of (001)-, (101)- and (100)-oriented, undoped rutile films were characterized by atomic force microscopy (AFM). Tapping mode AFM was used. Details of this analytical technique were given in §3.2.3. Figures 4.5, 4.6 and 4.7 are normal, as opposed to phase shift, AFM images of thin, medium and thick (001)-oriented films, respectively. For the remainder of this chapter these three thickness designations refer nominally to  $70\pm 10$  Å,  $400\pm 25$  Å and  $3350\pm 75$  Å. The gray scales of Figures 4.5 to 4.7 are 100 Å, 200 Å and 800 Å, respectively. Figures 4.8, 4.9 and 4.10 are images of thin, medium and thick (101)-oriented rutile films. The respective gray scales are 100 Å, 200 Å and 600 Å. Figures 4.11, 4.12 and 4.13 are images of thin, medium and thick (100)-oriented rutile films, respectively. The corresponding gray scales are 100 Å, 200 Å and 800 Å. All nine images are of representative  $1\ \mu\text{m}$  by  $1\ \mu\text{m}$  areas of a film's surface. Figure 4.14 is a plot of the root mean square (rms) roughness taken from each of the varying thickness images and a respective substrate as a function of orientation. These values in combination with the gray scales allow meaningful comparisons of the images.

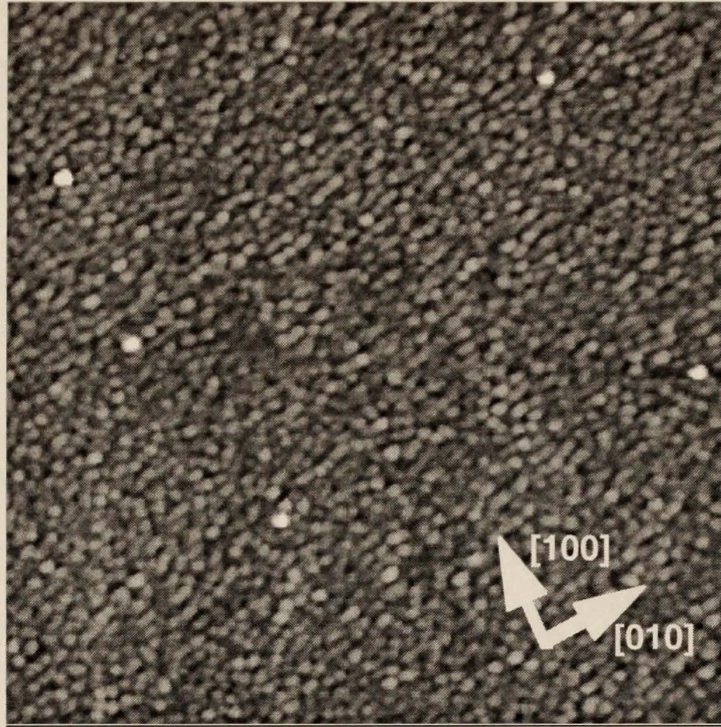


Figure 4.5 (001)-oriented 70 Å rutile film AFM image

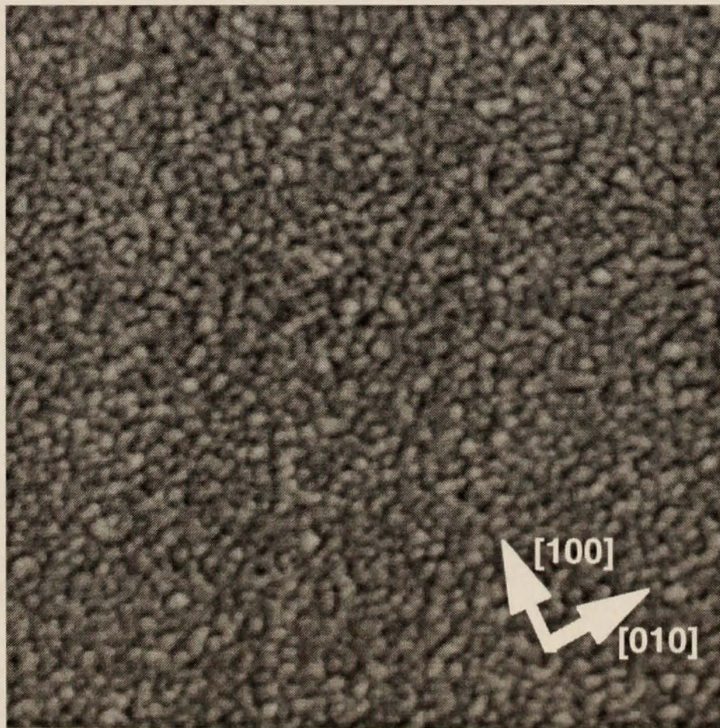


Figure 4.6 (001)-oriented 400 Å rutile film AFM image

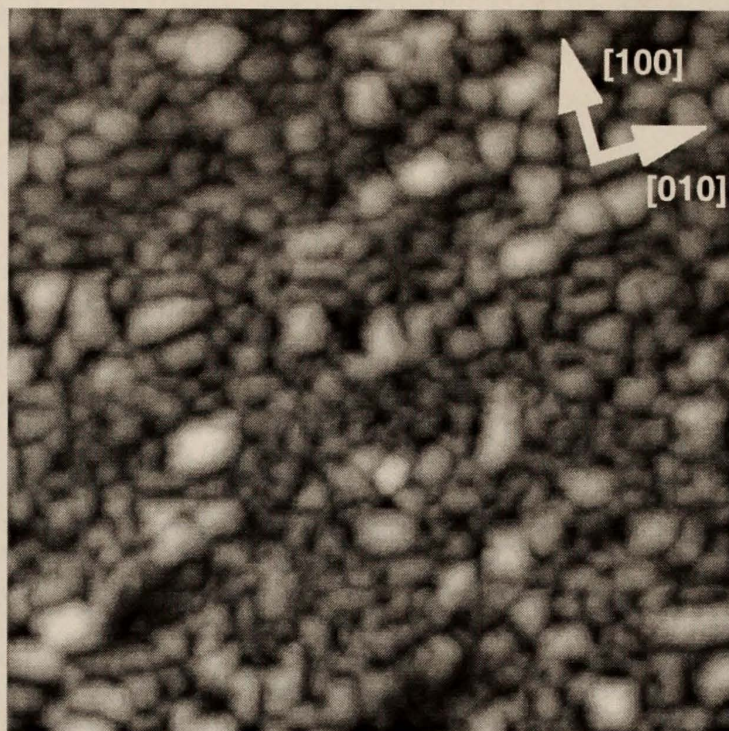


Figure 4.7 (001)-oriented 3350 Å rutile film AFM image

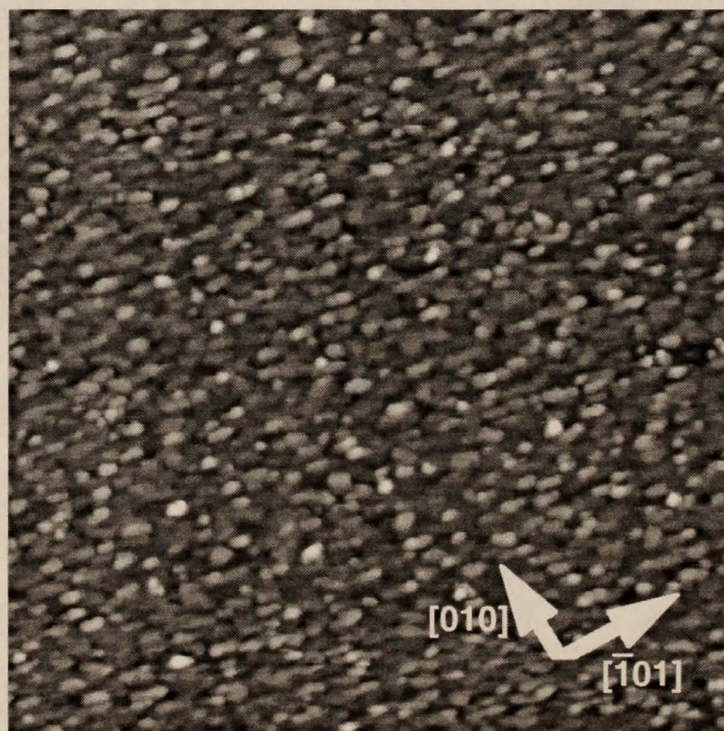


Figure 4.8 (101)-oriented 70 Å rutile film AFM image

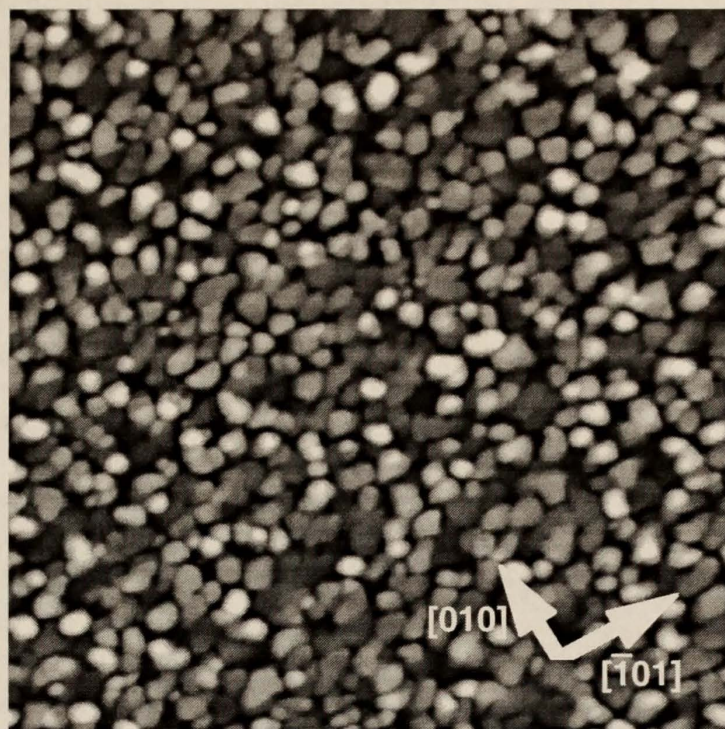


Figure 4.9 (101)-oriented 400 Å rutile film AFM image

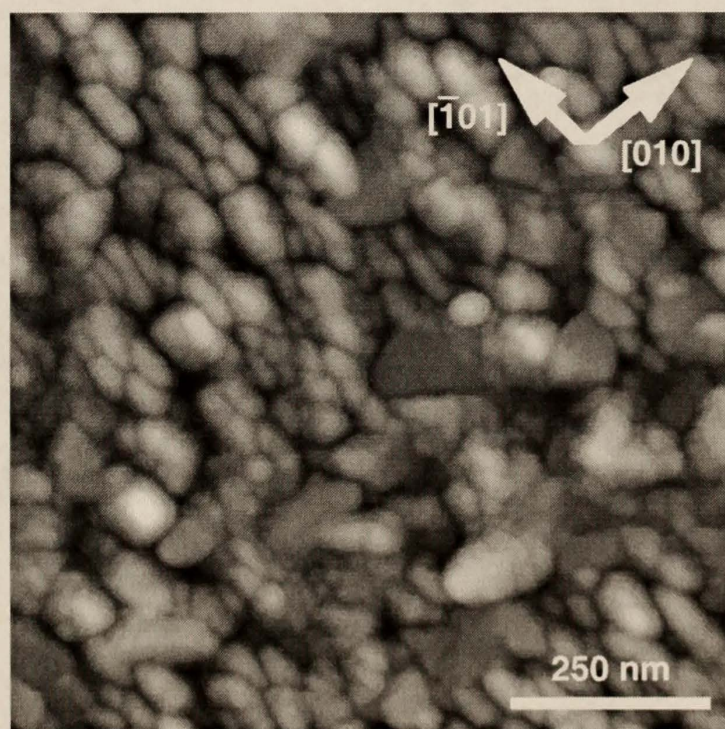


Figure 4.10 (101)-oriented 3350 Å rutile film AFM image

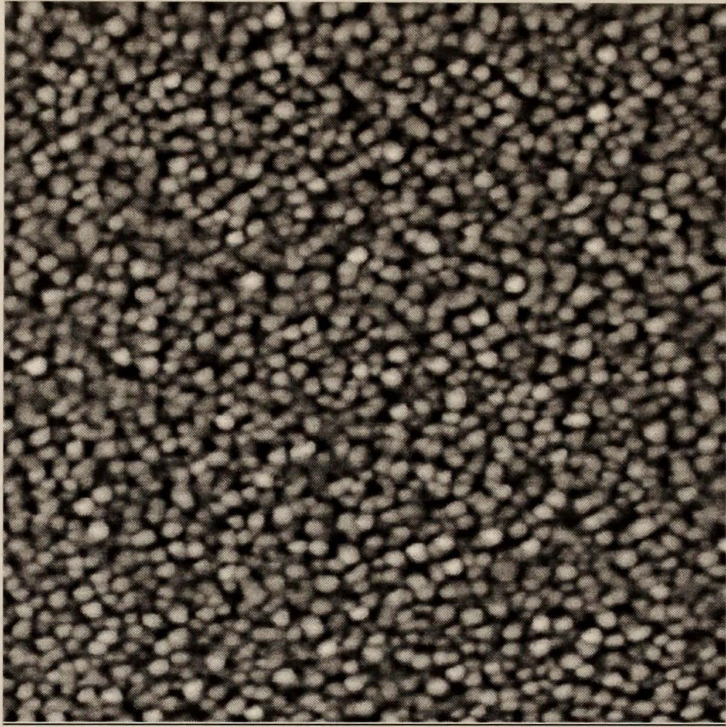


Figure 4.11 (100)-oriented 70 Å rutile film AFM image

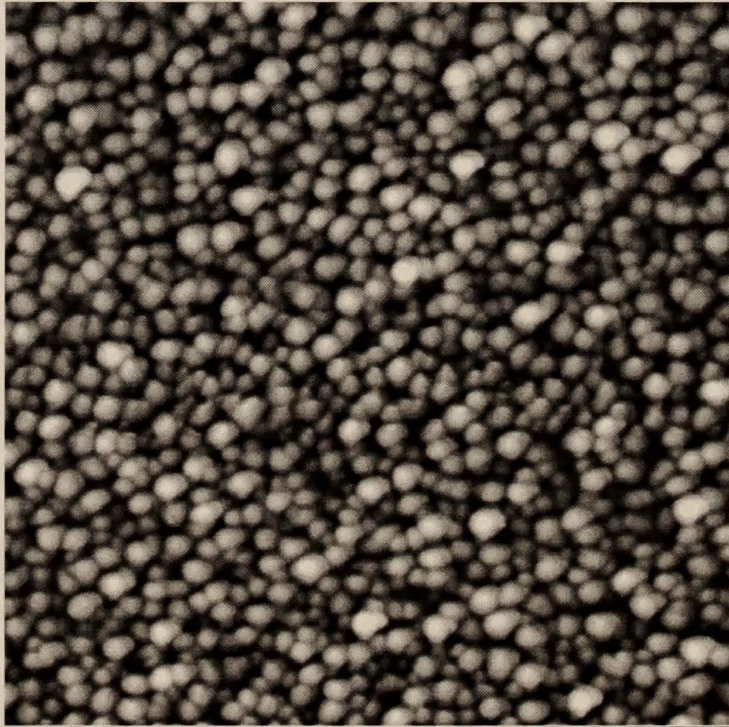


Figure 4.12 (100)-oriented 400 Å rutile film AFM image

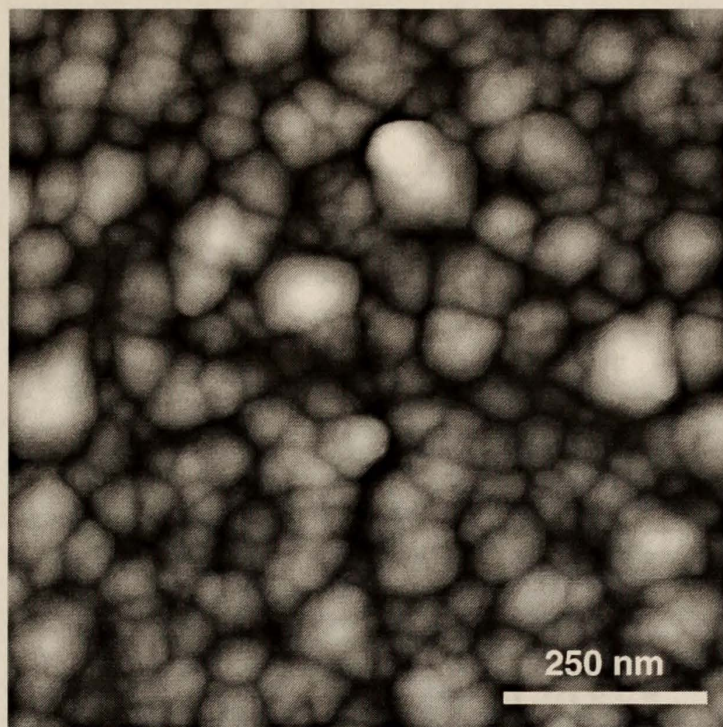


Figure 4.13 (100)-oriented 3350 Å rutile film AFM image

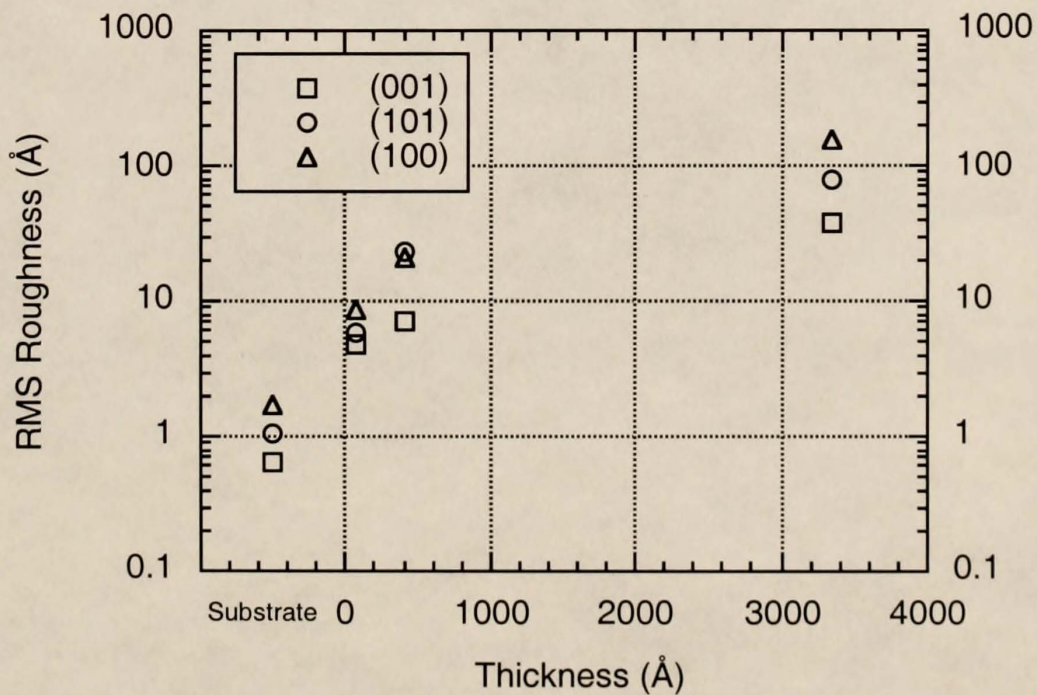


Figure 4.14 RMS roughness as a function of thickness taken from AFM images of undoped oriented rutile films and their respective sapphire substrates

Characteristic dimensions of the features shown in each oriented thickness image were measured using the analysis software which accompanied the atomic force microscope. This allowed substantially more accurate measurement of the planar dimensions as compared to using ratios with mechanical measurements. Of equal importance is that the software enabled measurement of a feature dimension normal to the plane of a film which is impossible to do otherwise.

Figure 4.15 shows the characteristic planar dimension of the features observed for each orientation plotted as a function of film thickness. The data suggest several important pieces of information about the films. First, the plot shows two sets of data points for (101)-oriented films. Obviously, the dimension represented by the open circles is approximately twice as large as the dimension represented by filled circles at all thicknesses. A non-unity ratio of these dimensions suggests elongation of the features in some direction. This elongation can be seen in the features of Figures 4.8 to 4.10. Figure 4.8 confirms this characteristic was present in the earliest stages of deposition. The heteroepitaxial investigations described previously found that the direction of elongation is parallel to  $[\bar{1}01]$ . Because heteroepitaxial growth was dependent on lattice matching between a film and its substrate, the degree of matching may have been a driving force for elongation. As was discussed in §2.1.3, matching between the oxide sublattices of rutile and sapphire is believed to be the driving force for heteroepitaxial growth of these films. Table 2.1 showed the anionic mismatch for (101)-oriented films to be 5.8% for  $[010]//[0001]$  but only 0.9% for  $[\bar{1}01]//[\bar{1}100]$ . The small mismatch along the  $[\bar{1}01]$  direction allowed growth to proceed in that direction with a smaller amount of stress on the material, and, therefore, fewer defects occurred than in other planar directions of the film.

The feature shape in the (001) and (100) orientations can also be analyzed in terms of stress due to lattice mismatch. Figures 4.5 to 4.7 of the (001)-oriented films have features which do not exhibit elongation in any direction. Table 2.1 showed the anionic mismatch in the  $[100]//[11\bar{2}0]$  and  $[010]//[0001]$  to be 3.6% and 5.7%, respectively.

Although the mismatch is larger in one direction than another, the smaller mismatch was still too large to induce observable preferential growth. Likewise, Table 2.1 showed the lattice mismatch between the three equivalent orientations of (100) rutile and (0001) sapphire to be 3.8% and 7.3%. The considerably smaller mismatch in one direction was too large to motivate elongation in that direction as demonstrated by the features shown in Figures 4.11 to 4.13.

Thin film stress is known to increase with film thickness.<sup>7,35</sup> This characteristic is illustrated in these rutile films by the non-linearity of the data in Figure 4.15. The planar dimensions of the features increased in size with increasing film thickness. A visual interpolation of the data suggest that the feature size did not, however, substantially increase for film thicknesses beyond the range of 1500 to 2000 Å. Stresses due to many layers of material being in compression or tension created defects as a relief mechanism. A limit on feature size in the film plane was the result.

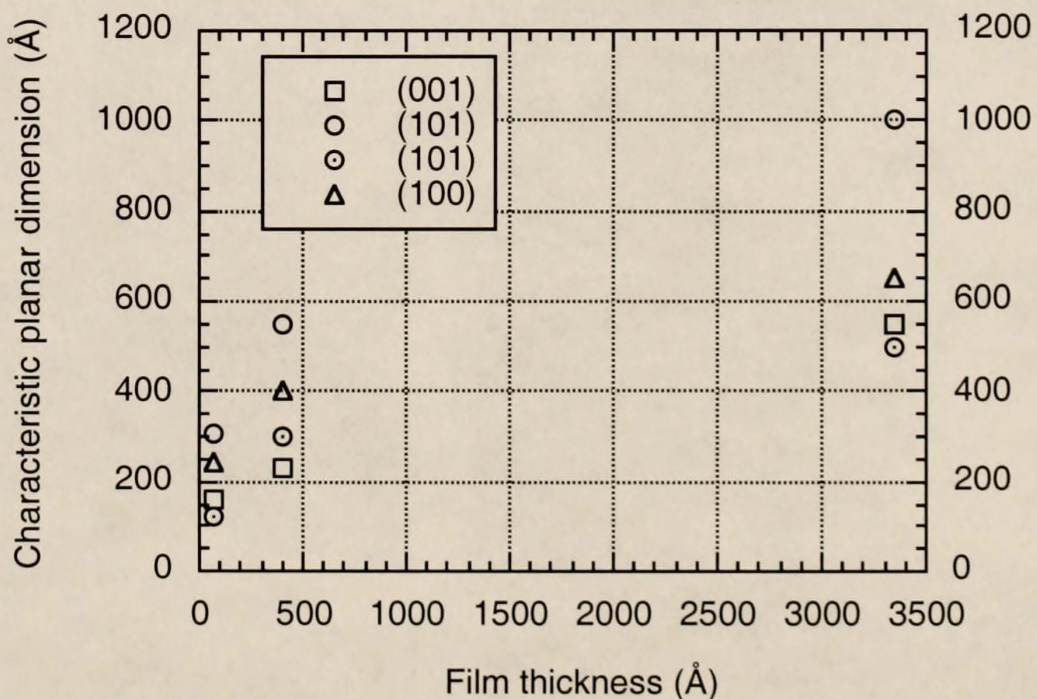


Figure 4.15 Characteristic planar dimension of surface features as a function of film thickness for undoped, oriented rutile films

Figure 4.16 is a plot of the ratio of the characteristic height to the planar dimension of the features observed for each orientation as a function of film thickness. Important insights into film growth mechanism can be gathered from this figure in conjunction with the AFM images. The thin film images of each orientation suggest an island-type growth mechanism from the earliest stages of deposition. This mechanism occurred when material was deposited at a higher rate than previously adsorbed material could transport across the growth surface to continually extend the growth surface in two dimensions. Although the thin film features for each orientation are obviously island-like, the data of Figure 4.16 suggest a degree of two-dimensional growth mechanism as well. The height to planar dimension ratio of these features varies from 5% to 13% for the three orientations. Correspondingly, the islands were growing at a faster rate in the film plane than normal to it.

The data of Figure 4.16 further suggest that this mixture of two- and three-dimensional growth mechanisms was not substantially altered for films that were approximately 400 Å thick. The features in the thin and medium thickness images for each orientation have similar appearances other than their size difference. The data for a (100)-oriented thick film indicated that the height approached the planar dimension of the features. The rms roughness value which is considerably larger than the other two orientations corresponds with this ratio. A comparison of the data for the two dimensions of a (101)-oriented film give evidence that the elongated dimension and height feature continued to increase at similar rates. The smaller dimension increased at a much slower rate. Finally, the ratio remained low for a (001)-oriented film at all thicknesses. This data corresponds with this orientation being the smoothest as indicated by its rms roughness value at each thickness in comparison to the other two orientations.

The cross-sectional views of the AFM images which were used to obtain the feature height dimension also allow an analysis of the feature shapes. The shapes and the angles measured from them indicate that (001)- and (101)-oriented film surfaces are faceted, but

the (100) surface was more difficult to resolve. An in-depth analysis of the facet planes and their relevance to the observed behavior of these films as gas sensors is taken up in the next chapter.

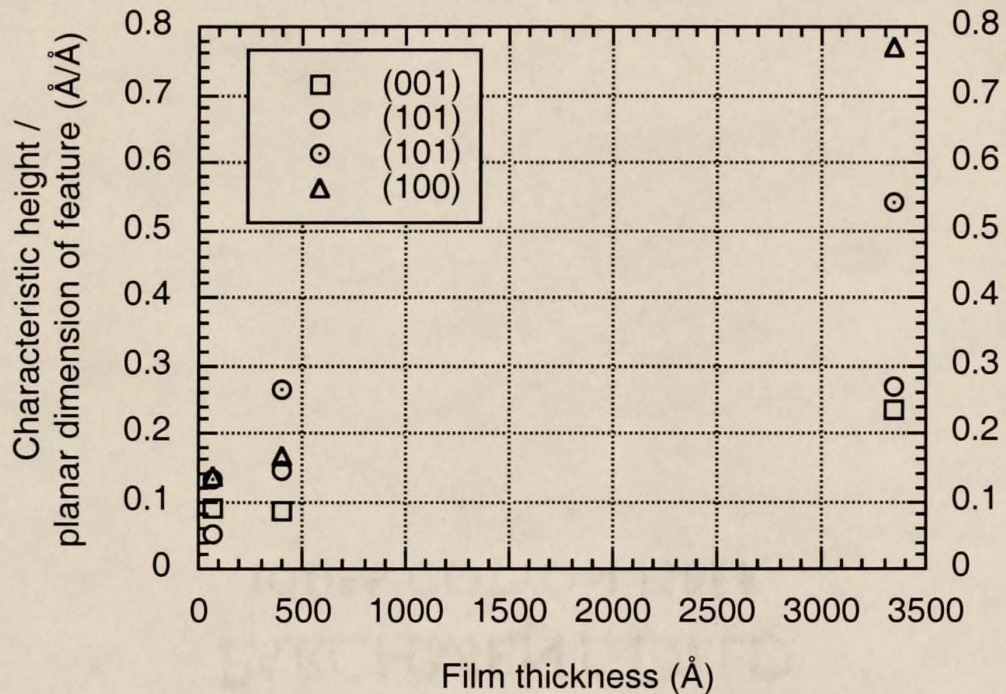


Figure 4.16 Ratio of characteristic height to planar dimension of surface features as a function of film thickness for undoped, oriented rutile films

**4.1.3.2 Substrate effects.** In the process of carrying out these morphology investigations, some interesting information was discovered concerning the surface characteristics of various substrates. An AFM image of a virtually smooth  $(10\bar{1}0)$ -oriented sapphire substrate representative of those used in the morphology investigations is shown in Figure 4.17. Similar images were obtained for  $(11\bar{2}0)$ - and  $(0001)$ -oriented sapphire substrates. The rms roughness data shown for the substrates in Figure 4.14 suggests that the surfaces were of like smoothness. Such clean surfaces were obtained using the methanol, deionized water, filtered air procedure described in §3.1.3. In spite of this procedure, AFM revealed that random substrates had an appreciable density of larger features. The composition of these features is unknown. They were, however, hard with

respect to the ability of phase contrast AFM imaging to differentiate between hard and soft materials.<sup>178</sup> In addition, they were found to be unremovable by any amount of surface cleaning. These characteristics suggest that the features were material which was inadequately removed after the polishing step in manufacturing the substrates. Figure 4.18 is a normal AFM  $0.5\ \mu\text{m}$  by  $0.5\ \mu\text{m}$  image of a  $(11\bar{2}0)$  sapphire substrate showing features typical of what was observed on each sapphire orientation.

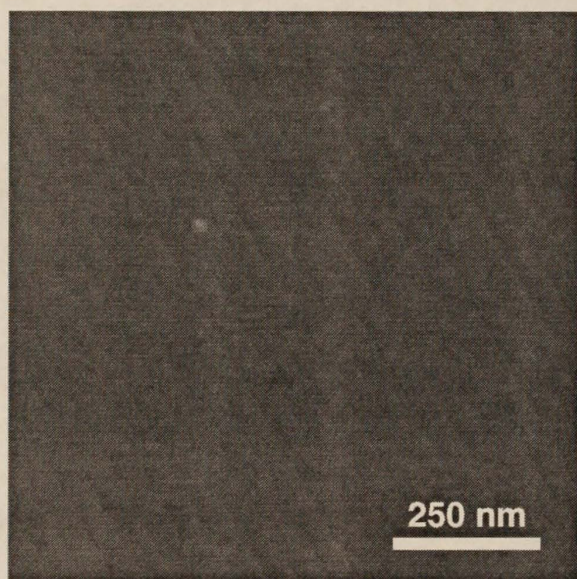


Figure 4.17 (0001)-oriented sapphire

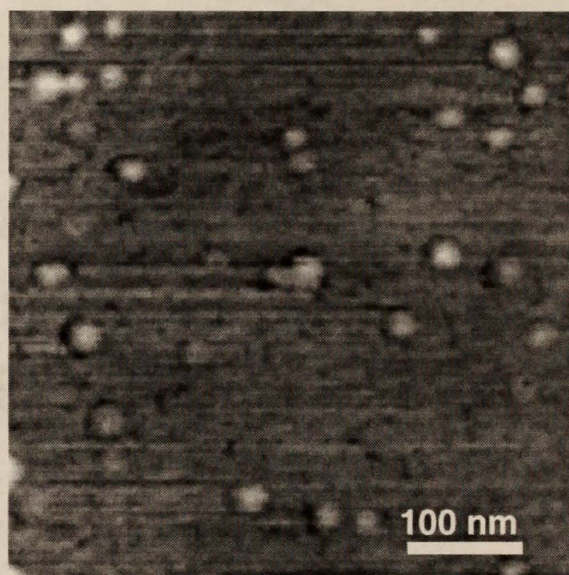


Figure 4.18  $(11\bar{2}0)$ -oriented sapphire with unremovable surface features

Figures 4.19 and 4.20 are AFM images of thin and thick  $(101)$ -oriented films grown on  $(11\bar{2}0)$  "featured" substrates. Figure 4.19 demonstrates that the features were areas of some degree of preferential growth. The characteristic dimension of the  $(11\bar{2}0)$  substrate feature is  $140\ \text{\AA}$  with a  $15\ \text{\AA}$  height. The thin film imaged in Figure 4.19 has large features which are approximately  $380\ \text{\AA}$  by  $200\ \text{\AA}$  and  $65\ \text{\AA}$  high, whereas the remaining material has a  $100\ \text{\AA}$  dimension with a  $10\ \text{\AA}$  height. This preferential growth creating larger islands of rutile material in the initial stages of deposition is believed to be responsible for the larger dimensions of many of the features observed in Figure 4.20 as compared to those seen in Figure 4.10. Cross-sectional views of each thick film image

showed that the features in both images can be modeled as trapezoidal prisms, but the relative dimensions on average are larger in Figure 4.20.

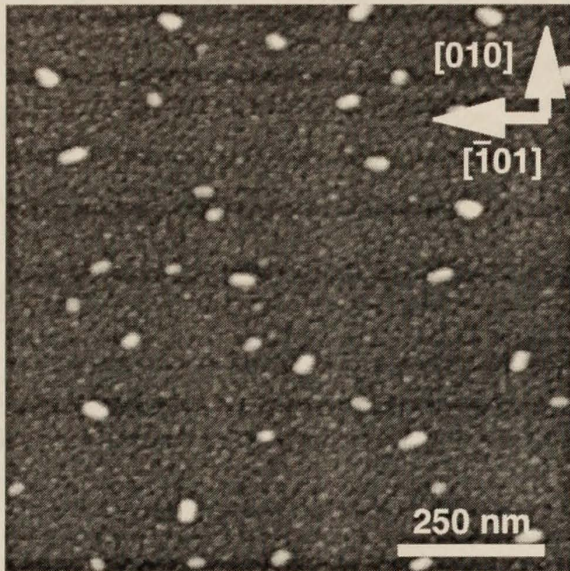


Figure 4.19 (101)-oriented 70 Å rutile film on "feathered" (1120) sapphire substrate

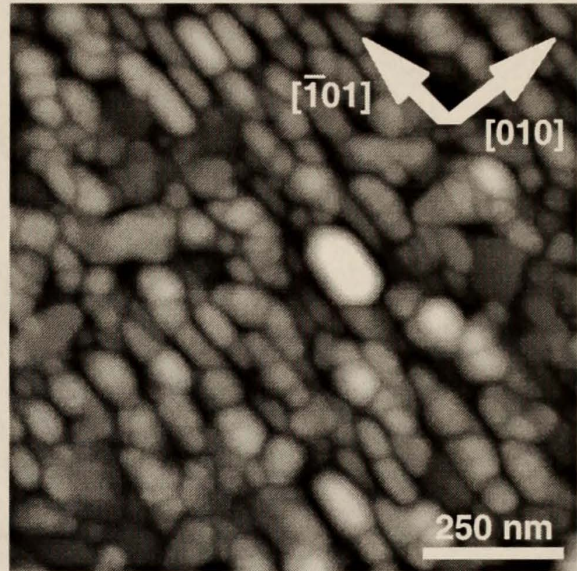


Figure 4.20 (101)-oriented 3350 Å rutile film on "feathered" (1120) sapphire substrate

#### 4.2 Doped Rutile Films

Doped rutile films with (001), (101) or (100) orientation were deposited by MOCVD using solid precursors by the same procedure as the undoped films described in the previous section. Films were doped with either Ga or Nb. These two dopants were chosen for a couple of reasons. One, with respect to Ti which has a 4+ oxidation state, Ga is an acceptor-type dopant as a result of its 3+ oxidation state. Similarly, Nb is a donor-type dopant because of its 5+ oxidation state. Two, the defect chemistry which results from acceptor or donor dopants was only of interest for the purposes of this thesis if the dopant atoms incorporated substitutionally at a Ti lattice site.  $\text{Ga}^{3+}$  and  $\text{Nb}^{5+}$  have atomic radii of 0.62 Å and 0.70 Å, respectively.<sup>189</sup> They are similar in size to  $\text{Ti}^{4+}$  which has an atomic radius of 0.68 Å. The dopant atoms therefore had little motivation to segregate and

form secondary phases in a film due to misfit strain. The growth of doped rutile films served two purposes. First, to advance the understanding of metal oxide thin film deposition with the incorporation of more than one metal. The findings are important to the deposition of materials such as ferroelectrics where compounds like lead zirconate titanate are being studied. Second, the known changes in the bulk and at the surface due to the defect reactions reviewed in §2.3.3.1 were studied for their effects on gas sensitivity.

#### 4.2.1 Deposition

4.2.1.1 Bulk dopant concentration. Rutherford backscattering spectrometry (RBS) was used to characterize the average dopant concentration in the films. A representative RBS spectra was shown in Figure 3.5 with an explanation of the analytical technique (§3.2.2). The 4  $\mu\text{C}$  of total charge used to characterize the thin films was not sensitive to any segregation of dopants to the surface or film-substrate boundary. Due to noise in the spectra, the technique was accurate to  $\pm 0.1$  at%.

RBS analysis of the doped films confirmed a nominal one-to-one ratio between dopant concentration in the dopant/Ti solid precursor mixture and the dopant concentration measured in a thin film. The relationship was observed for both Ga and Nb concentrations from 0.5 at% to 6.5 at% on a per Ti basis. This characteristic goes against what has typically been observed for multiple-metal oxide films grown by the MOCVD technique.<sup>190,191</sup> Several factors in combination are suggested as the cause of this behavior. Primary, is the unique procedure of mixing the powder precursor materials for a simultaneous sublimation of each species at the desired ratio. This was accomplished by setting the UV lamp to provide the heat necessary to sublime the precursor with a higher sublimation temperature (§3.1.2). Using separate rods for each precursor and a ratio of the sublimation rates was unable to accomplish this same feat at these doping levels. Second, is the deposition rate. Rutile films were deposited by MOCVD at around 37  $\text{\AA}/\text{min}$  as

opposed to IBSD at 4 Å/min. Growth of multi-metal oxide ferroelectric materials often takes place at rates on the order of 60 Å/min for research and much faster is desirable for production.<sup>192</sup> At significantly higher deposition rates, dopant incorporation efficiency in rutile films may have also fallen below one. Finally, there are the dopant-Ti ionic radii similarities cited earlier. Minimization of strain misfit energy is suggested as a key variable in attaining a high incorporation efficiency.

4.2.1.2 Surface dopant concentration. A small amount of dopant segregation to a film's surface did take place during deposition. X-ray photoelectron spectroscopy (XPS) was performed on samples doped with Nb or Ga at 1 at% according to RBS. The analyses identified approximately 6.5 at% Nb and 4.5 at% Ga in the respective samples. No Al from the substrate or other significant impurities were identified by XPS. The technique has a sample depth of approximately 100 Å with sensitivity decreasing as a function of depth. Since RBS profiles did not exhibit a dramatic change in dopant concentration near the surface or a decrease in the expected bulk value, the segregation depth must be on the order of 100 to 200 Å. This small degree of dopant segregation was most likely driven by a material's desire to be in as low an energy configuration as possible. The dopant atoms fit well at Ti sites, but their presence is imperfect in comparison to Ti. Moreover, whether Ga is compensated by O vacancies or Ti interstitials, both defects would serve to increase the strain energy of the crystal and are undesirable from an energy minimization standpoint. Segregation of dopant atoms established a space charge region which may play an important role in the analysis of gas sensor data.

XPS was also valuable for its ability to identify the oxidation state of dopant atoms in the films. Ga-doping of rutile is relatively unknown in the growth or gas sensor literature. The stable oxidation state of Ga is 3+, and no circumstances can be imagined under which it could be driven to exist as 2+ or 4+ in the rutile lattice. XPS confirmed that Ga atoms in the rutile films had a 3+ oxidation state. Figure 4.21 shows the binding

energy range of an XPS spectra for the Ga  $2p_{3/2}$  core electron of an (001)-oriented 1 at% Ga-doped film. Figure 4.22 is a plot of the  $2p_{3/2}$  core electron binding energy as a function of Ga oxidation state using the available citations.<sup>193,194</sup> The binding energy of the spectra peak correlates well with the binding energy cited for Ga in a 3+ oxidation state.

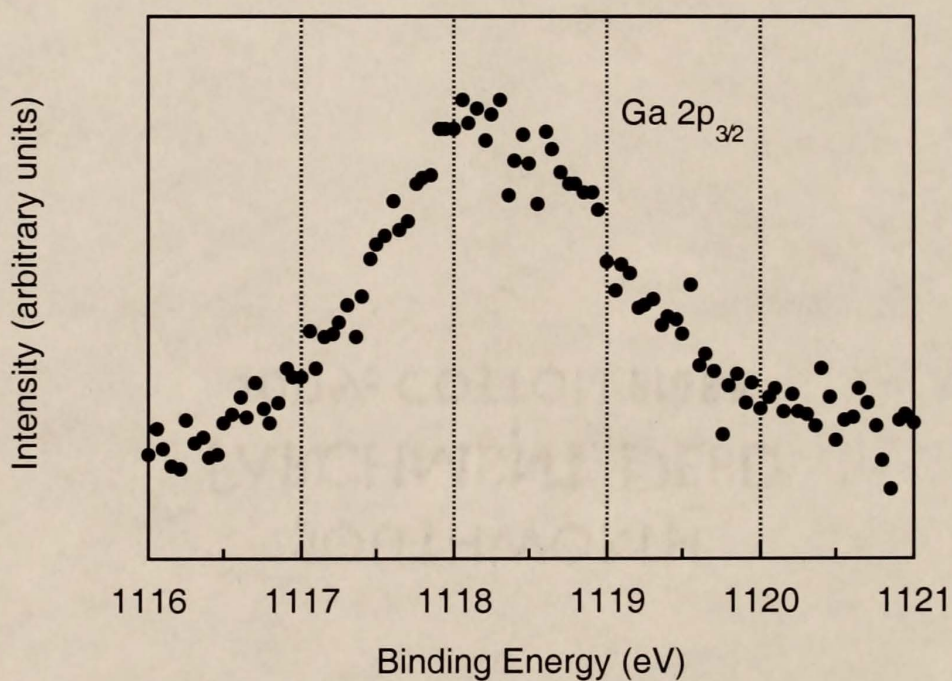


Figure 4.21 XPS spectra of Ga  $2p_{3/2}$  core electron binding energy for Ga atom in (001)-oriented rutile thin film

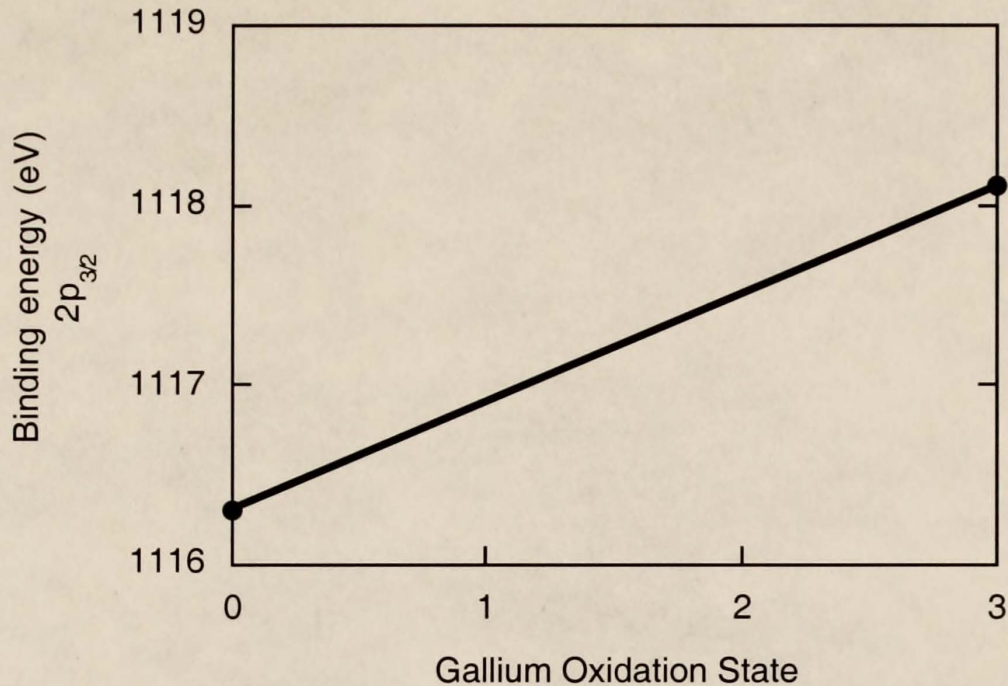


Figure 4.22 Ga  $2p_{3/2}$  core electron binding energy as a function of Ga oxidation state

Greater controversy exists as to the oxidation state of Nb in a rutile film. The same body of data for Nb-doped rutile films deposited homoepitaxially on (100)- and (110)-oriented substrates by molecular beam epitaxy has been published several times by Gao et al.<sup>195-198</sup> This group claims to have maintained the rutile structure to a Nb level of 20 at%. Their argument is that Nb was present in the metastable, reduced 4+ state because  $\text{NbO}_2$  has a rutile structure. The claim that obtaining a lower energy crystal structure was a strong enough force to overcome the thermodynamic drive toward complete oxidation in the presence of an oxygen plasma is a dubious one. A close examination of the corresponding XPS data used as further evidence for the presence of  $\text{Nb}^{4+}$  revealed an erroneous interpretation.<sup>197</sup> Figure 4.23 is a plot of the Nb  $3d_{5/2}$  core electron binding energy as a function of the Nb oxidation state. More than one source was obtained for each oxidation state.<sup>193,199-201</sup> First, Gao's data should be shifted by +0.1 eV to agree with the widely accepted value of 458.8 eV for Ti  $2p_{3/2}$  binding energy.<sup>193</sup> This shift would put their Nb  $3d_{5/2}$  values in complete agreement with the lower value for  $\text{Nb}^{5+}$ , 207.2 eV. Even

without a shift, their data ranges from 0.94 to 1.05 eV greater than the  $\text{Nb}^{4+}$  value of 205.9 eV shown in Figure 4.23. Their values are only 0.55 to 0.76 eV less than the largest value for a 5+ oxidation state, 207.6 eV. The reanalysis suggests that  $\text{Nb}^{5+}$  was present, and a novel material was not actually obtained.

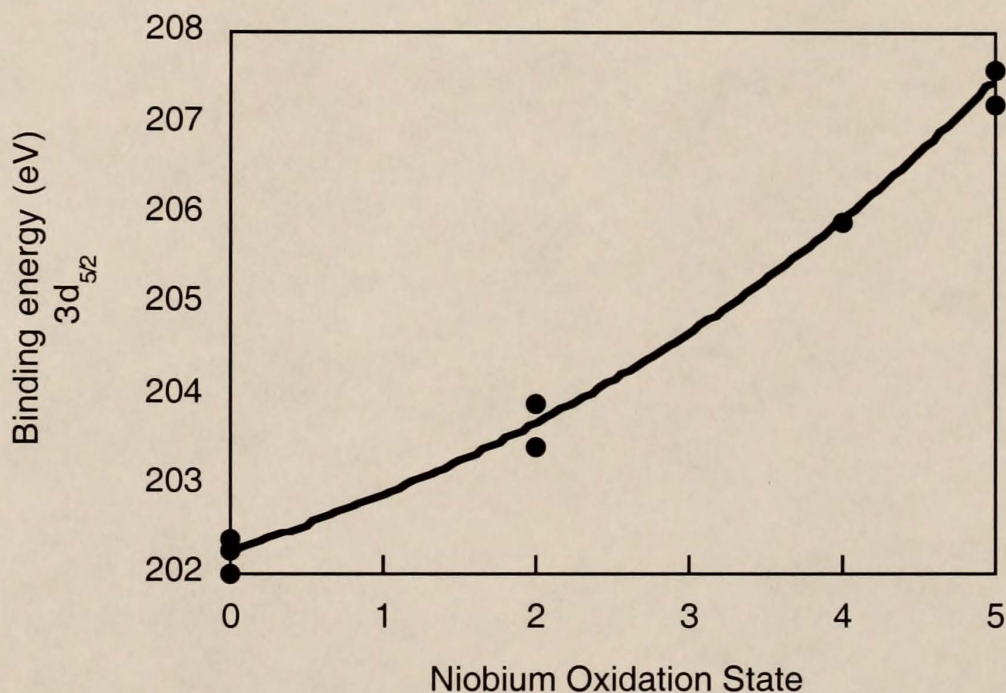


Figure 4.23 Nb  $3d_{5/2}$  core electron binding energy as a function of Nb oxidation state

Figure 4.24 shows the peaks corresponding to the Nb  $3d_{5/2}$  and  $3d_{3/2}$  core electrons from the XPS spectra of a (001)-oriented 1 at% Nb-doped rutile film. The binding energy of the  $3d_{5/2}$  core electron is around 207.5 eV. This value indicates that the Nb dopant atoms were in a 5+ oxidation state as judged by the literature data presented in Figure 4.23. In addition, substitutional incorporation of  $\text{Nb}^{5+}$  on a Ti cation site in a rutile lattice was shown in §2.3.3.1 to be compensated by an electron or a Ti vacancy. Evidence that Nb was electronically compensated in these films will be presented in conjunction with the gas sensor properties.

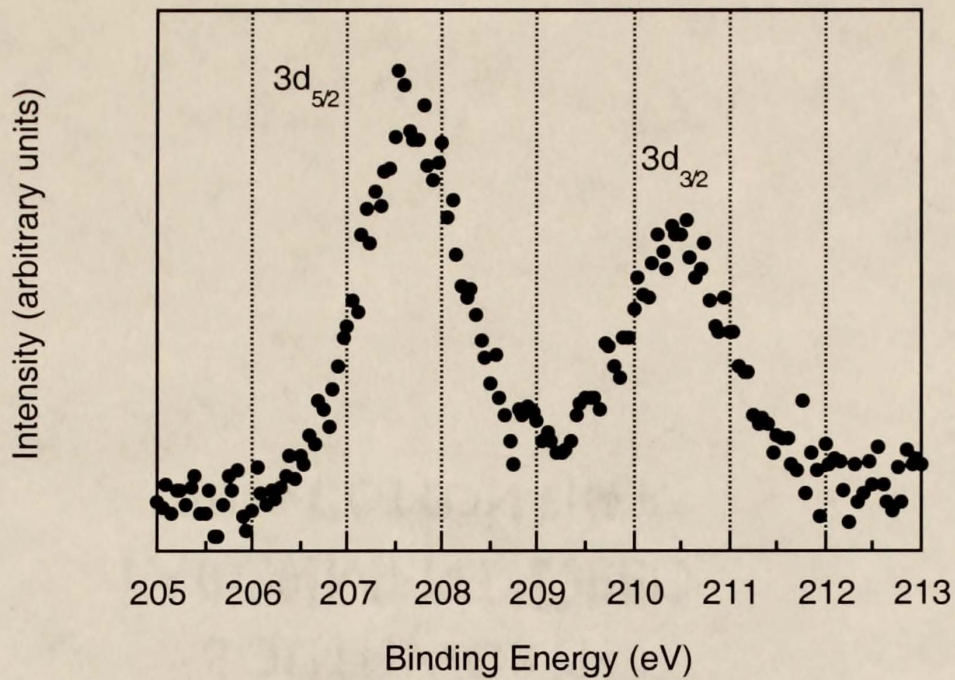


Figure 4.24 XPS spectra of Nb  $3d_{5/2}$  and  $3d_{3/2}$  core electron binding energies for Nb atom in (001)-oriented rutile thin film

#### 4.2.2 Nb-doping structural effects

4.2.2.1 Bulk crystal structure. Several aspects of the bulk crystal structure changes as a result of Nb doping were investigated by XRD. First, the lattice expansion normal to the plane of the film was investigated for 2 at% and 6.5 at% Nb doping. The surface normal is the only lattice parameter of a thin film which can be accurately measured because the impossible task of placing a film in a diffractometer perfectly flat with respect to the remaining geometry is correctable for a  $\theta$ - $2\theta$  scan. The correction was made by assuming that the single crystal substrate peak varied from its ideal angle value due to misalignment and shifting all  $2\theta$  values by the corresponding difference. A lattice parameter was then calculated using a corrected angle value for the respective rutile diffraction peak. At higher  $2\theta$  values and for higher intensity rutile and sapphire peaks, the secondary peak due to the  $\text{Cu } K\alpha_2$  radiation was present. The effect of this secondary peak on a peak resulting from  $K\alpha_1$  radiation is to shift the  $K\alpha_1$  peak slightly in the positive  $2\theta$ . A program designed to

subtract the  $K\alpha_2$  peak contained in the spectra analysis software was applied prior to using a second program to determine the area centroid of a peak. This area centroid was the  $2\theta$  value used to calculate a lattice parameter.

Figure 4.25 shows the measured change in (002) rutile plane d-spacing in (001)-oriented films as a function of Nb doping level. There is no (001) reflection for rutile. Figure 4.26 displays the same information for the (101) plane of rutile in (101)-oriented films. The error bars shown on the 2 at% Nb data points were calculated using data from several undoped films and are assumed to be representative of the doped data for which only single samples were available. The error is shown on the 2 at% Nb data point for presentation clarity.

The data of these two figures indicate several important film characteristics. First,  $d(002) = 1.4781 \text{ \AA}$  which is smaller than the literature value of  $1.4797 \text{ \AA}$ . This decrease indicates the lattice was in compression normal to the plane of the film. The film-substrate lattice matching which drives the heteroepitaxial growth shows that an (001)-oriented film is also in compression in the plane of the film. Second,  $d(101) = 2.4280 \text{ \AA}$  as compared to a literature value of  $2.4870 \text{ \AA}$ . This measurement is also like the compression known to be in the plane of a (101)-oriented film from film-substrate lattice mismatch calculations. The increase in d-spacing for each film indicates that the addition of Nb increased the lattice size. The lattice size was expected to increase due to the substitution of the larger Nb atoms on the Ti sites. Finally, the linearity of the plots suggest that Nb continued to be incorporated in a rutile lattice by the same mechanism over the 6.5 at% doping range. If the Nb were incorporated interstitially, the lattice would still be expected to expand. The expansion, however, would not likely be linear with the same slope as the substitution mechanism. If crystalline secondary phases were formed with increasing doping level, corresponding XRD peaks would be observed, and none were. Any amorphous or crystalline secondary phase would have a low probability of exhibiting the observed linear

expansion. An increase in lattice size as a result of the Nb doping of rutile is in agreement with the literature.<sup>110,111,202</sup>

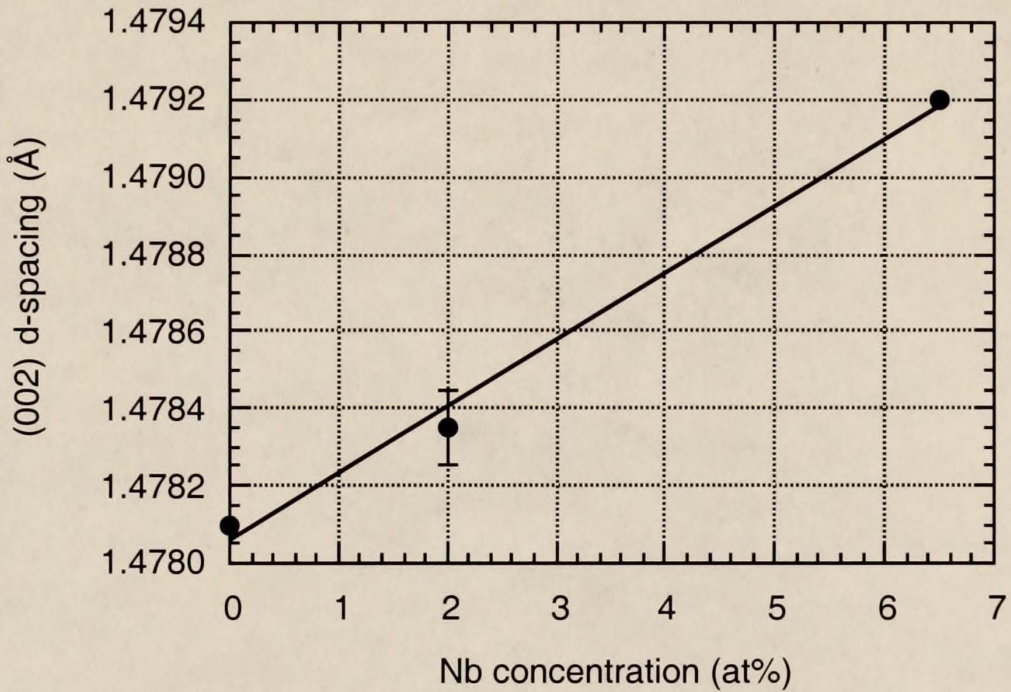


Figure 4.25 (002) rutile plane d-spacing as a function of Nb doping

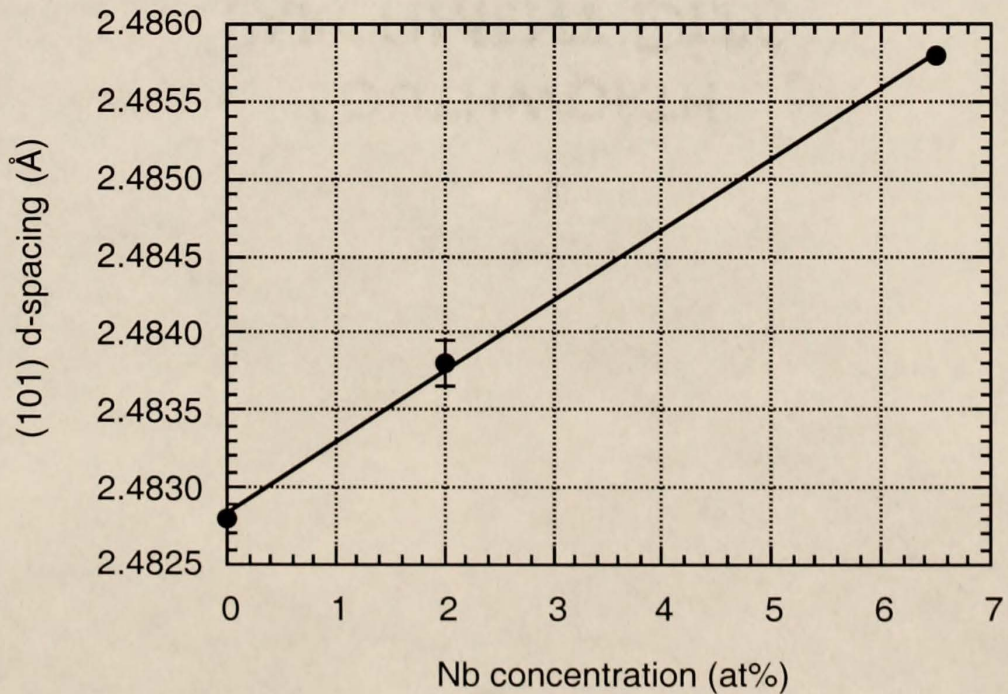


Figure 4.26 (101) rutile plane d-spacing as a function of Nb doping

The effects of Nb increasing the size of a lattice under compression are apparent in other XRD measurements which were used to investigate the structure of these films. The fwhm's of the  $\theta$  rc's of the (002) and (101) diffraction peaks as a function of Nb doping level are shown in Figure 4.27. The increasing fwhm values verify that a larger number of structural defects resulted from the Nb addition. The consistency of the plane-to-plane spacing in both orientations was diminished. The data also indicate that (001) films continued to exhibit a more well-ordered crystal structure than (101) films.  $\phi$  scans performed on Nb-doped films confirmed that heteroepitaxial growth was achieved. Figure 4.28 shows the fwhm measured from the peaks of a  $\phi$  scan of the (101) plane and the (110) plane of the (001)- and (101)-oriented films, respectively. The data indicate that in-plane orientational consistency was also decreased by Nb doping of both orientations. The  $\phi$  peak fwhm values cannot be compared between two film orientations. The heteroepitaxial growth of a Nb-doped (001)-oriented film is unknown in the literature.

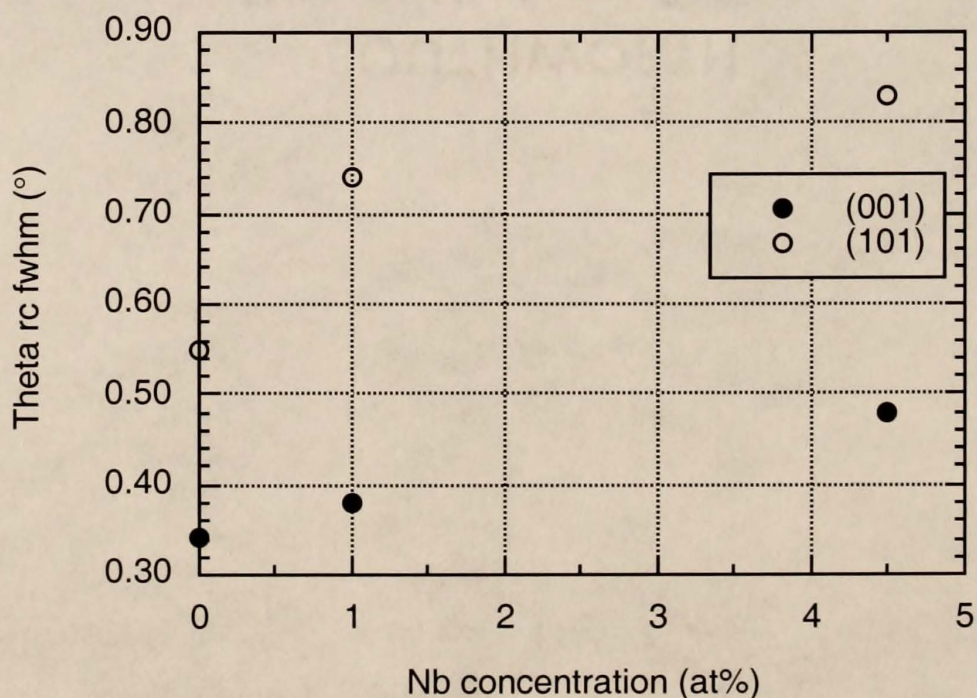


Figure 4.27 (001) and (101) rutile peak  $\theta$  rc fwhm as a function of Nb doping

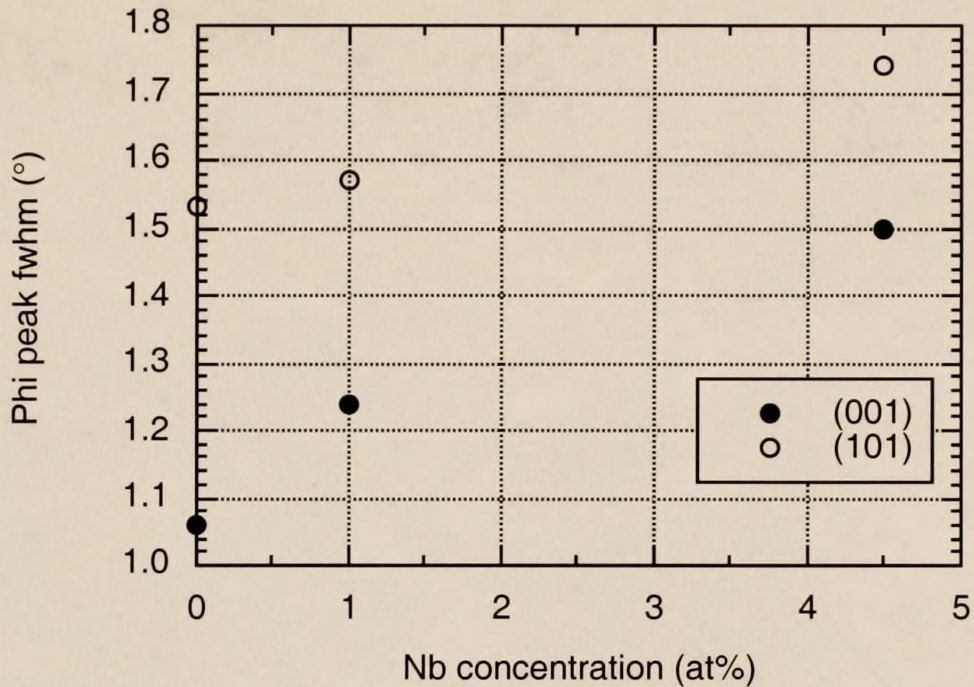


Figure 4.28 (001) and (101) rutile  $\phi$  scan peak fwhm as a function of Nb doping

4.2.2.2 Surface morphology. The surface morphology effects of Nb-doping were investigated by AFM. Figures 4.29 (a) and (b) are normal AFM images of thin and thick 1 at% Nb-doped (001)-oriented rutile thin films, respectively. "Thin" and "thick" are representative of the same nominal film thicknesses as in the previous discussion of undoped images,  $70 \pm 10 \text{ \AA}$  and  $3350 \pm 75 \text{ \AA}$ . Figures 4.30 (a) and (b) are the corresponding images of (101)-oriented films. Figures 4.31 (a) and (b) are images of thin and thick (100)-oriented 1 at% Nb-doped films. Meaningful comparisons can be made with the respective undoped images of each orientation among Figures 4.5 to 4.13 shown earlier. The gray scales for each thin and thick Nb-doped film image are  $100 \text{ \AA}$  and  $1000 \text{ \AA}$ , respectively, with the exception of the thick (001) orientation image which is only  $200 \text{ \AA}$ .

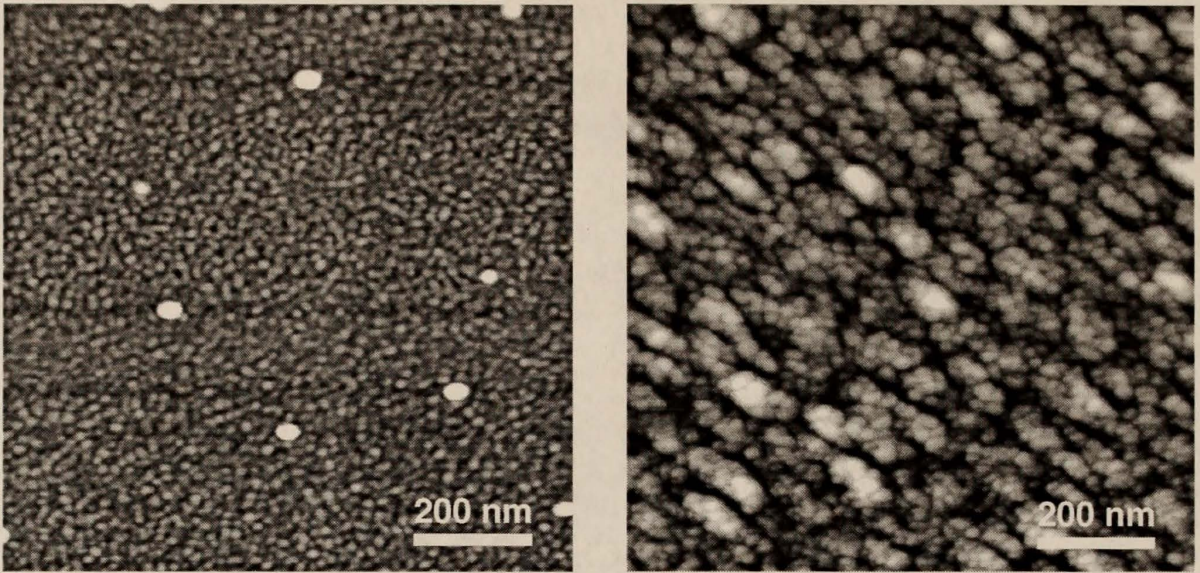


Figure 4.29 Nb-doped (001)-oriented thin film AFM images  
(a) 70 Å (b) 3350 Å

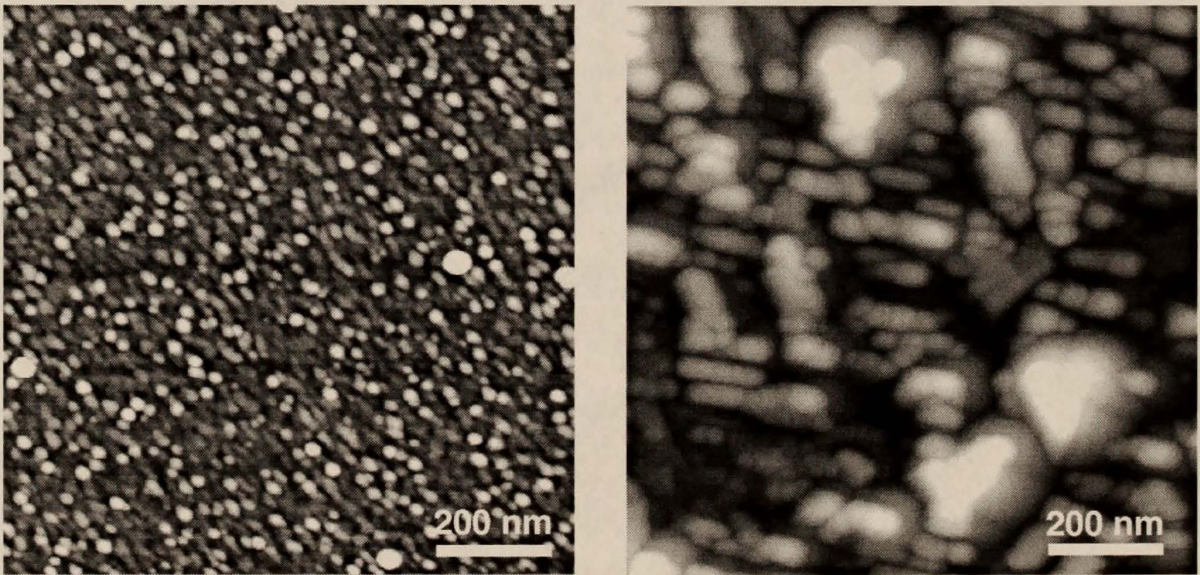


Figure 4.30 Nb-doped (101)-oriented thin film AFM images  
(a) 70 Å (b) 3350 Å

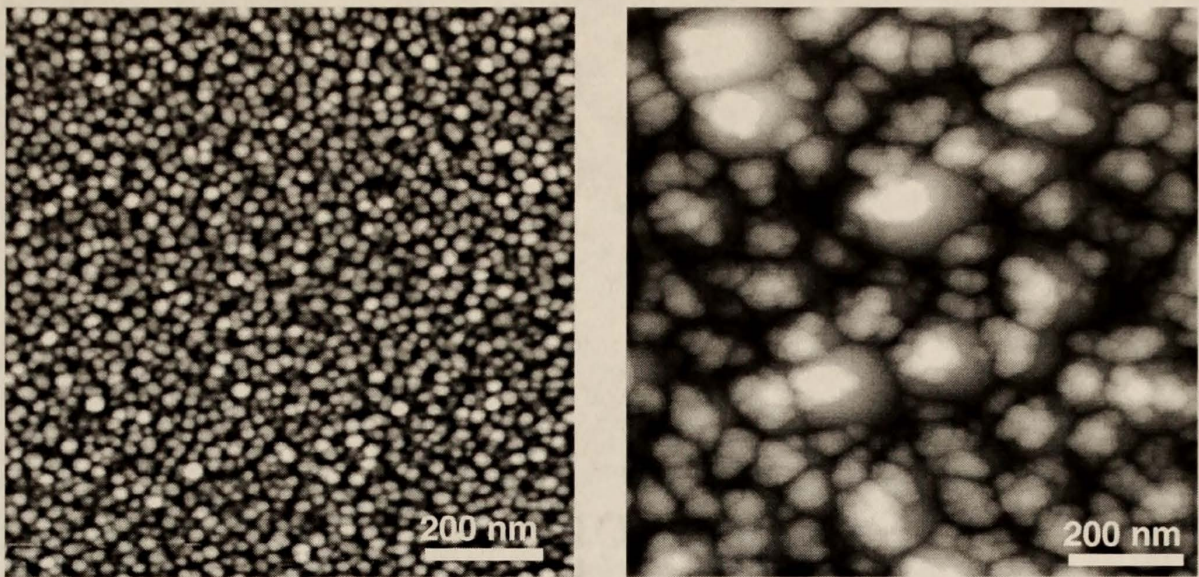


Figure 4.31 Nb-doped (100)-oriented thin film AFM images  
(a) 70 Å (b) 3350 Å

The feature sizes and rms roughness of the doped film images revealed a few important morphological comparisons to the undoped film images. First, no distinct changes were observed in the initial stages of growth due to doping. The height and planar dimensions of the features for each orientation were within 10% of the corresponding undoped feature sizes. Elongation was maintained in the  $[\bar{1}01]$  direction of a (101)-oriented film. The feature similarities suggest that the extra film stress due to the larger Nb atoms in the lattice did not cause a significant number of defects until a critical thickness greater than 70 Å. Second, the roughness as quantified by feature dimensions and rms values of a (100)-oriented film was not significantly increased by Nb doping. This finding indicates that the planar structure of this orientation is primarily determined by the poor film-substrate lattice matching discussed previously. Last, an (001)-oriented Nb-doped film is characterized by a lack of larger features observed in the image of an undoped film (Figure 4.7). The higher defect concentration due to the Nb appears to have deterred coalescence of the smaller, island-like features into larger ones.

### 4.2.3 Ga-doping structural effects

**4.2.3.1 Bulk crystal structure.** An XRD study of the bulk crystal structure changes resulting from Ga doping of rutile films was performed in a like manner to the investigation of Nb-doped films. In the case of Ga doping, the lattice expansion normal to the plane of (001)- and (101)- oriented films was investigated for doping at 5.0 at% and 6.5 at%. The film misalignment correction and  $K\alpha_2$  peak subtraction procedures were carried out to determine the rutile peak angle value. This value was used to calculate the d-spacing as before.

Figure 4.32 is a plot of the (002) d-spacing as a function of Ga concentration in an (001)-oriented film. Figure 4.33 displays the Ga concentration dependence of (101) d-spacing in a (101)-oriented film. The error bars were taken from the undoped films as in the case of Nb-doped film data. The positive slope of both data sets indicate that the addition of Ga increased the lattice size for both film orientations.

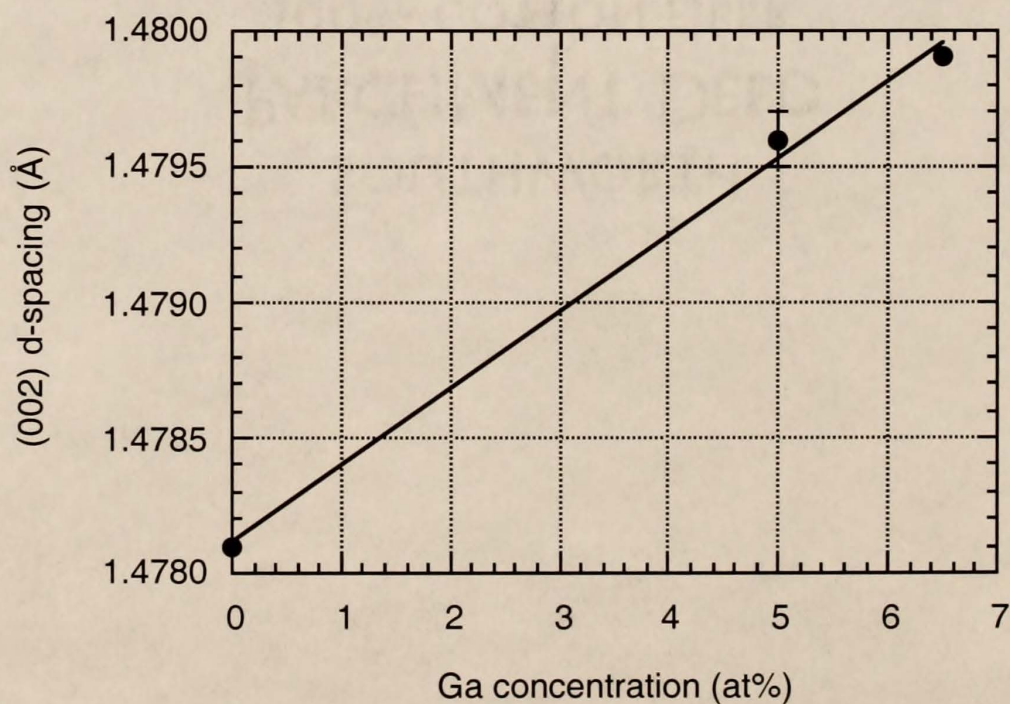


Figure 4.32 (002) rutile plane d-spacing as a function of Ga doping

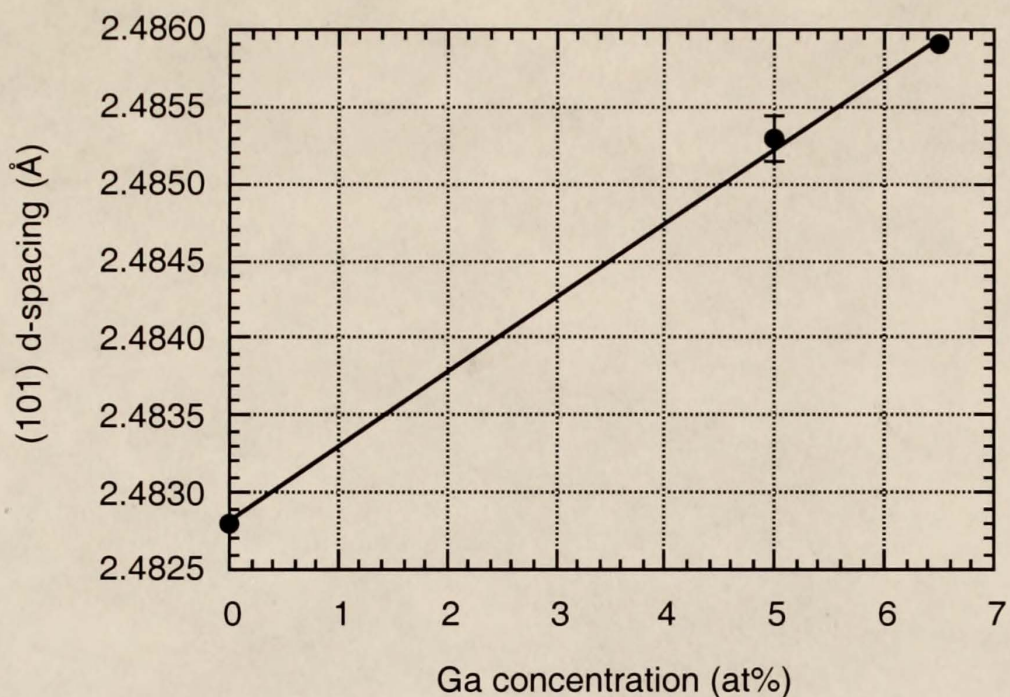


Figure 4.33 (101) rutile plane d-spacing as a function of Ga doping

In §2.3.3.1 the possible defect reaction equations corresponding to the substitutional inclusion of Ga on a cation site were shown. The compensating defects are either O vacancies or Ti interstitials. The literature indicates that Ti interstitials are the compensating defect only at high temperature and low  $\text{PO}_2$  in rutile films.<sup>79,80,82-85</sup> For an Al-doped film, the same behavior was observed with a transition to O vacancy compensation with decreasing temperature and increasing  $\text{PO}_2$ .<sup>80</sup> The Ga is expected to be compensated by O vacancies since these films were grown at a moderate temperature of 650 °C and high  $\text{PO}_2$  of 0.75 Torr in reference to the literature ranges for defect mechanism transition.

The analysis suggests that d-spacing was increased upon the introduction of Ga atoms compensated by O vacancies. Investigations of the lattice effects of Ga doping of rutile could not be found to aid in an analysis. The most probable cause of the lattice expansion observed is a repulsive interaction of the remaining atoms. When a larger O atom is missing, the positively charged neighboring atoms actually move slightly away

from one another out of repulsion as opposed to collapsing inward. A lattice volume expansion was also observed as a function of reducing  $\text{TiO}_2$  powder and only began to decrease at high levels of reduction near the phase transition boundary.<sup>203</sup> More applicable to the Ga-doped films is a study of Cr-doped powders.<sup>204</sup> The presence of  $\text{Cr}^{3+}$  was confirmed by XPS measurements. The a lattice parameter was found to increase linearly to the upper doping limit of the study, 4.5 at% Cr. The study cited O vacancy compensation of the acceptor-type Cr atoms due to the sample preparation of annealing in air. Because  $\text{Cr}^{3+}$  has a smaller ionic radius of 0.63 Å compared to  $\text{Ti}^{4+}$ , the lattice expansion cannot be attributed to an increased cationic radius. As was previously suggested here, the researchers correlated the expansion to the repulsive forces of the remaining atoms. The repulsion analysis follows the knowledge that in ionic solids lattice vacancies cause an expansion of the unit cell volume.<sup>205,206</sup> Although  $\text{TiO}_2$  is not purely ionic, it would be expected to follow this trend. Finally, if Ga were incorporated interstitially, a lattice expansion would still be observed. Modeling data, however, has shown that substitutional incorporation of Ga is far more energetically favorable than interstitial.<sup>100</sup>

The linearity of Figures 4.32 and 4.33 indicate that the O vacancy compensation of substitutional Ga atoms continued up to a 6.5 at% doping level. No unexpected XRD peaks which could be associated with secondary phases were observed. Neither is the linearity of lattice expansion likely to coincide with a formation of amorphous or secondary phases.

The effects of Ga expanding the rutile lattice under compression are apparent in other XRD measurements which were used to investigate the structure of these films. Figure 4.34 is a plot of the rc fwhm of the respective rutile peaks as a function of Ga concentration. As expected, the data indicate that a larger number of defects were present as a result of the dopant atoms. The defects decreased the d-spacing consistency in both orientations. The fwhm of (001)-oriented films exhibited a large increase at a 1 at% doping level and remained essentially constant for higher doping levels. This indicates that a large

change was caused in the structure by the initial introduction of extra stress. This change was capable of accommodating the increased stress of higher dopant concentrations without substantially further diminishing the planar spacing consistency. An orientational comparison shows that the (001)-oriented Ga-doped films had a more orderly structure than (101)-oriented films as in the cases of undoped and Nb-doped films.

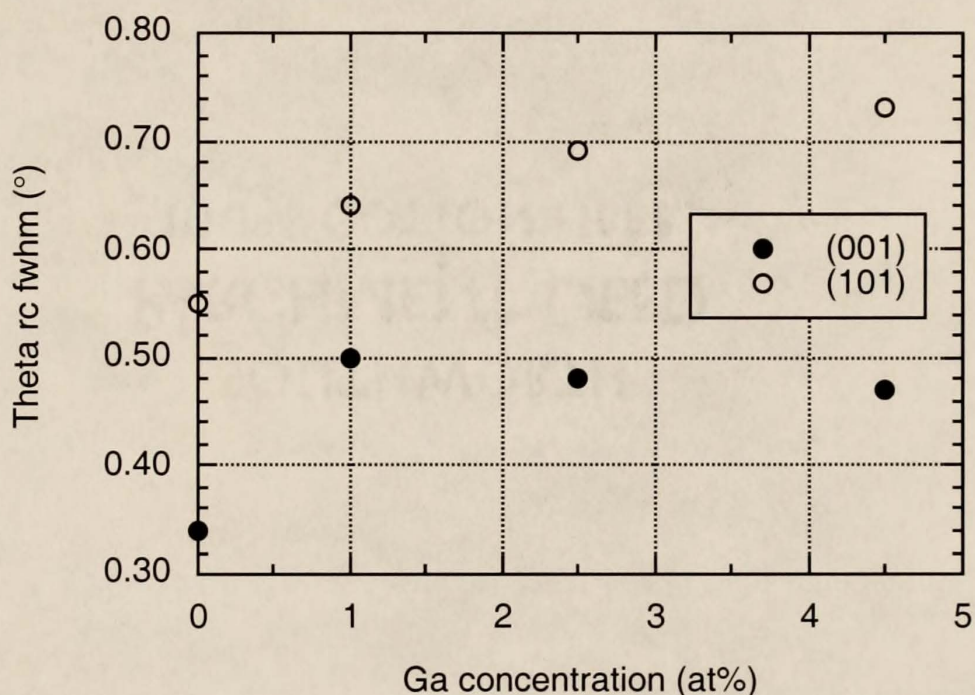


Figure 4.34 (001) and (101) rutile peak  $\theta_{rc}$  fwhm as a function of Ga doping

$\phi$  scans of Ga-doped films showed that heteroepitaxial deposition was achieved for both orientations. Figure 4.35 shows the fwhm measured from the peaks of a  $\phi$  scan of the (101) plane and the (110) plane of the (001)- and (101)-oriented films, respectively. The data indicate that in-plane orientational consistency was diminished by Ga-doping in an (001)-oriented film. For the (101) orientation, however, an initial increase in fwhm was measured followed by a decrease to values slightly smaller than an undoped film. The initial increase corresponds to an increase in defect density due to the Ga. The ensuing decrease is suggested to follow a decrease in the small (100) peak observed in  $\theta$ - $2\theta$  scans. The increase in defect density caused by the Ga atoms acts as a stress relief in the lattice at

large film thicknesses that was previously accommodated by a small amount of (100)-oriented material. The overall consistency of in-plane orientation was not significantly different for either stress compensation mechanism. The heteroepitaxial growth of Ga-doped (001)-oriented and (101)-oriented rutile thin films is unknown in the literature.

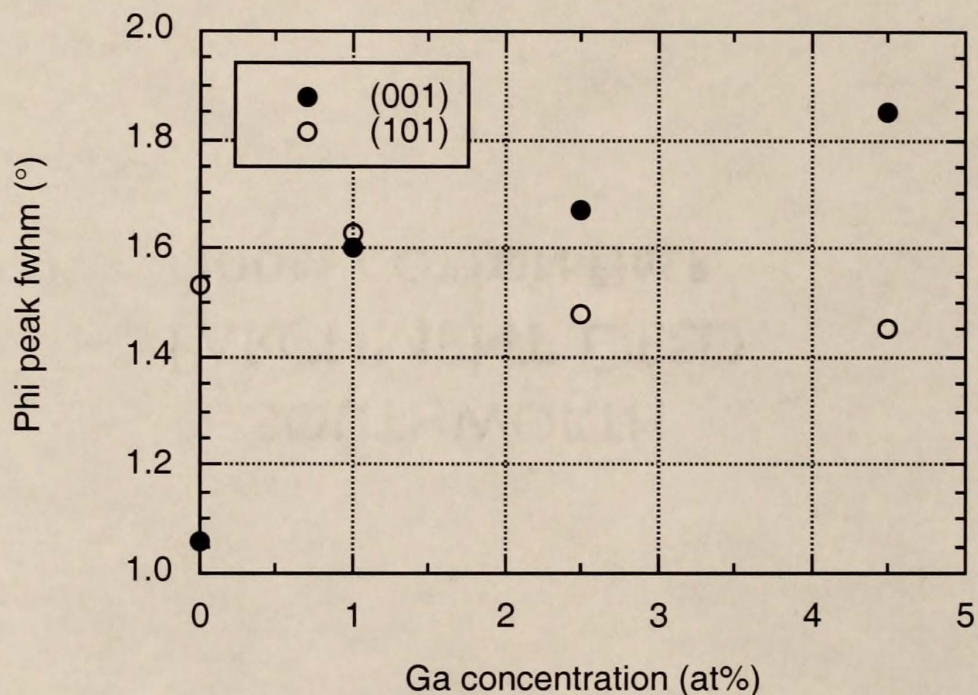


Figure 4.35 (001) and (101) rutile  $\phi$  scan peak fwhm as a function of Ga doping

4.2.3.2 Surface morphology. The surface morphology effects of Ga-doping were investigated by AFM. Figures 4.36 (a) and (b) are normal AFM images of thin and thick 1 at% Ga-doped (001)-oriented rutile thin films, respectively. "Thin" and "thick" are representative of the same nominal film thicknesses as in the previous discussion of undoped images,  $70 \pm 10 \text{ \AA}$  and  $3350 \pm 75 \text{ \AA}$ . Figures 4.37 (a) and (b) are the corresponding images of (101)-oriented films. Figures 4.38 (a) and (b) are images of thin and thick (100)-oriented 1 at% Ga-doped films. Meaningful comparisons can be made with the respective undoped images of each orientation among Figures 4.5 to 4.13 shown earlier.

The gray scales for each thin and thick Ga-doped film image are 100 Å and 600 Å, respectively, with the exception of the thick (001) orientation image which is 400 Å.

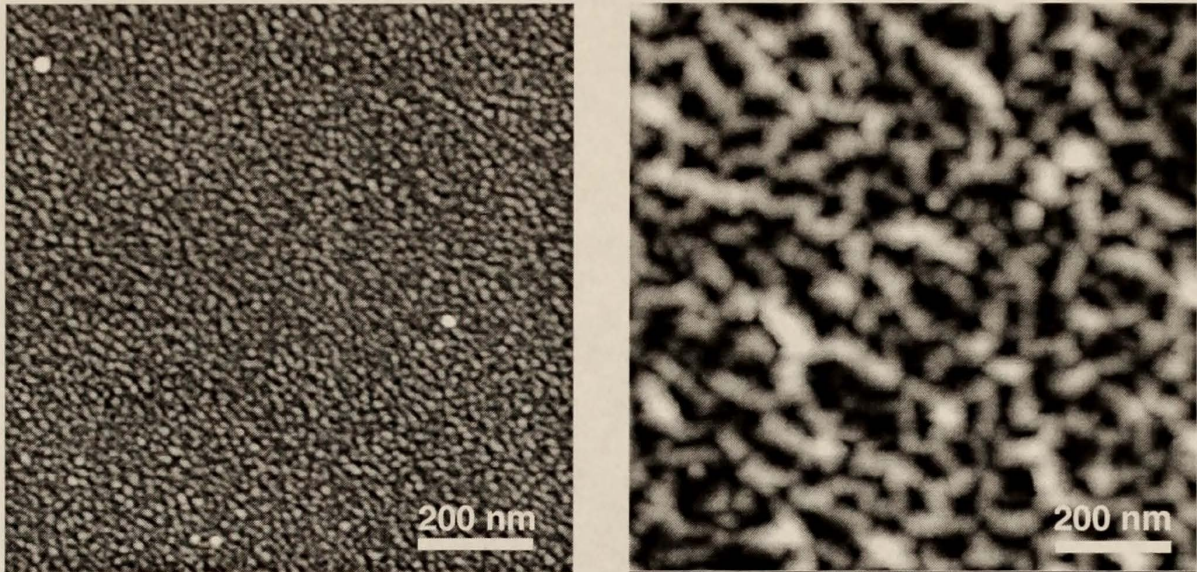


Figure 4.36 Ga-doped (001)-oriented thin film AFM images  
(a) 70 Å (b) 3350 Å

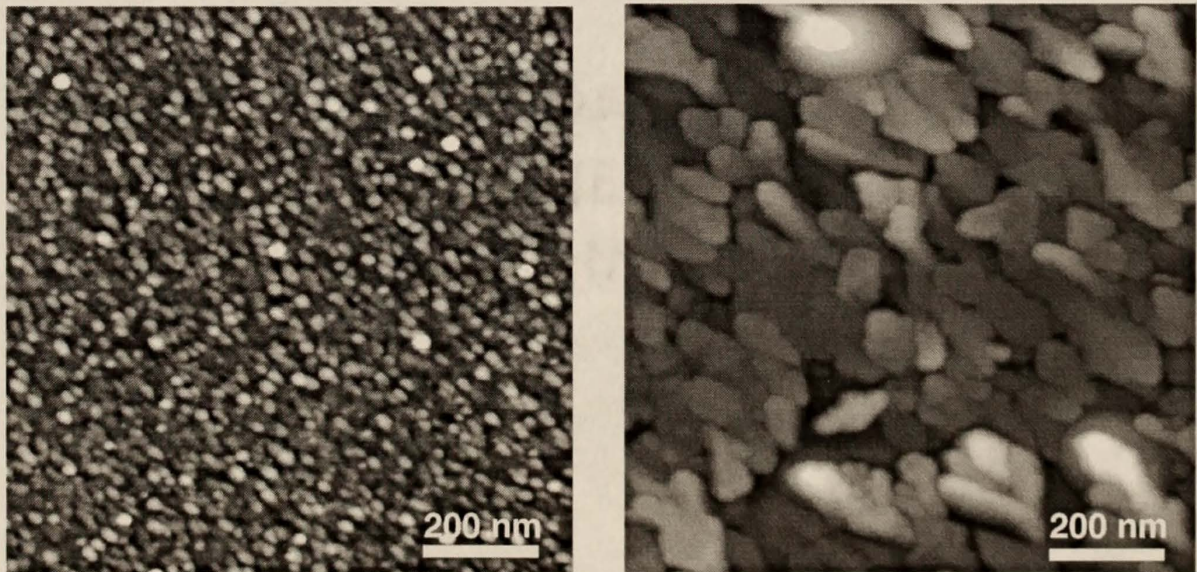


Figure 4.37 Ga-doped (101)-oriented thin film AFM images  
(a) 70 Å (b) 3350 Å

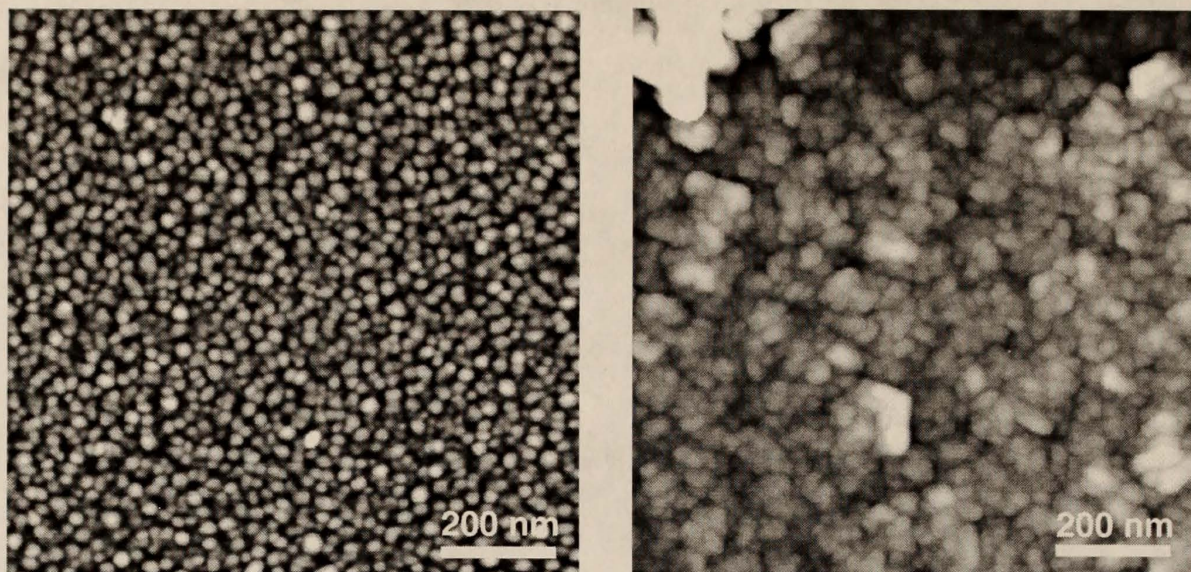


Figure 4.38 Ga-doped (100)-oriented thin film AFM images  
(a) 70 Å (b) 3350 Å

A comparison of the Ga-doped and undoped feature sizes and rms roughnesses demonstrated some notable differences. First, the height and planar dimensions of the thin film features did not significantly change with Ga doping for any of the orientations. Figure 4.37 (a) shows that preferential growth parallel to  $[\bar{1}01]$  was present as in the cases of undoped and Nb-doped films. The data indicate that film stress added by Ga did not cause a substantial number of defects to alter growth until higher thickness. Second, an (001)-oriented Ga-doped film is characterized by a lack of larger features found on an undoped film. The actual features which form the apparent morphology in Figure 4.36 (b) are less than twice as large as the very small islands of 4.36 (a). This corresponds to an increase in rms roughness by a factor of two over an undoped film. The smaller microstructure appears to have been unable to coalesce due to the effects of Ga. Third, a Ga-doped (100)-oriented surface contains considerably smaller, flatter features than an undoped film imaged in Figure 4.13. This morphology resulted from the prominence of anatase phase  $\text{TiO}_2$  in this Ga-doped orientation. The 5% anatase phase identified in undoped (100) films was attributed to film stress from a complex substrate relationship and high deposition rate. The problems were apparently compounded by the addition of Ga

which drove the anatase fraction over two-thirds. Finally, a greater density of the surface features imaged on a (101)-oriented Ga-doped film have a larger dimension normal to elongation than an undoped film. This characteristic may be a result of Ga doping being an alternative stress relief mechanism in thick (101)-oriented films as was demonstrated in the corresponding  $\phi$  scan peak fwhm data.

### 4.3 Summary

#### 4.3.1 Undoped Rutile Film Deposition

Heteroepitaxial rutile films were deposited using a solid precursor as the source of metal atoms. Film with an (001), (101) or (100) rutile crystal orientation were deposited on (10 $\bar{1}$ 0)-, (11 $\bar{2}$ 0)- and (0001)-oriented sapphire substrates, respectively. XRD analysis determined that the plane-to-plane spacing of a (100)-oriented film was most consistent having a  $\theta$  rc fwhm of 0.20°. The planar spacing consistencies of (001)- and (101)-oriented films were similar with values around 0.35° at high deposition temperature. XRD investigation of the heteroepitaxial nature of each orientation revealed the in-plane matching crystal directions in the film and substrate. The (100) orientation was found to have three equivalent in-plane alignments with respect to its sapphire substrate, and the (101) orientation was found to have a twin plane parallel to the film surface. The consistency of in-plane alignment indicated by  $\phi$  peak fwhm values was worst for (100)-oriented film for obvious reasons. The  $\phi$  peak fwhm values of (001)- and (101)-oriented films were similar at 1.1° and 1.5°, respectively.

The undoped film surface morphologies were investigated by AFM. Measurements taken from the AFM images were used to show that (001)- and (101)-oriented film surfaces were composed of facet planes in a uniform arrangement. An (001)-oriented film surface consisted of {101}-type facet planes which formed surface features similar to inverted

pyramids. The {101}- and {111}-type facet planes of a (101)-oriented film surface formed features shaped like trapezoidal prisms. XRD was used to show the direction of elongation of the surface features was  $[\bar{1}01]$ . This is the direction of smallest oxide sublattice mismatch between film and substrate. The mismatch in the other in-plane direction of a (101)-oriented film and in each in-plane direction of the other two film orientations were too large to produce feature elongation.

These bulk crystal and surface properties were shown to be in general agreement with the respective orientations of rutile films grown by IBSD. The deposition of (001)-oriented heteroepitaxial rutile films is unique to this work and the corresponding IBSD research.

#### 4.3.2 Doped Rutile Film Deposition

The rutile films were doped with Ga, an acceptor-type dopant, or Nb, a donor-type dopant. XRD was used to prove that heteroepitaxy was maintained to 6.5 at% of either dopant. The crystalline quality as indicated by  $\theta_{rc}$  and  $\phi$  peak fwhm values declined with increasing dopant concentration. An exception was found for the case of in-plane alignment of (101)-oriented films which improved with Ga doping. This behavior was related to a decline of the presence of small amounts of (100)-oriented material as a stress relief mechanism at large thicknesses.

XRD measurements further demonstrated that the lattices of (001)- and (101)-oriented films expanded linearly with increasing dopant concentration. The expansions were related to the larger size of the Nb atom substituted on a Ti lattice site and the O vacancy compensation of the smaller Ga atom substituted on a Ti site. The removal of a much larger anion caused lattice expansion due to repulsive forces among the remaining atoms as expected for a material which is nearly ionic.

Surface morphology changes were governed by the increased lattice stress caused by doping. Increased lattice stress resulted in a greater number of defects in the materials and therefore increases in the surface roughnesses of each orientation. An exception was observed for the (100) orientation where Ga doping resulted in a conversion to primarily anatase phase crystalline material. (101)-oriented films continued to exhibit elongation in the  $[\bar{1}01]$  direction under the influence of either dopant. The feature size actually increased with Ga doping corresponding to the decline in (100)-oriented material as measured by XRD.

## CHAPTER 5 RUTILE GAS SENSORS

### 5.1 Film Orientation Results Summary

The resistances of undoped rutile TiO<sub>2</sub> thin films with (001), (101) and (100) orientation were measured. The measured activation energies in dry and humid nitrogen and oxidizing atmospheres were very close to one another considering the associated error. Some small orientational differences may exist, but are not significant enough to affect the trends presented in the following calculations. The actual magnitude of those differences and their derivation will be discussed later.

The following equation is used to calculate electronic conductivity:

$$\sigma = 1/R (d / (l t)) \quad (5.1)$$

where

R = resistance ( $\Omega$ )

d = distance between contacts = 0.22 cm

l = contact length = 0.80 cm

t = film thickness (cm).

A second equation for calculating the electronic conductivity is

$$\sigma = n e \mu \quad (5.2)$$

where

n = density of conducting electrons (cm<sup>-3</sup>)

e = electronic charge = 1.6022e-19 C

$\mu$  = electronic mobility (cm<sup>2</sup>/V/sec).

With an appropriate value of  $\mu$ ,  $n$  can be calculated and multiplied by the sample volume ( $d$  l t) to give the total number of electrons conducting in a sample.

Figure 5.1 shows the resistance values measured in pure  $N_2$  ( $PO_2 < 1e-9$  atm) and a mixture of  $1.332e-3$  atm  $O_2$  in  $N_2$  at atmospheric pressure. The corresponding changes in the number of conducting electrons removed upon exposure to an oxidizing atmosphere as compared to the same sample tested in pure  $N_2$  for the three film orientations tested near  $240^\circ C$  are also shown. Due to the very high resistance of the (001)-oriented film, the  $240^\circ C$  value shown for that sample in a partial oxygen environment is an extrapolation from data taken at higher temperatures. The mobility value used in equation 5.2 for these calculations is taken from the work of Göpel,<sup>91</sup> as discussed below. According to Göpel's analysis, the mobility at  $240^\circ C$  is  $0.17 \text{ cm}^2/V/\text{sec}$ . The data suggest that the largest amount of oxygen was adsorbed and hence largest number of electrons removed from the (100)-oriented film followed by the (101)- and (001)-oriented films.

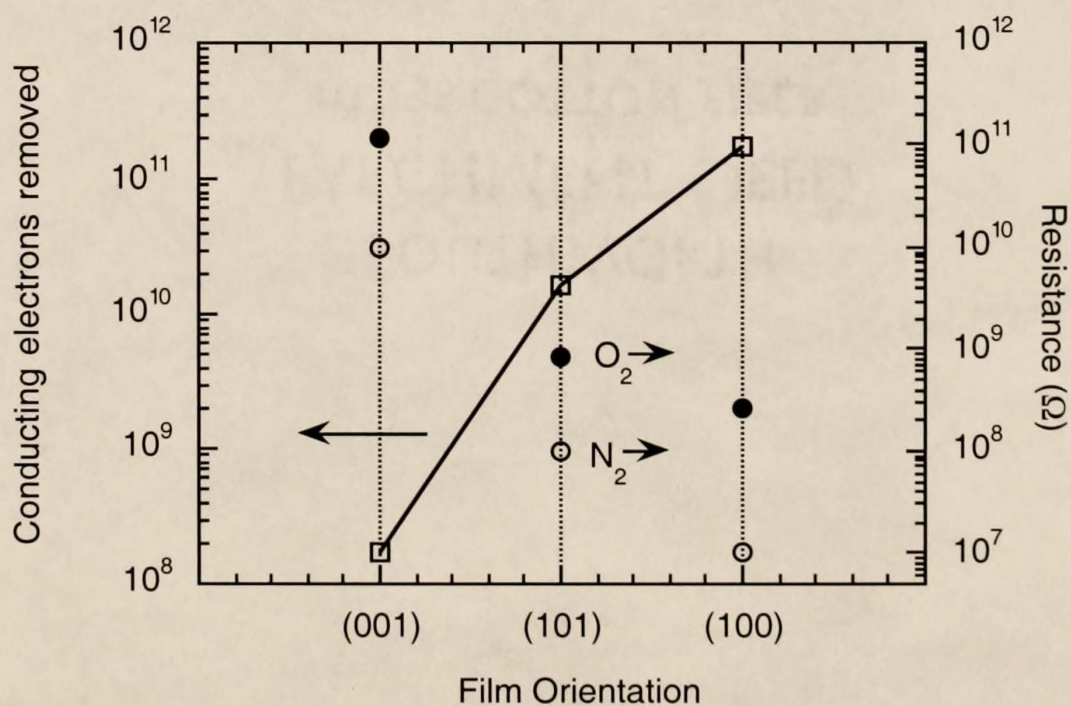


Figure 5.1 Conducting electrons removed as a function of film orientation calculated from resistance values measured in  $N_2$  and  $O_2$  atmospheres at  $240^\circ C$

Figure 5.2 shows the resistance values measured in pure  $N_2$  ( $PO_2 < 1e-9$  atm) and humidified  $N_2$  (saturated,  $21^\circ C$ ) and the corresponding changes in the number of conducting electrons added upon exposure to humidity. Using the mobility value as described above to calculate the absolute number of electrons added to a film, the data suggest a similar increase in the number of conducting electrons for (101)- and (100)-oriented films followed by a (001)-oriented film.

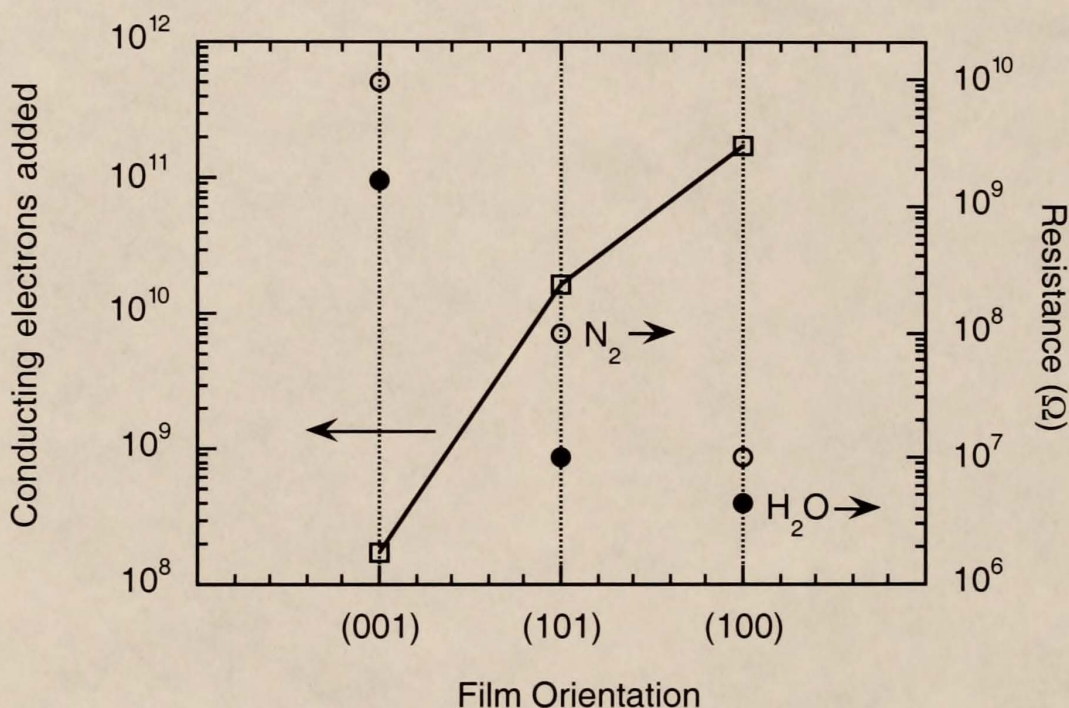


Figure 5.2 Conducting electrons added as a function of film orientation calculated from resistance values measured in  $N_2$  and humidified  $N_2$  atmospheres at  $240^\circ C$

## 5.2 Film Orientation Discussion

### 5.2.1 Measurements

The motivation for using electrochemical impedance spectroscopy to characterize the gas sensors was to ensure that changes in the material characteristics were being probed as opposed to those of the electrode or electrode material barrier. The impedance spectra

used to obtain the resistance values were single, symmetric semicircles. The only exceptions were for the highly resistive films where a method of approximation was used as described in §3.3.3.3. Some early experimentation in the effort to obtain consistent impedance data (§3.3.2.2), however, produced some different spectra. An undoped (001)-oriented film with contacts applied was heated to 500 °C at a rate of approximately 100 °C per minute, held for five minutes, and then cooled to 100 °C in less than one minute at a pressure below 1  $\mu$ Torr. The impedance spectra of this film showed two responses. As temperature increased from near 20 °C to 225 °C, the ratio of the resistance of the higher frequency to the resistance of the lower frequency response increased. This trend resulted in a single, symmetric response being observed at temperatures above 200 °C. The interpretation of this data was that the low frequency response was that of the electrode-material interface barrier, and the high frequency response represented the material. The barrier response was believed to have been observable in this instance because the temperature cycle had aged the electrodes. In combination with the decreased material resistance the electrode barrier response was therefore observable in the frequency / temperature domain of the experiment. Even with the effects of the temperature cycle, the electrode barrier resistance above 200 °C remained below  $1e4 \Omega$ . This interpretation of the two response spectra observed is supported by the literature.<sup>207-209</sup>

In addition, another film was subjected to this same type of heat treatment first with the two contacts separated by 4 mm. Impedance measurements were taken at a few temperatures before a third contact was placed on the film's surface which decreased the previous distance between the electrodes to nominally 2 mm. The film was placed back in the chamber and taken through the same heat treatment. Two responses were observed at low temperature for both contact geometries. The intersection of the higher frequency response on the real impedance axis for an electrode spacing of 2 mm was found to be approximately one-half of the higher frequency response intersection for a 4 mm electrode spacing as a function of sample temperature.

Based on these observations, the symmetric single response spectra used to derive the resistance values shown here are believed to be characteristic of the thin films. The response corresponding to an electrode barrier is theoretically present at the low frequency end of an observed response. Its magnitude is so small, however, that it cannot be observed as in the case of the reduced film described at temperatures above 200 °C.

## 5.2.2 Mechanisms

5.2.2.1 Film conductivity. Conductivity in the TiO<sub>2</sub> thin films in this study is believed to be a two step process. The first step is the thermal ionization of an electron from an oxygen vacancy. As discussed in §2.3.2.3 the electronic state of an oxygen vacancy has been predicted by modeling and measured by several methods to reside in the band gap from 0.62 to 1.0 eV below the conduction band edge.<sup>90,92-99</sup> Once the electron is activated into the conduction band, it is free to conduct over long distances without being retrapped.

The electron mobility is believed to be a function of phonon scattering as opposed to an activated hopping mechanism characteristic of small polarons. Göpel reviewed over forty conductivity studies of reduced and unreduced rutile and proposed the following equation for calculating mobility as a function of temperature

$$\mu = 1e6 T^{-2.5} \text{ (cm}^2\text{/V/sec)} \quad (5.3)$$

where T is the absolute temperature in Kelvin.<sup>91</sup> Such an inverse temperature dependence is in agreement with mobility being a function of phonon scattering as shown previously in Table 2.5.<sup>82-84,86-90</sup> This analysis also conforms to the work of Bogoroditskii and Frederikse on electronic mobility in Nb-doped TiO<sub>2</sub>.<sup>87,118</sup> The best possible effort was made to remove potential mobility differences in the (101)- and (001)-oriented films. Both

films contain the [010] direction in the plane of the film, and the resistance was measured in this direction on each sample.

5.2.2.2 Activation energy. The activation energy of conductance was calculated for all films in each atmosphere by obtaining a resistance value from the impedance data at several sample temperatures. The activated process follows the relationship

$$1/R = B \exp(-E_c/RT) \quad (5.4)$$

where

$E_c$  = activation energy of conductance (eV)

$k$  = Boltzmann constant =  $8.6173 \times 10^{-5}$  eV/K

$T$  = absolute temperature (K)

$B$  = constant,

so a plot of  $\ln(1/R)$  as a function of  $1/T$  has a slope of  $-E_c/R$ . Figure 5.3 shows a plot of the  $E_c$  values calculated as a function of undoped rutile film orientation in pure  $N_2$ , humidified  $N_2$  and low  $PO_2$  atmospheres. The error shown for each value is taken from repeated measurements at several temperatures, assuming this error to be the same at each temperature and calculating an error for the slope value,  $-E_c$ . The error in the values for an (001)-oriented film in  $N_2$  and low  $PO_2$  atmospheres are higher for two reasons. First, the error in the resistance values used is larger because they were taken near the high resistance limit of the measurement apparatus and estimated as described in §3.3.3.3. Second, fewer points were used to calculate the slopes because the data were taken at a higher than normal temperature range to obtain valid resistance values.

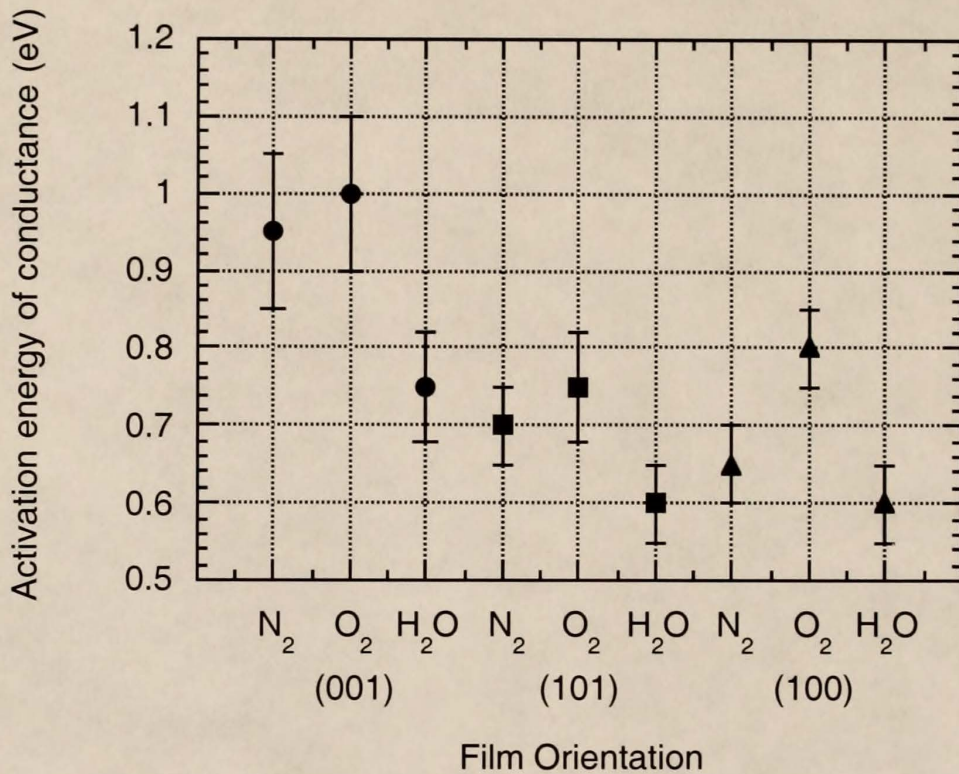


Figure 5.3 Activation energy of conductance as a function of film orientation in different atmospheres

The activation energies appear to slightly decrease and increase for humid and O<sub>2</sub> atmospheres, respectively, as compared to the N<sub>2</sub> atmosphere for each orientation. These apparent changes can be explained in reference to the conductivity mechanisms. When H<sub>2</sub>O is dissociatively adsorbed on the surface and electrons are donated to a material, an increase in the conductivity is observed. When the temperature is raised, the conductivity increases but the sticking coefficient of adsorbed H<sub>2</sub>O decreases slightly. Therefore, fewer electrons are available for activation to the conduction band which is observed as a smaller increase in conductivity for a given temperature change as compared to the increase in a N<sub>2</sub> atmosphere. This smaller conductivity increase results in a calculation of an apparent smaller activation energy. The activation energy, however, is the same. It is the decrease in the number of electrons available for activation that has actually changed. By the same analysis, an apparent increase in activation energy in the presence of O<sub>2</sub> can be explained.

In this case, as temperature is raised the  $O_2$  sticking coefficient decreases and a relatively larger number of electrons remain in the conduction band as opposed to a larger number of electrons being in the conduction band strictly from activation. This larger increase in the conductivity with respect to temperature change results in an apparent increase in the activation energy.

The data of Figure 5.3 also suggest some differences in activation energy with respect to orientation. The band structure of rutile  $TiO_2$  shows that there are distinct differences in the size of the band gap as a function of crystal orientation.<sup>75</sup> Changes in the band gap may account for the differences in oxygen vacancy energy level found in the literature (§2.3.2.3) and the activation energies of the thin films studied. This may come about due to the nature of these films, i.e. each orientation is under different amounts and types of stresses as a result of the film-substrate relationship. The band gap is expected to change as a function of these stresses, although the actual trends are not well known.

5.2.2.3 Oxygen sensitivity. The literature detailing the associative and dissociative adsorption of oxygen was reviewed in §2.3.4. A summary of what has been observed suggests that dissociative adsorption is associated with reduced Ti atoms present at the surface. The observation of a reduced Ti atom is equivalent to the observation of one or more oxygen vacancies, so it is not unexpected that the surface would seek to reduce its energy by filling that vacancy with available oxygen from the atmosphere. An electron is trapped when the O atom is bound to the surface, and the number of electrons available for conduction is reduced. The increase in the measured resistance that results is the source of the term "electron acceptor" for adsorbed oxygen. The equivalent physical model is that adsorbed oxygen represents acceptor states with energy levels in the band-gap of a film. Consequently, electrons will be removed from the conduction band to fill these lower energy states. This mechanism concurs with oxygen sensor behavior observed in all n-type conducting metal oxides from room temperature to over 1000 °C.

5.2.2.4 Humidity sensitivity. The literature detailing the associative and dissociative adsorption of water was also reviewed in §2.3.4. Like oxygen, a summary of what has been observed suggests that dissociative adsorption is a function of reduced Ti atoms being present at the surface. The nature of the adsorption mechanism is open to a larger amount of interpretation due to temperature effects and the role of the atoms surrounding the oxygen vacancy in assisting the dissociation. The excess electron of an adsorbed hydroxyl at an oxygen vacancy or an adsorbed proton on a neighboring oxygen is donated to the material and a decrease in resistance is measured. The corresponding physical model is that hydroxyls represent donors from which electrons will be removed to fill empty states with lower energy. Some portion of these donated electrons are then activated into the conduction band.

This mechanism is proposed for rutile above room temperature where there is no longer a coherent physisorbed layer of water. The more familiar type of humidity sensor reviewed in §2.2.2 operates at room temperature. For these materials proton conductivity occurs in a physisorbed surface layer of water, so high surface area is critical to sensitivity. As a confirmation of the electron donation mechanism described above, a thin film was allowed to sit in a humidified N<sub>2</sub> atmosphere until conduction was measured. The temperature was then slowly raised. The results of this experiment are shown in Figure 5.4 for a representative undoped film. Ninety-six hours were required to establish proton conductivity given the very small amount of surface area available on the thin film relative to the quick responses in porous thick films or ceramics. The figure shows the physisorbed layer desorbing and proton conduction decreasing until electronic conductivity is activated which increases with temperature.

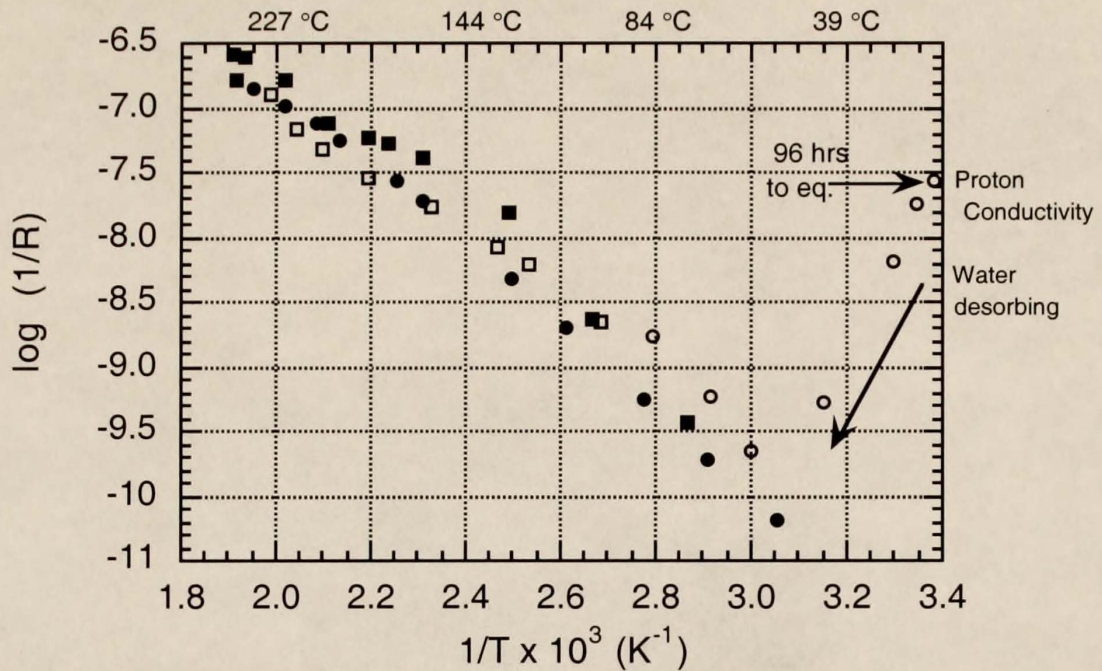


Figure 5.4 Surface proton conduction on undoped thin film near room temperature and electronic conductivity at higher temperatures measured over several temperature cycles

### 5.2.3 (101) and (001) Orientations Comparison

5.2.3.1 Surface Morphology. The most informative discussion of the results revolves around a comparison of the (101)- and (001)-oriented films. The physical characterization described in §4.1.2.1 and §4.1.2.2 has shown that these films are pure rutile with a consistent in-plane orientation. Recall that the (100)-oriented films contain up to five percent of the anatase phase of  $\text{TiO}_2$  and contain grains which may be oriented in three equivalent ways in the plane of the film.

If the surface of (001)-oriented rutile does not reconstruct, the surface Ti atoms would only be 4-coordinated with respect to oxygen. This surface would have a very high energy relative to the surface energies of other rutile orientations. In studies of the surface of crystals with bulk (001) orientation, the surface has been found to reconstruct into {101} type facets up to approximately 1000 °C.<sup>128,138,210-213</sup> {101} planes consist of 5-coordinated Ti atoms at the surface. Figure 5.5 shows an orientation stability diagram for

rutile at 1273K developed by Lowekamp.<sup>211</sup> This figure is interpreted like a 3-phase diagram. The diagram shows that films with (001) orientation will facet into {101}-type planes.

Figure 5.6 shows an AFM image of an MOCVD grown (001)-oriented film (a) as compared to an image of an IBSD film grown by Morris-Hotsenpiller (b).<sup>214</sup> Lowekamp attributed the square pit-like features of the IBSD film to intersections of {101} type facets, a schematic of which is shown in Figure 5.7.<sup>211</sup> The MOCVD film is substantially more rough with less well-defined surface features than the IBSD film because deposition by MOCVD occurs at approximately 40 Å/min as opposed to 4 Å/min in IBSD. The pit-type features can be viewed in several areas of Figure 5.6(a), one of which is highlighted by a box. The {101} planes of these features identified on the MOCVD film form angles of  $28 \pm 2^\circ$  with the plane of the film. The angle value between the (001) and {101} calculated from the rutile unit cell is  $32.7^\circ$ . Because the orientation stability figure shows that any surface near to (001) will facet into {101} planes, the difference in the real and theoretical angle values is attributed to the resolution of AFM for such small features. Based on these findings and the literature, it is proposed that the majority of an (001)-oriented MOCVD grown film surface also consists of {101} type facets. The Cerius<sup>2</sup> molecular modeling system from Molecular Simulations Inc. was used to create images of the intersections of the {101} type facets. At intersections in the [100] direction, the Ti atoms are 4-coordinated. Intersections along [010] consist of alternating 4- and 5-coordinated Ti atoms.

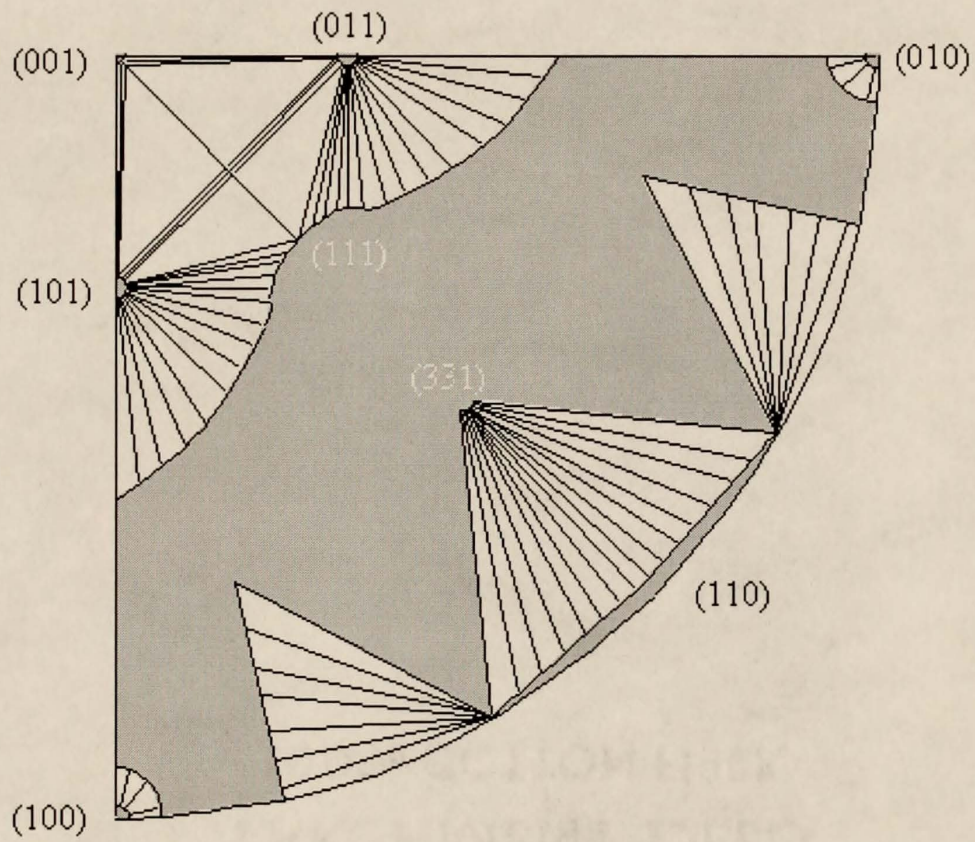


Figure 5.5 Orientation stability diagram for rutile at 1273K

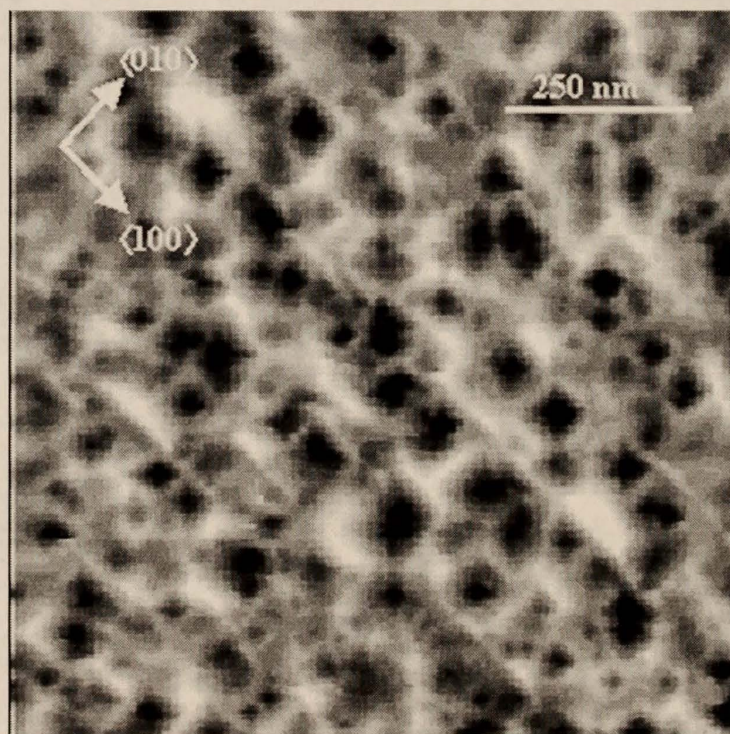
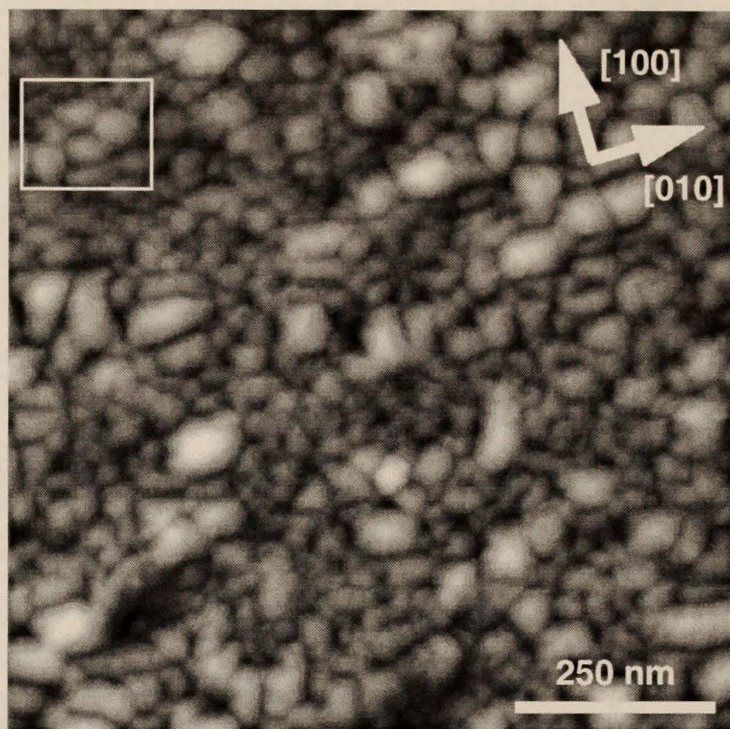


Figure 5.6 AFM images of (001)-oriented rutile thin films  
(a) deposited by MOCVD (b) deposited by IBSD

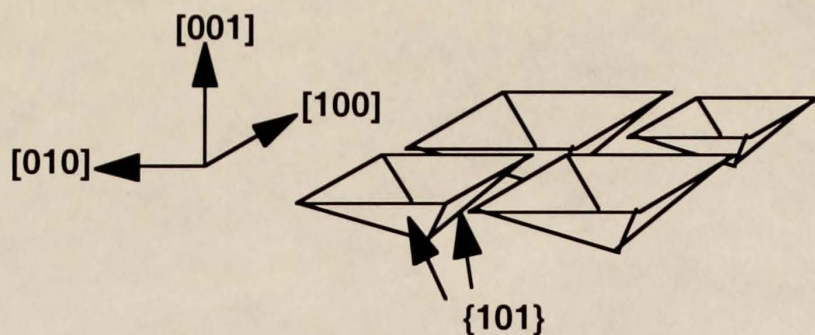


Figure 5.7 Schematic of facets on (001)-oriented rutile surface

Figure 5.8 shows AFM images of (101)-oriented films grown by MOCVD on (a) "smooth" and (b) "featured" substrates (§4.1.3.2) and grown by (c) IBSD. Figure 5.8(b) is included because it allows for a more rigorous analysis of the surface features in Figure 5.8(a). In conjunction with single-crystal faceting studies, Lowekamp proposed that the IBSD film surface consists of a mixture of {101} and {111} type facets as shown schematically in Figure 5.9.<sup>211</sup>

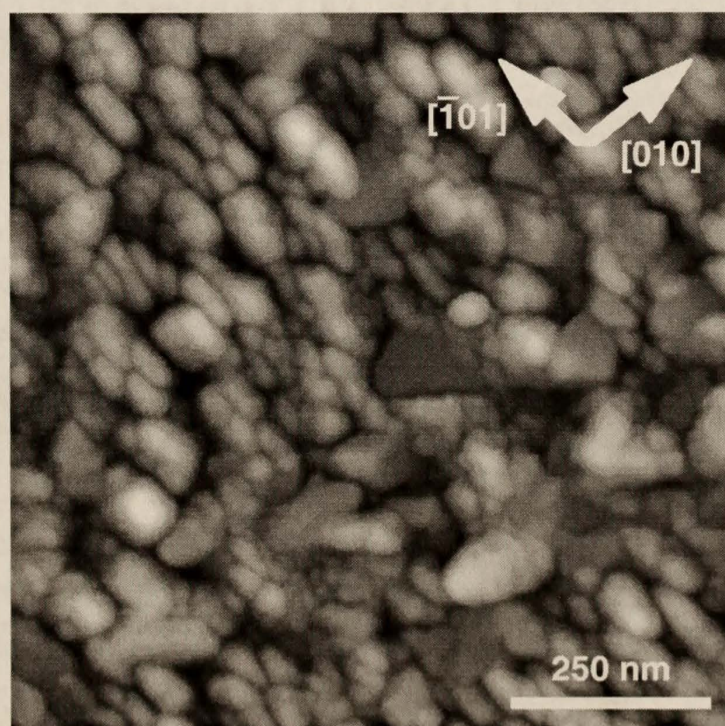


Figure 5.8 AFM images of (101)-oriented rutile films  
(a) deposited by MOCVD on "smooth" substrate

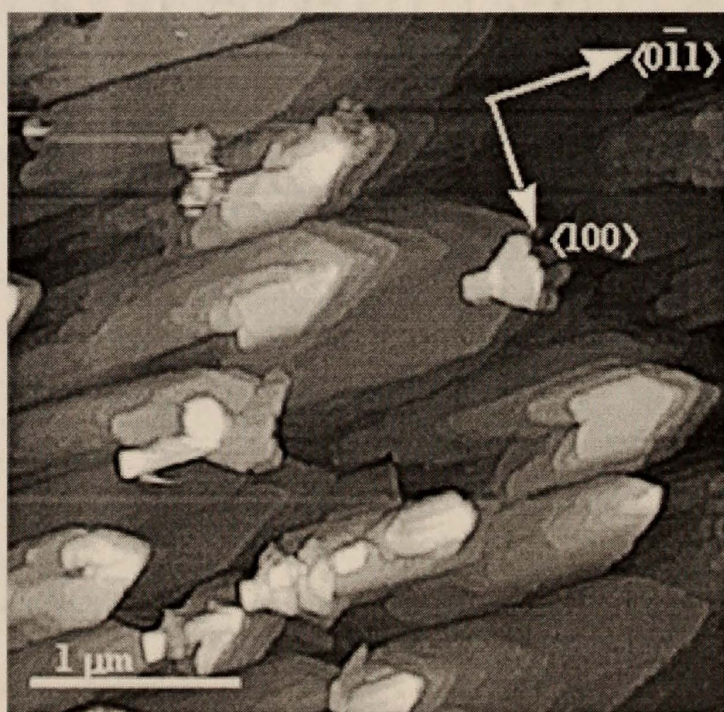
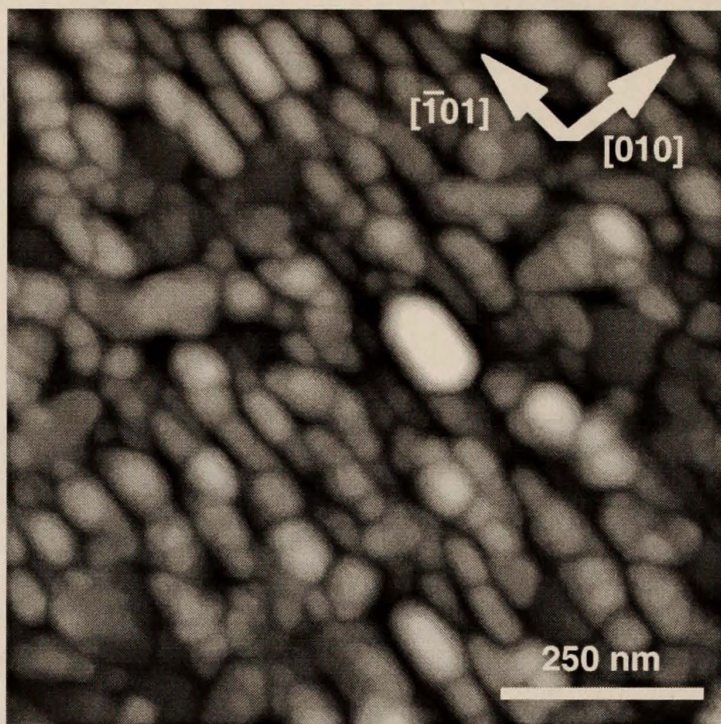


Figure 5.8 (continued) AFM images of (101)-oriented rutile films  
(b) deposited by MOCVD on "featured" substrate  
(c) deposited by IBSD

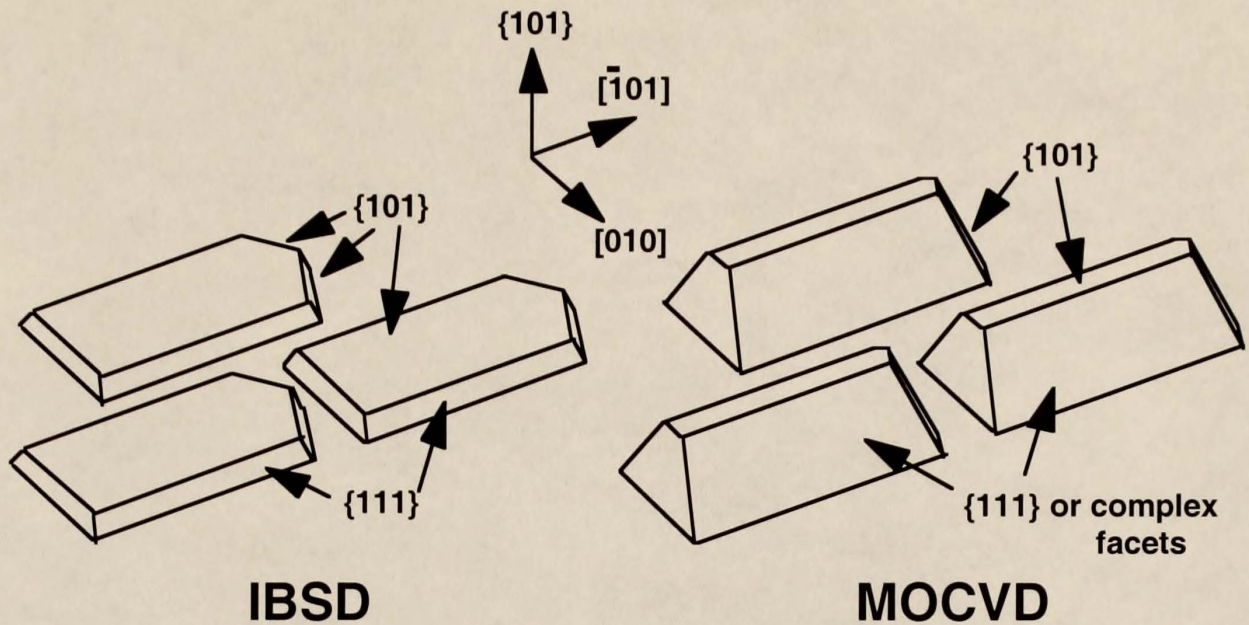


Figure 5.9 Schematic of facets on (101)-oriented rutile IBSD and MOCVD deposited surfaces

Also shown in Figure 5.9 is a proposed model for the faceted shape of the surface features of the films deposited by MOCVD. Analysis of a representative number of the largest features in Figure 5.8 (a) and all features in (b) reveals angles between the plane of the (101) surface and the side planes are consistent with the side planes being {111}. According to the crystal directions of these films shown in Figure 5.9 which were established by XRD, the {111} plane observed is the (111), and the plane away is the ( $\bar{1}\bar{1}1$ ). The theoretical value of the angle between (101) and these planes is  $61.6^\circ$ . The value measured from the AFM images was found to be  $58 \pm 2^\circ$  in acceptable agreement.

For some of the smaller features in Figure 5.8 (a) the angle of intersection was measured to be  $46 \pm 2^\circ$ . There are a couple of explanations for this data which are consistent with the surface feature model proposed. One is the decreased resolution of the AFM technique as the features get smaller and the feature being imaged is out of the plane of the film. Any rounding near the top of the feature image will cause a depression in the measured value of the angle as compared to the actual value. Another explanation is that

the planes are complex in nature. The orientation stability figure shows a large number of tie lines between the  $\{101\}$  orientation and complex planes which reside along the line between  $\{111\}$  and the  $\{011\}$  -  $\{010\}$  tie line. Higher order planes such as  $\{132\}$  exist in this region and are predicted by the figure to form stable surface facets on a (101) surface. Like the  $\{111\}$ , these planes would intersect (101) along  $[\bar{1}01]$  and would exhibit a more shallow angle of intersection consistent with the data from the AFM image.

As stated before,  $\{101\}$  planes contain 5-coordinated Ti atoms. The Cerius<sup>2</sup> molecular modeling system was used to create images of the facet planes and their intersections for the model in Figure 5.9. The small edges at  $\{101\}$  intersections are along  $\langle 1\bar{1}1 \rangle$  and contain 3- or 4-coordinated Ti's. The nearest neighbor Ti distance in  $\{101\}$  planes is 3.57 Å along  $\langle 1\bar{1}1 \rangle$ . By contrast,  $\{111\}$  planes contain a mixture of 3- and 5-coordinated Ti atoms, and their intersections with (101) along  $[\bar{1}01]$  also contain a mixture of 3- and 5-coordinated Ti atoms. The nearest neighbor Ti distance in  $\{111\}$  planes is 5.47 Å along  $\langle \bar{1}01 \rangle$  and 6.50 Å along  $\langle 110 \rangle$ .

Calculations using data taken from representative features in the AFM images show that approximately 80% of the total surface area is contained in the  $\{111\}$  facet planes with the remainder in the  $\{101\}$  facets. From the Ti atom densities at each surface and their known oxygen coordinations, Ramamoorthy calculated densities of 8.0 and 8.8 Ti dangling bonds / cm<sup>2</sup> for the  $\{101\}$  and  $\{111\}$  planes, respectively.<sup>213</sup> These values are in agreement with the surface images created using Cerius<sup>2</sup>. The dangling bond density values allow a calculation of the total number of dangling bonds on the (101) and (001) surfaces. The total tested surface area as determined from the AFM images is 0.20 cm<sup>2</sup> for a (101) film and 0.16 cm<sup>2</sup> for a (001) film. The resulting total number of dangling bonds is 1.73e14 for a (101) film and 1.30e14 for a (001) film. This calculation suggests that the surface density of dangling Ti bonds could be a factor in the improved adsorption characteristics of a (101) film over a (001) film. The difference is, however, not large enough to fully explain the (101) film's increased ability to adsorb oxygen or water.

The large differences in the nearest neighbor Ti distance stated above is another potential factor in the observed adsorption behaviors. On {111} planes the nearest Ti atoms are 5.47 and 6.50 Å away. These distances are approximately 1.9 to 2.9 Å greater than 3.57 Å which corresponds to the {101} planes. The close proximity of Ti atoms on the {101} planes could significantly reduce the number of 5-coordinated Ti atoms available for adsorption due to either steric or electrostatic interference from neighboring adsorbates. This interference effect would be diminished or non-existent on the {111} planes due to the substantially larger distances between surface Ti's. This characteristic of the {111} planes present on a (101) film is suggested as a possible factor in the improved water and oxygen adsorption characteristics of the (101) films.

5.2.3.2 Surface Chemistry. In addition to the discussion of the numbers and lattice spacing of Ti and O atoms in the rutile lattices presented above, an important analysis revolves around the adsorptive properties and chemical reactions of adsorbates as a function of the oxygen coordination of surface Ti atoms. The surface chemistry which occurs has been related to the surface Ti-coordination for a number of molecules. After faceting into {101} planes which consist only of 5-coordinated surface Ti atoms, the (001) surface has been shown to facet into {114} planes above 1473 K.<sup>128,138,212</sup> {114} planes consist of a mixture of 4-, 5- and 6-coordinated Ti atoms at the surface. Differences in the surface chemistry on {101} and {114} faceted (001) surfaces can then be attributed to the presence of 4-coordinated Ti. Barteau's group has utilized this difference in the study of organic reactions on rutile surfaces. The formation of dimethyl ether from methanol was observed to occur via disproportionation of pairs of methoxides adsorbed at 4-coordinated Ti's on the {114} faceted surface. No dimethyl ether was formed on a {101} faceted surface.<sup>215</sup> Also the formation of acetone via a bimolecular reaction of acetates was observed only on the {114} faceted surface because the reaction involved two acetates adsorbed at the same cation. This requires the presence of a 4-coordinated cation which

was only available on a {114}.<sup>216</sup> This same type of surface chemistry produced formaldehyde from the bimolecular coupling of two formates only on a {114} faceted surface.<sup>217</sup> These types of investigations confirm that the presence of reduced Ti cations are a driving force for increased surface activity, but more importantly they demonstrate that surfaces having reduced cations with lower than 5-coordination can be dramatically more reactive.

The relation of surface Ti-coordination to surface activity has also been applied as a partial explanation for the orientation dependence of photochemical reactions on rutile thin films and faceted single crystals.<sup>210,214</sup> The largest photoactivity differences were observed between (001)- and (100)-oriented films. Although both these surfaces are expected to contain 5-coordinated Ti's in the planar regions of their surfaces, the (001) surface was characterized by a considerably more well-defined structure of {101}-type facets. Recalling that the intersection of {101} facets consist of 3- and 4-coordinated Ti atoms, one interpretation of the data is that these edge sites contribute significantly to the increased photoactivity of the (001) bulk oriented film.

As a degree of confirmation to this analysis, the photochemical reactivities of rutile films grown by MOCVD were tested. Table 5.1 shows the results of the photoactivity test<sup>214</sup> as a function of orientation. The number shown for each orientation is the change in transmittance per second. All light going from the bulb to the photodetector corresponded to 100% transmittance. Upon exposure of a film to the light, as light was absorbed to take part in the reduction of  $\text{Ag}^+$  (from 0.1 M  $\text{AgNO}_3$  solution), the change in the amount of light being transmitted to the photodetector was measured in 0.1s intervals until only 98% of the light was being transmitted. The change in transmittance per second is then a measure of the speed and extent of reaction for the  $\text{Ag}^+$  reduction. Several variables are involved in this reaction. The UV radiation from the light serves to generate an electron-hole pair in the rutile, and both species must take part in a reaction for the process to go forward. The electron reduces the  $\text{Ag}^+$ , and the hole recombines with the excess electron

of the adsorbed  $\text{OH}^-$  from the aqueous solution. The belief of the researchers is that the adsorption of the  $\text{OH}^-$  is the rate limiting step in this photochemical process. The increased amount of Ti surface atoms with lower oxygen coordination would serve as more active sites for water adsorption and increase the extent of reaction.

Table 5.1 A measure of photoreactivity as a function of thin film orientation

Bulk Orientation	Measure of Photoreactivity ( $10^{-5}$ Transmittance / sec)
(101)	$225 \pm 20$
(100)	$147 \pm 10$
(001)	$82 \pm 10$

This interpretation is in excellent agreement with the (101)-oriented film exhibiting both increased adsorption of water and oxygen as a gas sensor and increased photochemical reactivity in the reduction of  $\text{Ag}^+$ . Based on this data the strongest argument for the observed improvement in adsorption characteristics of a (101)-oriented film deposited by MOCVD is the presence of a large number of 3-coordinated Ti atoms in the {111}-type facet planes. These planes were calculated to comprise approximately 80% of the surface area. On the (001) oriented films, Ti atoms with lower than 5-coordination are only found at the intersections of the {101}-type facets which would be present on a very small amount of the surface area. The confirmation of this relationship between surface cation oxygen coordination, gas sensitivity and photochemical reactivity is previously unknown in the literature.

5.2.3.3 Electron Mobility. As mentioned in the results section, the resistance of the (101)- and (001)-oriented films was measured in the same crystal direction, [010], in an

effort to remove any differences in mobility from the analysis. If the samples were single crystals cut from the same boule, this assumption could go unquestioned. These are heteroepitaxial thin films, however, and this assumption warrants more attention. As was shown in Table 2.1, the mismatch in the [010] direction between film and substrate is essentially the same at 5.7 - 5.8%. Perpendicular to this direction there are some distinct differences in the two films. For the (101) film parallel to  $[\bar{1}01]$  the mismatch is only 0.9%, hence the elongation of surface features in that direction. The mismatch along [100] perpendicular to [010] in the (001)-oriented film is much larger at 3.6%. In addition, there is a twin plane parallel to the surface plane in (101)-oriented films. These differences in the structures of the (101)- and (001)-oriented films demonstrate that even though we are measuring in the same crystal direction, some differences in the path(s) which an electron travels in each film still exist.

This poses the question, what difference in electron mobility between the two films would render the adsorption/sensitivity differences measured to be null? Figure 5.10 shows the absolute number of carriers added to the (101) film as a function of increasing mobility. For the assumed mobility value the number of carriers added to the (001) film was  $9.27e8$ .

The data show that an approximate value of  $30 \text{ cm}^2/\text{V}/\text{sec}$  or an over two order-of-magnitude increase in the mobility of the (101) film as compared to the mobility in the (001) film would be required for the observed effect to be only a function of mobility difference between the two films. Even mobility anisotropy in the same crystal is at most a factor of five ( $\mu_c/\mu_a$ ).<sup>87</sup> Based on literature values for mobility in this temperature range being on the order of 0.1 to  $1.0 \text{ cm}^2/\text{V}/\text{sec}$  the (101)-oriented film has a very low probability of having such a large mobility. Therefore, the data suggest that there is a real improvement in the adsorption ability of (101)-oriented rutile thin films deposited by MOCVD compared to (001)-oriented films as indicated by calculated changes in the number of conducting electrons.

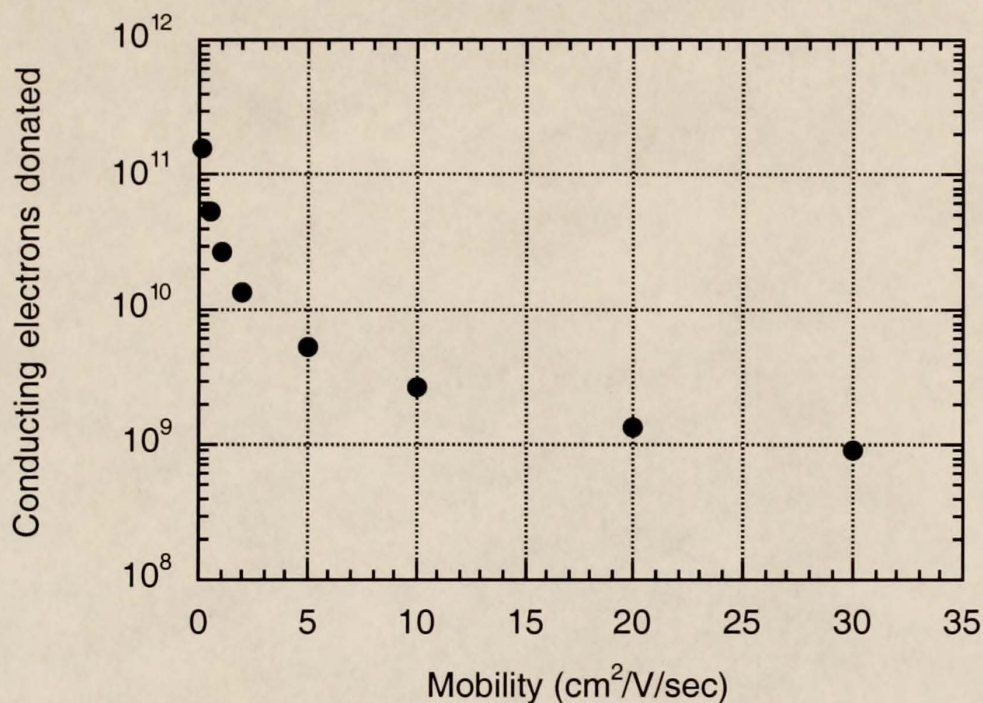


Figure 5.10 Calculated electrons donated to an undoped (101)-oriented film as a function of mobility

#### 5.2.4 (100) Orientation Discussion

According to the data of Figure 5.2, a (100)-oriented film exhibits a greater increase in conducting electrons when exposed to humidity than (101) and (001)-oriented films. Figure 5.1 show its oxygen sensitivity is approximately the same as a (101)-oriented film and better than a (001). Unfortunately, the morphological characteristics of the (100) orientation are too different from those of (101) and (001) and (100) IBSD films to draw any credible comparisons from the data.

Figure 5.11 shows representative AFM images for (100)-oriented films grown by MOCVD and IBSD.<sup>14</sup> The images show that the MOCVD film is very rough and does not exhibit regular surface features like the IBSD film. The rms roughness of the MOCVD film is 158 Å, whereas that of the IBSD film is only 4-5 Å. The surface roughness could contribute to the increased adsorption predicted by the resistance measurements. The (100)

surface is calculated to have 1.5 and 1.3 times more surface area than the (001) and (101) MOCVD surfaces, respectively, according to AFM images.

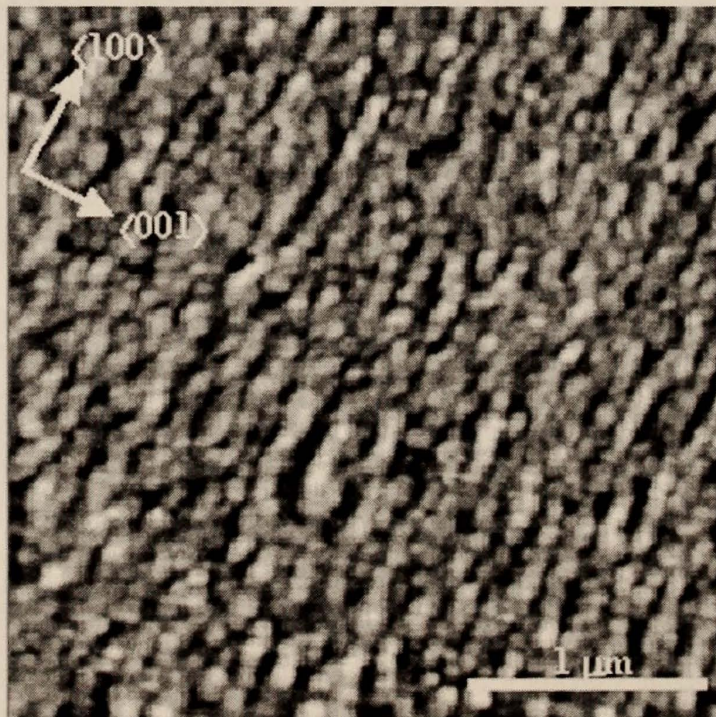
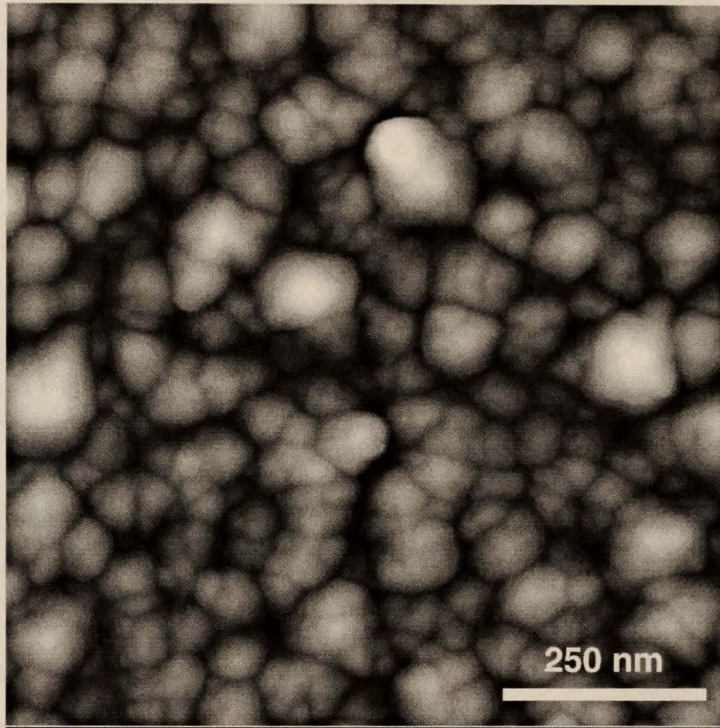


Figure 5.11 AFM images of (100)-oriented rutile films  
(a) deposited by MOCVD (b) deposited by IBSD

A cross-section of the MOCVD AFM image shows that the features are curved and highly variable in size. This is in contrast to the IBSD image where the features are more consistent in size and elongated in a common direction.<sup>14</sup> The faceted surface of the IBSD film consists of island-type structures with well-defined, flat planes. Lowekamp modeled the features as (100) planes having {110} facet steps in the elongated direction and {101} steps perpendicular to elongation.<sup>211</sup> The {110} planes have a mixture of 5- and 6-coordinated Ti atoms, and both {110} and {101} intersections with the (100) plane having 5-coordinated Ti atoms. Morris-Hotsenpiller's photoactivity data correspond well with this model. The (100) orientation was found to be the least photoactive which is in agreement with the absence of less than 5-coordinated Ti atoms even at facet intersections.

If the MOCVD surface facet were identical to that of the IBSD film, the MOCVD film would be much smoother and the Ti atoms would be 5-coordinated. Such a surface should exhibit the same general gas sensitivity as a {101}-faceted (001) surface because the {101} facets also contain 5-coordinated Ti's. With respect to the 5-coordinated Ti surface, Lowekamp predicted a very small area of stability against faceting near the (100) orientation. The faceting of the IBSD (100)-oriented film surface to {110} and {101} planes was suggested to be the result of these planes having low surface energies since the orientation stability diagram does not predict this structure. The orientation stability diagram shows just beyond the area of (100) stability, however, the surface is expected to facet into a combination of (100) and any number of complex planes. The result appears as a curved surface which actually consists of many complex planes with small surface areas. An example of this type of structure has been observed on a faceted single crystal.<sup>211</sup> Neither the surface Ti coordination nor the relative Ti density of this surface with complex facets can be measured or predicted. It is likely that Ti atoms which are less than 5-coordinated exist on these small facets or at their intersections. This is the strongest explanation for the (100)-oriented film having improved adsorption characteristics according to the data.

Another anomaly about the (100) film structure which deserves some discussion is that it contains approximately 5% anatase phase  $\text{TiO}_2$ . Historically, anatase was assumed to have similar electrical properties to rutile. In the last decade research has shown that the source of conduction electrons is a much more shallow donor level in comparison to the 0.6 to 1.0 eV deep oxygen vacancy level in rutile. Thus the conductivity in anatase is generally higher than that of rutile at the same temperature.<sup>218,219</sup> This discovery has motivated research into anatase as a sensor material. There has been particular success in sensing hydrogen, carbon monoxide and methanol.<sup>220-222</sup> The impedance response of the (100) films was, however, found to be singular and symmetric which implies that the conduction path is not crossing high resistance grain boundaries between the two phases. This data suggests that the small amount of anatase material contained in these films is not directly involved in the conduction or sensitivity behavior.

### 5.3 Film Composition Results Summary

Figure 5.12 is a summary plot of the measured resistance values and the calculated number of conducting electrons removed for (001)-oriented undoped, 1 at% Ga-doped, 1 at% Ga-doped thin layer on 0.05 at% Nb-doped ( $\text{Ga}^*$ ), and 1 at% Nb-doped rutile thin films. The resistance values were measured in pure  $\text{N}_2$  ( $\text{PO}_2 < 1\text{e-}9$  atm) and  $1.332\text{e-}3$  atm  $\text{O}_2$  in  $\text{N}_2$  around  $240^\circ\text{C}$ . The data indicate that the largest number of conducting electrons are removed from a Nb-doped film (resistance data points overlap in figure) followed by a film with a thin Ga-doped surface layer. A Ga-doped film shows a marginal improvement in the adsorption of  $\text{O}_2$  as compared to an undoped film.

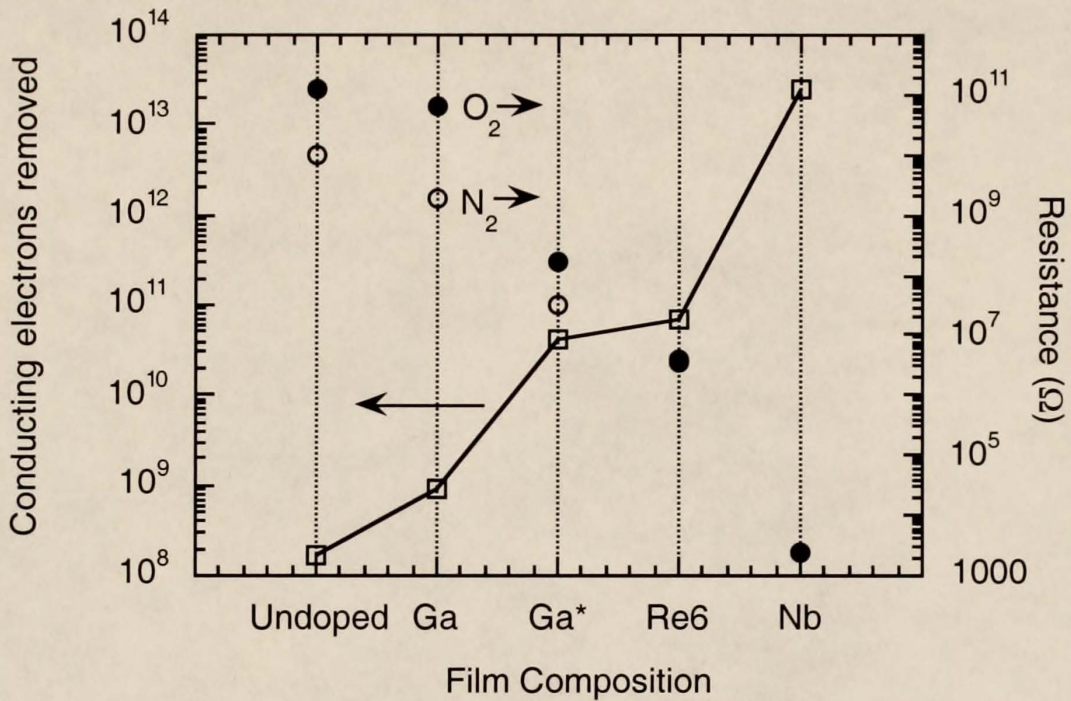


Figure 5.12 Conducting electrons removed as a function of film composition calculated from resistance values measured in N<sub>2</sub> and O<sub>2</sub> atmospheres at 240 °C

Figure 5.13 is a summary plot of the measured resistance values and the calculated number of conducting electrons donated by adsorbed water to the same set of films. The resistance values were measured in pure N<sub>2</sub> and humidified N<sub>2</sub> (saturated, 21°C) nominally at 240 °C. The data indicate that the largest increase in the number of conducting electrons was calculated for the 0.05 at% Nb-doped film with a thin 1 at% Ga-doped surface layer. An increase was measured for a Ga-doped film in comparison to an undoped film. No change in resistance was measured for a 1 at% Nb-doped film upon exposure to humidity, so no "conducting electrons added" data point is shown for that film.

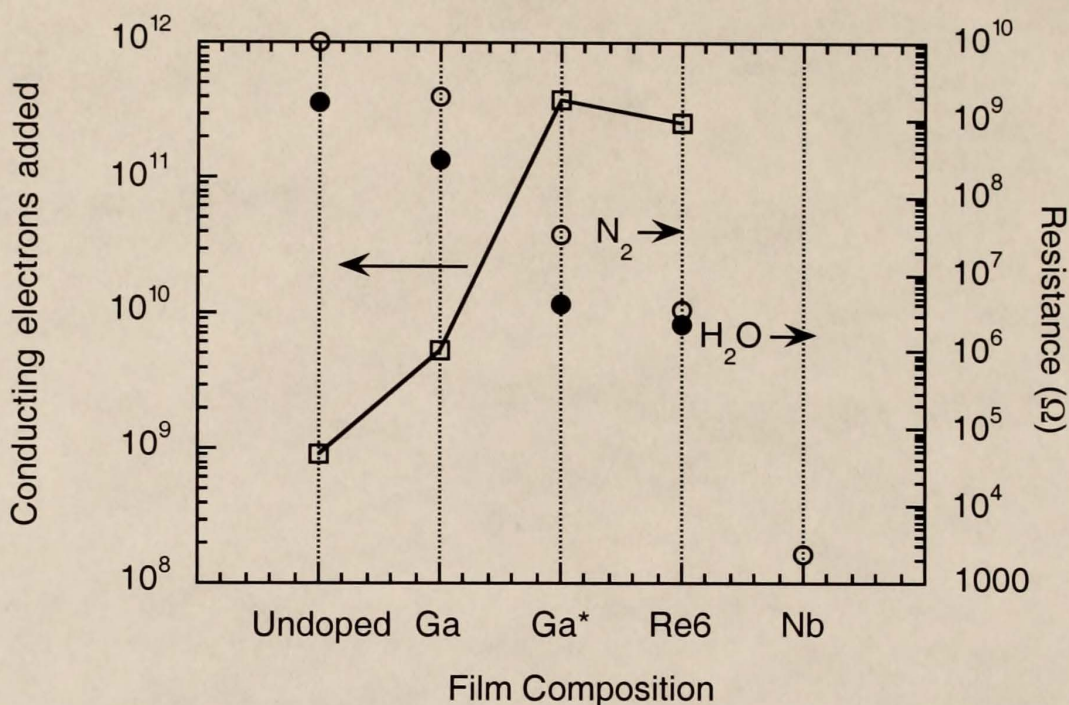


Figure 5.13 Conducting electrons added as a function of film composition calculated from resistance values measured in N<sub>2</sub> and humidified N<sub>2</sub> atmospheres at 240 °C

## 5.4 Nb-doped films

### 5.4.1 Nb-doped Film Results

The (001) orientation of rutile TiO<sub>2</sub> facets into {101} planes which contain two Ti atoms per (4.595 Å x 5.465 Å), resulting in a density of 7.964e14 Ti/cm<sup>2</sup>. The surface dimensions of the thin film tested were 0.22 cm x 0.80 cm. AFM revealed that the linear surface area of bulk (001)-oriented films should be multiplied by a factor of 1.012 to account for the increase in surface area due to roughness making a total of 1.418e14 Ti atoms on the surface of a film. XPS revealed approximately 6.5% Nb on a per Ti basis in the near surface region of a Nb-doped film. This gives a potential 9.22e12 Nb atoms at the film surface.

The resistance value at very low oxygen partial pressure (< 1e-6 Torr) obtained by impedance spectroscopy was 2330 Ω at 240°C. The conductivity calculated by equation

5.1 is  $3.807 (\Omega \text{ cm})^{-1}$ . In order to calculate the desired quantity,  $n$ , from equation 5.2, an appropriate value of the electronic mobility must be known. Frederikse<sup>87</sup> and Bogoroditskii<sup>118</sup> carried out conductivity tests on unreduced, Nb-doped single crystals. Both found that around 225 °C mobility is inversely related to temperature as a function of various scattering mechanisms according to the equation

$$\mu = A T^{-b} \quad (5.5)$$

where

$A$  = proportionality constant

$T$  = absolute temperature

$b$  = constant

and  $A$  is not a function of temperature. Using the data of Bogoroditskii, a value of  $1.85 \pm 0.05$  was found for  $b$  and a value of  $0.58 \pm 0.01 \text{ cm}^2/\text{V}/\text{sec}$  at 298K was found for  $\mu$ . Using these values and equation 5.5 to obtain a value for  $A$ , a value of  $0.23 \pm 0.01 \text{ cm}^2/\text{V}/\text{sec}$  was obtained for  $\mu$  at 498K. A fit of Frederikse's data gives  $b = 1.65 \pm 0.05$  and  $\mu = 0.80 \pm 0.05 \text{ cm}^2/\text{V}/\text{sec}$  at 298K which results in  $\mu = 0.35 \pm 0.07 \text{ cm}^2/\text{V}/\text{sec}$  at 498K. There is a relatively small disagreement between these values, so the value obtained from the data of Bogoroditskii will be carried forward due to the lower associated error.

Equation 5.2 was then used to calculate an electron density of  $1.03\text{e}20 \text{ cm}^{-3}$ . The electron density multiplied by the sample volume,  $3100\text{e}-8 \text{ cm} \times 0.22 \text{ cm} \times 0.80 \text{ cm}$ , gives the absolute number of electrons conducting in the sample,  $5.64\text{e}14$ . The resistance measured at an oxygen partial pressure of  $3.32\text{e}-3 \text{ atm}$  was  $2500 \Omega$ . The corresponding conductivity calculated from equation 5.1 is  $3.55 (\Omega \text{ cm})^{-1}$ .

The measured thermal activation energy of conduction was found to be unchanged within the error value at 0.04 eV before and after exposure of the film to oxygen. Therefore, the same mobility value was used in equation 5.2 to calculate the electron density which is  $9.63\text{e}19 \text{ cm}^{-3}$ . The absolute number of electrons conducting in the sample

was  $5.25 \times 10^{14}$ . If there was no change in the mobility, the difference in conductivity before and after exposure to oxygen is the change in the number of carriers,  $5.64 \times 10^{14} - 5.25 \times 10^{14} = 3.83 \times 10^{13}$ . In contrast, after a twenty-four hour exposure to humidified  $N_2$ , no decrease in resistance was observed.

#### 5.4.2 Nb-doped Films Discussion

5.4.2.1 Oxygen sensitivity. The proposed mechanism by which conducting electrons are removed resulting in the measured increase in resistance, is the adsorption of an oxygen molecule at a surface Nb which serves to trap an electron to complete the Nb-O bond. This is a desirable bond formation for a Nb atom because only four of its five valence electrons are occupied by lattice oxygen atoms in the rutile structure. Otherwise the electron is ionized at a very low activation energy into the conduction band.

The values for the number of electrons accepted by adsorbed oxygen,  $3.83 \times 10^{13}$  and the number of Nb atoms at the surface,  $9.22 \times 10^{12}$ , correspond well. There are a couple of ways that these values may be different which bring them even further into agreement. One is the concentration of Nb at the surface. The value of 6.5% Nb on a per Ti basis obtained by XPS has an error of approximately 1.5% of Nb. A larger amount of Nb at the surface would increase the number of adsorption sites for oxygen, bringing the two values into greater agreement.

Another possibility is that the true surface area of the film as measured by AFM could also be greater. AFM has limitations on the size and type of features it can accurately image. An ideally sharp tip has a lateral imaging limitation of 15 to 25 Å for a recessed feature. The resolution is worse for features which have a positive height dimension. These limitations exert themselves in the rounding of features which in reality have sharp edges. The extreme case would be if a large sloped plane contained many sets of small

steps 10 to 15 Å in size, AFM may only detect a smooth plane losing some actual surface area. An increase in surface area would increase the number of Nb atoms at the surface.

The electronic mobility may be greater than the value used in the calculations. This is the most distinct possibility for bringing the calculated values into complete agreement. Bogoroditskii and Frederikse both performed their studies on Nb-doped single crystal samples. The cutting, polishing and annealing stages of single crystal sample preparation are well-known sources for the introduction of impurities. These are separate from impurities in the molten source from which the original bulk crystal was grown. Impurities act as scattering centers in the crystal which may decrease the mobility. High purity growth is a distinct advantage of thin film deposition when carried out under vacuum using high purity sources. The mobility of the heteroepitaxial, single crystal thin films could therefore be higher than the mobility of bulk grown crystals. A small increase in the mobility from the value of  $0.23 \text{ cm}^2/\text{V}/\text{sec}$  used in the above calculations to a value of  $1.0 \text{ cm}^2/\text{V}/\text{sec}$  results in a value of  $9.0 \times 10^{12}$  electrons accepted by adsorbed oxygen. Such a value is well within the range of mobility data cited in the rutile conductivity literature for undoped films.<sup>82-84,86,88-90</sup> Furthermore, it is idealistic that adsorbing oxygen would have a sticking coefficient of 1.0 with respect to Nb. A higher mobility value in the range of  $1.0$  to  $2.0 \text{ cm}^2/\text{V}/\text{sec}$  decreases the number of electrons removed below the number of surface Nb atoms which allows for an adsorption sticking coefficient of less than 1.0.

5.4.2.2 Humidity sensitivity. No change in resistance was measured upon exposure of the Nb-doped (001) film to humid  $\text{N}_2$ . There are two applicable models which explain this behavior. One is related to the space charge region. Using a combination of XPS and RBS analyses, evidence for the segregation of Nb atoms to the surface was discovered. XPS probes approximately the top 100 Å of the film, and the sensitivity decreases over the 100 Å with depth into the film. The average Nb concentration was observed to be around 6.5 at% on a per Ti basis by XPS. RBS of the same film measured

1 at% Nb through the bulk of the film. The segregation of Nb atoms creates a positive space charge region. The dramatic decrease in resistance of a Nb-doped film makes it obvious that the Nb atoms are electronically as opposed to ionically compensated. The positive space charge region is balanced by a redistribution of the compensating electrons at the surface to maintain overall electroneutrality of the crystal. This concentration of negative charge at the surface is theoretically repulsive to the surface formation and bonding of negatively charged hydroxyls.

A second model proposes that the magnitude of negative charge at the surface is not large enough to repel all hydroxyl adsorption at undercoordinated Ti sites which potentially are still present. Therefore, adsorption occurs and electrons are donated to the conduction band in the same manner as in an undoped film. The number of electrons donated by this mechanism is, however, not large enough to be measured as a decrease in resistance because the resistance is already so low due to electronic compensation of the Nb atoms.

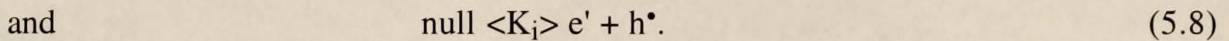
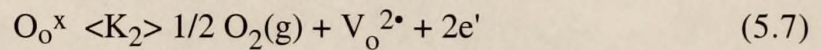
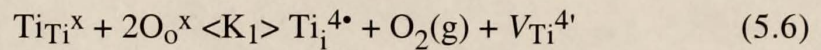
## 5.5 Other Compositions

### 5.5.1 Undoped and Ga-doped Films Results

Figure 5.12 shows that approximately  $7.1 \times 10^8$  more electrons were removed from the Ga-doped film as compared to the undoped film via the surface adsorption of  $O_2$ . Because the resistance values in a partial  $O_2$  atmosphere for undoped and Ga-doped films were so high, the values shown in the figure are extrapolations of data taken above  $240^\circ C$ . Also, on the order of  $4.4 \times 10^9$  more electrons were added to the Ga-doped film by water adsorption at this temperature (Figure 5.13).

### 5.5.2 Undoped Films Discussion

To analyze the sensor data of an undoped film, it is important to understand its conductivity mechanism. Activation energies around 0.8 eV indicate that the source of conduction electrons in the undoped films are oxygen vacancies. The high resistances result in a calculation of very low electron densities which raises the issue of the electrons being from oxygen vacancies created in the bulk or at the surface. Models for calculating the electron density in undoped TiO<sub>2</sub> films have been developed for the following set of equilibrium defect reaction equations discussed in §2.3.2.1, assuming the creation of fully ionized oxygen vacancies and titanium interstitials:



Holes are believed to be a minority defect in this regime, so equation 5.8 is not taken into account in the electroneutrality equation

$$4[\text{V}_{\text{Ti}}^{4'}] + n = 2[\text{V}_{\text{O}}^{2\bullet}] + 4[\text{Ti}_{\text{i}}^{4\bullet}].$$
 (5.9)

The corresponding equations for the equilibrium constants are

$$K_1 = [\text{Ti}_{\text{i}}^{4\bullet}] n^4 \text{PO}_2$$
 (5.10)

and

$$K_2 = [\text{V}_{\text{O}}^{2\bullet}] n^2 \text{PO}_2^{1/2}.$$
 (5.11)

In the limit of  $[V_o^{2\bullet}] \gg [Ti_i^{4\bullet}]$  which is assumed to be the case at 240 °C as discussed above

$$[Ti_i^{4\bullet}] = (K_1/K_2^2) (K_2/4)^{2/3} PO_2^{-1/3} \quad (5.12)$$

and  $[V_o^{2\bullet}] = (K_2/4)^{1/3} PO_2^{-1/6}$ . (5.13)

Marucco and several others have estimated values for  $K_1$  and  $K_2$  from conductivity measurements in the 1000 to 1400 °C range

$$K_1 = 3.3e11 \exp(-10.12 \text{ eV/kT}) \quad (5.14)$$

$$K_2 = 3.0e2 \exp(-4.57 \text{ eV/kT}) \quad (5.15)$$

which are based on the enthalpy of formation for  $[Ti_i^{4\bullet}]$  and  $[V_o^{2\bullet}]$ .<sup>83-85</sup> Figure 5.14 shows the values of  $[V_o^{2\bullet}]$  per mole  $TiO_2$  as function of  $PO_2$  at 240 °C. The corresponding  $[Ti_i^{4\bullet}]$  values are on the order of  $1e-30$  and are obviously negligible in determining  $n$ . The test volume of a 3300 Å thick film contains approximately  $2.75e-7$  moles of  $TiO_2$ . Using the  $[V_o^{2\bullet}]$  value at  $1e-9$  atm  $O_2$  ( $\sim 1e-6$  Torr) in the electroneutrality equation results in  $2.39e4$  electrons as opposed to the  $1.83e8$  conducting electrons calculated from resistance values. The low number of electrons calculated from the defect model indicates that bulk defects may not be the primary source of electrons in these undoped films. The error in extrapolating this high temperature model to 240 °C is, however, unknown and a better fit than has been calculated may exist. One reasonable alternative is that the source of electrons is oxygen vacancies created at or near the surface which have a lower enthalpy of formation. This is discussed later.

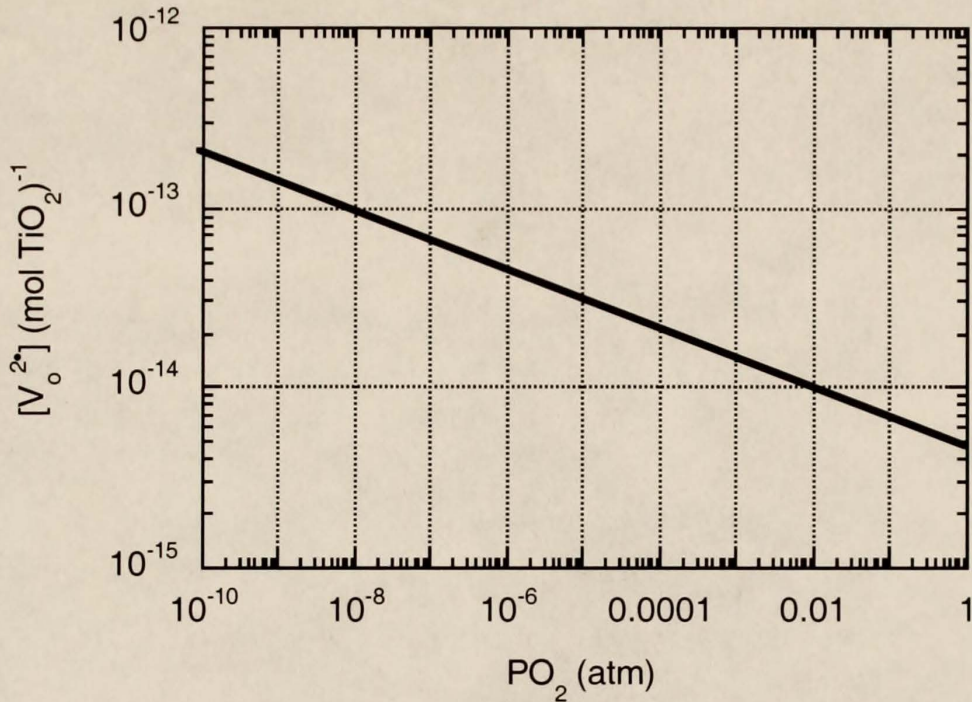


Figure 5.14  $[V_O^{2*}]$  calculation as a function of  $PO_2$  at 240 °C by Marucco model

In the limit of  $[V_O^{2*}] \gg [Ti_i^{4*}]$ , the data of Figure 5.14 show that equations 5.13 and 5.15 are the significant equations for calculating  $n$  from equation 5.9 around 240 °C. Using these equations, Figure 5.15 displays number of conducting electrons calculated at  $1e-9$  atm  $O_2$  for different values of the enthalpy of formation for a doubly ionized oxygen vacancy. Since we are proposing that the electrons result from oxygen vacancies created at or near the surface, the number of electrons is calculated using the moles of  $TiO_2$  in the top 100 Å of the film,  $8.3e-9$ . Figure 5.15 shows that an enthalpy of formation for  $[V_O^{2*}]$  around 3.0 eV is required to produce agreement with  $1.83e8$  conducting electrons calculated from resistance values.

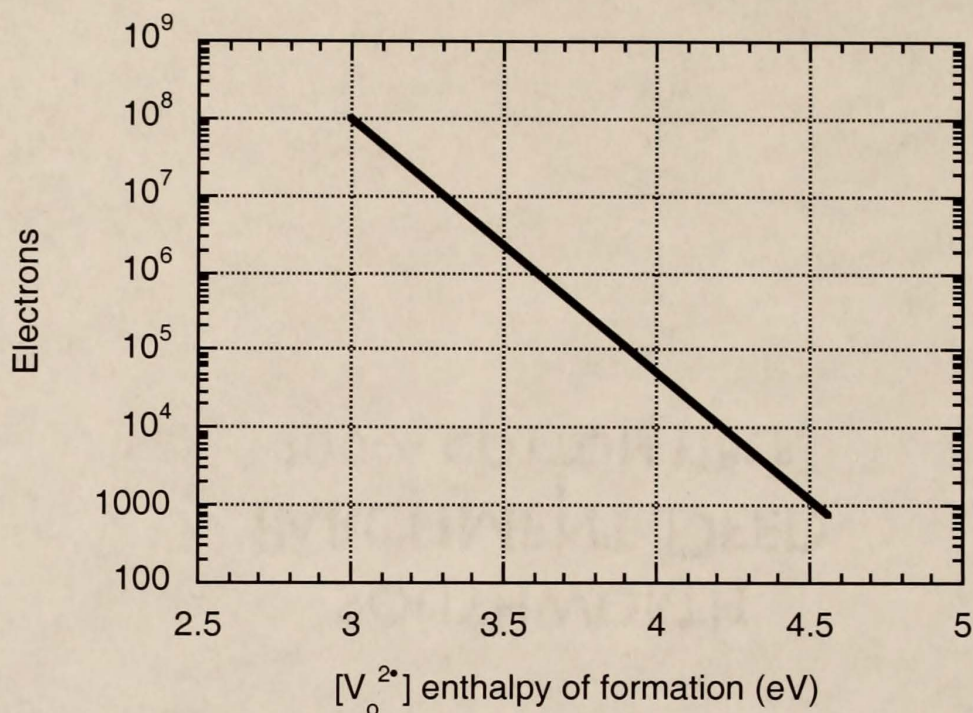


Figure 5.15 Calculated electrons resulting from  $[V_O^{2\bullet}]$  as a function of  $[V_O^{2\bullet}]$  enthalpy of formation

The enthalpy to create point defects in ionic crystals like  $TiO_2$  can be calculated from a Born-Mayer cycle, which involves three steps. They are the creation of charged imperfections in the crystal by removal of ions to the vapor, the transformation of gaseous ions to atoms, and the formation of the compound from the gaseous atoms.<sup>223</sup> Experimental data was found to conform well with this analysis by Fumi et al. for the formation of Schottky defects in  $NaCl$ .<sup>224</sup> Their work showed that the bulk of the total enthalpy of defect formation value is derived from the vacancy creation and migration of an ion through a crystal to the surface. Calculations found that a minimum of 25% of the total enthalpy value results from the migration barrier.

The 3.0 eV value for enthalpy of formation is around 34% less than the 4.57 eV value calculated by Marucco. The model with this enthalpy value also predicts  $9.6e6$  conducting electrons in  $1.332e-3$  atm  $O_2$ . This is in good agreement with  $1.5e7$  conducting electrons, the value calculated from extrapolated resistance measurements in the same  $PO_2$ .

Finally, by calculating  $K_2$  as a function of temperature, a value of  $[V_o^{2\bullet}]$  and hence  $n$  can be calculated as a function of temperature. Knowing that conductivity is proportional to  $n$  via equation 5.2, a plot of  $\ln n$  versus  $1/T(K)$  yields an activation energy of conduction predicted by this model. The value is 1.0 eV which reasonably matches the experimental value of  $0.8 \pm 0.1$  eV. Therefore, based on this model it is suggested that the conducting electrons in undoped rutile thin films at low temperatures are derived from oxygen vacancies created at or near the surface as opposed to in the bulk.

### 5.5.3 Ga-doped Films Discussion

As detailed in §2.3.3.1, acceptor-type dopants such as Ga are expected to incorporate substitutionally. They may be compensated by oxygen vacancies or Ti interstitials. Because many of the first rutile conductivity studies used single crystals which contained low levels of trivalent impurities, conductivity in Ga-doped material is assumed to follow the trend of oxygen vacancy compensation being dominant at low temperatures. Representative literature on the conductivity of Al-doped rutile, another common dopant with a 3+ oxidation state, also observed a transition from oxygen vacancy to Ti interstitial compensation with decreasing  $PO_2$  at temperatures in excess of 1000 °C in agreement with this trend.<sup>80</sup>

XPS measured 4.6 at% Ga on a per Ti atom basis in the near surface region of a Ga-doped film. As shown in the results section for the Nb-doped film, assuming a faceted surface of {101} planes there are  $6.53 \times 10^{12}$  Ga atoms at the surface. The defect equilibrium equation for oxygen vacancy compensation of Ga shows that one oxygen vacancy is created for every two Ga dopant atoms. This results, theoretically, in the creation of approximately  $3.2 \times 10^{12}$  more oxygen vacancies near the surface as compared to an undoped film.

The motivation for doping with Ga was that the large number of oxygen vacancies would increase the number of undercoordinated Ti atoms at the surface which serve as adsorption sites for water molecules. This should result in a significant increase in the amount of water adsorbed and be an improved humidity sensor. Figure 5.13 shows, however, that only  $4.4 \times 10^9$  more conducting electrons were added to a Ga-doped film as compared to an undoped film via water adsorption. As was discussed in more detail in the analysis of orientational effects, adsorption is believed to be enhanced via reduced Ti atoms which are coordinated with four or fewer oxygens. A one-to-one correlation between number of oxygen vacancies and increase in conducting electrons added was, therefore, not expected. A more significant improvement than was observed, however, was expected. Both explanations of the disagreement between theory and experiment and other means of improving humidity sensitivity / water adsorption were investigated.

5.5.3.1 Carbon monoxide sensitivity. One explanation for the lack of observed improvement in the conductivity in the presence of humidity is steric hindrances to water molecule adsorption. The theory is that the two hydrogen atoms of each adsorbed molecule may interfere with the adsorption of molecules at neighboring sites, so that all adsorption sites cannot be utilized. Another explanation is that hindrances may exist to the formation of  $\text{OH}^-$  which is the electron donating species. The water molecule must undergo a surface reaction to form the  $\text{OH}^-$  species. Several possibilities exist. Hydrogen atoms from neighboring adsorbates may bond together and desorb as  $\text{H}_2$ . Also, one of the H atoms may react with an O atom neighboring the adsorption site to form a second  $\text{OH}^-$ . Both of these reaction pathways complicate the transition from adsorbed molecule to electron donation.

To circumvent this problem, carbon monoxide was investigated. This molecule should not suffer from steric hindrances or the need to undergo surface reactions to form an electron donating species. The decrease in resistance upon exposure to CO was, however,

not found to be dramatically different than when a sample was exposed to water. The CO experiments suggest that the lack of observed improvement in electron donation by water after Ga-doping was not due to potential steric hindrances or the need to undergo surface reactions by the water molecule.

5.5.3.2 Sensitivity with other dopants. From a band structure point of view, the problem with acceptor doping to improve sensitivity to a donor molecule lies in the fact that for every oxygen vacancy created to potentially improve adsorption, two traps are introduced by the dopant atoms. Therefore, as charge must flow "downhill" from the adsorbed species into the solid material, donated electrons go into the valence band or traps until the Fermi levels of the adsorbed species and the material are equal. At this point the electrochemical potentials of the material and the adsorbed species are equal and no more charge flows.<sup>225</sup> If the traps are deeper with respect to the conduction band than oxygen vacancies which are argued to be the source of electrons in these films, the increase in number of conducting electrons upon adsorbing water to an acceptor doped as opposed to an undoped film will not be dramatic.

One possible solution to the effect of this deep trap is to use other acceptor dopants whose band gap state may have an energy level more similar to that of an oxygen vacancy or even closer to the bottom of the conduction band. As long as the dopant induced states are lower in energy than that of an adsorbed species, electrons can go immediately into them and then be activated into the conduction band. As discussed in §2.3.3.3, the literature suggests by way of modeling and experiment that different dopant atoms reside at different levels in the band gap.<sup>100,101</sup> Fe has two stable oxidation states, 2+ and 3+, which should have different energy levels from Ga and each other.

An Fe precursor from the TMHD solid precursor family was obtained. Films were grown with 1 at% Fe on a per Ti basis. RBS analysis confirmed the presence of 1 at% of Fe dopant in all three orientations of rutile. This film was tested under dry and humidified

$N_2$  conditions where the resistance near 240 °C was measured to be  $1.70e9 \Omega$  and  $2.40e8 \Omega$ , respectively. Using equations 5.1 and 5.2 and the mobility value derived from Göpel ( $0.17 \text{ cm}^2/\text{V}/\text{sec}$ ), these resistance values result in  $6.36e9$  conducting electrons being added to an (001)-oriented Fe-doped film. Figure 5.16 is a plot of absolute number of conducting electrons added for Fe-doped, Ga-doped and undoped (001)-oriented films. The figure illustrates that Fe-doping caused an inconsequential improvement in the number of conducting electrons added as compared to a Ga-doped film.

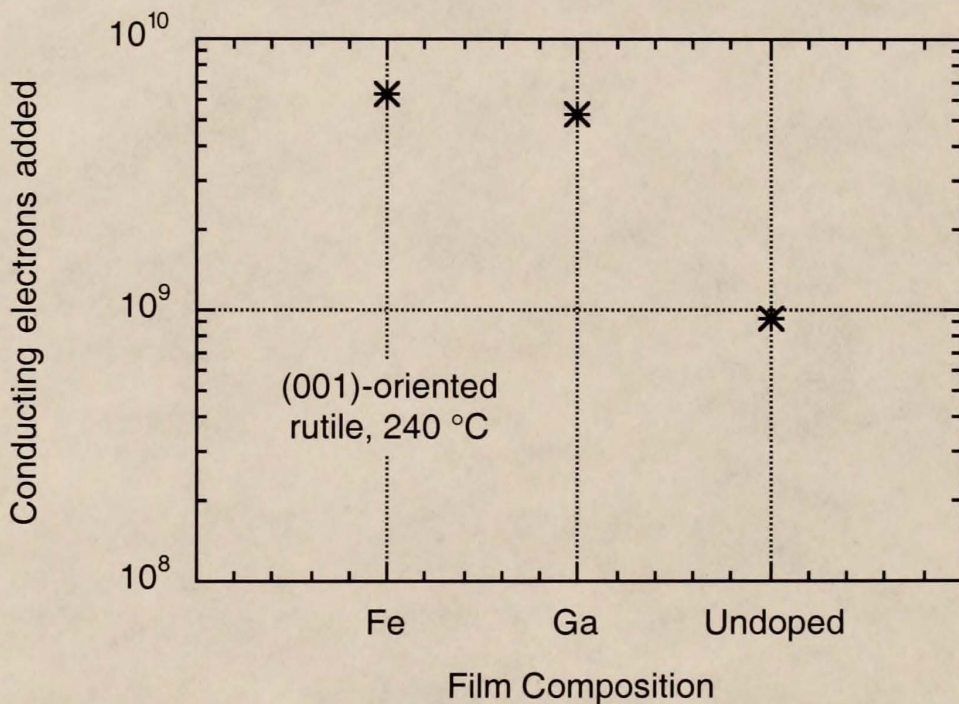
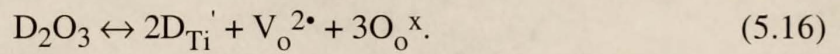


Figure 5.16 Comparison of conducting electrons added by humidity to an Fe-doped film compared to other compositions

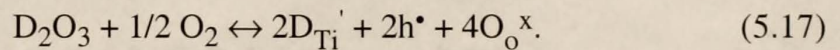
5.5.3.3 P-type conducting films. A second potential solution to improving sensitivity to donating species also relates to this physical model of charge transfer into the material. Ultimately, the lowest energy path of an electron transferring into a material would be to go straight into the valence band. If p-type conductivity were established in a material then electrons donated into the valence band would recombine with the holes, driving a material back toward n-type conductivity. In theory, one could observe greater

changes from adsorption of donor molecules, essentially n-type surface dopants, on a p-type material than on an n-type material.

P-type conductivity has been observed in large rutile single crystal and ceramic samples at high temperatures ( $\geq 800$  °C) and  $O_2$  partial pressures ( $\geq 10$  Torr). These samples contained acceptor dopants such as Fe,<sup>108</sup> Cr<sup>106</sup> and Mn.<sup>109</sup> For each of these dopants (D) stable in a 3+ oxidation state, the substitutional defect incorporation equation as shown previously is



At high  $PO_2$ , p-type conductivity comes about via the hole compensation of an acceptor-type dopant<sup>106,108,109</sup>



The following equation has been suggested for calculating the diffusion coefficient of O in  $TiO_2$ <sup>226</sup>

$$\mathcal{D} \text{ (cm}^2\text{/sec)} = 2e-3 \exp(-60 \text{ kcal / RT}). \quad (5.18)$$

Using this value and a simplified equation for estimating the diffusion time

$$x = (\mathcal{D} t)^{1/2} \quad (5.19)$$

where

t = time (sec)

x = diffusion distance (cm),

Figure 5.17 was created to show the time required to fully diffuse  $O_2$  throughout a  $3300 \text{ \AA}$  thick film. This data readily illustrates why the investigations of conductivity in unreduced rutile samples have been performed over temperature ranges above  $1150 \text{ K}$  and only a little lower for ceramic samples where porosity would be a tremendous aid to diffusion.

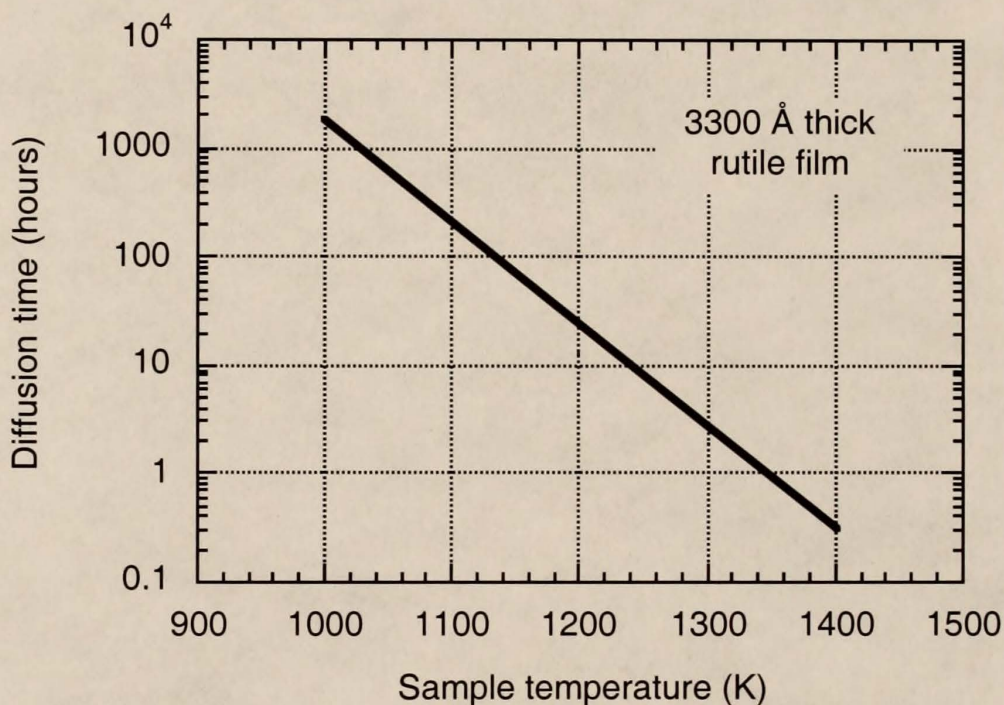


Figure 5.17 Estimated time required for O diffusion through a  $3300 \text{ \AA}$  thick rutile film as a function of temperature

The high temperature required to create a p-type material introduces a number of problems when applied to a rutile film. First, a film is grown around  $925 \text{ K}$ . Taking one above this temperature will increase the amount of interdiffusion between the substrate and film beyond what occurs during deposition. Interdiffusion is essentially increasing the concentration of an acceptor-type dopant, Al, in the first few hundred  $\text{\AA}$  of a film. Second, temperatures greater than  $1000 \text{ K}$  can potentially change the facet structure of a film surface. The (001) surface transitions from  $\{101\}$ -type facets to  $\{114\}$ -type facets around  $1473 \text{ K}$  and possibly lower. This change in a surface would enhance dissociative adsorption independent of n- or p-type conductivity, convoluting the results. The presence

of dopant atoms in a film brings on more problems. The diffusion coefficient of Fe has been measured as approximately  $4.6 \times 10^{-11}$  cm<sup>2</sup>/sec at 1273 K in air.<sup>227</sup> Using equation 5.19, and the 1.9 hours required for O<sub>2</sub> diffusion at 1300 K from Figure 5.17, Fe could diffuse around  $5.6 \times 10^4$  Å. Even if the diffusion coefficient were off by an order of magnitude, all the Fe in a film would have adequate time to move to lower energy positions at the surface or substrate interface. The literature suggests an even higher diffusion coefficient for Cr under the same conditions. These permanent changes in the crystal structure would also make comparing data taken before and after transition to p-type conduction difficult.

In spite of the inherent complications described above, (001)-oriented films doped with Ga, Fe and Cr at 1 at% were tested for p-type conductivity at several temperatures. The experimental conditions with the greatest chance of measuring p-type conductivity were a 700 °C sample temperature with 12 hour equilibration times at increasing PO<sub>2</sub> levels. With a total of over 72 hours between measurements at 0.21 and 0.97 PO<sub>2</sub>, no measurable change in the resistance of a Cr-doped film occurred. This data suggests that the calculation of O<sub>2</sub> diffusivity by equation 5.18 is reasonably accurate. The more significant conclusion is that the resistance changes due to O<sub>2</sub> exposure reported for film temperatures near 240 °C in this thesis are the results of changes in the very near surface region of a film.

5.5.3.4 Adsorption enhancement by a thin surface layer. The data reported for conducting electrons added by donor molecule adsorption on acceptor-doped films suggest that the large number of acceptor states (electron traps) negate the enhanced adsorption sites (undercoordinated Ti atoms) created by the increased number of oxygen vacancies. Another potential solution to this problem is to change only the very near surface region

with a thin acceptor-doped layer. This design dramatically decreases the overall number of acceptor states in a film while still increasing the number of surface oxygen vacancies and correspondingly the number of undercoordinated Ti's.

To maintain the comparability of the various donor molecule sensitivity enhancement strategies discussed thus far, an (001)-oriented rutile film was grown. The film was 0.05 at% Nb and nominally 3300 Å thick. On top of this, a nominally 80 Å thick 1 at% Ga-doped layer was grown. The motivation for growing the film with 0.05 at% Nb was to provide a source of electrons to compensate some portion of the deeper traps which would allow more of the electrons donated by adsorbed humidity to be activated to the conduction band from more shallow traps.

The impedance characteristics of the film were measured using an identical procedure as for all other films. The data suggest that the number of conducting electrons donated by adsorbed water appreciably increased as compared to undoped, Ga-doped and Fe-doped (001)-oriented films. Figure 5.18 shows the number of conducting electrons added as a function of composition where Ga\* denotes the film with only a Ga-doped surface layer.

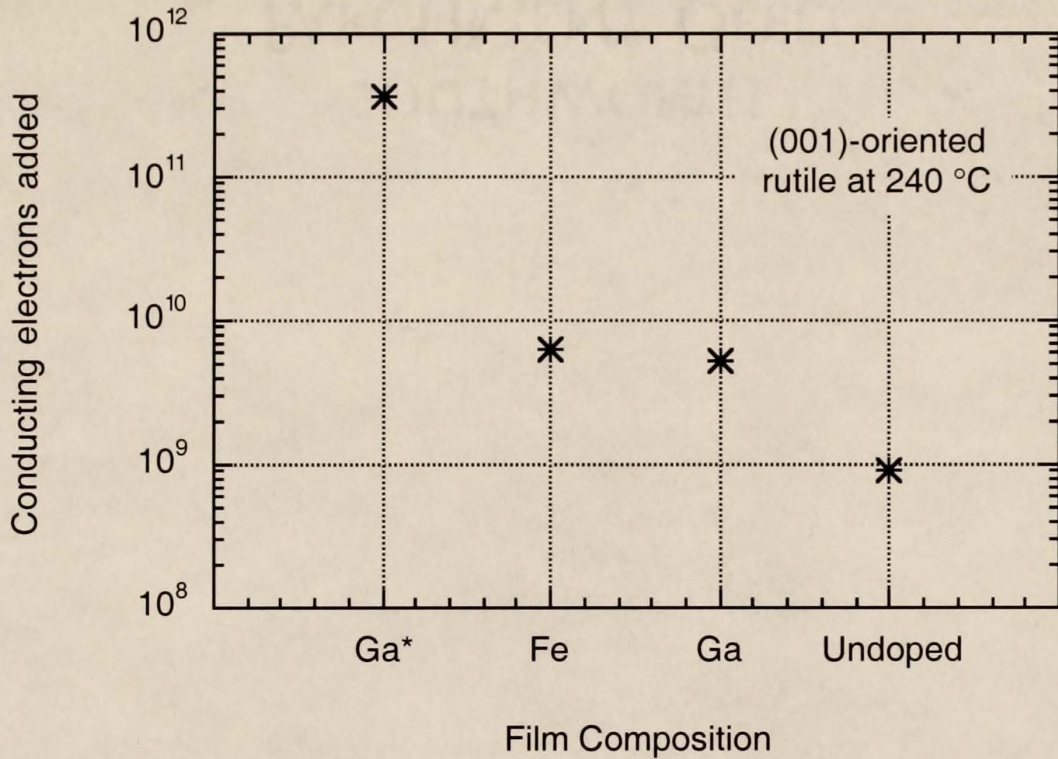


Figure 5.18 Comparison of conducting electrons added by humidity to a film with a Ga-doped surface layer (Ga\*) to other compositions

The UHV studies discussed in §2.3.4 suggest that the presence of undercoordinated Ti atoms should enhance the dissociative adsorption of any molecule which utilizes these sites. The effect of adsorbed oxygen on the number of conducting electrons should therefore be increased for this layered material as well. Figure 5.19 shows this to be the case. Although the decrease in number of conducting electrons is substantially less than what was observed for a Nb-doped film, the increase is still considerable in comparison to both undoped and Ga-doped films. This finding is significant because the  $O_2$  adsorption mechanism for Ga\* is proposed to be the same as for a Ga-doped or undoped film--via undercoordinated surface Ti atoms. In contrast,  $O_2$  adsorption is suggested to occur on surface Nb atoms of a Nb-doped film which improves adsorption and conducting electron removal by an alternative mechanism (§5.2.2).

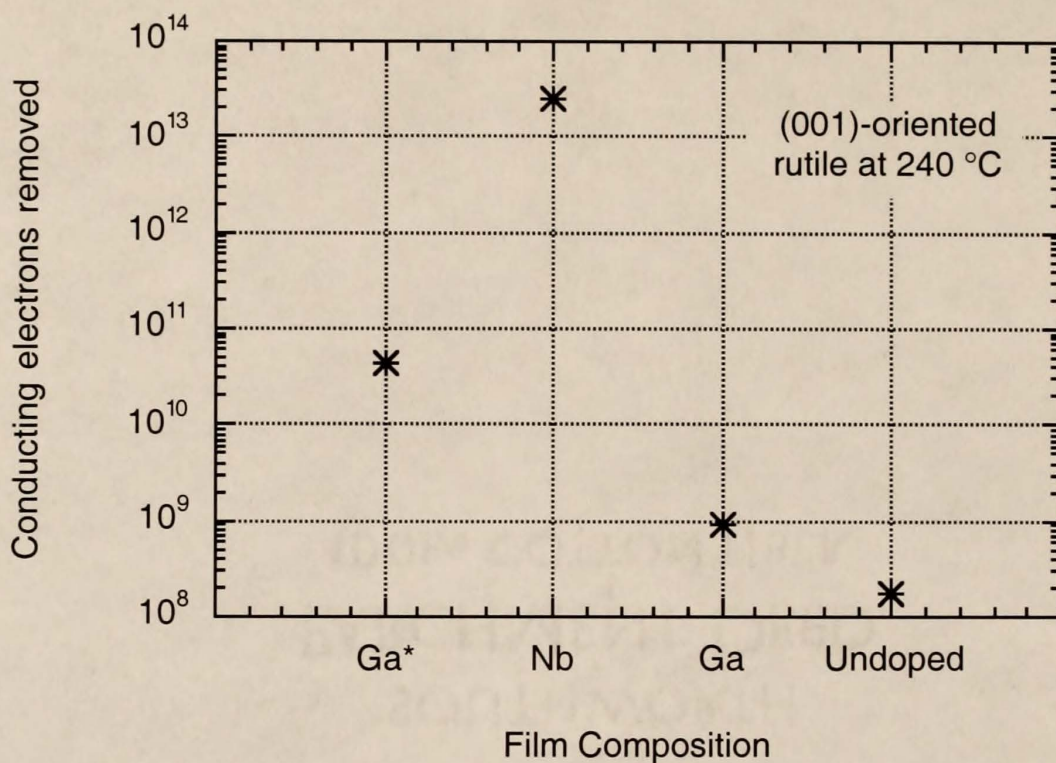


Figure 5.19 Comparison of conducting electrons removed by oxygen from a film with a Ga-doped surface layer (Ga\*) to other compositions

5.5.3.5 Adsorption enhancement by film reduction. In an effort to complete this analysis of adsorption enhancement via the creation of undercoordinated Ti atoms at the surface, undoped films which were reduced prior to testing were investigated. Reducing a film via the removal of O atoms by  $H_2$  at elevated temperatures should produce a population of surface Ti atoms which are less than 5-coordinated without introducing a deep level trap in contrast to acceptor-doping.

Two films were created for this investigation. Each was reduced by the following procedure. A film was placed in a 1.25 in. diameter quartz tube with o-ring sealed gas inlet and outlet. The quartz tube was placed in a horizontal furnace with the same diameter as the tube and approximately 18 in. long. The tube was flushed with five cycles of filling with high-purity  $N_2$  and evacuating for 20 seconds with house vacuum to minimize the  $O_2$  concentration.  $N_2$  containing 3.66%  $H_2$  was flowed through the tube at 150 sccm. The furnace was heated from room temperature to 500 °C in approximately 30 minutes. One

film was left at these conditions for 6 hours and another for 12 hours. Both films were cooled under continuous flow at the natural cooling rate of the furnace with no current. A little over 2 hours was required for the furnace temperature to fall below 100 °C, and the films were removed when the temperature was nominally 50 °C.

To maintain comparability with the previous changes in film composition, (001)-oriented films were used for this reduced film investigation. The procedure substantially reduced the films as shown in Figure 5.20 by the resistance values measured around 240 °C in a pure N<sub>2</sub> atmosphere. Resistances can be compared because the same contact geometry was used for the two reduced films (Re6, Re12) and an unreduced film (U). Before analyzing the responses of these films to humidity and O<sub>2</sub>, an analysis of the differences in their impedance spectra and activation energies is valuable. Figure 5.20 also shows the calculated activation energies (§5.2.2.2) for the reduced and unreduced films. One interpretation of the data is that Re6 represents a transition from an unreduced to a heavily reduced film. The link between activation energy and the source of conduction electrons is generally not analyzed in the rutile conductivity literature, and the sensor literature normally fails to even calculate an activation energy. The large and small activation energies for unreduced and reduced samples shown here are in agreement with the rutile conductivity literature summarized in Table 2.5. As was discussed in §5.2.2.1, the activation energies measured for unreduced samples agree with oxygen vacancy energy levels from various measurements and models. Linking the rutile conductivity literature for reduced samples and models of the oxygen vacancy energy levels in the reduced samples also produces a compelling explanation for the measured activation energies for reduced samples. Yu and Halley<sup>92</sup> extended their highly accurate model of electronic structure of rutile containing a single oxygen vacancy or titanium interstitial to multiple vacancies. The model predicted that when two oxygen vacancies shared the same octahedron surrounding a Ti atom, a new level was created at 0.22 to 0.26 eV below the conduction band. The actual depth of the level was a function of the two vacancies being at opposite or adjacent

vertices. This new donor level is in excellent agreement with the activation energy measured for Re6 and the H<sub>2</sub> reduced sample of Kim et al. from room temperature to 350°C.<sup>82</sup> An extension of this multiple oxygen vacancy defect level could be that more than two oxygen vacancies clustered in the same octahedron produces another even more shallow donor level. This extrapolation of the model would explain the activation energies below 0.1 eV found here for Re12 and those reported for other heavily reduced samples.<sup>87,89</sup> Unfortunately, electronic structure models for such highly complex lattice distortions have not been developed. An alternative explanation for the small activation energies of highly reduced samples is that the activation energy for electrons is much smaller than measured so that the conduction band has an essentially constant number of carriers. The activation energy measured would then be attributed to the mobility indicative of a "hopping" process for polaronic conduction. This mechanism was suggested by one study cited in Table 2.5, but the reported activation energy of the polaron was larger than the activation energy reported for conduction.<sup>87</sup>

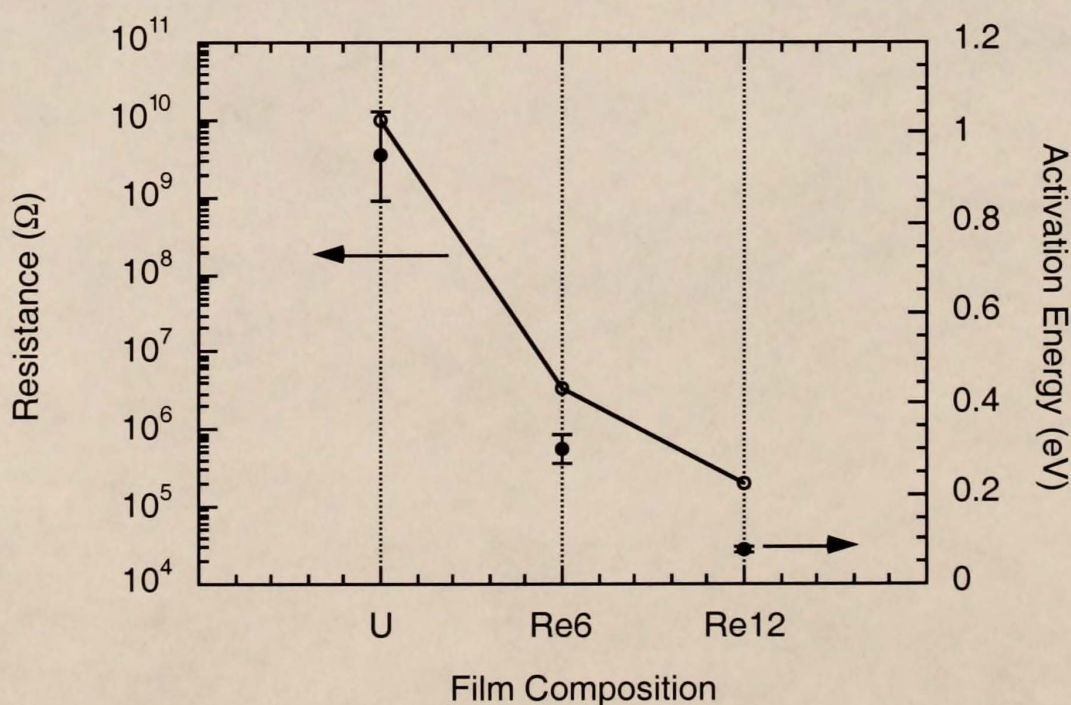


Figure 5.20 N<sub>2</sub> atmosphere resistance values measured at 240°C and calculated activation energies for (001)-oriented, reduced and unreduced samples

Whereas the spectra from which all previous data have been derived were symmetric, the spectra of Re6 was slightly depressed and that of Re12 was significantly depressed. Figures 5.21 and 5.22 show the spectra for the three atmospheres for Re12 and Re6, respectively. The peaks of Re12 spectra are depressed by approximately 15% and those of Re6 by approximately 5%.

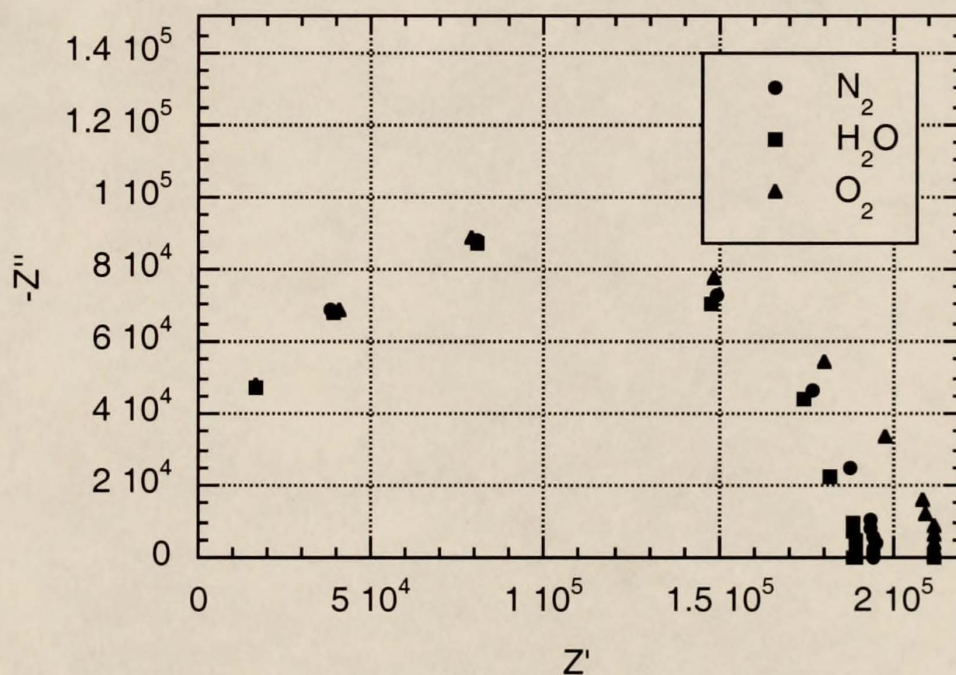


Figure 5.21 Impedance spectra as a function of atmosphere at 240 °C for (001)-oriented rutile film reduced 12 hrs in H<sub>2</sub> at 500 °C

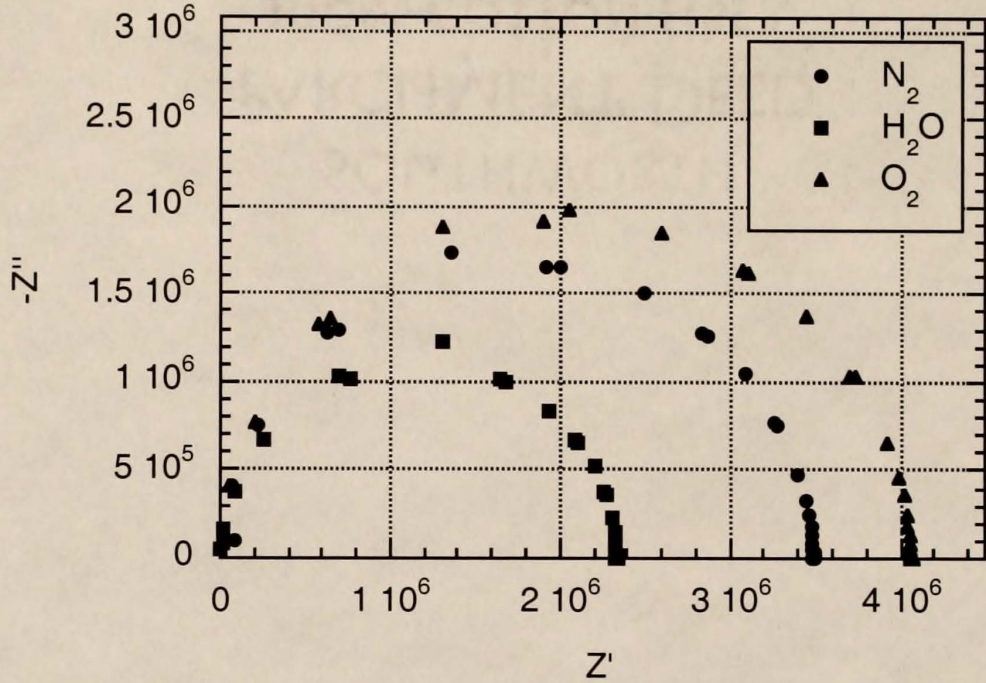


Figure 5.22 Impedance spectra as a function of atmosphere at 240 °C for (001)-oriented rutile film reduced 6 hrs in H<sub>2</sub> at 500 °C

A number of causes exist for non-ideal responses in electrochemical impedance measurements. For these thin films the most likely causes are non-uniform current distribution or two elements in series each consisting of a parallel resistor and capacitor. Given that Re12 has a very low resistance, it is possible that the current flows along paths not directly between the electrodes. Some portion of the film may also be more heavily reduced so that the current distribution is uneven. The equivalent circuit of the device could be represented by two elements, each a resistor and capacitor in parallel. If both elements had similar capacitances, their individual responses could be indistinguishable and represented by one depressed semicircle. As discussed in §5.2.1, a separate low-frequency response was observed for one type of sample and ascribed to the electrode-material barrier. In that case, however, the electrode had been aged by temperature cycles, and the resistance was less than  $1e4 \Omega$ . The significant depression of Re12 therefore appears to be the result of a non-uniform current distribution.

With the resistance values taken from the impedance plots, equations 5.1 and 5.2 were used exactly as for previous materials to calculate changes in the number of conducting electrons upon exposure to humidity or  $O_2$ . Figures 5.23 and 5.24 display those changes for  $O_2$  and humidity, respectively, for both reduced films, an unreduced film, and the film with a thin Ga-doped surface layer ( $Ga^*$ ).  $Ga^*$  was included because of its greatest success in both atmospheres for changes via the under-coordinated Ti adsorption site mechanism as compared to other compositions presented thus far.

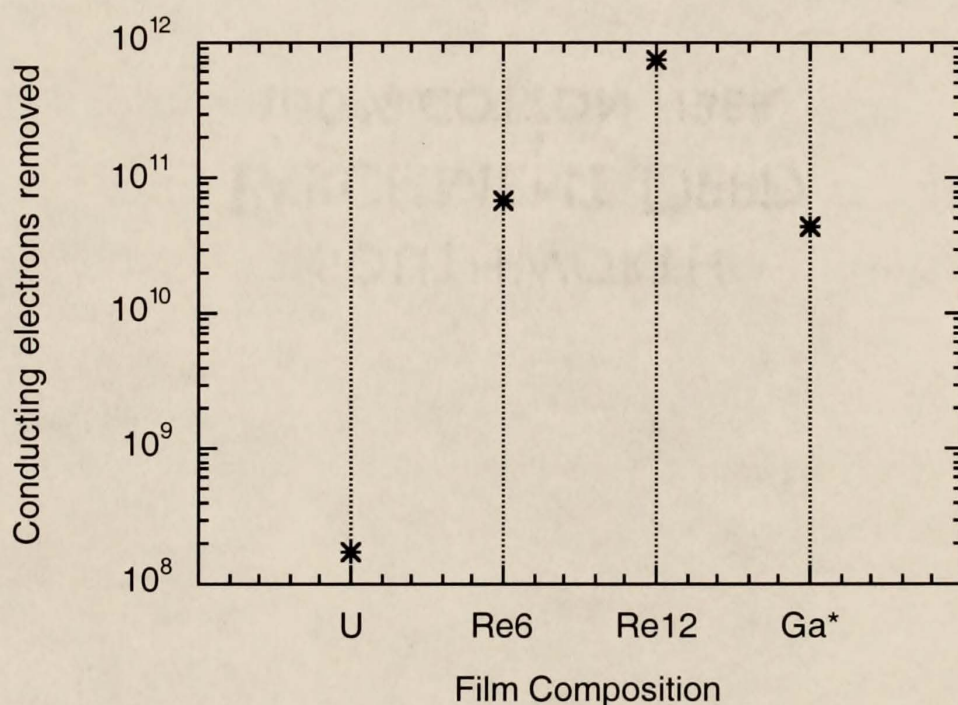


Figure 5.23 Comparison of conducting electrons removed by oxygen from reduced films to other compositions

Figure 5.23 exhibits that a large number of conducting electrons were removed from Re6 and Re12, comparable to and than  $Ga^*$ . Because of its substantially lower activation energy, more electrons are in the conduction band and thus available for removal from Re12 by adsorbed  $O_2$  is no surprise. Likewise, Figure 5.24 shows that equivalent numbers of conducting electrons were added to both reduced films and  $Ga^*$ .

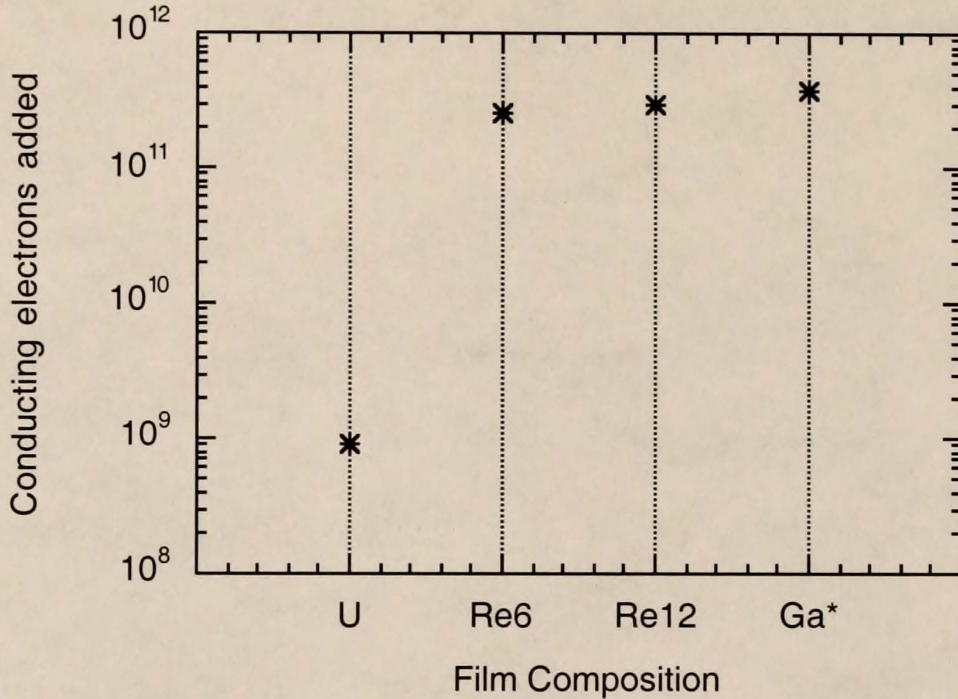


Figure 5.24 Comparison of conducting electrons added by humidity to reduced films to other compositions

As was discussed in reference to other compositional changes, adding electrons to a conduction band from an adsorbed donor molecule is a two step process. Electrons must enter a state of lower energy than they possess in the adsorbed species to transfer into a material. They can then be activated into the conduction band. The dominance of shallow donor states which provide a large number of electrons to the conduction band of Re12 do not enable the addition of a larger number of donated electrons into the conduction band in comparison to Re6 and Ga\*. An obvious explanation is that these most shallow levels are higher in energy than the adsorbed species. Donated electrons can therefore only take advantage of the deeper levels which correspond to those found in Re6. The physical model being Ti octahedra with two or fewer associated oxygen vacancies.

Ultimately, the reduced samples have successfully demonstrated a second means by which the number of active adsorption sites can be dramatically increased. Oxygen vacancies were created by removal of oxygen with  $H_2$  at an elevated temperature. This

reduction created Ti atoms which were coordinated to four or fewer O atoms. Equivalent surface Ti atoms were created to compensate the acceptor-type dopant but only in the near surface region where the vacancies are useful. This approach served to minimize the overall number of deep acceptor states created by the dopant. When present in larger numbers, these acceptor states had previously negated the effect of the oxygen vacancies.

#### 5.5.4 Mobility and Composition

The use of the same mobility value to calculate the changes in the number of conducting electrons for each composition is an assumption which deserves further explanation. A review of the literature and known trends for dopant effects on mobility in rutile show that the calculations are actually a conservative estimate of what has been proposed to occur in these films. The value of  $0.17 \text{ cm}^2/\text{V}/\text{sec}$  was taken from Göpel<sup>91</sup> who suggested equation 5.3. This equation was derived from approximately forty investigations of both reduced and unreduced samples. These sources represent the majority of rutile conductivity literature published prior to 1988, and very little has been done in this area in the ensuing time period. Göpel's summary makes a couple of important suggestions. First, the mobilities in reduced samples are not appreciably different from unreduced samples. Second, many of the early investigations performed circa 1955 on single crystals were afflicted by acceptor-type impurities such as Al. This compositional change also did not cause substantial fluctuations in the mobility.

An inverse temperature dependence suggests mobility is controlled by scattering mechanisms. What ever changes in mobility might occur from the introduction of dopants should be a decrease because dopant atoms represent scattering centers in comparison to Ti atoms. If mobility is decreased,  $n$  calculated from equation 5.2 is increased. Calculated changes in the number of conducting electrons would then be even larger than suggested as compared to undoped, unreduced material.

### 5.6 Engineering Sensitivity Assessment

For the application of sensors, sensitivity is the primary factor of interest. Although the thin films discussed in this work were designed as an investigative tool, it is important to assess their behavior with respect to engineering definitions of sensitivity. The majority of the engineering sensor literature defines sensitivity (S) as

$$S = R / R_0 \quad (5.20)$$

or 
$$S = (R - R_0) / R_0 \quad (5.21)$$

where

$R_0$  = resistance in initial atmosphere

and

R = resistance after perturbation of atmosphere

for gases which increase the resistance. The inverses of equations 5.20 and 5.21 are normally used for gases which decrease the measured resistance.

Figure 5.25 shows the sensitivity of undoped (001)-oriented (previously designated "U" in composition diagrams of this chapter) and (101)-oriented, 1 at% Ga-doped, 1 at% Nb-doped, 1 at% Ga-doped surface layer (Ga\*) and 6 hour reduced (Re6) (001)-oriented films to  $1.332 \times 10^{-3}$  atm O<sub>2</sub> calculated by equation 5.20. The equation and the figure make it obvious that, as in the case of 1 at% Nb-doping, the adsorption properties can be overenhanced to the detriment of engineering sensitivity. The most applicable sensors are those which exhibit large changes in resistance with changes in atmosphere. Also, the resistance change should fall in an easily measurable value range. Whereas, both

orientations of undoped films, Ga and Ga\* fulfill the first criteria, only Ga\* changes over a resistance range,  $3.35e7$  to  $1.70e8 \Omega$ , which is measurable with common AC or DC instruments. Figure 5.26 shows the sensitivity to humid  $N_2$  calculated by the inverse of equation 5.20 for the same set of samples, less Nb which exhibited no sensitivity to humidity (§5.4.2.2). Again Ga\* meets both criteria along with a (101)-oriented undoped film.

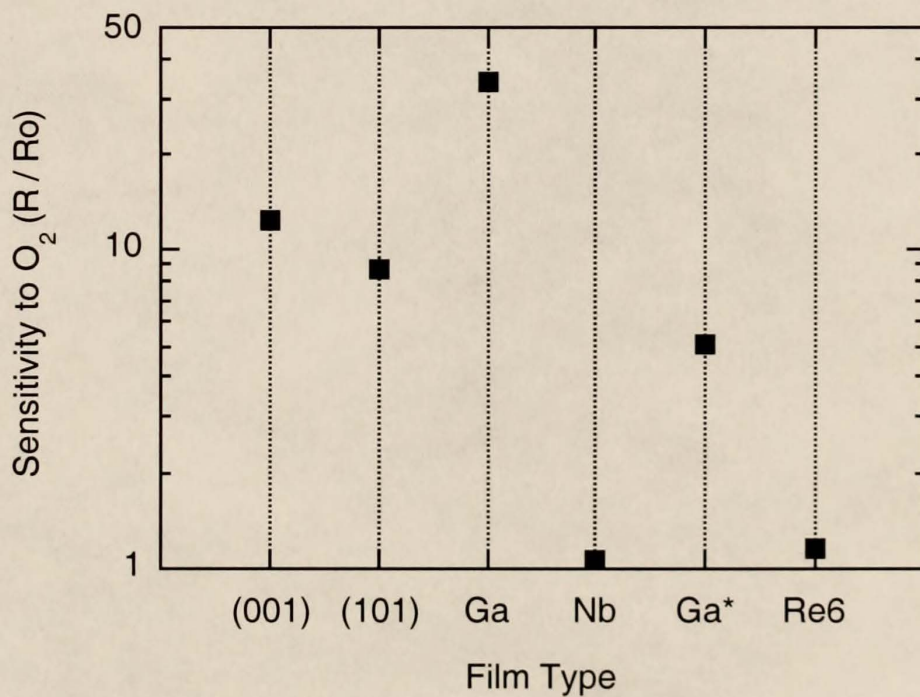


Figure 5.25 Sensitivity of various films to the introduction of  $1.332e-3$  atm  $O_2$  (R) to an atmosphere of less than  $1e-10$  atm  $O_2$  ( $R_0$ )

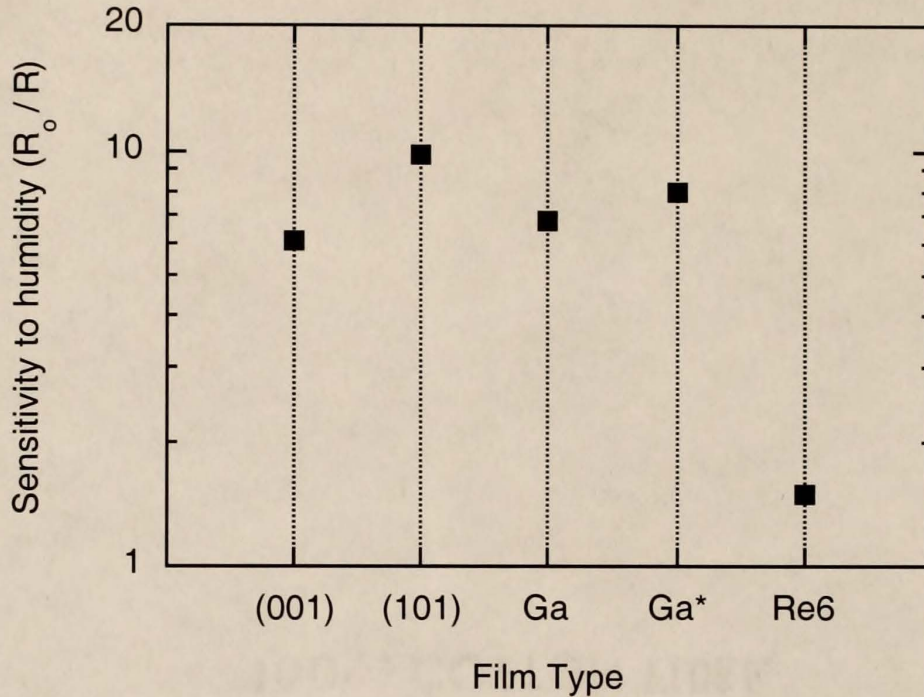


Figure 5.26 Sensitivity of various films to the introduction of humid  $N_2$  ( $R$ ) to an atmosphere of dry  $N_2$  ( $R_0$ )

The problem with equations 5.20 and 5.21 is that they are environmentally dependent, but there is no indication of that dependence in the equations. For example, the literature often shows plot of sensitivity to a gas as a function of device temperature without explicitly noting the initial and final conditions of the environment in which the resistances were measured. Comparisons of actual material or device sensitivity performance are, therefore, very difficult. This problem suggests that possibly a more valid equation for easing comparison of sensitivity performance would be

$$S = R / [R_0 (P_G - P_{G0})] \quad (5.22)$$

where  $P_{G0}$  and  $P_G$  are the initial and final partial pressure of a gas which increases the measured resistance, respectively. This value plotted as a function of partial pressure more accurately displays the sensitivity to large and small changes in a gas concentration without requiring excessive effort on the part of the reader. This quantity plotted as a function of

temperature need have only an inset defining  $P_{G0}$  and  $P_G$  to allow immediate comparison to other materials tested over a similar range. There are still no end of problems with making legitimate comparisons among the materials and procedures reported in the sensor literature. A simple change from the widely accepted equation 5.20 to equation 5.22 is suggested as a means of increasing the literature value to a researcher or device engineer.

### 5.7 Summary

The gas sensor properties of each undoped film orientation and (001)-oriented films with various compositions were investigated. Impedance spectroscopy was used to obtain resistance values of the actual materials, as opposed to a material-electrode barrier, as a function of temperature and environment. From the resistance values, conductivities and activation energies were calculated. These numbers were then used to calculate overall changes in the number of conducting electrons as a function of changing environment.

The results on gas sensor behavior presented as a function of bulk film orientation and changing composition were explained by a general mechanism. The presence of enhanced adsorption sites for oxygen or water corresponded to an increase in electron acceptance from or electron donation to a material, respectively. Enhanced adsorption sites on rutile films for both oxygen and water were created in several ways. First, the natural coordination of titanium at surface facet planes and intersections. The presence of three-coordinated titanium atoms on the {111}-type facet planes of a (101)-oriented film surface resulted in increased adsorption in comparison to an (001)-oriented film where titanium atoms coordinated to four or fewer oxygens were present only at facet intersections. Second, the oxygen vacancy compensation of Ga dopant atoms lowered the oxygen coordination of titanium atoms on an (001)-oriented film surface. Third, the same effect was created by removing oxygen with hydrogen at an elevated temperature. The confirmation of this relationship between surface cation oxygen coordination and gas

sensitivity which was supported by photochemical reactivity measurements is previously unknown in the literature.

A separate mechanism was proposed for the dramatic enhancement of oxygen adsorption on a Nb-doped film. Conductivity and activation energy measurements suggested that the donor-type dopant atom introduced a band gap state approximately 0.04 eV below. The shallow donor state resulted in an excessive number of conduction electrons in comparison to an undoped film. This characteristic was proposed to enhance the adsorption of acceptor-type molecules.

Ultimately, comparisons between the behaviors of materials on which enhanced adsorption sites were created and the traditional calculation of sensitivity (ratio of initial and final resistance values) for those same materials was very informative. The comparison suggested that both adsorption and resistivity must be optimized to engineer an ideal gas sensor. The sensor created with a thin, Ga-doped surface layer on top of a film doped with 0.05 at% Nb was created to demonstrate this idea of tailored materials. The thin Ga-doped surface layer served to enhance water adsorption through the creation of undercoordinated Ti atoms. The 0.05 at% Nb dopant concentration lowered the bulk resistance to a more readily measurable range ( $\sim 1e7 \Omega$ ) without reaching a value where the resistance could not be significantly changed by electron donation using the number of available adsorption sites on the film's surface.

## CHAPTER 6 METAL OXIDE FILM DEPOSITION

A series of growth experiments were carried out in the quartz reactor to investigate the deposition of metal oxides other than  $\text{TiO}_2$  from solid precursors. Using the growth conditions detailed in §3.1.1,  $\text{Ga}_2\text{O}_3$  was deposited using  $\text{Ga}(\text{TMHD})_3$  from the TMHD precursor family which was described in §3.1.2.  $\text{Al}_2\text{O}_3$  was deposited using  $\text{Al}(\text{TMHD})_3$ .

### 6.1 Gallium Oxide

As described in §2.4.1,  $\text{Ga}_2\text{O}_3$  has been investigated as a material for high temperature gas sensors. Any form of  $\text{Ga}_2\text{O}_3$ , amorphous or crystalline, will begin transitioning to the  $\beta$ -crystalline structure above  $800^\circ\text{C}$  in  $\text{O}_2$ . This material characteristic demands that a high temperature device be of the  $\beta$ -phase prior to application. Figure 6.1 (a) is an oblique schematic of the  $\beta$ - $\text{Ga}_2\text{O}_3$  unit cell. Because the unit cell is monoclinic and consists of a large number of atoms arranged in distorted tetrahedra and octahedra, the ball and stick representation shown here was not found in the literature. Ga atoms are represented by the smaller, black balls. Figure 6.1 (b) shows the same unit cell with the b-axis perpendicular to the page. The combination of these two figures adequately communicates the atom placement within and complexity of this unit cell. The literature has reported the deposition of amorphous  $\text{Ga}_2\text{O}_3$  as an insulating layer on  $\text{Si}$ <sup>149</sup> and the deposition of amorphous<sup>228</sup> and unidentified, non- $\beta$ -phase polycrystalline films<sup>152</sup> on sapphire as gas sensors.

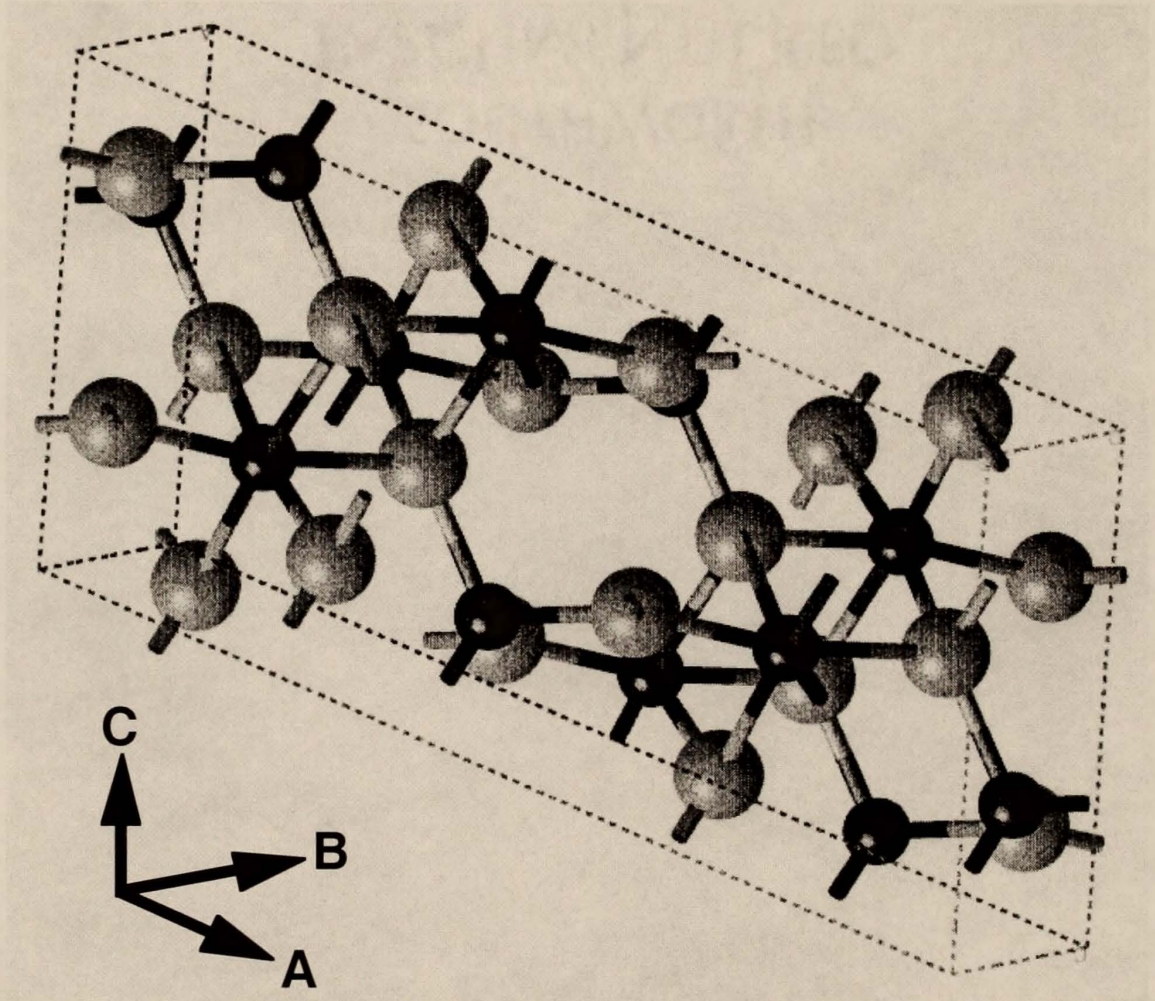


Figure 6.1 Schematic of  $\beta$ - $\text{Ga}_2\text{O}_3$  unit cell  
(a) Oblique

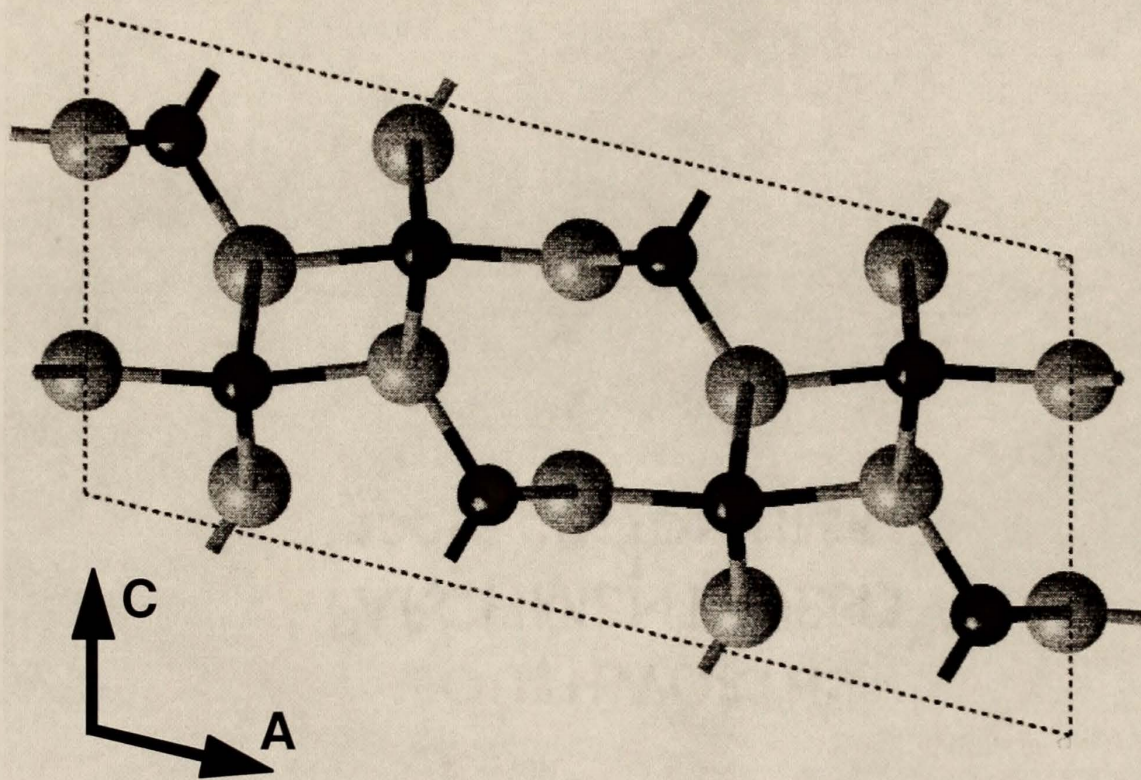


Figure 6.1 (continued) Schematic of  $\beta$ - $\text{Ga}_2\text{O}_3$  unit cell  
(b) Normal to b-axis

At a  $\text{Ga}(\text{TMHD})_3$  partial pressure of 2.2 mTorr and total pressure of 5.5 Torr,  $\text{Ga}_2\text{O}_3$  films deposited at a rate of  $11.7 \pm 0.8 \text{ \AA}/\text{min}$  with no significant substrate or temperature effect at 600 and 700 °C substrate temperatures. The lack of a temperature effect suggests that deposition took place under mass transfer limited conditions. Table 6.1 is an XRD data summary for the  $\text{Ga}_2\text{O}_3$  films grown.

Table 6.1. Summary of Ga<sub>2</sub>O<sub>3</sub> growth from Ga(TMHD)<sub>3</sub> precursor

Substrate	Substrate Temp. (°C)	Film Cryst. Orientation†	θ RC FWHM†
(0001) Al <sub>2</sub> O <sub>3</sub>	600	( $\bar{2}01$ ), ( $\bar{3}11$ )	0.78°, 0.55°
	700	( $\bar{2}01$ ), ( $\bar{3}11$ )	0.74°, 0.68°
(11 $\bar{2}0$ ) Al <sub>2</sub> O <sub>3</sub>	600 - 700	amorphous	---
		( $\bar{2}01$ ), (111)	
(111) Si	600	( $\bar{3}11$ )	0.18°
	700	( $\bar{3}11$ )	0.18°

\*P<sub>O<sub>2</sub></sub>=2.5 Torr, P<sub>Ga(TMHD)<sub>3</sub></sub>=2.2 mTorr, P<sub>Tot</sub>=5.5 Torr, 300 sccm total flow rate He + O<sub>2</sub>

†Values for unannealed films.

RBS revealed that stoichiometric Ga<sub>2</sub>O<sub>3</sub> films were deposited on (11 $\bar{2}0$ ) and (0001) sapphire. The primarily amorphous films deposited on the (11 $\bar{2}0$ ) sapphire were annealed for one hour at 800 °C in air in an attempt to increase the amount of crystalline material. XRD of the annealed films revealed a small amount of crystalline material which could only be attributed to Al<sub>22</sub>Ga<sub>2</sub>O<sub>34</sub>, a hexagonal unit cell compound resulting from interdiffusion at the film-substrate interface. In contrast, XRD identified peaks whose intensities were much larger with respect to the sapphire peak in films deposited on (0001) sapphire. Comparison of the XRD spectra to the published peak data for all phases of Ga<sub>2</sub>O<sub>3</sub> confirmed that oriented ( $\bar{2}01$ ) and ( $\bar{3}11$ ) β-phase material was deposited. The presence of differently oriented grains resulted in their relatively large mis-alignment perpendicular to the plane of the film as shown in Table 6.1. The θ rocking curve (rc) full-width-at-half-maximum (fwhm) values of the ( $\bar{2}01$ ) peak (2θ = 18.907°) and the ( $\bar{3}11$ ) peak (2θ = 38.371°) are greater than 0.5° for both films. Comparison of the spectra at the two growth temperatures showed several small, broad peaks only in the film grown at 700

°C. These peaks were identified as different phases of aluminum gallium oxide, and the consequences of their presence is a broadening of the  $(\bar{3}11)$  rc peak. The appearance of the corresponding higher order XRD peaks,  $(\bar{6}03)$  and  $(\bar{6}22)$ , was further evidence that these were  $\beta$ -Ga<sub>2</sub>O<sub>3</sub> films. XRD of similar films annealed at 800 °C in air for one hour revealed a decrease in the peak heights corresponding to the  $(\bar{2}01)$  and  $(\bar{3}11)$  reflections and the emergence of a new peak which was not representative of a  $\beta$ -Ga<sub>2</sub>O<sub>3</sub> orientation. The peak was found to be a result of Al<sub>22</sub>Ga<sub>2</sub>O<sub>34</sub> formation as in the case of the annealed film deposited on  $(11\bar{2}0)$  sapphire.

RBS analysis also showed that stoichiometric Ga<sub>2</sub>O<sub>3</sub> films were deposited on (111) Si at 600 and 700 °C substrate temperatures. Analysis of the XRD spectra showed that  $(\bar{3}11)$  oriented  $\beta$ -phase material was again present in the as-deposited films without annealing. As a further confirmation, the films were annealed in air at 800 °C for one hour. The peaks which appeared to correspond to  $(\bar{3}11)$   $\beta$ -Ga<sub>2</sub>O<sub>3</sub> and its associated higher order reflection  $(\bar{6}22)$  increased in size by approximately 30% and no new peaks were found as a result of the annealing. Values of 0.18° for the fwhm of the  $\theta$  rc of the  $(\bar{3}11)$  peak are shown in Table 6.1 for films deposited at both temperatures. These values indicate that the as-grown,  $\beta$ -phase crystalline material was highly oriented perpendicular to the growth plane of the film. An increase in the peak size after annealing indicates that the as-grown films consisted of partially amorphous-phase material.

To better understand how deposition of the observed orientations on (0001) sapphire and (111) Si occurred, the relative surface energies of the  $(\bar{2}01)$  and  $(\bar{3}11)$  planes were investigated using the three monoclinic unit cell facial planes for comparison. At equilibrium, metal oxide surfaces are oxygen terminated. Comparing the density of dangling oxygen bonds at those surfaces is a method for estimating their relative energies,<sup>96</sup> and an orientation with a low surface energy preferentially deposits in the absence of other influences. This statement is represented by Young's equation

$$\gamma_{sv} = \gamma_{fs} + \gamma_{vf} \cos\theta \quad (6.1)$$

where  $\gamma$  is the interfacial tension, and f, s and v represent film, substrate and vapor, respectively. A low surface energy corresponds to a low vapor-film interfacial tension.<sup>5</sup>

Because the monoclinic unit cell of  $\beta\text{-Ga}_2\text{O}_3$  consists of both octahedrally and tetrahedrally coordinated Ga atoms, the Cerius<sup>2</sup> molecular modeling system from Molecular Simulations Inc. was used to create images of the oxygen terminated surfaces of interest. The density of oxygen dangling bonds determined from these images is shown in Table 6.2. The relative energies of the (100) and (001) surfaces, and likely others, are smaller than the  $(\bar{2}01)$  and  $(\bar{3}11)$  surfaces which suggests that forces in addition to surface energy affected deposition.

Table 6.2 Dangling bond densities of surface oxygen atoms

$\beta\text{-Ga}_2\text{O}_3$ Orientation	Dangling O Bonds ( $\text{\AA}^{-2}$ )
$(\bar{3}11)$	0.187
$(\bar{2}01)$	0.193
(100)	0.170
(010)	0.239
(001)	0.161

If surface energy is not the dominant force for oriented growth, it is likely to be a relationship between the film and substrate crystal lattices. In rutile  $\text{TiO}_2$  deposition, the oxygen sublattice matching has been shown to be the motivating force for oriented growth on sapphire and  $\text{SrTiO}_3$ .<sup>42</sup> To perform the same analysis on these  $\beta\text{-Ga}_2\text{O}_3$  films, the oxygen terminated surface images mentioned above were also created for the substrates.

For (111) Si, XRD revealed the presence of a (211) oriented layer of "high" or  $\beta$ -quartz which was taken to be the true deposition surface. Each of the film and substrate images was used to create an image of the oxygen lattice parallel to the surface. The mismatch was found to be  $\leq 6\%$  in at least one direction for each  $\text{Ga}_2\text{O}_3$ -substrate pair. This value is comparable to the mismatch observed for the cited rutile deposition (Table 2.1, §2.1.3). The lower energy (001) and (100) surfaces do not exhibit any short-range oxygen sublattice matching, so the analysis in total suggests that film-substrate relationships played a greater role than surface energy in determining the  $\beta$ - $\text{Ga}_2\text{O}_3$  film orientation.

Having established the deposition of  $\beta$ -phase crystalline thin films, AFM was employed for the investigation of each film's surface roughness and morphologies. Figures 6.2 (a) through 6.2 (d) show the normal and phase contrast micrographs for the  $\text{Ga}_2\text{O}_3$  films on (0001) sapphire. The phase contrast micrographs allow a much more distinct observation of the extent of surface faceting. A comparison of Figures 6.2 (a) and (b) of the film grown at 600 °C to Figures (c) and (d) of the film grown at 700 °C brings an immediate conclusion that the 700 °C film has a much more highly faceted surface. The film deposited at 700 °C is also smoother with an RMS roughness of 51 Å and has a generally smaller average surface feature dimension of 1750 Å compared to 144 Å and 6600 Å, respectively, for the 600 °C film. Theoretically, by arguments of increased atomic mobility, one would expect a film grown at higher temperatures to have larger surface features indicative of larger grains. The presence of secondary aluminum gallium oxide phases which originated at the film substrate interface, however, inhibited the growth of larger grains during deposition at 700 °C. The faceting which is clearly shown in Figure 6.2 (d) as compared to Figure 6.2 (b) is an effect of increased atomic mobility at the higher deposition temperature. Faceting occurs when crystal planes lower in energy than the surface crystal plane are formed as a means of lowering the overall surface energy of the film.

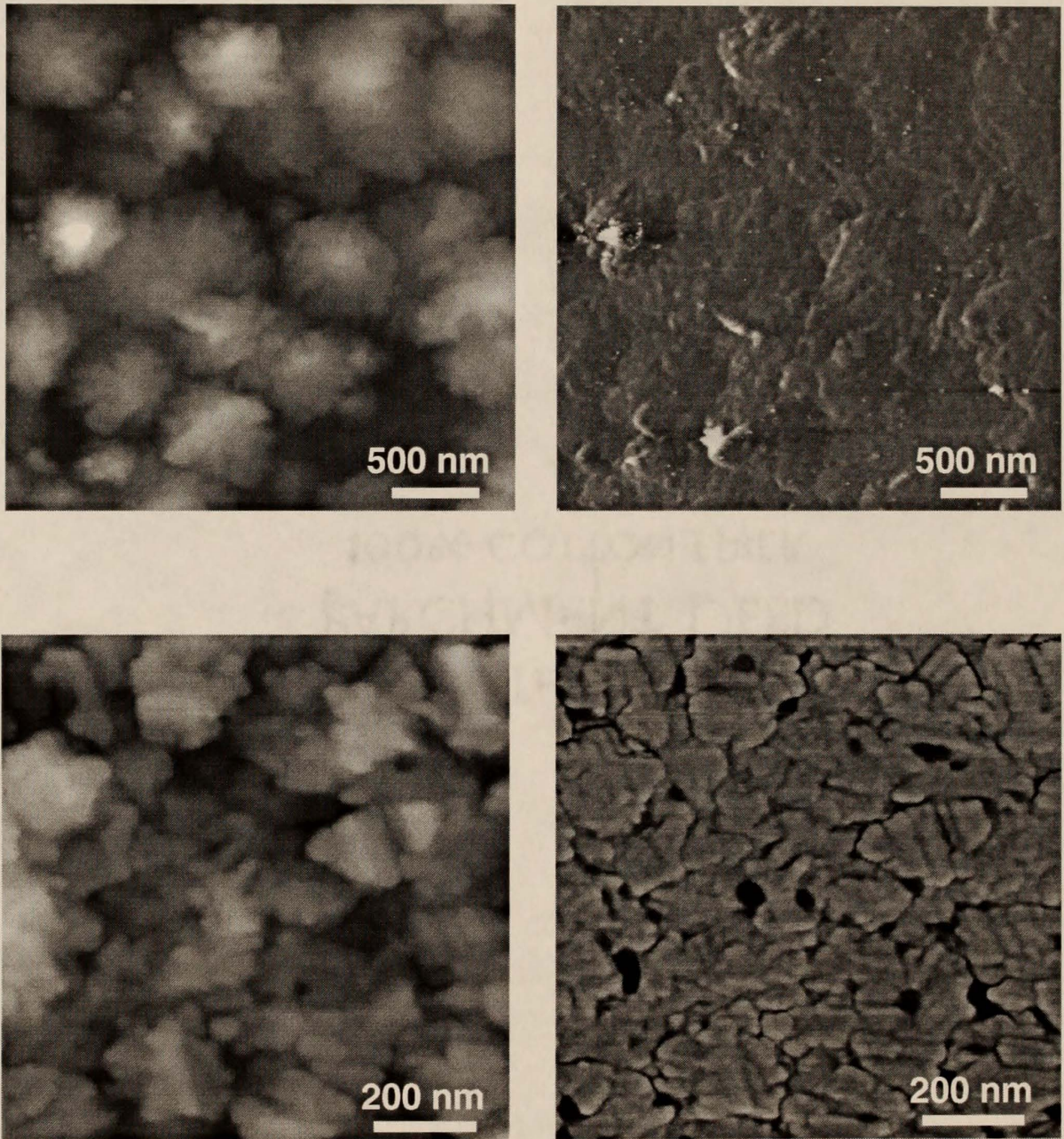


Figure 6.2 AFM images of  $\beta$ -Ga<sub>2</sub>O<sub>3</sub> deposited on (0001) sapphire  
(a) 600 °C deposition, normal image (b) 600 °C deposition, phase contrast image  
(c) 700 °C deposition, normal image (d) 700 °C deposition, phase contrast image

Figures 6.3 (a) through 6.3 (d) show the normal and phase contrast micrographs for the  $\text{Ga}_2\text{O}_3$  films on (111) Si. As in the case of the films grown on (0001) sapphire, a comparison of Figures 6.3 (a) and (b) for the film grown at 600 °C to Figures 6.3 (c) and (d) for the film grown at 700 °C reveals an increased amount of faceting on the surface for the higher temperature deposition. The average grain size at both temperatures is around 115 nm. The most interesting insights to be gained from these films grown on Si come from making comparisons to a film grown at 700 °C which has been annealed at 800 °C for one hour in air. Figures 6.4 (a) and (b) are 1  $\mu\text{m}$  normal mode and phase contrast micrographs of the annealed film. A careful study of Figure 6.3 (d) finds a high number of much smaller features between the larger, faceted grains. These smaller features appear to be far less abundant in Figure 6.4 (b) and there is a corresponding increase in average grain size to 145 nm. These small features are believed to be amorphous material, and if so, their decrease in density in the annealed film is in excellent agreement with the XRD data which showed a 30 % increase in the amount of crystalline material in the annealed film.

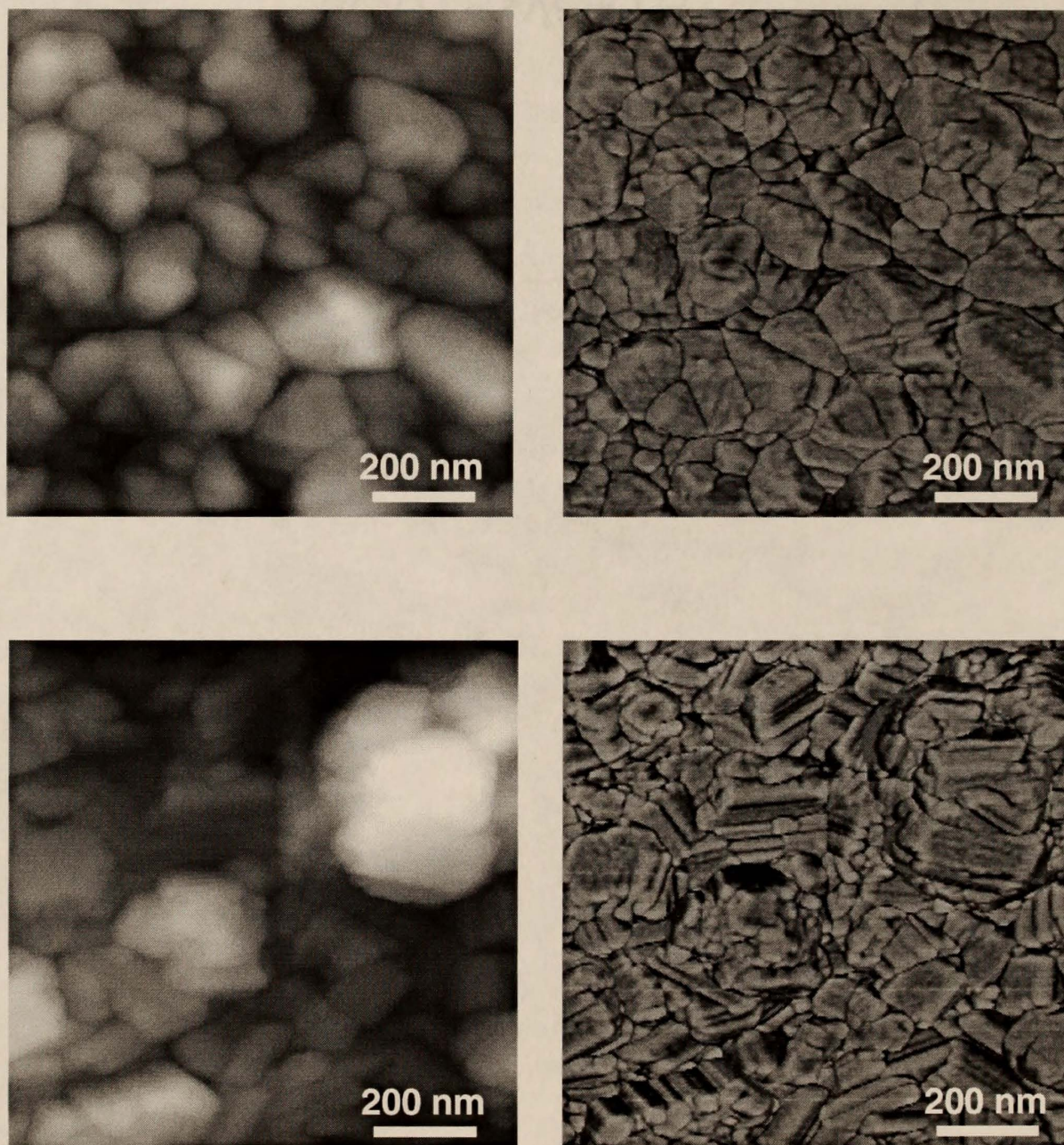


Figure 6.3 AFM images of  $\beta$ -Ga<sub>2</sub>O<sub>3</sub> deposited on (111) Si  
(a) 600 °C deposition, normal image (b) 600 °C deposition, phase contrast image  
(c) 700 °C deposition, normal image (d) 700 °C deposition, phase contrast image

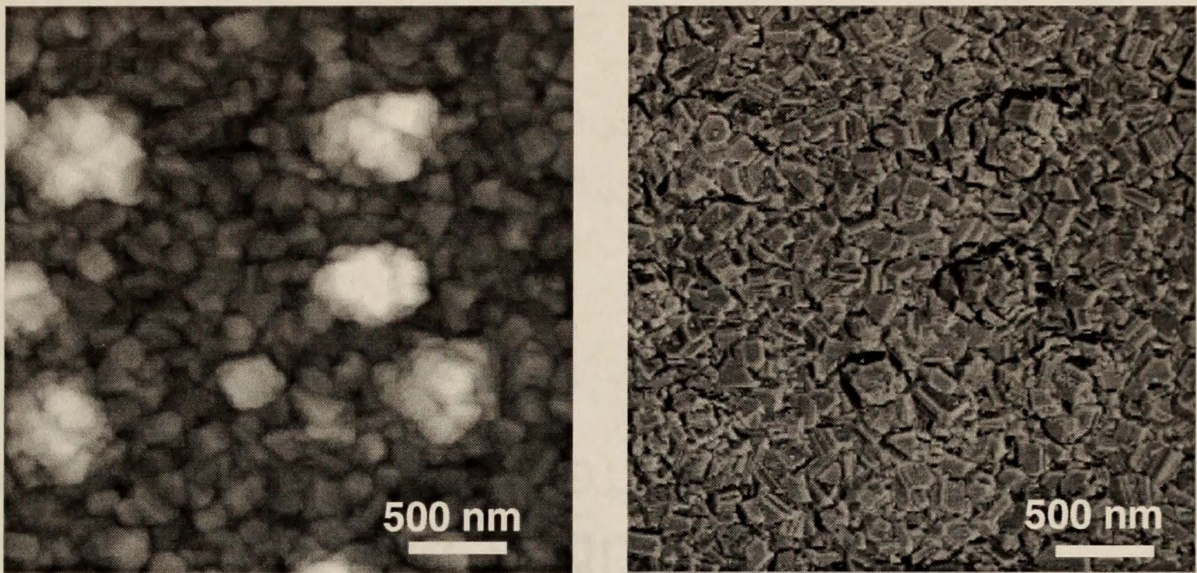


Figure 6.4 AFM images of  $\beta$ -Ga<sub>2</sub>O<sub>3</sub> deposited on (111) at 700°C and annealed at 800°C in air for one hour (a) normal image (b) phase contrast image

Finally, the preponderance of large features rising high above the films' surfaces shown in Figures 6.4 (a) and (b) strongly indicate that deposition proceeded by an island-type growth mechanism. The largest features stand as much as 1800 Å above the average plane of the films which is over 60 % of the average thickness found by RBS. This topography indicates that adsorbing material during deposition was more strongly bound to itself than the substrate surface. Also, the surface area is substantially increased which is a desirable characteristic for applications such as gas sensors.

## 6.2 Aluminum oxide

Al<sub>2</sub>O<sub>3</sub> has been widely applied as an insulating layer in electronic devices.<sup>161-163</sup> The electrical properties of amorphous films have been identified as satisfactory for the majority of these applications. If the goal, however, is to deposit a semiconducting layer on top of the insulating layer, the insulating layer must be crystalline with a consistent orientation parallel to the growth plane. The growth of such a high-quality film of  $\gamma$ -Al<sub>2</sub>O<sub>3</sub>

on (111) Si by molecular beam epitaxy at 750 to 900 °C substrate temperature has been reported by Ishiwara, et al.<sup>229</sup> Their substrates were pretreated by the Shiraki method<sup>230</sup> and the thin layer of native oxide was removed by heating in the growth chamber at 850 °C for 15 minutes.

At a nominal Al(TMHD)<sub>3</sub> partial pressure of 2.2 mTorr, crystalline  $\alpha$ -Al<sub>2</sub>O<sub>3</sub> films were deposited on (111) Si at a rate of  $6.2 \pm 0.5$  Å/min with no significant temperature effect at 600 and 800 °C substrate temperatures. The lack of a temperature effect indicates that deposition took place under mass transfer limited conditions as was observed for  $\beta$ -Ga<sub>2</sub>O<sub>3</sub> growth. Table 6.3 is a summary of amorphous and (11 $\bar{2}$ 0)-oriented  $\alpha$ -Al<sub>2</sub>O<sub>3</sub> on a variety of substrates. The  $\theta$  rc fwhm values listed for the (11 $\bar{2}$ 0)  $\alpha$ -Al<sub>2</sub>O<sub>3</sub> peak ( $2\theta = 37.785^\circ$ ) indicate that the grains were highly oriented. Other details from the XRD analysis not shown in Table 6.3 are as follows. First, the amount of crystalline material in the films increased by a factor of four from 600 to 800 °C as indicated by an increasing (11 $\bar{2}$ 0) peak height for films of the same thickness. Second, decreasing the Al(TMHD)<sub>3</sub> partial pressure from 4.4 to 0.44 mTorr at a total pressure 5.5 Torr, which resulted in a decrease of the overall growth rate from an average of 6.2 to 4.0 Å/min, did not produce a significant increase in the amount of crystalline material or its degree of orientation. Further XRD work was unable to establish that the grains of (11 $\bar{2}$ 0) material were all oriented in the same way with respect to the growth plane.

Table 6.3 Summary of Al<sub>2</sub>O<sub>3</sub> growth from Al(TMHD)<sub>3</sub> precursor

Substrate	Substrate Temp. (°C)	Film Cryst. Orientation	θ RC FWHM
(001) Rutile	600 - 700	Amorphous	---
(100) Rutile	400 - 700	Amorphous	---
(100) Si	600 - 800	Amorphous	---
(111) Si	400	Amorphous	---
	500	Amorphous	---
	600	(11 $\bar{2}$ 0)	0.19°
	700	(11 $\bar{2}$ 0)	0.24°
	800	(11 $\bar{2}$ 0)	0.30°

\*P<sub>O<sub>2</sub></sub>=2.5 Torr, P<sub>Al(TMHD)<sub>3</sub></sub>=2.2 mTorr, P<sub>Tot</sub>=5.5 Torr, 300 sccm total flow rate He + O<sub>2</sub>

Given the past achievement of (100)- and (001)-oriented rutile deposition on (0001) and (10 $\bar{1}$ 0) sapphire substrates, rutile substrates were tested as a possibility for oriented Al<sub>2</sub>O<sub>3</sub> growth. The results indicate, however, that over a temperature and precursor partial pressure range similar to rutile deposition, only amorphous Al<sub>2</sub>O<sub>3</sub> was grown. RBS analysis confirmed that the amorphous material was stoichiometric. One possible explanation for the non-crystalline growth is the large lattice mismatch between Al<sub>2</sub>O<sub>3</sub> and rutile. Although the mismatch is the same when depositing rutile, it is possible that differences in the elastic moduli of the two materials allows rutile to more easily adapt to the Al<sub>2</sub>O<sub>3</sub> surface. The data suggest this to be the case given that the elastic modulus of TiO<sub>2</sub> is approximately 200 kN/mm<sup>2</sup> as compared to 400 kN/mm<sup>2</sup> for Al<sub>2</sub>O<sub>3</sub>.<sup>5,223</sup> The rutile substrates may also have surface contaminants for which the degreasing procedure used did not adequately clean the surface.

In a literature search for other prospective substrates, a report of polycrystalline  $\text{Al}_2\text{O}_3$  deposition on (100) Si over a 700 to 900 °C temperature range by CVD using  $\text{AlCl}_3$ ,  $\text{CO}_2$ , and  $\text{H}_2$  was found.<sup>165</sup> No details were given for the substrate preparation. We deposited amorphous but stoichiometric  $\text{Al}_2\text{O}_3$  on (100) Si from 600 °C to the upper limit of the substrate heater, 800 °C. In a further effort to induce crystalline growth, we varied the precursor partial pressure from 0.44 to 4.4 mTorr at 600 °C. This endeavor also proved unsuccessful for deposition on both (100) Si and rutile substrates. One possible barrier to crystalline growth on (100) Si is that, in contrast to Si (111), no crystalline  $\text{SiO}_2$  peaks were found. This suggests that deposition occurred on an amorphous surface oxide layer.

An analysis of the relationship between the oxygen sublattices of the (211)  $\text{SiO}_2$  surface layer identified on (111) Si substrate and the  $(11\bar{2}0)$   $\alpha\text{-Al}_2\text{O}_3$  film was performed. A mismatch of only 5% was found in one of the directions,  $[2\bar{2}01] \text{Al}_2\text{O}_3 // [01\bar{1}] \text{SiO}_2$ , similar to the findings for the  $\beta\text{-Ga}_2\text{O}_3$  films. Therefore, the film-substrate oxygen sublattice relationship appears to have influenced the deposition of the observed  $\text{Al}_2\text{O}_3$  orientation.

### 6.3 Summary

Highly oriented films of  $(\bar{3}11)$   $\beta\text{-Ga}_2\text{O}_3$  were deposited on (111) Si and oriented films with a mixture of the  $(\bar{3}11)$  and  $(\bar{2}01)$  crystal planes were deposited on (0001) sapphire in the 600 to 700 °C substrate temperature range. Singly oriented  $\beta$ -phase  $\text{Ga}_2\text{O}_3$  which is crucial to high temperature sensor applications was deposited. Highly oriented thin films of  $(11\bar{2}0)$   $\alpha\text{-Al}_2\text{O}_3$  were also grown on (111) Si in the 600 to 800 °C substrate temperature range. Decreasing the growth rate by a factor of two was not found to affect the amount or degree of orientation of the crystalline material in these films. These changes also did not induce crystalline growth on (100) Si or rutile substrates. Oxygen sublattice

relationships between film and substrate were suggested as the driving force for the deposition of oriented, crystalline material for both compounds. The usefulness of the phase contrast imaging technique for more clearly displaying faceted surfaces was demonstrated.

## CHAPTER 7 CONCLUSIONS AND RECOMMENDATIONS FOR FUTURE WORK

The effects of surface chemistry, orientation and morphology on the gas sensing properties of rutile films were investigated. The motivation for this work was to improve the current state of limited understanding of gas sensing mechanisms in semiconducting materials. The MOCVD of rutile phase  $\text{TiO}_2$  heteroepitaxially on sapphire substrates was studied and thoroughly developed to prepare materials with well-defined physical characteristics for use in the gas sensor investigation.

### 7.1 Conclusions

#### 7.1.1 Undoped Rutile Film Deposition

Heteroepitaxial rutile films were deposited using a solid precursor as the source of metal atoms. Films with an (001), (101) or (100) rutile crystal orientation were deposited on (10 $\bar{1}$ 0)-, (11 $\bar{2}$ 0)- and (0001)-oriented sapphire substrates, respectively. XRD analysis determined that the plane-to-plane spacing of a (100)-oriented film was most consistent having a  $\theta$  rc fwhm of  $0.20^\circ$ . The planar spacing consistencies of (001)- and (101)-oriented films were similar with values around  $0.35^\circ$  at high deposition temperature. XRD investigation of the heteroepitaxial nature of each orientation revealed the in-plane matching crystal directions in the film and substrate. The (100) orientation was found to have three equivalent in-plane alignments with respect to its sapphire substrate, and the (101) orientation was found to have a twin plane parallel to the film surface. The consistency of

in-plane alignment indicated by  $\phi$  peak fwhm values was worst for (100)-oriented film for obvious reasons. The  $\phi$  peak fwhm values of (001)- and (101)-oriented films were similar at  $1.1^\circ$  and  $1.5^\circ$ , respectively.

The undoped film surface morphologies were investigated by AFM. Measurements taken from the AFM images were used to show that (001)- and (101)-oriented film surfaces were composed of facet planes in a uniform arrangement. An (001)-oriented film surface consisted of {101}-type facet planes which formed surface features similar to inverted pyramids. The {101}- and {111}-type facet planes of a (101)-oriented film surface formed features shaped like trapezoidal prisms. XRD was used to show the direction of elongation of the surface features was  $[\bar{1}01]$ . This is the direction of smallest oxide sublattice mismatch between film and substrate. The mismatch in the other in-plane direction of a (101)-oriented film and in each in-plane direction of the other two film orientations were too large to produce feature elongation.

These bulk crystal and surface properties were shown to be in general agreement with the respective orientations of rutile films grown by IBSD. The deposition of (001)-oriented heteroepitaxial rutile films is unique to this work and the corresponding IBSD research.

### 7.1.2 Doped Rutile Film Deposition

The rutile films were doped with Ga, an acceptor-type dopant, or Nb, a donor-type dopant. XRD was used to prove that heteroepitaxy was maintained to 6.5 at% of either dopant. The crystalline quality as indicated by  $\theta_{rc}$  and  $\phi$  peak fwhm values declined with increasing dopant concentration. An exception was found for the case of in-plane alignment of (101)-oriented films which improved with Ga doping. This behavior was related to a decline of the presence of small amounts of (100)-oriented material as a stress relief mechanism at large thicknesses.

XRD measurements further demonstrated that the lattices of (001)- and (101)-oriented films expanded linearly with increasing dopant concentration. The expansions were related to the larger size of the Nb atom substituted on a Ti lattice site and the O vacancy compensation of the smaller Ga atom substituted on a Ti site. The removal of a much larger anion caused lattice expansion due to repulsive forces among the remaining atoms as expected for a material which is nearly ionic.

Surface morphology changes were governed by the increased lattice stress caused by doping. Increased lattice stress resulted in a greater number of defects in the materials and therefore increases in the surface roughnesses of each orientation. An exception was observed for the (100) orientation where Ga doping resulted in a conversion to primarily anatase phase crystalline material. (101)-oriented films continued to exhibit elongation in the  $[\bar{1}01]$  direction under the influence of either dopant. The feature size on this orientation actually increased with Ga doping corresponding to the decline in (100)-oriented material as measured by XRD.

### 7.1.3 Rutile Gas Sensors

The gas sensor properties of each undoped film orientation and (001)-oriented films with various compositions were investigated. Impedance spectroscopy was used to obtain resistance values of the actual materials, as opposed to a material-electrode barrier, as a function of temperature and environment. From the resistance values, conductivities and activation energies were calculated. These numbers were then used to calculate overall changes in the number of conducting electrons as a function of changing environment.

The results on gas sensor behavior shown as a function of bulk film orientation and changing composition were explained by a general mechanism. The presence of enhanced adsorption sites for oxygen or water corresponded to an increase in electron acceptance from or electron donation to a material, respectively. Enhanced adsorption sites on rutile

films for both oxygen and water were created in several ways. First, the natural coordination of titanium at surface facet planes and intersections. The presence of three-coordinated titanium atoms on the {111}-type facet planes of a (101)-oriented film surface resulted in increased adsorption in comparison to an (001)-oriented film where titanium atoms coordinated to four or fewer oxygens were present only at facet intersections. Second, the oxygen vacancy compensation of Ga dopant atoms lowered the oxygen coordination of titanium atoms on an (001)-oriented film surface. Third, the same effect was created by removing oxygen with hydrogen at an elevated temperature. The confirmation of this relationship between surface cation oxygen coordination and gas sensitivity which was supported by photochemical reactivity measurements is previously unknown in the literature.

A separate mechanism was proposed for the dramatic enhancement of oxygen adsorption on a Nb-doped film. Conductivity and activation energy measurements suggested that the donor-type dopant atom introduced a band gap state approximately 0.04 eV below. The shallow donor state resulted in an excessive number of conduction electrons in comparison to an undoped film. This characteristic was proposed to enhance the adsorption of acceptor-type molecules.

Ultimately, comparisons between the behaviors of materials on which enhanced adsorption sites were created and the traditional calculation of sensitivity (ratio of initial and final resistance values) for those same materials was very informative. The comparison suggested that both adsorption and resistivity must be optimized to engineer an ideal gas sensor. The sensor created with a thin, Ga-doped surface layer on top of a film doped with 0.05 at% Nb was created to demonstrate this idea of tailored materials. The thin Ga-doped surface layer served to enhance water adsorption through the creation of undercoordinated Ti atoms. The 0.05 at% Nb dopant concentration lowered the bulk resistance to a more readily measurable value range ( $\sim 1e7 \Omega$ ) without reaching a value where the resistance

could not be significantly changed by electron donation using the number of available adsorption sites on the film's surface.

#### 7.1.4 Deposition of Other Metal Oxides

Highly oriented films of  $(\bar{3}11)$   $\beta$ - $\text{Ga}_2\text{O}_3$  were deposited on (111) Si and oriented films with a mixture of the  $(\bar{3}11)$  and  $(\bar{2}01)$  crystal planes were deposited on (0001) sapphire in the 600 to 700 °C substrate temperature range. Singly oriented  $\beta$ -phase  $\text{Ga}_2\text{O}_3$  which is crucial to high temperature sensor applications was deposited. Highly oriented thin films of  $(11\bar{2}0)$   $\alpha$ - $\text{Al}_2\text{O}_3$  were also grown on (111) Si in the 600 to 800 °C substrate temperature range. Decreasing the growth rate by a factor of two was not found to affect the amount or degree of orientation of the crystalline material in these films. These changes also did not induce crystalline growth on (100) Si or rutile substrates. Oxygen sublattice relationships between film and substrate were suggested as the driving force for the deposition of oriented, crystalline material for both compounds. The usefulness of the phase contrast imaging technique for more clearly displaying faceted surfaces was demonstrated.

### 7.2 Recommendations for Future Work

#### 7.2.1 Undercoordinated Surface Cation Reactivity

7.2.1.1 Zinc Oxide. Initial photoreactivity studies on oriented ZnO films for the reduction of Ag ions have been performed by Morris-Hotsenpiller. Photoreactivity has been shown to be inversely related to the oxygen coordination of Zn atoms at the film surfaces. Two problems exist with the material. The surfaces of both orientations which have been grown are considerably smoother than  $\text{TiO}_2$  films and do not exhibit a regular

faceting structure. Film smoothness could potentially be increased by increasing nucleation density. Nucleation density can be increased by depositing metal precursor in the absence of oxygen for a very brief time prior to deposition under normal conditions. Alternatively, the films could be annealed to induce faceting. Both of these approaches would serve to create surface structures on which the cation oxygen coordination could be more accurately defined as opposed to approximating based on the bulk film orientation. These materials could be tested for their photoreactivity and gas sensitivity as further confirmation of the enhanced adsorption site mechanism proposed in this research.

7.2.1.2 Sensitivity to other donor- or acceptor-type molecules. Since specific adsorption sites and mechanisms for conductivity changes have been identified, the mechanisms for other gas molecules could be investigated with a greater potential for making a significant contribution to the literature. Ethanol, for example, is essentially water with a methane group substituted for one hydrogen atom and therefore would be expected to behave as a donor-type molecule. The surface reactions that would have to occur to dissociate ethanol into a donor form analogous to  $\text{OH}^-$  in the case of water would, however, be substantially more complex. This reaction and its by-products are expected to be a function of the oxygen coordination of the cation on which the ethanol is adsorbed and the oxygen coordination of the nearest cation neighbors.

7.2.1.3 UHV analyses. Studying the sensitivity mechanisms of more complex molecules such as ethanol on thin film materials would be greatly aided by studying the adsorption/desorption properties of molecules by x-ray photoelectron spectroscopy and thermal programmed desorption. The combination of these two analytical techniques could identify the adsorption site, the state of the adsorbed species and the dissociation reaction products as a function of temperature. This information is important not only of its own

merit but also for the issue of selectivity because the sensitivity to a desired molecule must often be differentiated from a background of humid air or a mixture of hydrocarbons.

### 7.2.2 Tailored Materials

A thin 1 at% Ga-doped surface layer on a nominally 3300 Å thick 0.05 at% Nb-doped film was shown to optimize both water adsorption and traditional sensitivity. Another strong possibility exists for optimizing both these variables to create an oxygen sensor. Since most oxygen sensor applications are at temperatures on the order of 500 °C or higher, the issue of high resistivity for undoped or Ga-doped films becomes less significant. Using either film composition with a thin 1 at% Nb-doped surface layer to optimize oxygen adsorption has excellent potential for displaying a larger traditional sensitivity to oxygen than a simple undoped film.

### 7.2.3 P-type Conducting Sensors

As described in §5.5.3.3, semiconductor physics suggests that a p-type conducting material should exhibit good sensitivity to a donor-type molecule. For a variety of reasons discussed in that section, thin films are poor candidate materials for long-term stable, p-type sensors. An alternative approach could be to use a rutile single crystal and acceptor-dope it by annealing in acceptor atoms from a metal organic solution placed on the surface. Platinum contacts could be used at higher temperatures where hopefully p-type behavior could be observed without having to go to excessively high temperature where diffusion of the Pt or dopant atoms results in continually changing electrical behavior.

#### 7.2.4 Gallium Oxide Films

$\text{Ga}_2\text{O}_3$  films demonstrated substantial increases in amount of crystalline material and surface faceting as a function of deposition temperature and annealing.  $\text{Ga}_2\text{O}_3$  has been investigated as a sensor of various hydrocarbons, oxygen and hydrogen (§2.4.1.2). Investigation of the sensitivity changes as a function of crystallinity, crystal phase, and surface structure would be valuable research because no mechanism of any kind has been proposed for the gas sensitivity of  $\text{Ga}_2\text{O}_3$ .

## REFERENCES

1. A. M. Azad, S. A. Akbar, S. G. Mhaisalkar, L. D. Birkefeld and K. S. Goto, *Journal of the Electrochemical Society* 139 (1992) 3690.
2. P. T. Moseley, *Sensors and Actuators B* 6 (1992) 149.
3. A. Takami, *American Ceramic Society Bulletin* 67 (1988) 1956.
4. T. Y. Tien, H. L. Stadler, E. F. Gibbons and P. J. Zacmanidis, *American Ceramic Society Bulletin* 54 (1975) 280.
5. M. Ohring, *The Materials Science of Thin Films* (Academic Press, Inc., San Diego, 1992) p.704.
6. J. W. Matthews, *Materials Science and Technology* (1975) 379.
7. G. B. Stringfellow, *Reports on Progress in Physics* 45 (1982) 469.
8. G. Hass, *Vacuum* 2 (1952) 331.
9. R. N. Ghoshtagore, *Journal of the Electrochemical Society* 117 (1970) 529.
10. S. Hayashi and T. Hirai, *Journal of Crystal Growth* 36 (1976) 157.
11. K. S. Yeung and Y. W. Lam, *Thin Solid Films* 109 (1983) 169.
12. L. M. Williams and D. W. Hess, *Journal of Vacuum Science and Technology A* 1 (1983) 1810.
13. J. Aarik, A. Aidla, T. Uustare and V. Sammelselg, *Journal of Crystal Growth* 148 (1995) 268.
14. P. A. Morris Hotsenpiller, G. A. Wilson, A. Roshko, J. B. Rothman and G. S. Rohrer, *Journal of Crystal Growth* to be published (1995) .
15. W. T. Pawlewicz and R. Busch, *Thin Solid Films* 63 (1979) 251.
16. S. Schiller, G. Beister, W. Sieber, G. Schirmer and E. Hacker, *Thin Solid Films* 83 (1981) 239.
17. D. Wicaksana, A. Kobayashi and A. Kinbara, *Journal of Vacuum Science and Technology A* 10 (1992) 1479.
18. P. Löbl, M. Huppertz and D. Mergel, *Thin Solid Films* 251 (1994) 72.

19. M. D. Wiggins, M. C. Nelson and C. R. Aita, *Journal of Vacuum Science and Technology A* 14 (1996) 772.
20. N. Martin, C. Rousselot, C. Savall and F. Palmino, *Thin Solid Films* 287 (1996) 154.
21. F. Varnier, *Journal of Vacuum Science and Technology A* 8 (1989) 2155.
22. K. Fukushima and I. Yamada, *Applied Surface Science* 43 (1989) 32.
23. S. Miyake, K. Honda, T. Kohno and Y. Setsuhara, *Journal of Vacuum Science and Technology A* 10 (1992) 3253.
24. D. Leinen, J. P. Espinós, A. Fernández and A. R. González-Elipe, *Journal of Vacuum Science and Technology A* 12 (1994) 2728.
25. H. J. Frenck, W. Kulisch, M. Kuhr and R. Kassing, *Thin Solid Films* 201 (1991) 327.
26. Y. Kumashiro, Y. Kinoshita, Y. Takaoka and S. Murasawa, *Journal of the Ceramic Society of Japan* 101 (1993) 514.
27. W. G. Lee, S. I. Woo, J. C. Kim, S. H. Choi and K. H. Oh, *Thin Solid Films* 237 (1994) 105.
28. A. Nagahori and R. Raj, *Materials Research Society Symposium Procedures* 335 (1994) 117.
29. H.-K. Ha, M. Yoshimoto, H. Koinuma, B.-K. Moon and H. Ishiwara, *Applied Physics Letters* 68 (1996) 265.
30. K. K. Lai, A. W. Mak, T. P. H. F. Wendling, P. Jian and B. Hathcock, *Thin Solid Films* 332 (1998) 329.
31. B. Claflin, M. Binger, G. Lucovsky and H.-Y. Yang, *Materials Research Society Symposium Proceedings* 532 (1998) 171.
32. M. T. Wang, P. C. Wang, M. C. Chuang, L. J. Chen and M. C. Chen, *Journal of Vacuum Science and Technology B* 16 (1998) 2026.
33. N. B. Thomsen, A. Horsewell, K. S. Mogensen, S. S. Eskildsen, C. Mathiasen and J. Bottiger, *Thin Solid Films* 333 (1998) 50.
34. J. P. A. M. Driessen, A. D. Kuypers and J. Schoonman, *Surface Coating Technology* 110 (1998) 173.
35. G. B. Stringfellow, *Organometallic Vapor-Phase Epitaxy Theory and Practice* (Academic Press, Inc, San Diego, 1989) p.398.
36. R. N. Ghoshtagore and A. J. Noreika, *Journal of the Electrochemical Society* 117 (1970) 1310.
37. A. Heller, Y. Degani, D. W. Johnson and P. K. Gallagher, *Journal of Physical Chemistry* 91 (1987) 5987.

38. H. L. M. Chang, J. C. Parker, H. You, J. J. Xu and D. J. Lam, *Materials Research Society Symposium Procedures* 168 (1990) 343.
39. H. L. M. Chang, H. You, J. Guo and D. J. Lam, *Applied Surface Science* 48/49 (1991) 12.
40. H. L. M. Chang, H. You, Y. Gao, J. Guo, C. M. Foster, R. P. Chiarello, T. J. Zhang and D. J. Lam, *Journal of Materials Research* 7 (1992) 2495.
41. H. L. M. Chang, H. Z. Zhang, J. Guo, H. K. Kim and D. J. Lam, *Journal of Materials Research* 8 (1993) 2634.
42. S. Chen, M. G. Mason, H. J. Gysling, G. R. Paz-Pujalt, T. N. Blanton, T. Castro, K. M. Chen, C. P. Fictorie, W. L. Gladfelter, A. Franciosi, P. I. Cohen and J. F. Evans, *Journal of Vacuum Science Technology A* 11 (1993) 2419.
43. Z.-X. Chen and A. Derking, *Journal of Materials Chemistry* 3 (1993) 1137.
44. Y. Gao, K. L. Merkle, H. L. M. Chang, T. J. Zhang and D. J. Lam, *Electron microscopy study of MOCVD-grown TiO<sub>2</sub> thin films and TiO<sub>2</sub>/Al<sub>2</sub>O<sub>3</sub> interfaces* 209 (1990) 685.
45. K. Kamata, M. Kazunori, A. Seiki and F. Hiroyuki, *Journal of Materials Science Letters* 9 (1990) 316.
46. H.-Y. Lee and H.-G. Kim, *Thin Solid Films* 229 (1993) 187.
47. J.-P. Lu, J. Wang and R. Rishi, *Thin Solid Films* 204 (1991) L13.
48. J.-P. Lu and R. Raj, *Journal of Materials Research* 6 (1991) 1913.
49. N. Rausch and E. P. Burte, *Journal of the Electrochemical Society* 140 (1993) 145.
50. K. L. Siefering and G. L. Griffin, *Journal of the Electrochemical Society* 137 (1990) 814.
51. Y. S. Yoon, W. N. Kang, S. S. Yom, T. W. Kim, M. Jung, T. H. Park, K. Y. Seo and J. Y. Lee, *Thin Solid Films* 238 (1994) 12.
52. C. P. Fictorie, J. F. Evans and W. L. Gladfelter, *Journal of Vacuum Science and Technology A* 12 (1994) 1108.
53. C. Byun, J. W. Jang, I. T. Kim, K. S. Hong and B.-W. Lee, *Materials Research Bulletin* 32 (1997) 431.
54. V. A. Versteeg, C. T. Avedisian and R. Raj, *Journal of the American Ceramic Society* 78 (1995) 2763.
55. M. Ritala, M. Leskelä and E. Rauhala, *Chemistry of Materials* 6 (1994) 556.
56. T.-K. Won, S.-G. Yoon and H.-G. Kim, *Journal of the Electrochemical Society* 139 (1992) 3284.

57. S. B. Desu, *Materials Science and Engineering B* 13 (1992) 299.
58. G. Montesperelli, A. Pumo, E. Traversa, G. Gualtiero, A. Bearzotti, A. Montenero and G. Gnappi, *Sensors and Actuators B* 24-25 (1995) 705.
59. H. Shin, R. J. Collins, M. R. DeGuire, A. H. Heuer and C. N. Sukenik, *Journal of Materials Research* 10 (1995) 692.
60. H. Shin, R. J. Collins, M. R. DeGuire, A. H. Heuer and C. N. Sukenik, *Journal of Materials Research* 10 (1995) 699.
61. E. M. Logothetis and W. J. Kaiser, *Sensors and Actuators* 4 (1983) 333.
62. E. C. Subbarao, *Ferroelectrics* 102 (1990) 267.
63. M. Radecka and M. Rekas, *Journal of the Physics and Chemistry of Solids* 56 (1995) 1031.
64. C. S. Hwang and H. J. Kim, *The Korean Journal of Ceramics* 1 (1995) 21.
65. J. Sluneko, J. Holc, M. Hrovat and S. Bernik, *Journal of Materials Science Letters* 11 (1992) 782.
66. J. G. Fagan and V. R. W. Amarakoon, *American Ceramic Society Bulletin* 72 (1993) 119.
67. B. M. Kulwicki, *Journal of the American Ceramic Society* 74 (1991) 697.
68. S. P. Lee, J. Y. Rim and Y. K. Yoon, *Sensors and Materials* 7 (1995) 23.
69. E. Traversa, *Journal of the American Ceramic Society* 78 (1995) 2625.
70. K. Katayama, K. Hasegawa, Y. Takahashi and T. Akiba, *Sensors and Actuators A* 24 (1990) 55.
71. J.-H. Park and S. J. Park, *Journal of Materials Science: Materials in Electronics* 5 (1994) 300.
72. Y.-C. Yeh, T.-Y. Tseng and D.-A. Chang, *Journal of the American Ceramic Society* 73 (1990) 1992.
73. A. Bearzotti, A. Bianco, G. Montesperelli and E. Traversa, *Sensors and Actuators B* 18-19 (1994) 525.
74. S. Ito, S. Tomotsune and N. Koura, *Denki Kagaku Oyobi Kogyo Butsuri Kagaku* 60 (1992) 474.
75. J. B. Goodenough, A. Hamnett, G. Huber, F. Hulliger, M. Leiß, S. K. Ramasesha and H. Werheit, in: *Landolt-Börnstein, Numerical Data and Functional Relationships in Science and Technology*, Eds. K.-H. Hellwege and O. Madelung (Springer-Verlag, New York, 1984) Vol. 17g, p.133.
76. F. A. Grant, *Reviews of Modern Physics* 31 (1959) 646.

77. A. von Hippel, J. Kalnajs and W. B. Westphal, *Journal of Physics and Chemistry of Solids* 23 (1962) 779.
78. J. Nowotny, M. Radecka and M. Rekas, *Journal of Physics and Chemistry of Solids* 58 (1997) 927.
79. D. S. Tannhauser, *Solid State Communications* 1 (1963) 223.
80. J. Yahia, *Physical Review* 130 (1963) 1711.
81. R. N. Blumenthal, J. Baukus and W. M. Hirthe, *Journal of the Electrochemical Society* 114 (1967) 172.
82. K. H. Kim, E. J. Oh and S. J. Choi, *Journal of Physics and Chemistry of Solids* 45 (1984) 1265.
83. J.-F. Marucco, J. Gautron and P. Lemasson, *Journal of Physics and Chemistry of Solids* 42 (1981) 363.
84. R. N. Blumenthal, *Journal of Physics and Chemistry of Solids* 27 (1966) 643.
85. J. Son and I. Yu, *The Korean Journal of Ceramics* 2 (1996) 131.
86. D. C. Cronmeyer, *Physical Review* 87 (1952) 876.
87. H. P. R. Frederikse, *Journal of Applied Physics* 32 (1961) 2211.
88. B. Poumellec, J. F. Marucco and F. Lagnel, *Physics Status Solidi A* 89 (1985) 375.
89. E. Iguchi, K. Yajima, T. Asahina and Y. Kanamori, *Journal of Physics and Chemistry of Solids* 35 (1974) 597.
90. R. G. Breckenridge and W. R. Hosler, *Physical Review* 91 (1953) 793.
91. W. Göpel, U. Kirner and H. D. Wiemhöfer, *Solid State Ionics* 28-30 (1988) 1423.
92. N. Yu and J. W. Halley, *Materials Science Forum* 185-188 (1995) 389.
93. N. Yu and J. W. Halley, *Physical Review B* 51 (1995) 4768.
94. S. Munnix and M. Schmeits, *Journal of Vacuum Science and Technology A* 5 (1987) 910.
95. R. V. Kasowski and R. H. Tait, *Physical Review B* 20 (1979) 5168.
96. R. H. Tait and R. V. Kasowski, *Physical Review B* 20 (1979) 5178.
97. V. E. Henrich and R. L. Kurtz, *Physical Review B* 23 (1981) 6280.
98. Y. Aiura, Y. Nishihara, Y. Haruyama, T. Komeda, S. Kodaira, Y. Sakisaka, T. Maruyama and H. Kato, *Physica B* 194-196 (1994) 1215.

99. S. Kodaira, Y. Sakisaka, T. Maruyama, Y. Haruyama, Y. Aiura and H. Kato, *Solid State Communications* 89 (1994) 9.
100. D. C. Sayle, C. R. A. Catlow, P. M. A and P. Nortier, *Journal of Physics and Chemistry of Solids* 56 (1995) 799.
101. S. D. Mo, L. B. Lin and D. L. Lin, *Journal of Physics and Chemistry of Solids* 55 (1994) 1309.
102. J. Pennewiss and B. Hoffman, *Materials Letters* 5 (1987) 121.
103. R. A. Slepetyts and P. A. Vaughan, *The Journal of Physical Chemistry* 73 (1969) 2157.
104. K. S. Forland, *Acta Chemica Scandinavica* 20 (1966) 2573.
105. A. Bernasik, M. Radecka, M. Rekas and M. Sloma, *Applied Surface Science* 65/66 (1993) 240.
106. J. L. Carpentier, A. Lebrun and F. Perdu, *Journal of Physics and Chemistry of Solids* 50 (1989) 145.
107. A. R. Bally, E. N. Korobeinikova, P. E. Schmid, F. Levy and F. Bussy, *Journal of Physics D: Applied Physics* 31 (1998) 1149.
108. A. Bernasik, M. Rekas, M. Sloma and W. Weppner, *Solid State Ionics* 72 (1994) 12.
109. S. Fujitsu and T. Hamada, *Journal of the American Ceramic Society* 77 (1994) 3281.
110. N. Niizeki, *Advanced X-Ray Analysis* 11 (1968) 482.
111. M. Valigi, D. Cordischi, G. Minelli, P. Natale, P. Porta and C. P. Keijzers, *Journal of Solid State Chemistry* 77 (1988) 255.
112. R. S. Roth and L. W. Coughanour, *Journal of Research of the National Bureau of Standards* 55 (1955) 209.
113. N. G. Eror, *Journal of Solid State Chemistry* 38 (1981) 281.
114. R. T. Dirstine and C. J. Rosa, *Z. Metallkd.* 70 (1979) 322.
115. V. N. Bogomolov, I. A. Smirnov and E. V. Shadrichev, *Soviet Physics - Solid State* 11 (1970) 3214.
116. J. F. Baumard and E. Tani, *Physica Status Solidi A* 39 (1977) 373.
117. P. H. Zimmermann, *Physical Review B* 8 (1973) 3917.
118. N. P. Bogoroditskii, V. Kristya and I. P. Panova, *Soviet Physics - Solid State* 9 (1967) 187.

119. V. S. Lusvardi, M. A. Barteau, J. G. Chen, J. Eng, B. Fruhberger and A. Teplyakov, *Surface Science* 397 (1998) 237.
120. J. T. Mayer, U. Diebold, T. E. Madey and E. Garfunkel, *Journal of Electron Spectroscopy and Related Phenomena* 73 (1995) 1.
121. G. Lu, A. Linsebigler and J. T. Yates, *Journal of Physical Chemistry* 98 (1994) 11733.
122. U. Bardi, K. Tamura, M. Owari and Y. Nihei, *Applied Surface Science* 32 (1988) 352.
123. G. B. Hoflund, H. L. Yin, L. G. Austin, D. A. Asbury, H. Yoneyama, O. Ikeda and H. Tamura, *Langmuir* 4 (1988) 346.
124. A. Linsebigler, G. Lu and J. T. Yates, *Journal of Physical Chemistry* 100 (1996) 6631.
125. A. Linsebigler, C. Rusu and J. T. Yates, *Journal of the American Chemical Society* 118 (1996) 5284.
126. G. Lu, A. Linsebigler and J. T. Yates, *Journal of Physical Chemistry* 99 (1995) 7626.
127. J. C. S. Wong, A. Linsebigler, G. Lu, J. Fan and J. T. Yates, *Journal of Physical Chemistry* 99 (1995) 335.
128. R. L. Kurtz, *Surface Science* 177 (1986) 526.
129. W. S. Epling, C. H. F. Peden, M. A. Henderson and U. Diebold, *Surface Science* 412/413 (1998) 333.
130. J. M. Pan, B. L. Maschhoff, U. Diebold and T. E. Madey, *Journal of Vacuum Science and Technology A* 10 (1992) 2470.
131. R. L. Kurtz, R. Stockbauer and T. E. Madey, *Surface Science* 218 (1989) 178.
132. P. Jones and J. A. Hockey, *Transactions of the Faraday Society* 67 (1971) 2679.
133. P. Jones and J. A. Hockey, *Journal of the Chemical Society, Faraday Transactions* 1 68 (1972) 907.
134. V. E. Henrich, G. Dresselhaus and H. J. Zeiger, *Solid State Communications* 24 (1977) 623.
135. W. Lo, Y. W. Chung and G. A. Somorjai, *Surface Science* 71 (1978) 199.
136. S. Bourgeois, F. Jomard and M. Perdereau, *Surface Science* 279 (1992) 349.
137. M. A. Henderson, *Surface Science* 319 (1994) 315.
138. L. E. Firment, *Surface Science* 116 (1982) 205.
139. P. B. Smith and S. L. Bernasek, *Surface Science* 188 (1987) 241.

140. F. J. Bustillo, E. Roman and J. L. de Segovia, *Vacuum* 39 (1989) 659.
141. F. J. Bustillo, E. Roman and J. L. de Segovia, *Vacuum* 41 (1990) 19.
142. R. Roy, V. G. Hill and E. F. Osborn, *Journal of the American Chemical Society* 74 (1952) 719.
143. S. Geller, *The Journal of Chemical Physics* 33 (1960) 676.
144. J. A. Kohn, G. Katz and J. D. Broder, *American Mineralogy* 42 (1957) 398.
145. J. Ahman, G. Svensson and J. Albertsson, *Acta Crystallographica C* 52 (1996) 1336.
146. K. Osaza, T. Ye and Y. Aoyagi, *Japanese Journal of Applied Physics* 32, Pt. 2 (1993) L329.
147. T. Hariu, S. Sasaki, H. Adachi and Y. Shibata, *Japanese Journal of Applied Physics* 16 (1977) 841.
148. M. Passlack, N. E. J. Hunt, E. F. Schubert, G. J. Zydzik, M. Hong, J. P. Mannaerts, R. L. Opila and R. J. Fischer, *Applied Physics Letters* 64 (1994) 2715.
149. P. Wu, Y.-M. Gao, R. Kershaw, K. Dwight and A. Wold, *Materials Research Bulletin* 25 (1990) 357.
150. K. Osaza, T. Ye and Y. Aoyagi, *Journal of Vacuum Science and Technology A* 12 (1994) 120.
151. M. Fleischer and H. Meixner, *Journal of Materials Science Letters* 11 (1992) 1728.
152. P. P. Macri, S. Enzo, G. Sberveglieri, S. Gropelli and C. Perego, *Applied Surface Science* 65/66 (1993) 277.
153. T. A. Jones, J. G. Firth and B. Mann, *Sensors and Actuators* 8 (1985) 281.
154. M. Fleischer and H. Meixner, *Sensors and Actuators B* 5 (1991) 115.
155. M. Fleischer, L. Hollbauer and H. Meixner, *Sensors and Actuators B* 18-19 (1994) 119.
156. M. Fleischer and H. Meixner, *Journal of Materials Science Letters* 11 (1992) 1728.
157. M. Fleischer and H. Meixner, *Sensors and Actuators B* 13-14 (1993) 259.
158. J. Frank, M. Fleischer and H. Meixner, *Sensors and Actuators B* 48 (1998) 318.
159. H. Meixner, J. Gerblinger, U. Lampe and M. Fleischer, *Sensors and Actuators B* 23 (1995) 119.
160. A. Callegari, P. D. Hoh, D. A. Buchanan and D. Lacey, *Applied Physics Letters* 54 (1989) 332.

161. E. Ciliberto, I. Fragala, R. Rizza, G. Spoto and G. C. Allen, *Applied Physics Letters* 67 (1995) 1624.
162. L. G. Meiners, *Thin Solid Films* 113 (1984) 85.
163. K. P. Pande, V. K. R. Nair and D. Gutierrez, *Journal of Applied Physics* 54 (1983) 5436.
164. H. Wado, T. Shimizu and M. Ishida, *Applied Physics Letters* 67 (1995) 2200.
165. V. J. Silvestri, C. M. Osburn and D. W. Ormond, *Journal of the Electrochemical Society* 125 (1978) 902.
166. H. D. van Corbach, V. A. C. Haanappel, T. Fransen and P. J. Gellings, *Thin Solid Films* 239 (1994) 31.
167. V. A. C. Haanappel, H. D. van Corbach, T. Fransen and P. J. Gellings, *Thin Solid Films* 230 (1993) 138.
168. R. Solanki, W. H. Ritchie and G. J. Collins, *Applied Physics Letters* 43 (1983) 454.
169. T. Kobayashi, M. Okamura, E. Yamaguchi, Y. Shinoda and Y. Hirota, *Journal of Applied Physics* 52 (1981) 6434.
170. S. M. Baumann, C. C. Martner, D. W. Martin, R. J. Blattner and A. J. Braundmeier, *Nuclear Instruments and Methods in Physics Research B* 45 (1990) 664.
171. Y. Kim, S. M. Lee, C. S. Park, S. I. Lee and M. Y. Lee, *Applied Physics Letters* 71 (1997) 3604.
172. Z. Lu, R. Hiskes, S. A. DiCarolis, R. K. Route, R. S. Feigelson, F. Leplingard and J. E. Fouquet, *Journal of Materials Research* 9 (1994) 2258.
173. B. D. Cullity, *Elements of X-ray Diffraction* (Addison-Wesley, Reading, MA, 1978) p.555.
174. B. E. Warren, *X-ray Diffraction* (Addison-Wesley, Reading, MA, 1969) p.381.
175. W.-K. Chu, J. W. Mayer and M.-A. Nicolet, *Backscattering Spectrometry* (Academic Press, New York, 1978) p.384.
176. S. N. Magonov and D. H. Reneker, *Annuals Reviews of Materials Science* 27 (1997) 175.
177. S. N. Magonov, J. Cleveland, V. Elings, D. Denley and M. H. Whango, *Surface Science* 389 (1997) 201.
178. R. S. McLean and B. B. Sauer, *Macromolecules* 30 (1997) 8314.
179. M. A. van Dijk and R. van der Berg, *Macromolecules* 28 (1995) 6773.

180. A. Zangwill, *Physics at Surfaces* (Cambridge University Press, Cambridge, UK, 1988) .
181. D. Briggs and J. C. Riviere, *Practical Surface Analysis*, Eds. D. Briggs and M. P. Seah (John Wiley & Sons, West Sussex, UK, 1990) Vol. 1, p.85.
182. W. Hirschwald, *Surface and Near-Surface Chemistry of Oxide Materials*, Eds. J. Nowotny and L. C. Dufour (Elsevier, Amsterdam, 1988) Vol. 1, p.61.
183. C. D. Wagner, W. M. Riggs, L. E. Davis and J. F. Moulder, *Handbook of X-ray Photoelectron Spectroscopy* (Perkin-Elmer Corporation, Eden Prairie, MN, 1979) .
184. A. Berrighoven, *Secondary Ion Mass Spectrometers-Basic Concepts, Instrumental Aspects, Applications and Trends* (Wiley, New York, 1987) .
185. J. A. McHugh, *Methods of Surface Analysis* (Elsevier, Amsterdam, 1975) .
186. R. S. Drago, *Physical Methods for Chemists* (Harcourt Brace Jovanovich, Orlando, 1992) p.750.
187. A. Joshi, L. E. Davis and P. W. Palmberg, *Methods of Surface Analysis* (Elsevier, Amsterdam, 1975) .
188. K. Fukushima, G. H. Takaoka and I. Yamada, *Japanese Journal of Applied Physics* 32 (1993) 3561.
189. M. A. Malati and W. K. Wong, *Surface Technology* 22 (1984) 305.
190. H. Y. Chen, J. Lin, K. L. Tan, Z. C. Feng, B. S. Kwak and A. Erbil, *A multi-technique analysis of MOCVD-grown lead lanthanum titanate (Pb<sub>1-x</sub>La<sub>x</sub>)TiO<sub>3</sub> thin films on quartz substrates* 493 (1997) 493.
191. B. C. Hendrix, F. Hintermaier, D. A. Desrochers, J. F. Roeder, G. Bhandari, M. Chappuis, T. H. Baum, P. C. Van Buskirk, C. Dehm, E. Fritsch, N. Nagel, W. Honlein and C. Mazure, *MOCVD of SrBi<sub>2</sub>Ta<sub>2</sub>O<sub>9</sub> for integrated ferroelectric capacitors* 493 (1997) 225.
192. O. Auciello, J. F. Scott and R. Ramesh, *Physics Today* 51 (1998) 22.
193. J. F. Moulder, W. F. Stickle, P. E. Sobol and K. D. Bomben, *Handbook of X-ray Photoelectron Spectroscopy* (Perkin-Elmer Corporation, Eden Prairie, MN, 1995) .
194. G. Schoen, *Journal of Electron Spectroscopy Related Phenomena* 2 (1973) 75.
195. Y. Gao and S. A. Chambers, *Epitaxial growth and characterization of Nb<sub>x</sub>Ti<sub>1-x</sub>O<sub>2</sub> rutile films by oxygen-plasma-assisted molecular beam epitaxy* 401 (1995) 85.
196. Y. Gao and S. A. Chambers, *Journal of Materials Research* 11 (1996) 1025.
197. Y. Gao, Y. Liang and S. A. Chambers, *Surface Science* 348 (1996) 17.
198. Y. Gao and S. A. Chambers, *Materials Letters* 26 (1996) 217.
199. M. K. Bahl, *Journal of Physics and Chemistry of Solids* 36 (1975) 485.

200. J. M. Honig, A. P. B. Sinha, W. E. Wahnsiedler and H. Kuwamoto, *Physica Status Solidi B* 73 (1976) 651.
201. R. Nyholm and N. Martensson, *Solid State Communications* 40 (1981) 311.
202. K. Sakata, *Journal of the Physical Society of Japan* 26 (1969) 1067.
203. M. E. Straumanis, T. Ejima and W. J. James, *Acta Crystallographica* 14 (1961) 493.
204. M. Valigi, D. Gazzoli, P. Natale and P. Porta, *Gazzetta Chimica Italiana* 116 (1986) 391.
205. N. F. Mott and M. J. Littleton, *Transactions of the Faraday Society* 34 (1938) 485.
206. A. Cimino and M. Marezio, *Journal of Physics and Chemistry of Solids* 17 (1960) 57.
207. M. A. Alim, *Active and Passive Electronic Components* 19 (1996) 139.
208. A. K. Jonscher, *Dielectric Relaxation in Solids* (Chelsea Dielectrics Press Ltd, London, 1983) p.374.
209. M. A. Seitz, *The International Journal for Hybrid Microelectronics* 3 (1980) 7.
210. J. B. Lowekamp, G. S. Rohrer, P. A. Morris Hotsenpiller, J. D. Bolt and W. E. Farneth, *The Journal of Physical Chemistry B* 102 (1998) 7323.
211. J. B. Lowekamp, (1998) .
212. G. E. Poirier, B. K. Hance and J. M. White, *Journal of Vacuum Science and Technology B* 10 (1992) 6.
213. M. Ramamoorthy, D. Vanderbilt and R. D. King-Smith, *Physical Review B* 49 (1994) 16721.
214. P. A. Morris Hotsenpiller, J. D. Bolt, W. E. Farneth, J. B. Lowekamp and G. S. Rohrer, *The Journal of Physical Chemistry B* 102 (1998) 3216.
215. K. S. Kim and M. A. Barteau, *Surface Science* 223 (1989) 13.
216. K. S. Kim and M. A. Barteau, *Journal of Catalysis* 125 (1990) 353.
217. H. Idriss, V. S. Lusvardi and M. A. Barteau, *Surface Science* 348 (1996) 39.
218. L. Forro, O. Chauvet, D. Emin, L. Zuppiroli, H. Berger and F. Levy, *Journal of Applied Physics* 75 (1994) 633.
219. R. Sanjines, H. Tang, H. Berger, F. Gozzo, G. Margaritondo and F. Levy, *Journal of Applied Physics* 65 (1994) 2945.
220. S. A. Akbar and L. B. Younkman, *Journal of the Electrochemical Society* 144 (1997) 1750.

221. A. M. Azad, S. A. Akbar and L. B. Younkman, *Journal of the American Ceramic Society* 77 (1994) 3145.
222. H. Tang, K. Prasad, R. Sanjines and F. Levy, *Sensors and Actuators B* 26-27 (1995) 71.
223. W. D. Kingery, H. K. Bowen and D. R. Uhlmann, *Introduction to Ceramics* (John Wiley & Sons, New York, 1976) p.1032.
224. F. G. Fumi and M. P. Tosi, *Discussions of the Faraday Society* 23 (1957) 92.
225. N. Serpone and E. Pelizzeti, (1989) 650.
226. P. Kofstad, *Nonstoichiometry, diffusion, and electrical conductivity in binary metal oxides* (John Wiley & Sons, Inc., New York, 1972) p.382.
227. J. Sasaki, N. L. Peterson and K. Hoshino, *Journal of Physics and Chemistry of Solids* 46 (1985) 1267.
228. M. Fleischer, W. Hanreider and H. Meixner, *Thin Solid Films* 190 (1990) 93.
229. H. Ishiwara and A. Tanemasa, *Applied Physics Letters* 40 (1981) 66.
230. A. Ishizaka and Y. Shiraki, *Journal of the Electrochemical Society* 133 (1986) 666.
231. K. Hoshino, N. L. Peterson and C. L. Wiley, *Journal of Physics and Chemistry of Solids* 46 (1985) 1397.
232. J. A. S. Ikeda and Y.-M. Chiang, *Journal of the American Ceramic Society* 76 (1993) 2437.
233. J. F. Baumard and E. Tani, *Journal of Chemical Physics* 67 (1977) 857.
234. J. Gautron, J. F. Marucco and P. Lemasson, *Materials Research Bulletin* 16 (1981) 575.

APPENDIX  
SAFETY DOCUMENTATION FOR GAS SENSITIVITY EXPERIMENTS

DuPont Company  
Central Research & Development  
Experimental Station

## STANDARD OPERATING PROCEDURE

**Job Description:** Environmentally Controlled Conductivity Measurement Chamber Tests

**Significant Safety Precautions:** Standard procedure requires loosening, tightening, and movement of heavy flange requiring leather gloves to avoid hand injury. Carbon monoxide gas is used in some phases of experiment requiring complete ventilation of all process gases to hood.

<u>Job Steps</u>	<u>Safety Key Points</u>
<b>1.0 Equipment Set-Up</b>	
1.1 Check that house air is pressurized and house air to mass flow controllers (MFC) valve 11 is open.	
1.2 Connect dry nitrogen inlet pipe to chamber inlet valve.	
<b>2.0 Load Sample</b>	
2.1 If chamber is evacuated, carry out <b>Fill Chamber with Gas (8.0)</b> procedure.	
2.2 Turn on thermocouple (TC) readout to observe sample temperature. Controller must display 25°C or less. Turn off TC readout.	2.2 Sample should be cool before removing from chamber.
2.3 Disconnect four BNC cables from bridge.	2.3 Disconnects electrical connection from bridge to sample.

<b>Job Steps</b>		<b>Safety Key Points</b>	
2.4	Check that sample heater plug is disconnected. Disconnect if necessary.	2.4	If sample heater is turned on, contact with wiring internal to chamber may cause severe electric shock.
2.5	Put on leather gloves.	2.5	Steps 2.6-2.9 create potential for pinching or scraping hands.
2.6	Loosen bolts of chamber top flange using 0.5" socket wrench.		
2.7	Place small screwdriver 0.75" into leak test hole on flange. Lift screwdriver head slowly until flange loosens from chamber.		
2.8	Remove flange and place knife edge down on paper towel on table top.		
2.9	Remove copper gasket.		
2.10	Remove leather gloves.		
2.11	Place sample holder on glass finger in chamber with sample resting directly on heater disk. Connect lead wires to sample holder.		
2.12	Put on leather gloves	2.12	Steps 2.13-2.14 create potential for pinching or scraping hands.
2.13	Put flange back on top of chamber. Tighten bolts with 0.5" socket wrench.		
2.14	Reconnect 4 BNC cables to bridge.		
<b>3.0</b>	<b>Unload Sample</b>		
3.1	Carry out steps 2.1-2.9 of <b>Load Sample (2.0)</b> procedure.		
3.2	Remove lead wires from sample holder.		
3.3	Remove sample holder and sample from chamber.		
3.4	Carry out steps 2.12-2.14 of <b>Load Sample (2.0)</b> procedure.		
<b>4.0</b>	<b>Turbo Pump Start-Up</b>		
4.1	All flanges must be in place and tightened. Close chamber gas inlet valve 1, chamber gas outlet valve 2, and gas mixing inlet valve 3.		
4.2	Open turbo pump valve 9 by rotating handle counterclockwise.		

<b>Job Steps</b>	<b>Safety Key Points</b>
4.3 Press button marked "ON/OFF" on turbo pump.	
<b>5.0 Turbo Pump Shutdown</b>	
5.1 Close turbo pump valve 9 by rotating handle clockwise.	
5.2 Press button marked "ON/OFF" on turbo pump.	
<b>6.0 Engage Cryo Pump to Chamber</b>	
6.1 Note: Cryo pump remains on at all times. It is only engaged or disengaged from pumping on conductivity chamber.	
6.2 Carry out <b>Turbo Pump Start-Up (4.0)</b> procedure.	
6.3 Wait until Turbo Pump pressure gauge reaches 10 mTorr.	
6.4 Turn on cold cathode pressure gauge.	
6.5 Wait until cold cathode pressure gauge reaches $1.0 \text{ E-3 mTorr}$ .	
6.6 Carry out <b>Turbo Pump Shutdown (5.0)</b> procedure.	
6.7 Open cryo pump valve 10 by rotating handle counterclockwise.	
<b>7.0 Disengage Cryo Pump from Chamber</b>	
7.1 Close cryo pump valve 10 by rotating handle clockwise.	
<b>8.0 Fill Chamber with Gas</b>	
8.1 Note: Always fill chamber with dry nitrogen gas. After establishing continuous flow, convert to other gas.	8.1 Potential danger if hazardous gas over pressurizes the chamber and escapes via the relief valve.
8.2 Carry out <b>Turbo Pump Shutdown (5.0)</b> or <b>Cryo Pump Disengagement (7.0)</b> if applicable.	
8.3 Open valve 4 on outlet line which exposes analog pressure gauge and pressure relief device to chamber.	8.3 Quartz viewport rated for 30 psig. 20 psig pressure relief device to avoid damage due to high pressure.
8.4 Place MFC 1 3-way valve 5 in "fill" position (pointing left).	

<b>Job Steps</b>	<b>Safety Key Points</b>
8.5 Place 3-way valve 6 leading to inlet (front of table) in bypass mode (pointing left).	
8.6 Turn MFC 1 and 2 on. Adjust flow rates. Can't be set above 150 sccm.	
8.7 Wait 5 minutes for flow to equilibrate then turn valve 6 to process (pointing right).	
8.8 Turn inlet valve 1 45 degrees.	
8.9 After 5 minutes turn inlet valve 1 fully open.	
8.10 Open valve 4 on outlet line which exposes analog pressure gauge and pressure relief device to chamber.	
8.11 When analog pressure gauge displays greater than 1.0 psig, open outlet valve 2.	
<b>9.0 Sample Temperature Control</b>	
9.1 Turn on vary AC.	
9.2 Use TC readout to set vary AC to obtain desired sample temperature.	
<b>10.0 Sample Cool Down</b>	
10.1 Cool down sample at desired rate using vary AC.	
10.2 Turn off vary AC.	
<b>11.0 Conversion to Humidified Gas</b>	
11.1 Carry out <b>Fill Chamber with Gas (8.0)</b> procedure.	
11.2 Close valves 1 and 2. Switch valve 6 to bypass.	
11.3 Turn valve 5 on MFC1 to bubbler (pointing right).	
11.4 Turn off MFC2.	
11.5 Disconnect nitrogen gas line from inlet and plug dry nitrogen line.	
11.6 Connect humidified gas line to inlet.	

<b>Job Steps</b>		<b>Safety Key Points</b>
11.7	Open valves 1 and 2.	11.7 Procedure review required for disposal of outlet gas if gas other than compressed air or nitrogen is used with water.
<b>12.0 Gas Mixing</b>		
12.1	Place gas mixing 3-way valve 7 in bypass position (pointing right).	
12.2	Turn on nitrogen MFC 1 if necessary and place valve 5 in "gas mixing" position (pointing left).	
12.4	Turn on MFC of gas to be mixed with nitrogen.	
12.5	Adjust flows of nitrogen MFC 1 and MFC 2 and gas to be mixed to desired flowrates.	
12.6	After 5 minutes to establish steady-state flow, place valve 7 in process position (pointing left).	
12.7	Open valve 3 to allow flow to chamber.	
<b>13.0 Conversion to Carbon Monoxide Gas</b>		
13.1	Carry out <b>Fill Chamber with Gas (8.0)</b> procedure if necessary.	13.2- 13.8 Inhalation of carbon monoxide may cause nonspecific discomfort such as nausea, headache or weakness, and significant deterioration of brain function. Carbon monoxide is a chemical asphyxiant. Monitor operation while carbon monoxide is in use. Personal monitor must be worn by operator while in Lab 1 with equipment. Personal monitor will be left with equipment during operation if operator is out of Lab 1 as a possible warning device during lab reentry or to other occupants.
13.2	Open carbon monoxide inlet valve 8 to gas mixing apparatus.	
13.3	Follow <b>Gas Mixing (12.0)</b> procedure.	
13.4	After completion of desired experiments, turn off carbon monoxide MFC. Close carbon monoxide inlet valve 8 to gas mixing apparatus.	
13.5	Adjust nitrogen MFC 2 flow through gas inlet and MFC 1 flow through mixing apparatus each to 150 sccm.	
13.6	Flow nitrogen through chamber for one hour.	13.6 One hour flow of nitrogen at 300 sccm allows for a complete volumetric displacement of all gas previously in chamber and outlet pipe.
13.7	Turn off nitrogen MFC's 1 and 2.	

<b>Job Steps</b>		<b>Safety Key Points</b>	
13.8	Carry out <b>Turbo Pump Start-Up (4.0)</b> procedure allowing pressure to reach $1 \times 10^{-5}$ Torr.	13.8	Chamber must be adequately evacuated of all carbon monoxide.
13.9	Carry out <b>Turbo Pump Shut Down (5.0)</b> procedure.		
13.10	Carry out <b>Fill Chamber with Gas (8.0)</b> procedure.		

### **Emergency Shutdown Procedure**

Turn heater vary AC off and leave room.

### **Lock-Out Procedure**

When the equipment is not to be energized, either due to maintenance or operating conditions:

- Place a pin through the plug to prevent accidental powering of the device.
- Put a lock-out tag on the plug containing the name of the person who locked out the piece of equipment.

### **Material Balance**

All gases that flow into system either flow out or are evacuated by a pump and, in turn, flow out the pump's exhaust.

### **Heat Balance**

All heat generated by the sample heater is absorbed by the chamber walls and is dispensed to the surrounding atmosphere via convection. The lab environment is controlled by constant sources of cooled and heated air which are designed to adjust to the additional heat loads from equipment such as this reactor.

### **MSDS**

The pertinent MSDS sheets are attached.

CR&D PROCESS SAFETY MANAGEMENT (PSM)  
Equipment Safety Audit Package  
ESA

The Equipment Safety Audit Checklist is to be used in evaluating the safety of NEW, LABS AND SEMI-WORKS, or any other equipment which line management feels a need to review.

The checklist is not intended to replace Process Hazards Analysis or Process Hazards Reviews for new processes or process changes. It is designed to evaluate the hardware involved in the process, and therefore become a part of a PHA or PHR.

#### Procedure

Before a new, modified, or relocated piece of equipment is put into service, an Equipment Safety Audit Checklist must be completed. The equipment proprietor is responsible for of CR&D Safety Group may be invited to attend, but is not required.

During the audit, upgrades to the equipment and/or operating procedures will be identified and agreed to by the audit team. These upgrades will be documented on the checklist, and the team will sign off.

After upgrades have been made, the proprietor will sign a verification and then the checklist becomes an Operating Approval.

Additional instructions and clarifications are contained within the checklist.

#### Central Research and development Equipment Safety Audit Checklist

The following checklist is to be used to evaluate the safety of EQUIPMENT to be used in research and development in a laboratory environment. It is not intended as a substitute for a formal Process Hazards Analysis of new or modified chemical processes. Consult with a CR&D Safety Group representative before proceeding.

Equipment: Environmentally Controlled Conductivity Measurement Chamber

Location: Bldg./Room: E306/Lab 1

Responsibility of: D.R. Burgess

Ext. 58105    Science Section: Chemical Science

#### Brief Description of Equipment and Intended Use:

The environmentally controlled conductivity measurement chamber consists of a stainless steel chamber, turbo and cryo pumps, sample heater capable of 350°C, and provisions for the introduction of dry or humidified gases (nitrogen, oxygen, and

carbon monoxide). The purpose of the equipment is to measure the resistance of a thin film which is electrically connected from within the chamber to an impedance bridge on the outside. The bridge is controlled by a computer and places a one volt potential across a film over a wide frequency range.

### Potential Physical Hazards

(Check [x] All That Apply - N/A For Those Not Applicable)

	x or N/A
I. Mechanical Motion	_____
II. Electrical	<u>  XX  </u>
III. Storage & Transportation of Raw Materials	_____
IV. Storage & Transportation of Products	_____
V. Compressed Gases and/or Air (One sheet per gas)	<u>  XX  </u>
VI. Liquids under Pressure (One sheet per liquid)	_____
VII. High or Low Temperatures	<u>  XX  </u>
VIII. Radioisotopes	_____
IX. X-Ray	_____
X. Non-Ionizing Radiation	
A. Infrared, Microwave, Radio Ultraviolet	
B. Lasers	_____
XI. High Noise	_____
XII. Procedures	<u>  XX  </u>
XIII. Environmental	_____
XIV. Other	<u>  XX  </u>
XV. Area	<u>  XX  </u>
XVI. Authorized Operators Sign Off Sheet	_____
XVII. Corrections to be Made, and Sign Off Sheet	_____

II. Electrical  
(Wilm. Area SHE Procedures, 1-1, 1-2, 1-3, 1-4, 1-5, 1-6)

Complete the following:

Equipment Voltage	Equipment Amperage
110	15-Mass flow controllers
110	15-Pressure gauge, current variants
110	15-Sample heater
220	25-Cryo pump

Is unit properly grounded?  Y  (Y/N)

Is unit properly wired? (Y/N)  Y  Any temporary wiring  N  (Y/N)

Has unit been inspected?  Y  (Y/N)

Multiple power sources present  Y  (Y/N)

Main Disconnect Switch(s) (MDS): Location(s) - Panel 1A: Right of doorway  
when looking into lab

Labeling of All Switches:

Voltage -	220	110	110	110
Fed From -	23	24	26	31
Amperage -	25	15	15	15
Equipment Fed -	Cryo Pump	MFC's	P meas., VaryAC's	Sample heater

Interlocks  N  (Y/N) Identify

Quarterly Interlock Inspection Log  N  (Y/N)

Location of Log  NA

Stored Energy (Y/N)  N  Where

Labelled (Y/N) Warning Signs Required  NA  (Y/N)

Consequences to research due to the loss of electrical power (describe)  
Sample heater will cool down, pump(s) will cut off, and gases will stop flowing.  
None of these actions pose a safety hazard.

Consequences of restoration of electrical power (describe)  
All equipment comes back on. Gases flow or pumping resumes and heater goes  
back to set temperature. None of these actions pose a safety hazard.

## V. Compressed Gases (Wilm. Area SHE Procedures, 11-1, 11-2, 11-3, 11-4)

Gas Oxygen  
 (Spell Out Name Of Gas, No Abbreviations)

Max Primary Pressure 20 PSIG Max Operating Pressure 20 PSIG

Primary Gas Source (Type) Cylinder

Pressure Relief Device Setpoint 60 PSIG

Are all components (Valves, gauges, hoses, etc.) rated above pressure relief device setpoint? Y (Y/N)

If NO, list components and pressure ratings.

Any safety interlocks? N (Y/N)

If YES, what are they?

Quarterly Log? N (Y/N), Location?

Are gauges located properly? Yes

Are gauges the proper range for application? Yes

Any mis-matched fittings or tubing? No

Have pressure regulators been inspected? Y (Y/N)

If YES, what is the date? 7/99

Does relief device outlet point in safe direction? Yes

Has relief device been inspected/tested? Y (Y/N)

If YES, what is the date? 7/99

Is gas flammable? N (Y/N) If YES, what precautions have been taken?

Is gas corrosive? N (Y/N) If YES, what precautions have been taken?

Where is gas cyl. kept when in service? Outside laboratoty in cylinder bay

Where is gas cyl. stored when not in use? Outside laboratoty in cylinder bay

V. Compressed Gases (Wilm. Area SHE Procedures, 11-1, 11-2, 11-3, 11-4)

Gas Nitrogen  
(Spell Out Name Of Gas, No Abbreviations)

Max Primary Pressure 20 PSIG Max Operating Pressure 20 PSIG

Primary Gas Source (Type) Cylinder

Pressure Relief Device Setpoint 60 PSIG

Are all components (Valves, gauges, hoses, etc.) rated above pressure relief device setpoint? Y (Y/N)

If NO, list components and pressure ratings.

Any safety interlocks? N (Y/N)

If YES, what are they?

Quarterly Log? N (Y/N), Location?

Are gauges located properly? Yes

Are gauges the proper range for application? Yes

Any mis-matched fittings or tubing? No

Have pressure regulators been inspected? N (Y/N)

If YES, what is the date? Not applicable for nitrogen

Does relief device outlet point in safe direction? Yes

Has relief device been inspected/tested? N (Y/N)

If YES, what is the date? Not applicable for nitrogen

Is gas flammable? N (Y/N) If YES, what precautions have been taken?

Is gas corrosive? N (Y/N) If YES, what precautions have been taken?

Where is gas cyl. kept when in service? Outside laboratoty in cylinder bay

Where is gas cyl. stored when not in use? Outside laboratoty in cylinder bay

V. Compressed Gases (Wilm. Area SHE Procedures, 11-1, 11-2, 11-3, 11-4)

Gas Carbon monoxide  
(Spell Out Name Of Gas, No Abbreviations)

Max Primary Pressure 20 PSIG Max Operating Pressure 20 PSIG

Primary Gas Source (Type) Cylinder

Pressure Relief Device Setpoint 60 PSIG

Are all components (Valves, gauges, hoses, etc.) rated above pressure relief device setpoint? Y (Y/N)

If NO, list components and pressure ratings.

Any safety interlocks? N (Y/N)

If YES, what are they?

Quarterly Log? N (Y/N), Location?

Are gauges located properly? Yes

Are gauges the proper range for application? Yes

Any mis-matched fittings or tubing? No

Have pressure regulators been inspected? Y (Y/N)

If YES, what is the date? 6/2000

Does relief device outlet point in safe direction? Yes

Has relief device been inspected/tested? Y (Y/N)

If YES, what is the date? 6/2000

Is gas flammable? N (Y/N) If YES, what precautions have been taken?

Is gas corrosive? N (Y/N) If YES, what precautions have been taken?

Where is gas cyl. kept when in service? Outside laboratoty in cylinder bay

Where is gas cyl. stored when not in use? Outside laboratoty in cylinder bay

## VII. High or Low Temperatures

Operating Temperature 437 °F / 225 °C (Provide Both)

Method of Heating or Cooling  
Resistance heaters

Surface Temperatures, Normal Operations 122 °F / 50 °C (Provide Both)  
(Insulation required for higher than +140°F, [+60°C] or lower than -20°F, [-29°C])

Warning signs or barricades needed? Yes

Describe "May be HOT" sign

Personal Protective Equipment Required  
Standard Operating Procedure does not require contact with equipment when it is heated. If need arises, wear leather gloves.

Can rapid temperature rise or fall create hazard? N (Y/N)

If Yes, what safeguards are in place? NA

Are Safety Interlocks in use? N (Y/N)

Interlock quarterly inspection log NA (Y/N)

Location of inspection log NA

## XII. Procedures

Have procedures been written containing the following sections?

### 1. EMERGENCY PROCEDURES?

Shut-down  Y  (Y/N)

Spills  Y  (Y/N)

### 2. OPERATING PROCEDURES:

Normal Start-Up?  Y  (Y/N)

Normal Operation?  Y  (Y/N)

Normal Shutdown?  Y  (Y/N)

Completed Authorized Operator and PPE Certification?  Y  (Y/N)

Are Procedures Posted  Y  (Y/N)

3. Lockout Procedure:  Y  (Y/N)

4. Operating Hazards (including chemical and mechanical)?  Y  (Y/N)

5. Line Break Procedure?  Y  (Y/N)

6. Personal Protective Equipment?  Y  (Y/N)

7. Procedure for Modifications?  Y  (Y/N) Modifications will be discussed with line management and safety prior to being made.

8. Compliance with Bldg. Roof Entry Procedure:  N  (Y/N)

## XIII. Environmental Procedures, Registrations and/or Permits

1. Waste Disposal Procedures?  Y  (Y/N)

2. Sample of completed waste tag?  Y  (Y/N)

3. Emission Registration (<10 lb/day)?  (<0.2)  Y  (Y/N) Reg. # 92/0436-0

4. Emission Permit (= or >10 lb/day)?  N  (Y/N) Permit # APC-

## XIV. Other

## Describe potential hazards

Removal of 8 inch O.D. flange on top of chamber presents opportunity for hand injury during bolt removal and flange removal.

During chamber fill procedure, pressure can build.

## Physical hazard prevention methods

Wear leather gloves during flange/bolt removal.

Pressure gauge to observe when chamber has reached atmospheric pressure and 20 psi pressure relief installed.

## Describe potential ergonomic hazards and corrective methods/measures

Top flange which is often removed is in horizontal position but is five feet off the ground. Removal/replacement requires standing on a kick stool.

## Special Training or Procedures

None

## Special Warnings or Devices Required

None

## XV. Area

Limit on personnel in attendance.

No

Special area requirements (High Noise, Biological Safety Lab, etc.) (Wilm. Area SHE Procedures, 10-4, 21-13)

No

Barricade required   N   (Y/N)

Special Signs, Alarms   N   (Y/N)

Do the potential hazards or business value warrant increased Fire Detection/Suppression in the area (i.e., detectors, sprinklers, etc.).   N   (Y/N)

Describe location of nearest Emergency Exits

Front of lab to hallway. Rear corner of lab to adjacent lab.

Location of nearest:

Fire Alarm/Evacuation Alarm Hallway outside laboratory

Fire Extinguisher Hallway outside laboratory

Safety Shower/Eye Wash In laboratory

Telephone (with Emergency sticker[X-53131]) In laboratory

Lone Worker   Y   (Y/N)

(Wilm. Area SHE Procedure 14-6)

After hours Operation   Y   (Y/N)

(Wilm. Area SHE Procedure 14-8)

Unattended Operation   Y   (Y/N)

(Wilm. Area SHE Procedure 14-14)

Special procedure for above

None

Posted Operating Procedures   Y   (Y/N)

Emergency Procedures   Y   (Y/N)

Emergency Contacts (2), and phone numbers posted on door   Y   (Y/N)

## Research Safety Review Checklist

Purpose  
Audit Date

The Research Safety Review Checklist is to be used in evaluating the safety of new, modified, or relocated experiments or tests which present a low potential hazard to employees, equipment and facilities, or the environment.

This checklist is intended to be used for those experiments or processes which present a low potential hazard, and therefore do not require a full Process Hazard Review (PHR). This checklist may become part of the a PHA or PHR if the experiment or test is expanded in size or complexity.

### Procedure

Before a new, modified, or relocated experiment or test is started, this Research Safety Review Checklist must be completed. The researcher in charge is responsible for completing the checklist and arranging a review with his/her management. Participation by a representative of the CR&D Safety Group is optional (recommended but not required).

During the review, upgrades to the process and/or apparatus and operating procedures will be identified by the review team. These upgrades will be documented on the checklist, and the team will sign-off.

After upgrades have been completed, the researcher will sign a verification, and then the checklist becomes a Test Authorization.

Additional instructions and clarification are contained within the checklist.

Experiment: Environmentally Controlled Conductivity Measurement Chamber      Location: E306/Lab 1

Researcher: D. R. Burgess    Ext. 8105    Office Location 262/206

Science Section Chemical Science      Manager K. Saturday

### Brief Description of Process:

The environmentally controlled conductivity measurement chamber consists of a stainless steel chamber, turbo and cryo pumps, sample heater capable of 350°C, and provisions for the introduction of dry or humidified gases (nitrogen, oxygen, and carbon monoxide). The purpose of the equipment is to measure the resistance of a thin film which is electrically connected from within the chamber to an impedance bridge on the outside. The bridge is controlled by a computer and places a one volt potential across a film over a wide frequency range.

A. Has the process been defined by completing the following information?

- 1.Process description (including chemistry of reactions)? Yes
- 2.Process flow diagram/equipment drawing? Yes
- 3.MSDS? Yes
- 4.Heat balance? Yes
- 5.Material balance? Yes

# Attach all of the above documentation to this checklist

B. Have the following potential hazards been evaluated, and have the necessary precautions been taken? Describe for each.

1.Toxicity of solids, liquids, and gases associated with the process? (Consult MSDS)

Yes. Procedure for disposal of carbon monoxide

2.Reactivity and explosion hazards of solids, liquids, and gases associated with the experiment or process?(Consult MSDS and \* 2-2, 2-3, 11-1, 20-8, 20-13)

Yes. Chamber has 20 psi pressure relief device

3.Corrosiveness of solids, liquids, and gases associated with the process? (Consult MSDS and and \* 2-20)

Not applicable

4.Ignition sources such as sparking motors, switches, alarms, exposed heaters, etc.? (\*2-1)

Not applicable

5.Fuel sources such as feedstocks, products, solvents, gaseous reaction products, insulation, etc., in the area that could be ignited? (Consult MSDS and \* 2-1)

Not applicable

6.Sound level exposure? (\* 10-4)

Not applicable

7.Nuclear radiation? (Consult Exp. Station Radiation Procedure, available from the CR&D Safety Group)

Not applicable

8.Radiation's such as ultraviolet, infrared, microwaves, lasers, X-rays, etc. (\*5-11,21-7,21-12)

Not applicable

9. Pressure system failure (projectiles, shrapnel, sprays from leaks, etc.)? (\* 11-1, 11-2, 11-3, 11-4))

Yes. Chamber has 20 psi pressure relief device

10. Electrical (e.g., bonding, grounding, sources identified/labeled)? (\* 1-3, 1-4, 1-5, 1-6)

Yes. Wired and inspected by site electrician. Equipment is grounded

11. Pressure and temperature transients?

Yes. "May be HOT" sign

12. Ergonomics (spacing, access to equipment, physical requirements of job)(\* 5-3)

Yes

13. Other

Not applicable

C. Have the following environmental considerations been taken into account?

1. Identification and resolution of potential air, water and soil pollution ?

Not applicable

2. Identification and development of written disposal methods for all feedstocks, intermediates, products, and wastes?

Yes

3. Identification of Toxic Substances Control Act problems and initiation of appropriate paperwork?

Not applicable

4. Have air emissions and air emission rates been calculated and reported to the Site Environmental Group?

Not applicable

D. Have the following been provided in designing and constructing the equipment/apparatus assembly?

1. Piping and Instrumentation diagram/mechanical drawing, including:

- a. Pressure relief valves and/or rupture disks where necessary (vessels, positive displacement pumps, blocked-in lines, blocked-in heat exchangers, compressors, etc.) with no valves or restrictions of any kind in the lines between the equipment and the protective devices? Yes
1. Properly sized? Yes
  2. Proper set pressure? Yes
- b. Proper relief and blowdown system with no valves or restrictions of any kind in the lines between the protective devices and the point of discharge?  
Not applicable
- c. Emergency overflow lines?  
Not applicable
- d. Emergency shutdown system?  
Not applicable
- e. Suitable alarms, shutdowns, interlocks, purges, etc., built into bring unit to a safe automatic shutdown in the event of an emergency such as:
1. Loss of instrument air? No
  2. Loss of steam? Not applicable
  3. Loss of cooling water? No
  4. Loss of electric power? No
  5. Loss of fuel? Not applicable
  6. Severe leakage by rupture of piping or equipment, by leakage from stuffing boxes or mechanical seals, or due to corrosion? Not applicable
  7. Fire in the area of the unit? Yes
  8. Other Not applicable
- f. Alarms for all critical variables (high/low temperature, high/low pressure, high/low flow, high/low level, etc.)? Not applicable
- g. Automatic shutdown of unit or certain pieces of equipment if certain critical variables are exceeded (high/low temperature, high/low pressure, high/low flow, high/low level, etc.)? Not applicable
- h. Fail-safe positioning of control valves and solenoid valves in the event of instrument air loss or electrical failure? Yes
- i. Pressure, temperature, flow, and level measurement devices installed at all critical points? Yes
- j. Suitable devices to prevent the flow or backup of materials into undesirable areas? Yes
- k. Suitable interconnect methods to utility systems such as water, gas, electricity, etc. (e.g., use of "back flow preventer valve" in a potable water system)? Yes
- l. Automatic detection devices for:
1. Toxic materials? Yes
  2. Combustible mixtures? No
  3. Radiation? No
  4. Oxygen detection? No

5.Fire? Yes

If Yes, describe: Sprinkler system

m.Backup pumps, compressors, etc., where required for safety? Not applicable

2.Detailed design for all processing equipment (pressure vessels, pumps, compressors, heat exchangers, etc.), including:

a.Designed in accordance with DuPont Engineering Standards where applicable? ASME code stamped appropriate. Yes

b.Proper materials of construction with consideration for corrosion, fatigue, stress cracking, embrittlement, strength, toughness, etc. Special care should be taken when using glass. Yes

c.Proper design and material for seals and gaskets? Yes

d.Proper design pressures and temperatures? Yes

e.Guards on all rotating, reciprocating, and conveying equipment? Yes

3.Detailed piping design in accordance with DuPont Engineering Standards where applicable? Not applicable

4.Equipment construction, testing, and inspection in accordance with DuPont Engineering Standards?

a.Pressure equipment? Yes

b.Steam piping? Not applicable

5.Vessel identification, tagging, and record keeping in accordance with the Site procedure? Yes

E. Has an operating procedure been written containing the following sections?

1.Emergency Procedures?

a.Shut-down? Yes

b.Spills? Yes

2.Operating Procedures:

a.Normal Start-Up? Yes

b. Normal Operation? Yes

c. Normal Shutdown? Yes

d. Completed Authorized Operator and PPE Certification? Yes

3. Lockout Procedure

4. Operating Hazards (including chemical and mechanical)? Yes

5. Line Break Procedure? Yes

6. Personal Protective Equipment? Yes

7. Procedure for Modifications? Yes

8. Waste Disposal Procedures? Yes

F. Have the following aspects of your process been considered?

Raw Materials:

1. What Raw Materials: are used in your process?  
Nitrogen, oxygen, carbon monoxide, water

2. Are any of the Raw Materials: (check all that apply)?

- Carcinogen
- Developmental Toxin
- Flammable
- Light Sensitive
- Mutagen
- Peroxidizable
- Pyrophoric
- Radioisotope
- Reactive With Air
- Reproductive Toxin
- Shock Sensitive
- Temperature Sensitive
- Toxic/Poison
- Biological

3. How will these Raw Materials: be stored?  
Cylinders

4.If refrigeration is required, is the refrigerator or freezer alarmed?  
Not applicable

G. Review of Incidents  
With management

H. Review of PPE and complete certification (examples of certifications available from CR&DSafety)  
Completed

I. Have the following storage and transportation aspects of your materials been considered?

1.How will you transport Raw Materials: through the building or across the site?  
Cylinder cart for gas cylinders

2.Will Raw Materials: be shipped off site?  
No

a.If Yes, have you provided a copy of the completed paperwork for shipping Raw Materials: off site?

3.If your Raw Materials: display any of the above listed characteristics, is the ductwork certified as leakproof?  
No

4.If your Raw Materials: display any of the above listed characteristics, will roof entry be prohibited while you are running?  
No

J. Have the following storage and transportation aspects of your product been considered?

1.Is the product (check all that apply and describe)

- Carcinogen
- Developmental Toxin
- Flammable
- Light Sensitive
- Mutagen
- Peroxidizable
- Pyrophoric
- Radioisotope

- Reactive With Air
- Reproductive Toxin
- Shock Sensitive
- Temperature Sensitive
- Toxic/Poison
- Biological

2. How will the product be stored?

No storage

3. If refrigeration is required, is the refrigerator or freezer alarmed?

Not applicable

4. How will you transport the product through the building and across the site?

No transport

5. Will the product be shipped off site?

No

a. If Yes, have you provided a copy of the completed paperwork for shipping the product off site?

6. If your product displays any of the above listed characteristics, is the ductwork certified as leakproof?

No

7. If your product displays any of the above listed characteristics, will roof entry be prohibited while you are running?

No

K. Area: Has the area been evaluated, and have the following safety items been considered? Describe the reason or location for each.

1. Is there a limit on personnel in attendance while operating?

No

2. Are there special area requirements, (BSL, High Noise, etc.)? (\* 10-4, 21-13)

No

3. Is a barricade required?

No

4. Are special signs or alarms needed?

Yes. "May be HOT"

5. Exit from laboratory or area, standard and emergency?

Yes. Exits located in front and rear corner of lab

6. Location of the nearest Fire and/or Evacuation alarm?

Yes. Hallway outside lab

7. Location of the nearest Fire Extinguisher?

Yes. Hallway outside lab

8. Location of the nearest Safety Shower and/or Eye Wash?

Yes. Inside lab

9. Location of the nearest telephone, and does it have a X-53131 Emergency Sticker?

Yes. Inside lab

10. Will there be any unattended operation of this process?

Yes

If yes, what special procedures will be implemented?

No special procedures. In process or evacuation mode, failure of any component does not present a safety hazard. There will be no unattended operation while carbon monoxide is in use.

11. Will this process be operated by a lone worker? (\*14-6)

Yes

12. Will this process be operated after normal working hours? (\* 14-8)

Yes

If yes, what special procedures will be implemented?

No after hours operation with carbon monoxide

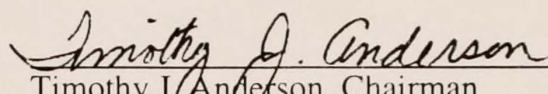
13. Are the Emergency Contacts (2), and phone numbers posted on the door?

Yes

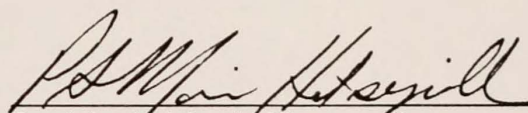
## BIOGRAPHICAL SKETCH

Born in Greenville, SC, Darren R. Burgess received his bachelor's degree in chemical engineering from Clemson University in 1992. The work on his doctoral dissertation in chemical engineering at the University of Florida was conducted under the supervision of Professor Timothy J. Anderson. The experimental portion of the degree requirements was performed at the Experimental Station of The DuPont Company's Central Research and Development division under the supervision of Dr. Patricia A. Morris Hotsenpiller.

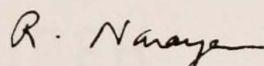
I certify that I have read this study and that in my opinion it conforms to acceptable standards of scholarly presentation and is fully adequate, in scope and quality, as a dissertation for the degree of Doctor of Philosophy.

  
Timothy J. Anderson, Chairman  
Professor of Chemical Engineering

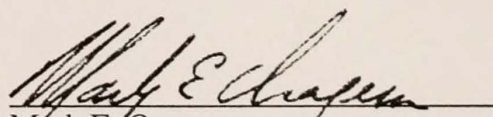
I certify that I have read this study and that in my opinion it conforms to acceptable standards of scholarly presentation and is fully adequate, in scope and quality, as a dissertation for the degree of Doctor of Philosophy.

  
Patricia A. Morris Hotsenpiller  
Research Associate, The DuPont Co.

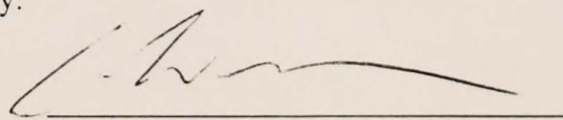
I certify that I have read this study and that in my opinion it conforms to acceptable standards of scholarly presentation and is fully adequate, in scope and quality, as a dissertation for the degree of Doctor of Philosophy.

  
Ranganathan Narayanan  
Professor of Chemical Engineering

I certify that I have read this study and that in my opinion it conforms to acceptable standards of scholarly presentation and is fully adequate, in scope and quality, as a dissertation for the degree of Doctor of Philosophy.

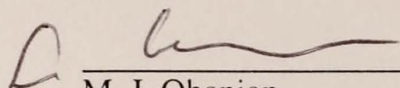
  
Mark E. Orazem  
Professor of Chemical Engineering

I certify that I have read this study and that in my opinion it conforms to acceptable standards of scholarly presentation and is fully adequate, in scope and quality, as a dissertation for the degree of Doctor of Philosophy.

  
Eric D. Wachsman  
Assistant Professor of Materials  
Science and Engineering

This thesis was submitted to the Graduate Faculty of the College of Engineering and to the Graduate School and was accepted as partial fulfillment of the requirements for the degree of Doctor of Philosophy.

August 1999



---

M. J. Ohanian  
Dean, College of Engineering

---

Winfred M. Phillips  
Dean, Graduate School